Inner detector alignment and top-quark mass measurement with the ATLAS detector

Tesi doctoral en Física
Regina Moles Valls
Dir. Dr. Salvador Martí i García
València, 2014

Universitat de València
Facultad de Física
Departament de Física Atòmica, Molècular i Nuclear

Dr. Salvador Martí i García,
Investigador Científic del CSIC

CERTIFICA:

Que la present memòria, "***Inner Detector Alignment and top-quark mass measurement with the ATLAS detector***", ha sigut realitzada sota la meva direcció en el Departament de Física Atòmica, Molecular i Nuclear de la Universitat de València per Regina Moles Valls i constitueix la seva tesi per obtar al grau de doctor en Física per la Universitat de València.

I per a que conste, en cumpliment de la legislació vigent, firme el present certificat en Burjassot a 19 de Febrer de 2014.

Sign. Dr. Salvador Martí i García

Contents

CHAPTER

1 Particle Physics overview

The Standard Model (SM) of particle physics is the theory that describes the fundamental constituents of the matter and their interactions. This model constitutes one of the most successful scientific theories ever built and provides a very elegant framework to explain almost all the processes in particle physics. Moreover, the SM has demonstrated to be highly predictive since it postulated the existence of many of the elementary particles as the $W^{\pm}$, Z^0 and H bosons and the top quark before their experimental confirmation. Despite all its great achievements, there are some questions that can not be answered nowadays by the SM. These ones do not invalidate the theory but only show that it is still incomplete. To cover these gaps in the theory some extensions as well as new theories have been proposed. The predictions from both, the SM and the new models, need to be confirmed experimentally. Here, the top quark, which is the heaviest known elementary particle, plays an important role. Due to its large mass it is involved in processes that can confirm or dispel some of the SM predictions. The top quark can also open the door to study new physics phenomena beyond the Standard Model (BSM).

This chapter is organized as follows: Section 1.1 presents a basic theoretical introduction to the SM and some of its experimental results, Section 1.2 introduces the top-quark physics and describes the important role of the top-quark mass in the SM and beyond.

1.1 The Standard Model

The SM tries to explain all physics phenomena based on a small group of elementary particles and their interactions. The concept of elementary has been evolving trough the years. Nowadays, the elementary particles, considered without internal structure, can be classified in three groups: leptons, quarks and bosons. Both leptons and quarks are spin $\frac{1}{2}$ particles called fermions and are organized in three families. One the other hand, the bosons are integer spin particles. The main properties of these particles can be seen in Figure 1.1. The electron (e), discovered by Thomson in 1897, was the first disclosed SM particle. The muon (μ) and tau (τ) leptons have the same properties as the electron except for their higher masses. These massive leptons do not appear in ordinary matter because they are unstable particles. Other familiar leptons, the neutrinos, were first postulated as decay products of some unstable nuclei. There are three neutrino classes associated to the three lepton families: ν_e, ν_μ and ν_τ. In addition to leptons, also hadrons, as protons and neutrons, are observed in nature. These hadrons are not elementary particles but formed by quarks that are indeed the elementary particles of the SM. The quarks are not seen in free states but there are many experimental evidences of their existence [1, 2, 3].

The particles interact through four fundamental forces which are associated with the force carriers bosons of integer spin. These forces, explained in more detail below, are: the electromagnetic, the weak, the strong and the gravity. Nowadays the SM only accommodates the first three forces but many exten-

sions and new theories try to unify all of them.

- The electromagnetic interaction occurs between particles which have electric charge. It is at the origin of the bounding of the electrons in the atoms. The photon (γ), which is a neutral massless particle, is its associated boson. Since the photon is massless the interaction has infinite range.
- The weak interaction is liable of the radioactive decay of the nucleus trough the exchange of Z^0 and $W^{\pm}$ bosons. These intermediate particles have very large masses which limit the range of the interaction, being this limit of the order of 10^{-18} m.
- The strong interaction is responsible for holding the protons and neutrons together in the atomic nuclei. The intermediate bosons of this force are the gluons which are massless particles that carry color charge. Due to this charge the gluons can interact between them producing therefore the confinement of the quarks inside hadrons. The range of this interaction is of the order of the medium size nucleus (10^{-15} m).
- Gravitation acts between all types of particles. Supposedly, its associated boson is the undiscovered graviton with a mass speculated to be lower than 10^{-32} eV [4]. This interaction, with an infinite range, can be considered negligible between elementary particles.

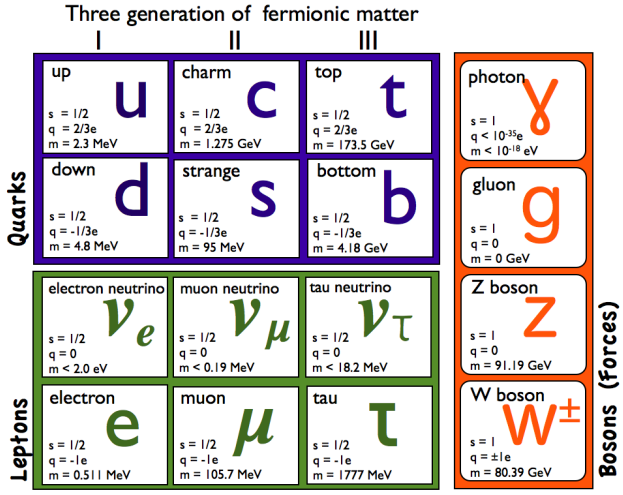

Figure 1.1: Representation of the SM particles. The fermions are separated in three families or generations. The bosons are the carriers of the fundamental forces. In addition, the Higgs boson, not included in the table above, is the SM particle in charge of generating the mass of the other particles. The properties reported on the table are: the spin (s), the electric charge (q given in units of charge electron) and the mass (m) [4]. Each particle has an antiparticle associated with the same mass but opposite charges.

In the quantum mechanics formalism the SM is written as a gauge field theory that unifies the electroweak (EW) interaction (unification of electromagnetic and weak forces) and the quantum chromodynamics (QCD). It is based on the symmetry group $SU(3)_C \otimes SU(2)_L \otimes U(1)_Y$, which represents the strong, the weak and the electromagnetic interaction respectively. The lagrangian of the SM describes the dynamics and the kinematics of the fundamental particles and their interactions. It has been built as a local invariant gauge theory [5]. The requirement of the local invariance introduces automatically the terms for the gauge bosons and also those that describe their interactions with matter. The insertion of

the mass terms in the lagrangian violates the local gauge symmetry. Nevertheless, these terms can not be removed given that some experimental results reveal that the weak intermediate gauge bosons are massive particles. This problem is solved by the spontaneous symmetry breaking (SSB) through the Higgs mechanism.

In order to apply the Higgs mechanism to give mass to $W^{\pm}$ and Z^0, the Higgs field, that breaks the electroweak symmetry, is introduced like the complex scalar field $\phi(x)$ with the following lagrangian ($\mathscr{L}$) and potential ($V(\phi)$):

$$\mathscr{L} = (\partial_\nu \phi)(\partial^\nu \phi)^\dagger - V(\phi) \qquad V(\phi) = \mu^2 \phi\phi^\dagger + \lambda(\phi^\dagger\phi)^2 \tag{1.1}$$

where μ is the coefficient of the quadratic term and λ the coefficient associated to the quartic self-interaction between the scalar fields. Imposing the invariance under local gauge transformation, the masses of the weak bosons are automatically generated, while the photon and gluon particles remain massless. After the SSB mechanism, the gauge fields are 8 massless gluons for the strong interaction, 1 massless photon for the electromagnetic interaction and 3 massive bosons ($W^{\pm}$ and Z^0) for the weak interaction.

Despite the prediction of the Higgs boson with a mass term of $M_H = \sqrt{-2\mu^2}$, the SM doesn't give a hint of its mass because μ is a priori an unknown parameter. The Higgs searches at LEP, Tevatron and also at the LHC have been progressively excluding most of the permitted mass regions. Recently a new particle has been discovered by the ATLAS and CMS experiments at the LHC [6]. The new particle has a mass $\sim$ 126 GeV and its properties are compatible with those predicted for the SM Higgs boson. Figure 1.2 shows the results obtained by the ATLAS detector with the data recorded during 2011 and 2012. This discovery is the outcome of the intense experimental and theoretical work to reveal the mass generator mechanism.

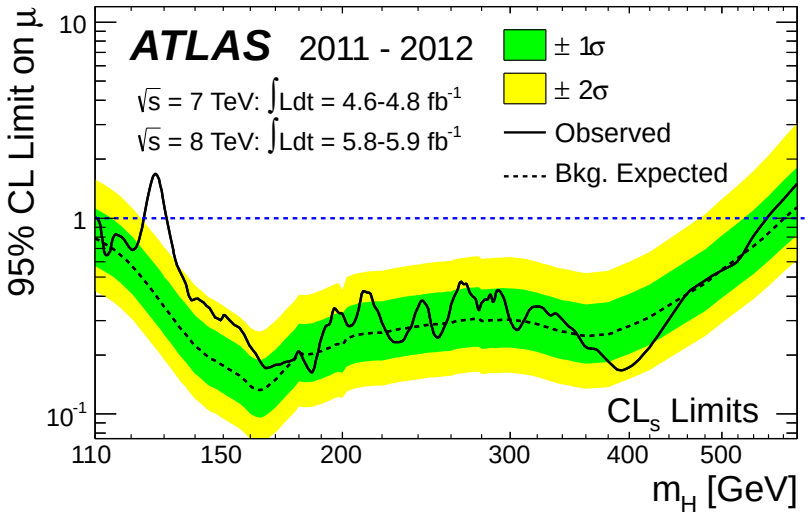

Figure 1.2: ATLAS combined search results: the observed (solid) 95% confidence level (CL) upper limit on the signal strength (μ) as a function of M_H and the expectation (dashed) under the background-only hypothesis. The dark and light shaded bands show the $\pm$ 1 σ and $\pm$ 2 σ uncertainties on the background-only expectation [6].

Currently, many of the experimental observations in particle physics seem to be consistent with the

SM. The LHC detectors have also re-checked this theory by doing precise measurements on quantities well known matching their theoretical expectations. Figure 1.3 shows the total production cross section of several SM processes as measured with the ATLAS experiment in proton-proton ($p - p$) collision at the LHC. These measurements are compared with the corresponding theoretical results calculated at Next-to-Leading-Order (NLO) or higher. The analyses were performed using different datasets and the luminosity used for each measurement is indicated next to each data point.

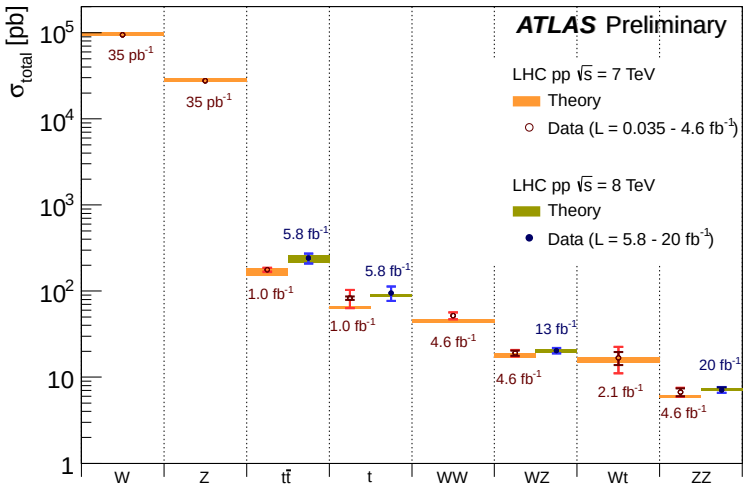

Figure 1.3: Summary of some SM cross section measurements compared with the corresponding theoretical expectations calculated at NLO or higher. The dark-colored error bar represents the statistical uncertainty. The lighter-colored error bar represents the full uncertainty, including systematics and luminosity uncertainties [7].

Despite the great success of the SM, there are still some theoretical problems and some not well understood experimental results. Some of these issues are reported below [8]:

- Unification of the forces: the great success of the unified electroweak theory motivates the research for unifying the strong interaction too. The Grand Unified Theory (GUT) tries to merge these forces in only one interaction characterized by a simple coupling constant. A naive extrapolation of the trend of the strong and EW interaction strengths from low to high energies suggests that the couplings might become equals at the unification mass of $\sim 10^{15}$ GeV. In addition, there are other theories that go one step further to join also the gravity. The unification scale for the four forces, called Planck mass, is expected to be of the order of $\sim 10^{19}$ GeV.
- Hierarchy problem: the hierarchy problem is related by the fact that the Higgs mass is unnaturally small. The theoretical calculation of the Higgs mass includes the loop quantum corrections associated to every particle that couple to the Higgs field up to certain scale. Considering the Planck scale, this calculation gives divergent masses that clashes with the current LHC results and all other indications from the SM results.
- Dark matter: it's known that the luminous matter in the universe, which emits electromagnetic radiation that can be detected, is only a 4.9% of the total existing matter [9]. Observation of the relative motion of the clusters and galaxies can not be explained only by this amount of matter. Despite of the experimental proves that the dark matter exists, its nature is yet unknown.

- Neutrino masses: experimental results show that neutrinos have small but finites masses instead of zero contrary to what usually the SM assumes. The neutrino oscillation effect can not occur with massless particles in the SM framework.

- Matter-Antimatter asymmetry: the SM treats the antiparticles as particles with the same masses but opposite internal charges. Nowadays, it is known there is an imbalance between matter and antimatter which origin is not understood yet. The violation of the CP symmetry in the SM can contribute to this unbalance. Nevertheless, the current experiments have observed that this effect is small to explain the present matter antimatter asymmetry. In front of that, new models would be required to explain this observation.

To address the opening questions and also to accommodate the experimental observations many theories are being developed. A very elegant theory to cover physics BSM is called Supersymmetry (SUSY) [8]. SUSY extends the SM by incorporating new supersymmetric particles with properties similar to the SM particles except for their spin. The fermionic superpartners will have a spin 0 while the bosonic supertpartners will have spin $\frac{1}{2}$. These superparticles could contribute to the called dark matter. They also can solve the hierarchy problem since the loop contribution of one particle to the Higgs mass is cancelled by the loop contribution of its superpartner. Moreover, the supersymmetry also introduces an ambitious scheme to unify gravity with the other forces.

According to the most common version of the theory, the decay of a superparticle has to have at least one superparticle in the final state, and the lightest particle of the theory must be stable. This provides an excellent candidate for dark matter. To verify supersymmetry it is necessary to detect superparticles, so that's why the spectrum of the superparticles is being extensively explored at LHC. No hint of supersymmetry has been observed up to now and many exclusion limits have been quoted in the recent years [7].

In front of the proliferation of new theories developed to solve the SM problems, further evidence and experimentation are required to determine their reliability. The top quark, due to its special properties (huge mass and fast decay), can help in the verification of the SM and also in the validation of its extensions.

1.2 Top-quark physics in the SM and beyond

The top quark was discovered in 1995 at the Tevatron accelerator in Chicago, USA [10, 11]. Its discovery was a great success of the SM because it confirmed the existence of the predicted weak isospin partner of the bottom quark. At hadron colliders, the top quark is predominantly produced through strong interaction and decays in a short time ($\sim 10^{-25}$ s [12]) without hadronizing. Its decay is almost exclusively through the single mode $t \to Wb$ (> 99%). According to the SM, the top quark is a fermion with an electric charge of q_{top} =(2/3)e and it is transformed under the group of color $SU(3)_C$.

The LHC can be regarded as a top quark factory. During the Run I[1] data taking, ATLAS recorded more than 6 millions of $t\bar{t}$ pair candidates and few millions of single top candidates. This huge amount of data facilitates the measurements of the top-quark properties with a high precision and also new physics searches. Many of these properties have already been studied at the LHC:

[1]During the first three years of operation, the LHC has completed a run of unprecedented success (Run I) accumulating ~5 fb^{-1} of integrated luminosity at 7 TeV and ~20 fb^{-1} of integrated luminosity at 8 TeV of $p-p$ collision in ATLAS and CMS detectors.

- **Mass**: it is intrinsically important for being the mass of one of the fundamental particles. Moreover, its large mass (~40 times higher than the following massive quark) confers it an important role in the radiative corrections having high sensitivity to physics BSM. Accurate measurement of its mass have been performed at the Tevatron [13] and the LHC [14]. More details about the relevance of the top-quark mass will be presented in the following subsections and in Chapter 5.

- **Cross Section:** the $t\bar{t}$ cross section at LHC has been measured to be 177^{+11}_{-9} pb at 7 TeV [15] and 241±32 pb at 8 TeV in the l + *jets* channel [16]. The ATLAS $t\bar{t}$ cross-section measurements compared with their theoretical predictions can be seen in Figure 1.4 (left). The single top quark is produced through the electroweak interaction. The s-channel, t-channel and Wt production cross-section have been also measured in ATLAS [17, 18, 19]. Their results compared with the theoretical predictions are shown in Figure 1.4 (right).

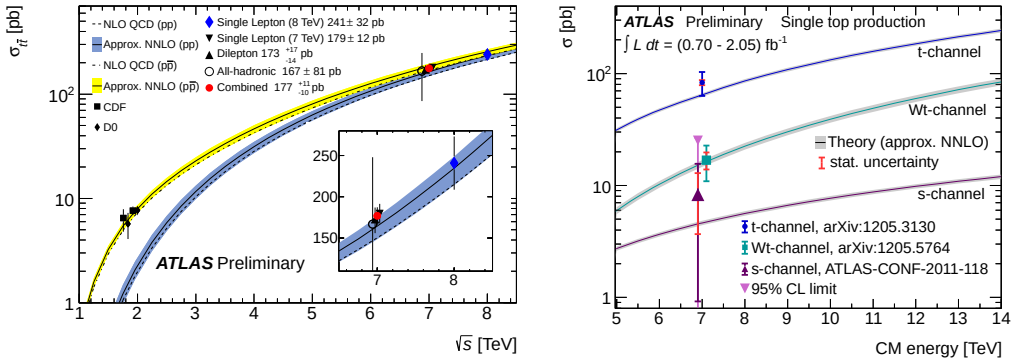

Figure 1.4: Left: Summary plot showing the top pair production cross section as a function of the LHC center of mass energy ($\sqrt{s}$). The experimental results in the various top decay channels (and their combination) at 7 TeV and the recent result at 8 TeV are compared to an approximate Next-to-Next-to-Leading-Order (NNLO) QCD calculation. Right: Summary of measurements of the single top production cross-section as a function of the center of mass energy compared to the corresponding NNLO theoretical expectation for different production mechanisms.

- **Charge:** the prediction of the top-quark charge in the SM is q_{top} =(2/3)e. Nevertheless, some exotic scenarios postulate a different charge: q_{top} =(-4/3)e. The top-quark charge measurement in ATLAS gives a good agreement with the SM and excludes the exotic scenarios with more than 8 standard deviations (σ) [20].

- **Charge Asymmetry:** the SM predicts a symmetric $t\bar{t}$ production under charge conjugation at leading-order (LO) and small asymmetry at NLO due to the initial and final gluon emision. The $gg \rightarrow t\bar{t}$ is a symmetric process while $q\bar{q} \rightarrow t\bar{t}$ is not because the top quarks are emitted in the direction of the incoming quark and the anti-top quarks in the direction of the incoming anti-quarks. For $p - \overline{p}$ colliders, as Tevatron, the charge asymmetry is measured as a forward-backward asymmetry. Recent asymmetry measurements at Tevatron have shown a 2-3σ excess over the SM expectations [21, 22]. On the other hand, $p - p$ colliders, as the LHC, present an asymmetry between the central and forward region. Several processes BSM could affect this asymmetry, nevertheless the current ATLAS results are consistent with the prediction of the SM [23].

- **Spin:** the top-quark spin properties have been studied through the angular distribution of the two leptons in the di-lepton topology. Anomalies in the spin sensitive distribution could reveal BSM physics. However ATLAS results show a spin correlation in agreement with the NLO SM predictions. The hypothesis of zero spin correlation is excluded at 5.1 standard deviations [24].

- **Anomalous couplings:** the top-quark physics also involves searches for anomalous interactions. The polarization of the W in the top-quark decays is sensible to the structure of the Wtb vertex. The effective lagrangian of this vertex includes anomalous couplings which are null in the SM. Any deviation from zero in the measurement of these coupling requires necessarily physics BSM. The present ATLAS measurements are consistent with the SM predictions [25, 26].

- **Rare decays:** according to the SM, the Flavour Changing Neutral Current (FCNC) are forbidden at tree level and suppressed at higher orders. Nonetheless, extensions of the SM with new sources of flavour predict higher rates for FCNCs involving the top quark. The current ATLAS results show no evidences for such processes [27, 28].

- **Resonances:** many models of physics BSM predict the existence of new resonances that may decay into top-quark pairs. The $t\bar{t}$ invariant mass spectrum is searched for local excesses deviating from the SM prediction. The current ATLAS results do not show any evidence of the $t\bar{t}$ resonances. The most studied models have been excluded in the range between 0.5 TeV and 2 TeV at 95% CL [29].

1.2.1 Top-quark mass

The top-quark mass (m_{top}) is one of the fundamental parameters of the SM. As all the other fermion masses and coupling constants, it also depends on the renormalization scheme. Thus m_{top} has to be understood within a theoretical framework. Nonetheless, contrary to the lepton mass, the quark mass definition has intrinsic limitations since quarks are colored particles and do not appear as asymptotic free states. The Appendix A shows the masses of some leptons and quarks for different renormalization schemes.

There are different top-quark mass definitions:

- **Pole mass ($m_{\text{top}}^{\text{pole}}$) [30]:** this mass is defined in the on-shell scheme in which it is assumed that the renormalized mass is the pole of the propagator. The infrared renormalons plagued the pole mass with an intrinsic non perturbative ambiguity of the order of Λ_{QCD} [2]. Hence, the $m_{\text{top}}^{\text{pole}}$ can not be measured with an accuracy better than the order of Λ_{QCD}.

- **Running mass ($m_{\text{top}}^{\overline{\text{MS}}}$) [31]:** this mass is defined in the modified Minimal Subtraction scheme ($\overline{MS}$) where the renormalized lagrangian parameters become energy dependent. The running masses should be understood within the QCD lagrangian (or dynamics). Generally speaking, the mass not only influences the available phase space for a given process, but also its amplitude via the renormalization group equation, which may depend on the energy scale, and part of that dependence goes through the running mass.

- **Kinematic mass:** the experimental measurements are principally based on a kinematic reconstruction of the top-quark decay products. The mass measurement is commonly extracted by comparing the data with the MC distributions generated at different top-quark masses. In this case, the quantity measured merely corresponds to the top-quark MC mass parameter which is not well defined in any theoretical scheme. Nevertheless the difference between this kinematic mass and the top-quark pole mass is expected to be of the order of 1 GeV [32, 33].

[2] Λ_{QCD} is the QCD parameter that characterize the confinement as: $\lim_{Q\to\Lambda_{\text{QCD}}} \alpha_s(Q^2) \to \infty$, where Q is the energy scale.

1.2.2 Top-quark mass in the EW precision measurements

The EW observables measured with high accuracy serve as an important tool for testing the SM theory. The validation of this theory is done by an accurate comparison of the experimental results and the EW precision measurements extracted from the EW fit [34]. In this fit, the most accurate value of the EW parameters together with their theoretical predictions (incorporating higher orders quantum corrections) are taken into account. The EW fit results can be also used to predict or constraint some other parameters of the model. For example, the $W^{\pm}$ and Z^0 masses have been predicted by the SM being:

$$M_Z \cdot \cos\theta_W = M_W = \frac{1}{2} \cdot v \cdot \alpha_e \tag{1.2}$$

where v is the vacuum expectation value, α_e is the electroweak coupling, θ_{W} is the mixing angle and M_Z and M_W are the boson masses. The first simple prediction is directly extracted from Equation 1.2: the M_Z has to be bigger than M_W. This prediction is in agreement with the experimental measurements: $M_W = 80.385 \pm 0.015$ GeV and $M_Z = 91.1876 \pm 0.0021$ GeV from [4].

In the gauge scalar sector, the SM lagrangian contains only 4 parameters that can be traded by α_e, θ_W, M_W and M_H. Alternative one can choose as free parameters the Fermi constant (G_F), α_e, M_Z and M_H with the advantage of using three of the SM parameters with higher experimentally precision. The relation between them is shown in equation 1.3.

$$\sin\theta_W = 1 - \frac{M_W^2}{M_Z^2} \qquad\qquad M_W^2 \sin\theta_W = \frac{\pi\alpha_e}{\sqrt{2}G_F} \tag{1.3}$$

These equations are calculated at tree level, nevertheless higher order corrections generate additional terms. Quantum corrections offer the possibility to be sensitive to heavy particles, which are only kinematically accessible through virtual loop effects. The top-quark mass enters in the EW precision measurements via quantum effects. In contrast to the corrections associated to the other particles of the SM, the top-quark mass gives sizable corrections owing to its large mass. For instance, a m_{top} of 178 GeV gives quadratic corrections to M_W with a sizable effect of 3% [35].

If one assumes that the new boson discovered by the ATLAS and CMS experiments is the SM Higgs boson, briefly explained in Section 1.1, all the SM fundamental parameters are accessed experimentally for the first time. At this point, one can overconstrain the SM and evaluate its validity. The compatibility of each of the EW parameters can be studied taking into account the differences between its experimental results and the EW fit prediction (the parameters under test are considered free parameters in the EW fit). For example, the impact on the indirect determination of the W mass, mixing angle and top-quark mass have been studied and all of them have shown a good agreement [36]. The main goal of the EW precision fit is to quantify the compatibility of the mass of the discovered boson with the EW data. The uncertainty of many of these indirect predictions are dominated by the top-quark mass error, which motivates the measurement of the top-quark mass with a high precision.

Figure 1.5 shows the agreement between the experimental measurements and the EW fit predictions for the top and W masses. The contours display the compatibility between the direct measurements (green bands and data point), the fit results using all data except the M_{W}, m_{top} and M_{H} measurements (grey contour areas), and the fit results using all data except the experimental M_{W} and m_{top} measurements (blue contour areas). The observed agreement demonstrates the impressive consistency of the SM.

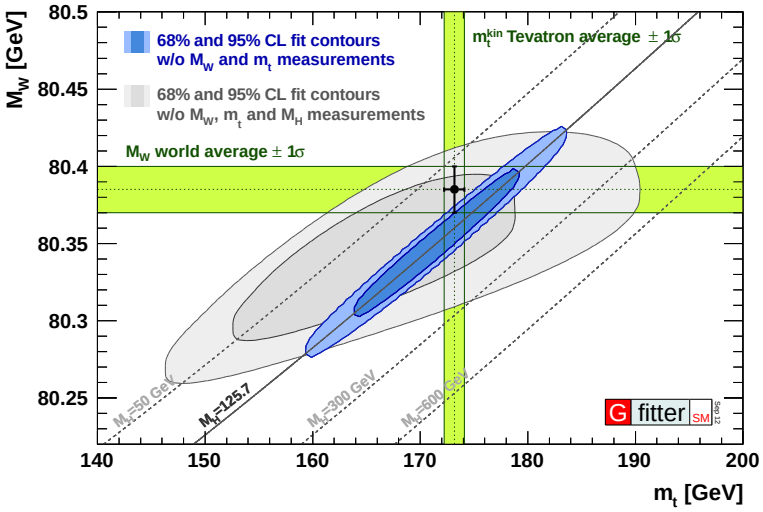

Figure 1.5: Contours of 68% and 95% confidence level obtained from scans of fits with fixed variable pairs M_{W} vs m_{top}. The narrower blue and larger grey allowed regions are the results of the fit including and excluding the M_{H} measurements respectively. The horizontal bands indicate the 1σ regions of the M_{W} and m_{top} measurements (world averages)[36].

1.2.3 Top-quark mass in the stability of the electroweak vacuum

The discovery of a new particle compatible with the SM Higgs boson brings to the table questions inaccessible until now. For example, the discussion about the stability of the electroweak vacuum in the SM has been recently reopened [37, 38]. The Higgs potential is the way adopted by the SM to break the electroweak symmetry. The crucial question here is what Higgs boson mass allows the extrapolation of the SM up to higher scales while still keeping the electroweak vacuum stable. The latest NNLO calculations have been used to obtain a vacuum stability condition extrapolated up to the Planck scale. This condition from [37] is shown in Equation 1.4.

$$M_H \geq 129.2 + 1.8 \times \left(\frac{m_{\mathrm{top}}^{\mathrm{pole}} - 173.2\ \mathrm{GeV}}{0.9\ \mathrm{GeV}} \right) - 0.5 \times \left(\frac{\alpha_s(M_Z) - 0.1184}{0.0007} \right) \pm 1.0\ \mathrm{GeV} \tag{1.4}$$

The equation critically depends on the Higgs boson mass (M_H), the strong coupling constant (α_s) and the top-quark pole mass ($m_{\mathrm{top}}^{\mathrm{pole}}$). If one assumes that the new boson discovered at LHC corresponds to the SM Higgs boson, the Higgs mass is known being $M_H \sim 124 - 126$ GeV [6]. The strong coupling constant has been also measured with high accuracy: $\alpha_s(M_Z) = 0.1184 \pm 0.0007$ [4]. Finally, the third parameter is the top-quark pole mass which has been explained in Section 1.2.1. In order to see if the expected M_H accomplishes the vacuum stability condition, the latest top-quark mass measurement has been used as input. The $m_{\mathrm{top}}^{\mathrm{pole}}$ has been derived from the $m_{\mathrm{top}}^{\overline{\mathrm{MS}}}$ measurement extracted from present cross section analysis at Tevatron [39]. Using this mass value as input, the stability condition gives a limit of $M_H \geq 129.4 \pm 5.6$ GeV which is compatible with the mass of the recent boson discovered within its error. Figure 1.6 illustrates the electroweak vacuum areas for the absolute stability (given by Equation 1.4), metastability (regime reached when the condition given by Equation 1.4 is not met and the EW vacuum lifetime overshoots the age of the universe) and instability (regime attained when the condition given

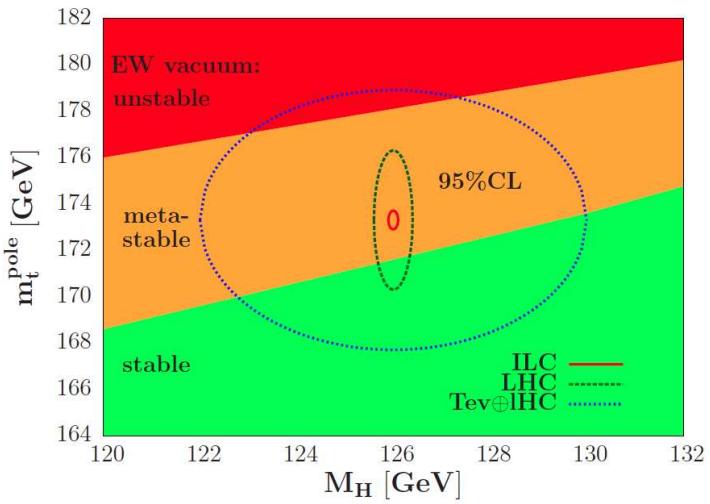

Figure 1.6: Areas in which the SM vacuum is absolutely stable, metastable and unstable up to the Planck scale [37]. The 2σ ellipses in the $[M_H, m_{top}^{pole}]$ plane have been obtained from the current top-quark and Higgs mass measurements at the Tevatron and the LHC experiments. Also the uncertainty from future measurements at the LHC and at the ILC have been included.

by Equation 1.4 is not met and the EW vacuum lifetime is shorter than the age of the universe) in the $[m_H, m_{top}^{pole}]$ plane at the 95% confidence level. The achievable resolution on future LHC and International Linear Collider (ILC) results have been also added.

More precise determination of the stability of the electroweak vacuum must include a more accurate top-quark pole mass measurement. In this way, the future e^+e^- linear collider could be used to determine the top-quark pole mass with an accuracy of few hundred MeV.

CHAPTER

2 The ATLAS Detector at the LHC

The Large Hadron Collider (LHC) is the most powerful particle accelerator built up to date. It is located at CERN (*European Organization for Nuclear Research*) in the border between France and Switzerland, close to Genève. The LHC is a hadronic machine designed to collide protons at a center of mass energy of 14 TeV. Such high energies open the door to physics regions unexplored until now. The proton beams collide in four points of the ring where the detectors are installed. ATLAS is one of two multi-purpose detectors built to investigate the different physics produced by the LHC collisions. It is composed by many sub-detectors which have been designed to accomplish specific requirements. Since the start of the LHC operation in 2009 this accelerator has been improving its performance: increasing the luminosity and the beam energy up to 4 TeV (8 TeV collisions). Also the ATLAS detector has been operating with an efficiency higher than 90% during all data taking periods. This impressive performance has permitted to store an integrated luminosity of 26.5 fb^{-1} (combining the integrated luminosity obtained at energies of 7 TeV and 8 TeV during 2011 and 2012). Thanks to the good design, construction and operation of the machine and detectors many results have been obtained and some of the goals of the ATLAS detector have already been achieved.

This chapter is organized as follows: Section 2.1 presents the LHC machine and its main properties and parameters, Section 2.2 introduces the ATLAS detector giving an overview of its sub-systems and their main functionalities and requirements.

2.1 The LHC

The LHC [40], with a circumference of 27 Km and located ~100 m underground, is the biggest accelerator at CERN [41] facility. This machine accelerates two proton beams in opposite directions and makes them to collide in the points of the ring where the detectors are installed. The LHC has been built to allow an extensive study of the particle physics at the TeV scale.

To achieve the design energies of the LHC, the protons need to be pre-accelerated before their insertion into the main ring. The CERN has an accelerator complex [42] composed by a succession of machines that speed up particles to increase their energies in several steps. The acceleration of the protons starts in the LINACS, linear accelerators, reaching an energy of 50 MeV. These beams are transferred to the circular accelerator PS Booster, which provides an energy of 1.4 GeV. Straightaway, the bunches are inserted into the Proton Synchrotron to get an energy of 26 GeV and finally into the Super Proton Synchrotron to reach an energy of 450 GeV. The latest element of this chain is the LHC with a design energy of 7 TeV per beam.

To accomplish the goals of the LHC, both high beam energies and high beam intensities are required.

In order to provide high beam intensities the $p-p$ beams instead of the $p-\overline{p}$ beams have been chosen due to their easier production and storage. Therefore, being a $p-p$ collider, the LHC needs two separate pipes to drive the particles in opposite rotation directions. Because of the space limitation in the tunnel a twin-bore system has been developed to allow two beam channels sharing the same mechanical and cryostat structure. In the interaction regions, where both beams use the same pipe, an optimized crossing angle has been implemented in order to avoid parasitic collisions. On the other hand, the higher energies only can be reached with NbTi superconducting magnets operating with a magnetic field of ~8 T. To get these fields they are cooled down to 1.9 K using superfluid liquid helium. There are different types of magnets along the ring: 1232 dipoles to guide the beam through its trajectory, 392 quadrupoles to focus the beams and sextupoles and multipoles to control the beam instabilities.

At the designed luminosity ($\mathcal{L}$[1]) of 10^{34} cm^{-2} s^{-1}, on average, more than 25 interactions will take place per bunch crossing. This high luminosity allows the study of many interesting processes with low cross sections.

The protons will be bundled together into 2808 bunches with 115 billion protons per bunch. The two beams collide at discrete intervals never shorter than 25 nanoseconds. In addition to proton beams the LHC has been also designed to collide heavy ions [43]. The LHC operational design parameters for protons and ions running conditions are shown in Table 2.1.

Design beam parameters	$p-p$	$Pb-Pb$
Injection energy	0.45 GeV	177.4/nucleon GeV
Beam energy	7 TeV	2760 GeV/nucleon
Dipole Field	8.33 T	8.33 T
Luminosity	10^{34} cm^{-2} s^{-1}	10^{27} cm^{-2} s^{-1}
Bunch spacing	25 ns	100 ns
Particles per bunch	1.15×10^{11}	7.0×10^{7}
Bunches per beam	2808	592

Table 2.1: The main LHC design parameters for proton-proton and heavy ion collisions.

To study the LHC physics, four big detectors have been installed in the collision points. The construction of these detectors has been a challenge due to the high interaction rates, extreme radiation damage and particle multiplicities produced by the LHC.

There are two general purpose detectors, ***A T**oroidal **LHC** **A**pparatu**S*** (ATLAS) [44] and the ***C**ompact **M**uon **S**olenoid* (CMS) [45], which have been designed to cover all the possible physics for proton-proton and nuclei-nuclei interactions. These detectors may operate with a designed peak luminosity of $\mathcal{L} = 10^{34}$ cm^{-2} s^{-1} for proton operation. Having two independent detectors is vital for cross-checking of the discoveries made. On the other hand, ***L**arge **H**adron **C**ollider **b**eauty* (LHCb) [46] and ***A L**arge **I**on **C**ollider **E**xperiment* (ALICE) [47] are specialized detectors focused on specific phenomena. The LHCb is a single-arm spectrometer with a forward angular coverage focused on the study of the heavy flavour physics. The LHCb has been designed to run at low luminosity with a peak of $\mathcal{L} = 10^{32}$ cm^{-2} s^{-1}. Finally, the ALICE detector has been built to study the physics of strong interacting matter at extreme energy densities where the quark-gluon plasma is formed. The peak luminosity for the nominal lead-lead ion operation is $\mathcal{L} = 10^{27}$ cm^{-2} s^{-1}. A schematic view of these detectors overimposed on their specific locations in the LHC ring is shown in Figure 2.1

[1]The luminosity $\mathcal{L}$ is defined as the number of particles per unit of time and area, and it only depends on beam parameters: $\mathcal{L} = f\frac{n_1 n_2}{4\pi\sigma_x\sigma_y}$ where f is the bunches crossing frequency, n_i the number of particle per bunch and $4\pi\sigma_x\sigma_y$ is the beam section area.

In addition, there are two small LHC detectors focused on the forward physics that is not accessible to the general-purpose experiments: the *Total elastic and diffractive cross-section measurement* experiment (TOTEM) and the ***L**arge **H**adron **C**ollider **f**orward* experiment (LHCf). TOTEM [48] is dedicated to the precise measurement of the $p-p$ interaction cross-section and accurate monitoring of the LHC luminosity. LHCf [49] uses forward particles produced by the LHC collisions as a source to simulate cosmic rays in laboratory conditions. Moreover, the ***Mo**nopole and **E**xotics **D**etector **a**t the **L**HC* experiment (MOEDAL) [50] has been approved to be installed in the LHC ring to directly search for a hypothetical particle called magnetic monopole.

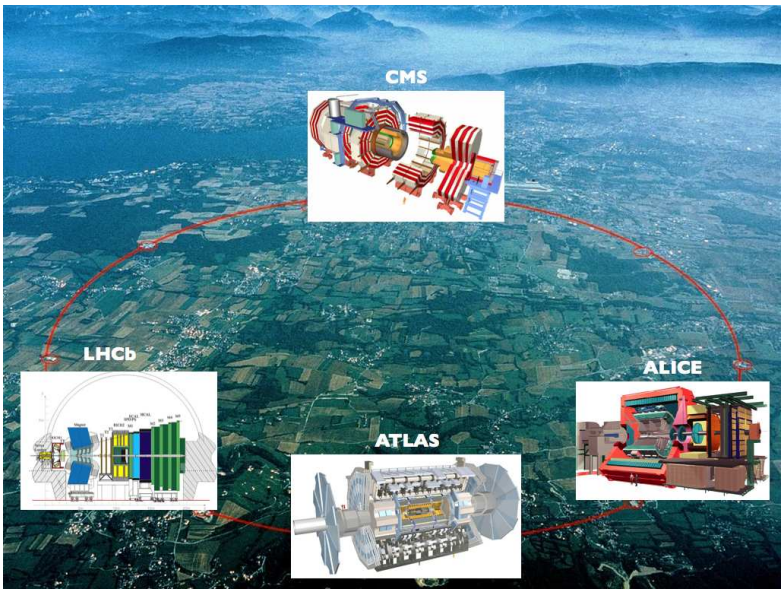

Figure 2.1: Schematic pictures of the four main experiments installed at the LHC ring: ATLAS, LHCb, CMS and ALICE.

2.2 The ATLAS Detector

The ATLAS detector [44] is a general purpose experiment built to fully exploit the physics produced by the LHC. It will provide many accurate measurements ranging from precision physics within the SM all the way to new physics phenomena. At the LHC design luminosity, a large number of particles emerge from the interaction point every collision creating a high-track multiplicity in the detector. The ATLAS detector has been designed to work under these conditions. The layout of the ATLAS experiment can be seen in Figure 2.2. This detector weights 33 tones and it is 45 m long and 22 m tall. Its large size allows a good momentum resolution of the charged particles. It is composed by different sub-detectors installed around the beam pipe. In general all of them presents the same structure: cylindrical layers around the beam pipe in the central (barrel) part and discs perpendicular to the beam direction in the forward (end-cap) region. This layout covers hermetically the space around the interaction point allowing a whole reconstruction of the events. Each sub-detector has been developed for measuring a specific property of the particles. The most internal one is the Inner Detector (ID) which is responsible of the pattern recognition, the momentum measurement of the charge particles and the reconstruction of the primary and the secondary vertices. The ID is surrounded by a solenoid magnet [51] that with a 2 T magnetic

field bends the trajectories of the charged particles. The following detectors are the calorimeters which are the responsible of measuring the energy of the particles: the liquid-argon electromagnetic calorimeter measures the energy of the electrons, positrons and photons while the hadronic calorimeter measures the energy deposited by the hadrons. The outermost detector is the Muon Spectrometer (MS) that identifies the muons with a high momentum resolution. A toroidal magnet is located close of the MS generating a strong bending for the muons. All ATLAS sub-systems have shown an excellent performance during the first years of running operating with high data taking efficiency [52]. The integrated luminosity recorded by ATLAS was 45 pb^{-1} in 2010; 5.2 fb^{-1} in 2011 and 21.3 fb^{-1} during 2012 [53]. Thanks to this amount of data many of the SM properties have been confirmed and also new particles have been discovered.

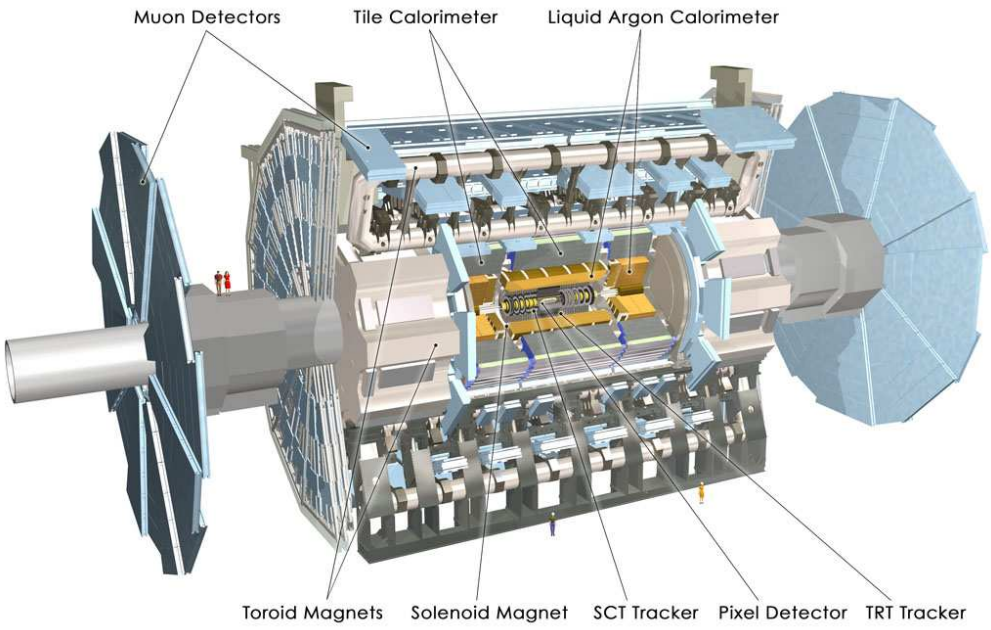

Figure 2.2: Schematic layout of the ATLAS detector.

2.2.1 Inner Detector

The Inner Detector [54] is the innermost ATLAS tracking system. At the LHC design luminosity it will be immersed in a very large track density environment. The ID has combined different technologies to provide hermetic and robust pattern recognition, excellent momentum resolution and high accuracy for both primary and secondary vertex reconstruction. The ID is composed by three sub-detectors: the Pixel detector, the SemiConductor Tracker detector (SCT) and the Transition Radiation Tracker detector (TRT). Therefore, the ID information is based on a combination of, from inside out: pixel, silicon strip and straw tube detectors. The ID, which has a cylindrical geometry with a length of 7 m and a diameter of 2.3 m, surrounds the LHC beam pipe. It is immersed in a 2 T magnetic field generated by a solenoid. The superconducting magnet, with a diameter of 2.5 m and a length of 5.3 m, is shorter than the ID which causes a non-uniform field specially towards the end-caps. Nevertheless these inhomogeneities in the forward region have no major consequences since they are mapped and included in the track reconstruction. This magnetic field makes possible the determination of the p_{T} by measuring the curvature of the charged

tracks. The ID layout can be seen in Figure 2.3 (left).

The main goal of the Pixel detector [55] is to determine the track impact parameters for the vertex reconstruction. It is composed by 1744 identical silicon pixel modules with a pixel size of 50 μm $\times$ 400 μm. They are mounted in three cylindrical layers around the beam axis in the barrel region and three discs perpendicular to the beam axis in the end-cap region. This layout generates on average 3 pixel hits per track. The intrinsic resolution of the pixel detector is 10 μm in the rϕ (parallel to the most sensitive direction of the module) and 115 μm in the long pixel direction (along the beam pipe for the barrel modules and radial for the end-cap ones).

The SCT detector [56] aids in the measurement of the particle momenta. It is composed by 4088 modules installed in 4 layers in the barrel and 9 discs in each of the end-caps. Each SCT module is formed by two silicon micro-strips detectors of 80 μm pitch glued back-to-back with a stereo angle of 40 mrad. The detector information is combined to provide on average 4 space points per track. There are 5 different module designs, one for the barrel layers and 4 for the end-cap discs. The micro-strip silicon detectors have an intrinsic resolution of 17 μm in the rϕ direction (across the strips) and 518 μm along the strips.

The TRT [56] helps in the pattern recognition and momentum measurement. The TRT produces on average 30 hits per track. The technology used is based on ~300.000 straw tube filled with gas elements with 4 mm of diameter and variable length depending on the zone of the detector. The intrinsic resolution of the TRT is 130 μm in the perpendicular direction to the straw.

The combination of precision tracker detectors at small radius with the TRT detector in the outermost part provides a pattern recognition with high precision in the rϕ and z coordinates. Tracks with p_{T} larger than 500 MeV are reconstructed efficiently in a pseudo-rapidity (η) range of $|\eta| < 2.5$. Figure 2.3 (right) shows the reconstruction efficiency for muons, pions and electrons with a p_{T} of 5 GeV. The muon detection efficiency is close to 100% for all $|\eta|$ range while for electrons and pions the efficiency follows the shape of the amount of material in the ID as a function of $|\eta|$ [54].

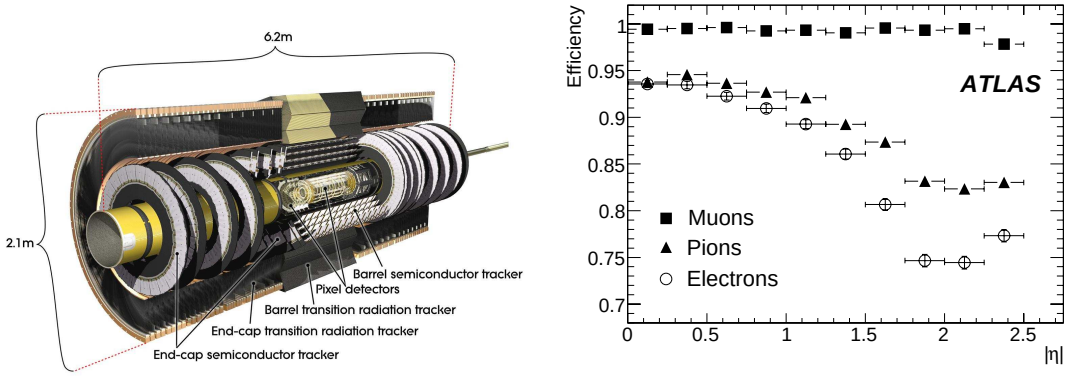

Figure 2.3: Left: Picture of the Inner Detector layout. Right: Track reconstruction efficiencies as a function of $|\eta|$ for muons, pions and electrons with p_T = 5 GeV. The inefficiencies for pions and electrons reflect the shape of the amount of material in the inner detector as a function of $|\eta|$ [54].

2.2.2 Calorimetry system

The calorimetry system [54] is the detector in charge of measuring the energy of the particles. It is composed by the electromagnetic calorimeter (EM) and the Hadronic calorimeter. The EM calorimeter must be able to detect efficiently electrons, positrons and photons within a large energy range, from 5 GeV to 5 TeV, and also to measure their energies with a linearity better than 5% (Figure 2.4 right). Moreover the hadronic calorimeter provides a high quality and efficient jet reconstruction. The ATLAS calorimeter is composed of a number of sample detectors that offer near hermetic coverage in pseudorapidity range ($|\eta| < 4.9$). The sampling calorimeters consist of a dense absorber material to fully absorb initial particles and detection material to produce the output signal proportional to the input energy. The depth of the calorimeter is large enough to fully contain the showers, avoiding the contamination of the MS with possible particles that could escape of the calorimeter and enter into it deteriorating the muon reconstruction (punch-trough effect). The EM calorimeter depth is larger than 22 X_0 [2] , in the barrel and more than 24 X_0 in the end-cap; the radial depth of the hadronic calorimeter is approximately 7.4 λ[3] in the barrel and more than 10 λ in the end-cap. The total thickness is the adequate to provide a good resolution for high energy jets and good E_T^{miss} energy reconstruction. The layout of the ATLAS calorimeter is shown in Figure 2.4 (left).

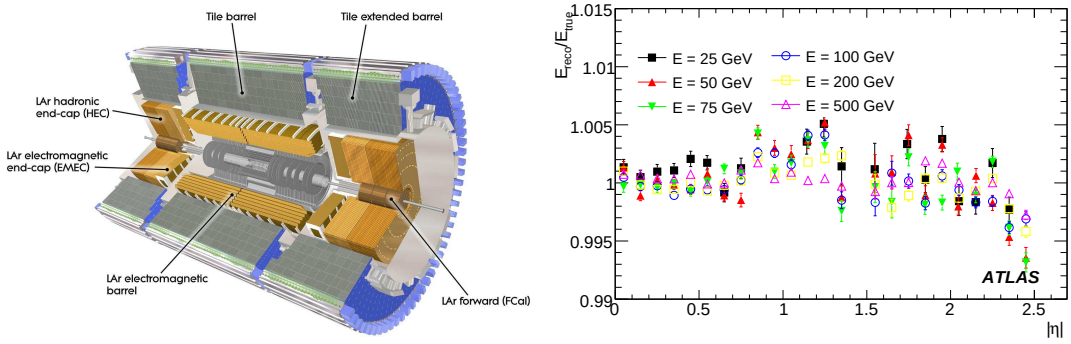

Figure 2.4: Left: Picture of the ATLAS calorimeter layout. Right: Linearity of the energy measured by the EM calorimeter for electrons of different energies. It is better than 5 ‰ for the energy range studied [54].

The EM calorimeter is a lead-Liquid Argon (LAr) detector with an accordion shape covering the complete ϕ symmetry. It is divided in two parts: the barrel part ($|\eta| < 1.475$) composed of two identical half-shells and two end-caps ($1.375 < |\eta| < 3.2$) formed by coaxial shells with different radius. The lead plates are used as absorber material. Their variable thickness in the barrel region and also in the end-caps, have been chosen to optimize the energy resolution. The liquid argon has been selected as the active medium providing good intrinsic linear response and stability over time. The expected energy resolution in the EM calorimeter is $\frac{\sigma_E}{E} = \frac{10\%}{\sqrt{E}} \oplus 0.7\%$. In addition, a presampler detector has been installed before the calorimeter to take into account the previous energies looses due to the interaction of the particles with the material of the ID detector.

The hadronic calorimeter is located around the EM calorimeter. It is composed by three barrel parts,

[2] X_0 is the mean distance over which a high-energy electron loses all but 1/e of its energy by bremsstrahlung or 7/9 of the mean free path for pair production by a high-energy photon [4].

[3] The interaction length λ is defined to be the mean path length needed to reduce the number of relativistic charge particles by a factor 1/e as they pass trough the matter.

the central one with $|\eta| < 1.0$ and two extended barrel region covering $0.8 < |\eta| < 1.7$. This sampling calorimeter uses steel plates as absorber and scintillator tiles as active material giving a total thickness of 7.4 λ. The Hadronic End-cap Calorimeter (HEC), located behind the EM end-cap, presents two independent wheels per end-cap. The copper plates are interleaved providing the absorbent medium and the LAr is also used here as active material. The expected energy resolution of the barrel and end-cap hadronic calorimeter is $\frac{\sigma_E}{E} = \frac{50\%}{\sqrt{E}} \oplus 3\%$ for single pions.

The Forward Calorimeter (FCal) is located beyond the HEC, its extensive coverage, $3.1 < |\eta| < 4.9$, gives uniformity as well as reduces the radiation background in the muon spectrometer. It is composed of three modules extended in depth until 10 λ; the first one uses copper as absorber material and provides a good optimization of the EM measurements while the second and third use tungsten as absorber material to measure the energy of the hadronic interactions, all of them using LAr as active material. The expected energy resolution is $\frac{\sigma_E}{E} = \frac{100\%}{\sqrt{E}} \oplus 10\%$ for single pions.

2.2.3 Muon Spectrometer

The Muon Spectrometer [54] has been built to provide a clean and efficient muon reconstruction with a precise momentum measurement over a wide momentum range, from few GeV to few TeV. Isolated muons with high transverse momentum are commonly involved in interesting physics processes of the SM and also BSM. An efficient muon reconstruction and clever trigger system is vital to identify these events.

The MS is the largest ATLAS detector, it covers a pseudorapidity range of $|\eta| < 2.7$ and is divided in a barrel region, which contains three concentric cylinders to the beam axis ($|\eta| <1$), and the end-cap region with four discs perpendicular to the beam direction ($1 < |\eta| < 2.7$). The MS makes use of four types of technologies: the Monitored Drift Tubes (MDT) and the Cathode Strip Chamber (CSC), both used for the tracking reconstruction, and the Resistive Plate Chamber (RPC) and Thin Gap Chambers (TGC) used for the trigger system. The MDT's chambers, located in the barrel region, are drift tubes that provide high precision measurements of the tracks in the principal bending direction of the magnetic field. The measurement precision of each layer is better than 100 μm in the η-coordinate. The CSC situated in the forward region are composed by multi-wire proportional chambers which provide a position resolution better than 60 μm. The trigger system is formed by the RPC, gaseous detectors, in the barrel region and the TGC, multi-wire proportional chambers, in the end-cap region. The layout of the muon spectrometer can be seen in the Figure 2.5 (left).

The muon magnet system [51] originates the deflection of the muon tracks. It consists of 8 superconducting coils in the barrel and two toroids with eight coils in the end-cap. It is a superconducting air-core magnet that provide an average field strength of 0.5 T and a bending power of 3 T·m in the barrel and 6 T·m in the end-cap.

The combination of all these technologies immersed in a magnetic field allow a precise measurement of the muon momentum. Figure 2.5 (right) shows the total muon spectrometer momentum resolution as a function of p_T (red line) and the individual effects that contribute to the final resolution (different colors). At low momentum, the resolution is dominated by fluctuations in the energy loss of the muons traversing the material in front of the spectrometer. In the intermediate momentum range, the multiple scattering plays an important role and for high momentum muons the resolution is limited by the detector performance, alignment and calibration.

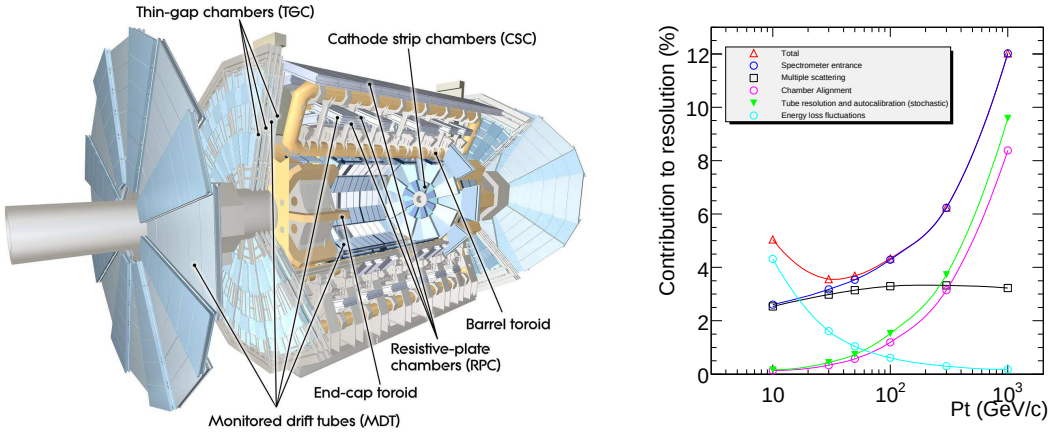

Figure 2.5: Left: Picture of the Muon Spectrometer layout. Right: Contributions to the momentum resolution for muons reconstructed in the Muon Spectrometer as a function of transverse momentum for $|\eta| < 1.5$. Different contributions can be seen in the picture [54].

2.2.4 Trigger

The ATLAS trigger and data acquisition system [54] is composed by three processing levels designed to store the most interesting events, as not all collisions can be recorded, neither are all of them interesting. The Figure 2.6 (left) shows the levels of the ATLAS trigger chain: the Level 1 (L1) [57], hardware based trigger, the Level 2 (L2), based on software trigger algorithms, and the Event Filter (EF) [58] also based on software information. The trigger chain must reduce the output data rate by a factor of 10^5 from the initial 40 MHz at nominal conditions to 200 Hz. This huge rejection should accomplish while maintaining the high efficiency for the low cross section processes that could be important for new physics. The different luminosity conditions in the LHC require variable trigger settings, during the low luminosity periods the trigger has been working with loose selection criteria and pass-trough mode but with the increasing of luminosity the use of higher thresholds, isolation criteria and tighter selection triggers were needed to reject the background (those events without interesting physics). Figure 2.6 (right) shows the rates for the L1, L2 and EF trigger (up right) and for several physics trigger chains (bottom right) as a function of the instantaneous luminosity.

The L1 trigger is based on hardware decisions, it receives the full LHC data at 40 MHz and has to make a decision each 2.5 μs to reduce the rate until 75 kHz. The L1 is based on calorimeter and muon spectrometer information. It uses multiplicities and energy thresholds of some objects reconstructed in the LAr and Tile calorimeters together with different track segments reconstructed in the muon spectrometer. The combination of these information produces a total of 256 L1 decision trees. Each of these configurations can be prescaled with a factor N that basically means that only 1 of N events pass to the L2. This prescaled factor can be tuned during the run to adapt the conditions if the LHC peak luminosity varies. The jumps on Figure 2.6 (bottom right) show the effect of the prescaling.

The L2 trigger is software based. This trigger reconstructs the objects in the region of interest (RoI). The RoI is defined as a window around the L1 seed axis. The L2 uses finer detector granularity, optimal calibration and more accurate detector description of the ID than the L1. The combination of the information of different sub-detectors can be matched to provide additional rejection and higher purity. On

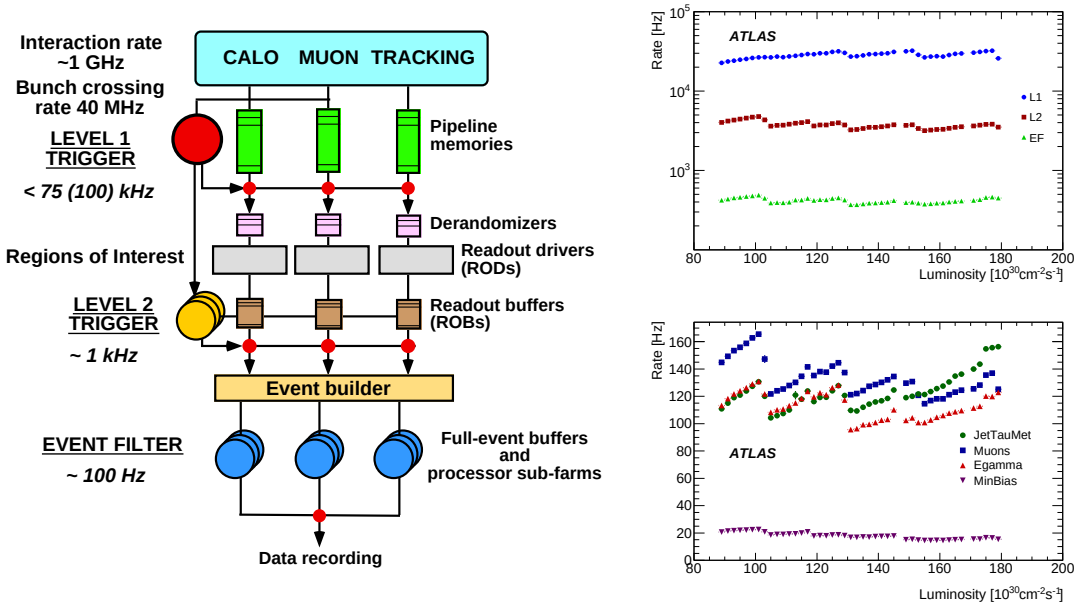

Figure 2.6: Left: Schematic picture of the trigger chain. Right: Total output trigger rates as a function of instantaneous luminosity in a sample run from 2010 period I data for each trigger level (up right) and different physics trigger chains (bottom right) [59].

average, the processing of one event at L2 takes 10 μs and reduces the output rate to 2 kHz.

Finally the EF, based on software algorithms, must provide the additional rejection to reduce the output rate to 200 Hz. The EF also works in a seed mode, nevertheless it has access to the full data information. The off-line reconstruction algorithms are used to get the rejection needed at this stage. On average, the EF can spend 4 seconds to process one event.

2.2.5 Grid Computing

The ATLAS data distribution model, based on grid technologies, has been developed to cover the necessities of the collaboration. Basically this model allows the storage of huge amounts of LHC data as well as simulated events (~PB/year) and also provides a good access irrespectively of their location (high bandwidth needed). Moreover many CPUs are needed to be continuously available to run the analysis of thousands of users. The ATLAS computing model presents a hierarchy structure of sites called Tiers. The ATLAS raw data is stored at the only Tier-0 located at CERN. After the first pre-processing, the data is transferred to 10 Tier-1 around the world and then copied to 80 Tier-2 which can offer an adequate computing power for the analysers. The last step of the chain are the ATLAS Tier-3 which are analysis computing resources under the control of individual institutes.

CHAPTER

3 ATLAS Reconstruction

After a proton-proton collision, many objects arise from the interaction point. In order to know what physics processes have occurred in the collision, the emerging objects need to be reconstructed efficiently and accurately. Basically, the particle reconstruction is the process of converting the recorded detector signals into measurements associated to the emerging particles. In this process there are several stages, the first step is based on the track and calorimeter cluster detector information. Tracks are one of the most important objects in high energy physics experiments since they represent the path of the charged particles through the detector. Particle properties as point of origin, direction and momentum can be obtained from the reconstructed tracks. The ATLAS tracking system is composed by the Inner Detector and the Muon Spectrometer. On the other hand, the passage of interacting particles through the calorimeters produce signals in the cells of these detectors. The cells are grouped in clusters that are used to measure the energy of neutral and charged particles. The cluster reconstruction is performed in both electromagnetic and hadronic calorimeters. Finally, the ATLAS software algorithms interpret all this information to create the objects that represent the real particle properties.

This chapter summarizes the main ATLAS particle reconstruction aspects related with this thesis. Section 3.1 introduces the ATLAS reference frames used to define the position of the detector measurements which are used as input information for the reconstruction. Section 3.2 presents a short report of the track reconstruction, basically focused on the Inner Detector because of the importance for the ID alignment. Section 3.3 describes briefly the ATLAS objects, in more detail those involved in the top-quark mass analysis.

3.1 Coordinate systems

Different coordinate systems are defined within the ATLAS detector. The most relevant frames for this thesis are those used to describe the ID geometry used in the alignment: the Global and the Local coordinate frames [60].

Global Coordinate Frame

The Global coordinates (X, Y, Z) of the ATLAS detector are defined as follows: the origin of the coordinate system corresponds to the nominal $p-p$ interaction point, the beam direction coincides with the Z axis and the X-Y plane is determined by the transverse plane to the beam direction. The positive X direction is taken towards the center of the LHC ring, the positive Y axis points to the surface and the Z positive direction coincides with the direction of the solenoid magnetic field. The Global Coordinate Frame can be seen in Figure 3.1 (left) for a longitudinal view of the ID detector.

Local Coordinate Frame

The local frame (x', y', z') is built for each detector module or alignable structure. The frame's origin of each module is at its geometric center. The x' axis points along the most sensitive direction of the module; therefore this axis coincides with the direction along the short pitch side of the pixel modules, across the strips of the SCT and across the straws for the TRT detector. The y' axis is parallel to the long side of the modules and the z' direction is the normal to the module plane formed by x' and y' direction. The Local Coordinate Frame for each detector module can be seen on the right side of Figure 3.1.

The hit is always reconstructed in the local reference frame. While for the pixel detector the idea is straightforward, for the SCT and TRT some clarifications are needed. For the SCT, there are two local frames associated to the two micro-strip detectors in one module, the information contained in both planes is used to get the SCT hit coordinate. On the other hand, to compute the TRT measurements the x coordinate is associated to the radial distance to the track.

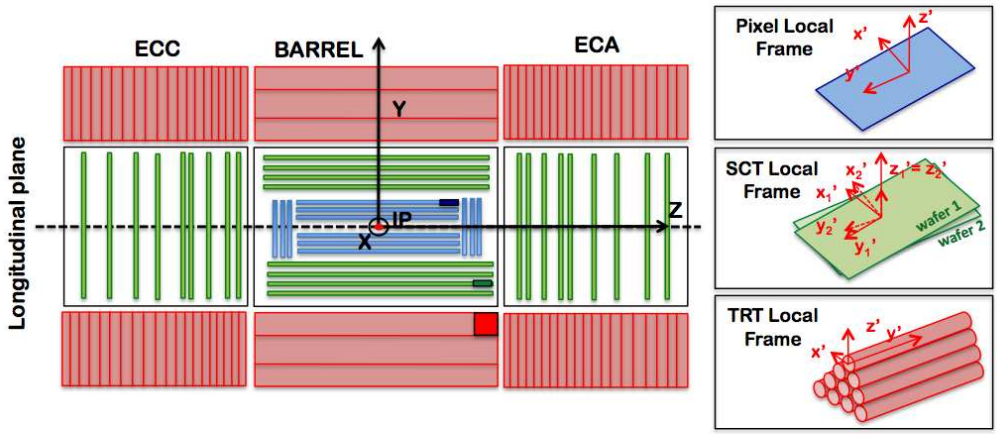

Figure 3.1: Left: Schematic longitudinal view of the ID detector geometry: Pixels (blue), SCT (green) and TRT (red). In this view the Global frame is represented by the black arrows. The dark boxes correspond to the position of the arbitrary selected detector modules. Right: Local frame for each detector module: Pixel (up), SCT (middle) and TRT (bottom).

3.2 Track reconstruction

Track reconstruction of charged particles is one of the most important ingredients in high energy physics experiments. The ATLAS tracker detectors have been designed to provide an excellent momentum resolution of the efficiently reconstructed tracks in a high particle multiplicity environment. Moreover the ID is also designed to identify primary and secondary vertices.

Tracks reconstruction process

The ATLAS track reconstruction software follows a flexible and modular design to cover the requirements of the ID and the MS. A common Event Data Model [61, 62] and detector description have been built to standardise all the reconstruction tools. The track reconstruction in the ID can be summarized in three steps:

- **Pre-processing.** During the data acquisition the read out of each sub-detector is performed and the data is stored in the form of byte streams which are subsequently converted in raw data objects. In the pre-processing stage these raw data are converted as input for the track finding algorithms. The produced clusters are transformed into space points in the local coordinate system. The pixel clusters provide two dimensional position on a fixed module surface that can be transformed directly to a 3D space point. In the SCT detector, the space points are obtained combining the clusters of the two sensors that compose the module into a sort of effective space point. Finally the TRT information is converted into calibrated drift circles. The TRT drift tube information doesn't provide any measurement along the straw tube so they can not be used to provide space points, instead they are treated as projective planes.
- **Track Finding.** Different tracking strategies have been optimized to cover different physics processes in ATLAS. The default tracking algorithm, called inside-out, exploits the high granularity of the pixel and SCT detectors to find tracks originated very close to the interaction point. The track seed is built from groups of four silicon space points. These track candidates are then extrapolated towards the SCT outer edge to form silicon tracks. Such candidates are fitted applying different quality cuts that let remove the outliers (hits far away from the track), resolve the ambiguities and reject the fake tracks. The selected tracks are further projected into the TRT to associate the drift-circles to the track. Finally the track fit is done using the combined information of the three sub-detectors. This algorithm reconstructs primary tracks with high efficiency, nevertheless the tracks originated in photon conversion and material interaction processes rarely pass the requirements in the number of silicon hits. A complementary finding algorithm called backtracking is used to recover these secondary tracks. The backtracking algorithm searches track segments in the TRT and the candidates are extrapolated into the SCT and pixel detectors.
- **Post-processing.** At this stage a dedicate iterative vertex finding algorithm is used to reconstruct primary vertices [63]. Moreover, algorithms in charge of reconstructing the secondary vertices and photon conversions are also applied at this stage.

Track parameters

Inside the ID, the charged particles describe helical trajectories due to the solenoid magnetic field. These trajectories are parametrized using a set of five parameters $\boldsymbol{\pi} = (d_0, z_0, \phi_0, \theta, q/p)$. All these parameters, shown at Figure 3.2, are defined at the perigee, which is the point of closest approach of the trajectory to the Z-axis. d_0 is the transverse impact parameter defined as the distance of the track to the perigee in the XY plane. d_0 is defined to be positive when the direction of the track is clockwise with respect to the origin. z_0 is the longitudinal impact parameter that corresponds to the z coordinate of the perigee. These impact parameters can be also calculated with respect to the primary vertex or beam spot. ϕ_0 is the azimutal angle of the tangent line to the trajectory measured around the beam axis in the X-Y plane. The positive X axis corresponds to $\phi = 0$ and the positive Y axis to $\phi = \pi/2$. The polar angle θ is measured with respect to the beam axis covering a range of $\theta \epsilon [0, \pi]$. Instead of θ, another related

quantity, the pseudorapidity, defined as η = -ln tan(θ/2) is commonly used. Finally, q/p represents the charge of the particle over its momentum and it is related with the curvature of the tracks.

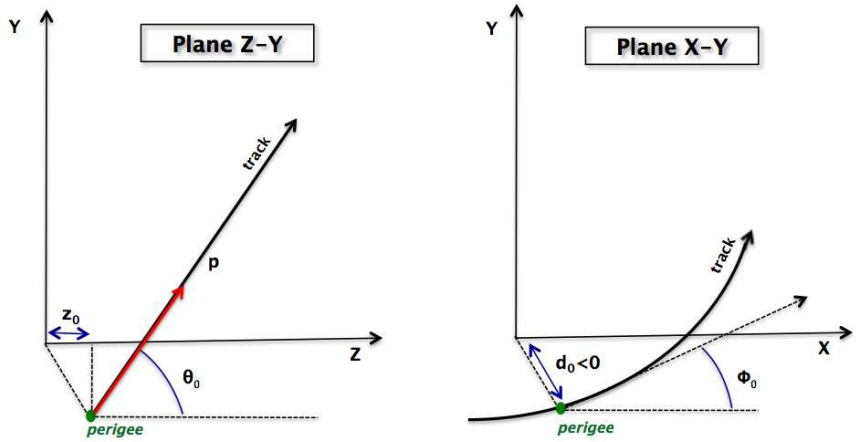

Figure 3.2: A graphical representation of the track parameters in the longitudinal (left) transverse (right) planes. The global reference frame has been used to define the track parameters.

The resolution of the track parameters can be expressed as a function of the p_T:

$$\sigma_\pi = \sigma_\pi(\infty)(1 \oplus p_\pi/p_T) \tag{3.1}$$

where $\sigma_\pi(\infty)$ is the asymptotic resolution expected at infinite momentum and p_π is a constant representing the p_T value for which the intrinsic and the Multiple Coulomb Scattering (MCS) terms are equal for the parameter π under consideration. This expression works well at high p_T (where the intrinsic detector resolution is the dominant term) and at low p_T (where the resolution is dominated by the MCS). Table 3.1 shows the values of $\sigma_\pi(\infty)$ and p_π for the barrel, where the amount of material is minimum, and for the end-cap regions, where the larger quantity of material is located. For computing these values, the effects of misalignment, miscalibration and pile-up[1] have been neglected.

Track Parameters	0.25⩽$\|\eta\|$⩽0.50		1.50⩽$\|\eta\|$⩽1.75	
	$\sigma_\pi(\infty)$	p_π (GeV)	$\sigma_\pi(\infty)$	p_π (GeV)
q/p_T	0.34 TeV^{-1}	44	0.41 TeV^{-1}	80
ϕ	70 μrad	39	92 μrad	49
cotθ	0.7×10^{-3}	5.0	1.2×10^{-3}	10
d_0	10 μm	14	12 μm	20
$z_0$sinθ	91 μm	2.3	71 μm	3.7

Table 3.1: Expected track parameter resolutions at infinite transverse momentum ($\sigma_\pi(\infty)$), and transverse momentum at which the MCS contribution equalises that from the detector resolution (p_π).The values are shown for barrel and end-cap detector regions. Isolated single particles have been used with perfect alignment and calibration in order to indicate the optimal performance.

[1] Pile-up is the term given to the extra signal produced in the detector by $p-p$ interactions other than the primary hard scattering.

3.3 Object reconstruction

The ultimate objective of the reconstruction algorithms is the creation of physic objects to be used in the analyses. All the detector information is combined to reconstruct the signature that the particles have left throughout the detectors. Sometimes the output of this process is not unique because distinct algorithms can interpret the same data in different ways producing different final objects. Since a proper interpretation is vital for the physics analysis those different objects created with the same data must be removed. This process is known as overlap removal and its analysis dependent.

This following subsection will briefly describe the reconstruction of the ATLAS objects following the standard selection and calibration for top-quark analyses [64]. This selection has been used to extract the top-quark mass presented later in chapter 5.

Muons:

Muons are one of the easiest particles to identify because they cross the entire ATLAS detector producing signal in the MS. The reconstruction of the muon candidate [65] has been performed using MUID [66], an algorithm which combines track segments from the muon chambers and from the ID. These segments are refitted as one track with a tight quality definition. Retained μ candidates must have a transverse momentum $p_T > 20$ GeV and $|\eta| < 2.5$ limited by the ID detector coverage. Isolation[2] criteria are used to suppress the background originated from heavy quark flavour decays. The energy deposited in a cone around the muon axis with $\Delta R = \sqrt{\Delta\phi^2 + \Delta\eta^2} < 0.2$ (criteria known as EtCone20) has to be smaller than 4 GeV and the sum of the transverse momenta of the tracks within a cone of $\Delta R < 0.3$ (known as PtCone30) has to be smaller than 2.5 GeV. Moreover an overlap removal between muons and jets following the criteria dR(μ, jet) < 0.4 is applied in order to remove those muons coming from the semileptonic decay of mesons. The selected muons are required to match the muon trigger used in the data taking. For 2011 the muon trigger chain were `mu18` and `mu18_medium` based on L1_MU and L1_MU11 respectively with a p_T threshold of 18 GeV for combined muons. The muon efficiencies for isolation, trigger, reconstruction and identification have been measured using tag and probe methods (T&P). The scale factors (SF) derived to match the data and the Monte-Carlo are within 1% of unity.

Electrons:

The electron candidate [65] is characterized by a reconstructed track in the ID associated to a shower in the EM calorimeter with almost all its energy absorbed before arriving to the hadronic calorimeter. The candidates are selected if $E_T > 25$ GeV and $|\eta| < 2.5$ excluding the calorimeter crack region[3]. The tight criteria (`tight++`[4]) used implies stringent selection cuts on calorimeter, tracker and combined variables to provide a good separation between electrons and jets (fake electrons). An isolation requirement based on the EtCone20 and PtCone30 criteria calculated at 90% of efficiency is required to suppress the QCD multijet background. The selected electrons have to match the electron trigger defined for each data period. During 2011 the triggers used were `triggerEF_e20_medium`, `triggerEF_e22_medium` and `triggerEF_e22vh_medium1`. Moreover `triggerEF_e45` was also used to avoid efficiency looses due to electrons with high p_T. The electron reconstruction and efficiency have been measured with T&P methods and their SF calculated as a function of η and E_T.

[2] A particle is isolated when the energy of the reconstructed tracks and clusters around its direction doesn't exceed a certain threshold value.

[3] The crack region is defined in η as follows: $1.37 < |\eta| < 1.52$

[4] The tight++ criteria uses E/p, pixel innermost layer information and potential identification of the TRT.

Taus:

Although taus are also charged leptons, from the experimental detector point of view they are very different from electrons and muons. Around 35% of the taus decay to electron or muon plus neutrinos, while the rest of the time they decay into hadrons plus a neutrino. The leptonic tau decay produces genuine electrons and muons which are hard to distinguish from prompt ones. On the other hand, the hadronic taus are not treated as a simple objects but are composed by jets and E_T^{miss}. More details about the hadronic tau reconstruction can be found in [67].

Photons:

Photons can be efficiently identified in ATLAS by two experimental signatures [65]. One is through the photons that suffer a conversion in the material of the ID since they produce an electron-positron pair with a vertex displaced from the interaction point. The other photons which do not undergo conversion are characterized by EM showers not associated to any ID track.

Jets:

A jet is reconstructed from a bunch of particles (charged and neutrals) that have been grouped together. The idea steams from the hadronization of quarks and gluons (that carry color charged into color singlet hadrons). They are commonly clustered using Anti-Kt algorithm [68] with a cone size of $R = 0.4$. The constituents of the calorimeter jets are topological clusters (topocluster) formed by groups of calorimeter cells. The energy of the topoclusters is defined as the sum of the energy of the included cells and the direction points to the center of ATLAS.

Jets are reconstructed at the electromagnetic scale (EMSCALE). It accounts correctly for the energy deposits in the calorimeter due to the electromagnetic showers produced by electrons and photons. This energy is established using cosmic and collision data. Moreover a calibration at hadronic scale must be applied to calibrate the energy and momentum of the jets. The hadronic jet energy scale is restored using derived corrections from data and MC [69]. ATLAS EM+JES calibration applies a jet-by-jet correction depending of the E and η of the reconstructed jets at EM scale. This calibration has several steps:

- **Pile-up correction:** the measured energy of reconstructed jets can be affected by the non hard scattering processes produced by additional $p - p$ collisions in the same bunch crossing. The energy at EM scale is amended by an offset correction for pile-up.
- **Jet origin and direction corrections:** calorimeter jets are reconstructed using the geometrical center of the detector as a reference to calculate the direction of the jet and their constituents. To compute this correction each topocluster points back to the primary hard scattering vertex and the jet is recalculated. This correction improves the jet angular resolution. Other problems arise from the fact that the jet direction can be biased from the poorly to better instrumented regions of the calorimeter. This correction is very small for most of the region of the calorimeter but it is larger in the transition regions and needs to be considered.
- **Jet energy correction:** this correction restores the reconstructed jet energy to the energy of the MC truth jet. The calibration is derived using the isolated jets that match an isolated truth jet within $\Delta R < 0.3$. The final jet energy scale calibration is parametrized as a function of the energy and the η of the jet. The EM-scale energy response is given by the ratio between the reconstructed jet energy and the truth jet energy calculated for different bins of E and η. Once these jet energy scale corrections have been applied, the jets are considered to be calibrated at the EM+JES scale.

This calibration has been performed using simulation studies and validated with data. For the top-quark mass analysis only those jets in the $t\bar{t}$ events with a $p_T > 25$ GeV and $|\eta| < 2.5$ respect to the primary vertex will be selected. In order to choose pure hard scattering jets and to reduce pile-up biases, a cut in the jet vertex fraction (JVF) [5] has been applied ($|JVF| > 0.75$) [70]. To remove the possible overlap information, jets with the axis within a $\Delta R < 0.2$ from the electron direction are removed from the event. Furthermore, a jet quality criteria is imposed to remove jets not associated to real energy deposits in the calorimeters coming from hardware problems, LHC beam conditions and cosmic-ray showers.

b-jets:

The identification of the *b*-quark originated jets is based on their specific properties: long lifetime, large *B* hadron mass and large branching ratio into leptons. The algorithm used has been the MV1 which combines the output of the three *b*-tagging algorithms (JetFitter, IP3D and SV1 [71]) with the p_T and the η of the jets in a neural network to determine a final tagging discriminator weight. The nominal efficiency of the *b*-tagging algorithms with a working point fixed to 0.601713 corresponds to 70%. Those jets with a weight higher than the operating point are labelled as *b*-tagged jets, while those jets non tagged as *b* are considered as light-quarks initiated jets or simply light jets.

Missing Transverse Energy: $E_{\mathrm{T}}^{\mathrm{miss}}$

The neutrinos pass trough the detector without interacting. They are undetectable particles but their presence can be inferred from the missing energy in the transverse plane. The $E_{\mathrm{T}}^{\mathrm{miss}}$ [72] is defined as the event momentum imbalance in the transverse plane to the beam axis, where momentum conservation is expected. In the transverse plane, the imbalance momentum vector is obtained from the negative vector sum of the momenta of all detected particles. Thus, the $E_{\mathrm{T}}^{\mathrm{miss}}$ has to be computed with the information of the following objects: electrons, muons, jets and calorimeter cell out term (which takes into account the energy not associated with the previous objects).

$$E_{x(y)}^{miss} = E_{x(y)}^{miss,e} + E_{x(y)}^{miss,jet} + E_{x(y)}^{miss,softjet} + E_{x(y)}^{miss,calo,\mu} + E_{x(y)}^{miss,CellOut} \tag{3.2}$$

Pile-up

The object reconstruction presented in this section is hardly affected by the pile-up that, as stated before, refers to the amount of data in the detector which is not originated from the hard-scattering interaction that fires the trigger. It consists basically of two overlapping effects:

- **In-time pile-up:** this contribution comes from the multiple $p-p$ interaction occurring simultaneously to the event of interest. The particles produced in these additional collisions can bias the reconstruction of the event under study. The in-time pile-up, that mainly affects the jet energy measurements, lepton isolation and $E_{\mathrm{T}}^{\mathrm{miss}}$ determination, can be studied as a function of the number of primary vertexes in the event.
- **Out-of-time pile-up:** this contribution arises from the previous and subsequent bunch-crossings due to the large calorimeter integration time. The number of interactions per bunch crossing has been used to parametrize the out-of-time pile-up. For the data used to perform the top-quark mass analysis presented in this thesis the average number of interactions per bunch crossing was found to be of the order of 10 [53].

[5] The JVF discriminant is the fraction of each jet's constituents p_{T} contributed by each vertex. For a single jet_i, the JVF with respect to the vertex vtx_j is written as: $\mathrm{JVF}(jet_i, vtx_j) = \frac{\sum_k p_{\mathrm{T}}(trk_k^{jet_i}, vtx_j)}{\sum_n \sum_l p_{\mathrm{T}}(trk_l^{jet_i}, vtx_n)}$

An example of the mentioned objects can be seen in the display of the Figure 3.3. This picture represents a di-leptonic $t\bar{t}$ event where both W bosons stemming from the $t \to Wb$ process decay into a lepton and its corresponding neutrino. The final state is characterized by the presence of two isolated leptons, missing transverse energy ($E_{\mathrm{T}}^{\mathrm{miss}}$) and two b-jets (emerging from the direct top-quark decay ($t \to Wb$)).

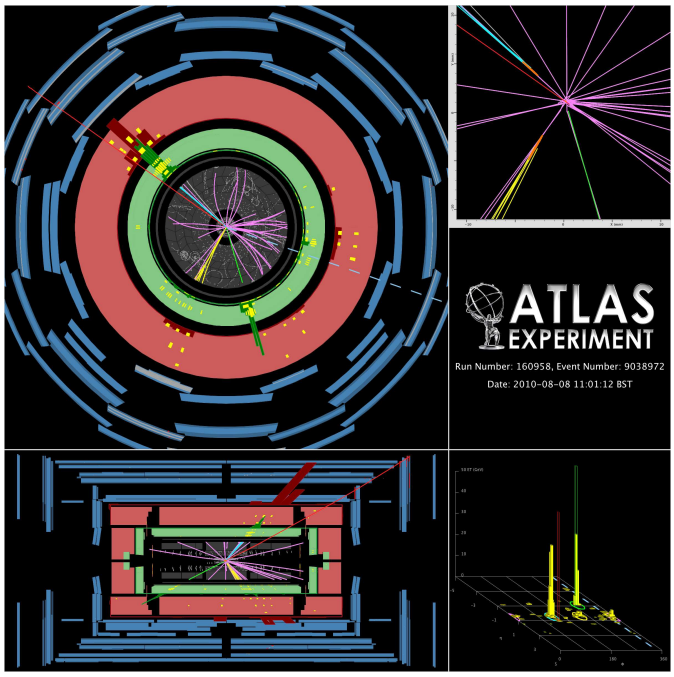

Figure 3.3: Event display of a $t\bar{t}$ e-μ di-lepton candidate with two b-tagged jets. The electron is shown by the green track pointing to a calorimeter cluster, the muon by the long red track intersecting the muon chambers, and the missing $E_{\mathrm{T}}^{\mathrm{miss}}$ direction by the dotted line on the XY view. The secondary vertices of the two b-tagged jets are indicated by the orange ellipses on the zoomed vertex region on the bottom right plot [73].

CHAPTER

4

Alignment of the ATLAS Inner Detector with the Globalχ^2

The ATLAS detector is composed by different specialized sub-systems segmented with a high granularity. Each of these sub-detectors is formed by thousand of devices with small intrinsic resolution with the aim of measuring the properties of the particles with high accuracy. Usually, the position of these modules in the final detector, after the assembly and installation, is known with worse precision than their intrinsic resolutions. This fact impacts in the reconstructed trajectory of the particles, thus degrading the track parameters accuracy and affecting inevitably the final physics results. In order to avoid this problem, the location and orientation of the module detectors must be determined with high precision. This is known as alignment.

This chapter introduces the techniques and procedures used to align the ATLAS Inner Detector (ID). The ID is composed by three sub-detectors: Pixel, SCT and TRT. The Pixel and the SCT are based on silicon pixel and micro-strip technologies respectively while the TRT is a gaseous detector. The Globalχ^2 algorithm has been mainly used for the alignment of the silicon tracker detector which consists of 1744 pixel detectors and 4088 SCT modules. Each alignable structure has 6 degrees of freedom (DoFs) corresponding to the alignment parameters: three translations that define the position (T_X, T_Y and T_Z) and three rotations that provide the orientation (R_X, R_Y and R_Z). Thus, the whole silicon system involves nearly 35.000 DoFs. On the other hand, the hundred of thousands DoFs of the TRT have also to be aligned. The precise determination of this large number of DoFs with the required accuracy is the challenge of the ID alignment.

This chapter is organized as follows: Section 4.1 presents the alignment requirements of the ATLAS ID tracking system, Section 4.2 introduces the generalities of the track-based alignment algorithms, Section 4.3 describes the algebraic formalism of the Globalχ^2 method, Section 4.4 shows the different ID geometry levels, Section 4.5 explains the weak modes, Section 4.6 enumerates the datasets used for the alignment, Section 4.7 summarizes some alignment validation tests and Section 4.8 presents the first ID alignment constants with real data. Section 4.9 reviews the recent alignment developments and Section 4.10 mentions the impact of the ID alignment in physics. Finally, the ID alignment conclusions are summarized in Section 4.11.

4.1 The Inner Detector alignment requirements

The ID system is responsible for reconstructing the trajectories of charged particles and measuring their properties as momentum, impact parameters, etc. The ID alignment is a crucial ingredient for the

physics measurements since many of the reconstruction algorithms (vertex reconstruction, lepton identification, b-tagging algorithms,...) are based on tracks. In order to achieve the required accuracy, highly segmented detectors are mandatory, and on top of that, optimal detector alignment and calibration are essential to exploit the entire detector capabilities. The requisites for getting an excellent ID detector performance, which are related among others with the accuracy of the alignment, the precise knowledge of the magnetic field and the exact mapping of the material in the ID, are summarized in [74]. The momentum determination depends directly on the solenoid magnetic field, thus field map has to be measured with an accuracy better than 0.02%. The knowledge of the ID material is important to understand the energy losses of the particles via Multiple Coulomb Scattering. Unless corrected, this effect reduces the reconstructed p_{T} and introduces a bias in the momentum measurement. Therefore, an excellent material detector knowledge with an accuracy better than 1% is necessary [75]. The ID capabilities can also be compromised by the detector misalignments. Uncertainties in the relative position of the detector elements can be introduced during the stages of construction, assembly, installation as well as during the operation due to the hardware changes (magnetic field ramping, cooling system failures, etc). In order to achieve the ATLAS physics goals the ID alignment must not lead to a degradation of the track parameters no more than 20% with respect to their intrinsic resolution. The track reconstruction performance studies done with MC samples showed that the required resolutions for the silicon tracker detector are 7 μm for the Pixels and 12 μm for the SCT, both in $R\phi$ direction [56]. For the TRT the required resolution was found to be 170 μm per straw tube [56]. Nevertheless, more ambitious challenges require a knowledge of the alignment constants with a precision of the order of the micrometer in the transverse plane in order to get a transverse momentum resolution of about 1%.

4.2 Track-Based Alignment

The alignment of the ID tracking system is done using track-based algorithms. These methods permit to determine the position of each detector module within the required precision ($O(\mu\mathrm{m})$ [76]). The key element of the alignment algorithms are the trajectories of the charged particles since the quality of the track fit is directly related with the detector misalignments. One track has a good quality when all its associated hits are close to its trajectory, by contrast, its quality is worse when the hits deviate significantly from the reconstructed track. Therefore, the distance between the hit measured and the extrapolated track is used to find the detector misalignments. In the alignment framework, this distance is called residual (r) and it is defined as follows:

$$r = (\boldsymbol{m} - \boldsymbol{e}\,(\boldsymbol{\pi}, \boldsymbol{a})) \cdot \boldsymbol{u} \tag{4.1}$$

where $\boldsymbol{e}(\boldsymbol{\pi}, \boldsymbol{a})$ represents the extrapolated point of the track into the detector element. This position depends on the track ($\boldsymbol{\pi}$) and the alignment ($\boldsymbol{a}$) parameters of that element. The quantity $\boldsymbol{m}$ gives the position of the measurement in the sensor and $\boldsymbol{u}$ is the vector pointing along the sensing direction. In general $\boldsymbol{m}$ could depend on the alignment parameters, although, as the calculations are performed in the module local frame, it does not, because $\boldsymbol{m}$ is given by the logical channel and it is completely fixed in this frame.

Figure 4.1 shows a simplified sketch of the alignment process. The installed geometry (blue boxes) represents the real position of the detector modules. When one particle crosses perpendicularly the detector (black arrow) produces a hit in each module (orange stars). Once the hits have been recorded, the track is reconstructed using the apparent detector geometry (boxes with discontinuous line). If the apparent geometry doesn't correspond to the real one, then the track is not correctly reconstructed. In order to find the real position of the sensors, the ID alignment uses an iterative χ^2 minimization method based on the residual information (mathematical formalism shown in Section 4.3). Sometimes the misalignments

can not be totally recovered. In these cases, the bias in the trajectories can not be completely eliminated but at least they are considerably reduced.

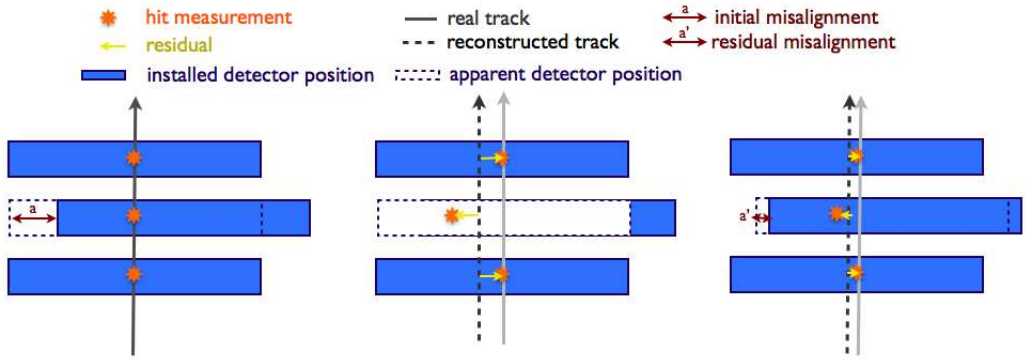

Figure 4.1: Schematic picture of the alignment procedure. Three different steps are shown: a real track crossing the installed detector geometry (left), reconstructed track using the apparent detector geometry (middle) and reconstructed track after detector alignment (right).

Different track-based algorithms were proposed in order to align the Inner Detector:

- The **Robust [77]** is an iterative method based on centred and overlap residual measurements. It allows the alignment of the detector sensors in the most sensitive directions: local x and local y. Moreover, if the overlap residuals are measured with sufficient precision, the algorithm is able to perform corrections also in the local z direction. This algorithm correlates the position of the modules within one ring or stave through the overlap residuals and therefore, makes easier the identification of radial detector deformations.
- The **Local**χ^2 [78] and **Global**χ^2 [79] algorithms are iterative methods based on a χ^2 minimization. The Globalχ^2 uses linear residuals which are defined within the planar sensor (two dimensional residuals). On the other hand, the ATLAS implementation of the Localχ^2 algorithm uses the distance of closest approach (DOCA[1]) residuals to compute the alignment. The differences in the mathematical formalism of both approaches are explained in Section 4.3.

All of them were implemented within the ATLAS software framework (Athena [80]) and they were extensively tested and used during the commissioning and detector operation.

Related with the detector alignment there are several important concepts/quantities that need to be introduced:

Residual definition: the track-hit residuals can be computed in two different ways: biased and un-biased. Both residuals are calculated as the distance between the hit measurement (as recorded by the sensor) and the extrapolated track-hit, but they differ in their computation. If the extrapolated track doesn't contain the hit of the module under test, the obtained residual is called un-biased. By contrast, when all hits are included in the tracking, the residuals are called biased. Hence, by construction the biased residuals are smaller than the unbiased. The alignment algorithms commonly use biased residuals while the ATLAS ID monitoring usually works with the un-biased.

[1]The DOCA residuals are the 3-dimensional residuals computed as the distance of closest approach of the track-hit to the cluster.

Pull definition: the pulls are defined as the residual divided by the standard deviation of the residuals (σ_r):

$$pull = \frac{r}{\sigma_r} = \frac{r}{\sqrt{\sigma^2_{hit} \pm \sigma^2_{ext}}} \tag{4.2}$$

where σ_{hit} is the intrinsic detector resolution and σ_{ext} is the standard deviation of the track extrapolation. The sign depends on the residual type being positive for the un-biased and negative for the biased residuals. The pulls should follow a normal distribution (N(0,1)) with mean zero and standard deviation equal to one. These quantities are very sensitive to wrong assumptions or misalignments since any deviation from the expected behaviour, N(0,1), can indicate problems as a bias in the data points, wrongly assigned uncertainties or incorrect assumed model. Therefore, these quantities are often used to identify the goodness of the alignment corrections.

Error Scaling (ES): the error scaling tool [81] provides a handle to scale the errors of the detector measurements that enter in the track fit. The differences between the measurement errors provided by the clustering and those seen by the tracking may be caused by the detector misalignments or calibrations effects. These differences are expected to be larger during the initial data taking and also after physical detector changes. The error scaling can be used in order to inflate the hit error (σ_0) as follow: $\sigma^2 = a^2\sigma_0^2 + c^2$. The first term scales the error in order to cover possible overall miscalibration. The factor a allows the correction of the effects correlated with the measurement error. The second one includes a constant term (c) that absorbs effects which are not correlated with the measurement hit itself as for instance random sensor misalignments. This tool has been implemented for the barrel and end-cap zone of each ID sub-detector.

4.3 The *Global*χ^2 algorithm

The Globalχ^2 is the main ID alignment algorithm. It is based on the minimization of a χ^2 equation built from residual information. A simplified χ^2 is shown in equation 4.3.

$$\chi^2 = \sum_t \sum_h \left(\frac{r_{th}(\boldsymbol{\pi}, \boldsymbol{a})}{\sigma_h} \right)^2 \tag{4.3}$$

where t represents the set of reconstructed tracks and h the set of associated hits to each track. The r_{th} depicts the track-hit residual for each hit of the track and σ_h the hit error. This χ^2 equation can accommodate different tracking devices, diverse residual definitions, detector correlations, etc. The χ^2 can be written in a more generic form using matrix and vector algebra as:

$$\chi^2 = \sum_t \boldsymbol{r}\,(\boldsymbol{\pi}, \boldsymbol{a})^T \; V^{-1} \; \boldsymbol{r}\,(\boldsymbol{\pi}, \boldsymbol{a}) \tag{4.4}$$

In order to build the ID residual vector $\boldsymbol{r}$, several considerations have to be taken into account. For example, the Pixel detector has two residuals per module, since they can provide measurements in two dimensions ($R\phi$ and η). The SCT also has two residuals associated to each module coming from the stereo and non-stereo sides. Considering only the silicon tracker, the dimension of the residual vector is twice the number of detector modules. As pointed out before, the residuals depend on the five track parameters (Section 3.2) and also on the location of each module that is fixed by the six alignment parameters. Finally, V represents the covariance matrix that accommodates the hit errors. If one considers a null correlation between the modules, V is diagonal. On the other hand, the MCS correlates different detector

devices because the measurement in a given module is determined by the scattering angle suffered by the particle in the previous one. Thus, by including the MCS in the calculations the terms out of the diagonal are filled. Therefore, the total covariance matrix can be written as $V_{hit} + V_{MCS}$ where the hit error as well as the material effects are taken into account.

As explained before, the χ^2 has a minimum at the real detector geometry. Then, the correct position of the modules can be computed by doing a χ^2 minimization with respect to $\boldsymbol{a}$.

$$\frac{d\chi^2}{d\boldsymbol{a}} = 0 \longrightarrow \sum_t \left(\frac{d\boldsymbol{r_t}(\boldsymbol{\pi},\boldsymbol{a})}{d\boldsymbol{a}}\right)^T V^{-1}\boldsymbol{r_t}(\boldsymbol{\pi},\boldsymbol{a}) = 0 \tag{4.5}$$

The total derivative of the χ^2 has a term related with the alignment parameters and other with the track parameters:

$$d\chi^2 = \frac{\partial\chi^2}{\partial\boldsymbol{\pi}}d\boldsymbol{\pi} + \frac{\partial\chi^2}{\partial\boldsymbol{a}}d\boldsymbol{a} \longrightarrow \frac{d\chi^2}{d\boldsymbol{a}} = \frac{\partial\chi^2}{\partial\boldsymbol{\pi}}\frac{d\boldsymbol{\pi}}{d\boldsymbol{a}} + \frac{\partial\chi^2}{\partial\boldsymbol{a}} \tag{4.6}$$

The key of the Globalχ^2 method [79] is to assume that the dependence of the track parameters with respect to the alignment parameters is not null ($\frac{d\pi}{da} \neq 0$). This can be easily understood because moving the sensor location will relocate the hits, and when fitted these ones will produce new track parameters. This derivative introduces correlations between the modules used to reconstruct the entire track.

Track fit:

Before determining the alignment parameters, the tracks that are used to compute the residuals have to be identified. First, the solution of the $\boldsymbol{\pi}$ for every track with an arbitrary detector alignment must be found. In this sense, the minimization of the χ^2 versus the track parameters needs to be calculated:

$$\frac{d\chi^2}{d\boldsymbol{\pi}} = \frac{\partial\chi^2}{\partial\boldsymbol{\pi}} = 0 \longrightarrow \left(\frac{\partial\boldsymbol{r_t}(\boldsymbol{\pi},\boldsymbol{a})}{\partial\boldsymbol{\pi}}\right)^T V^{-1}\boldsymbol{r_t}(\boldsymbol{\pi},\boldsymbol{a}) = 0 \tag{4.7}$$

As the alignment parameters do not depend on the track parameters, the total derivative becomes a partial derivative. In order to obtain the solution, a set of initial values ($\boldsymbol{\pi_0}$) is considered to compute the track parameters corrections ($\delta\boldsymbol{\pi}$) trough the minimization process. The final parameters are $\boldsymbol{\pi} = \boldsymbol{\pi_0} + \delta\boldsymbol{\pi}$. The residuals will change with the track parameters in this way:

$$\boldsymbol{r} = \boldsymbol{r}(\boldsymbol{\pi_0},\boldsymbol{a}) + \left.\frac{\partial\boldsymbol{r}}{\partial\boldsymbol{\pi}}\right|_{\pi=\pi_0}\delta\boldsymbol{\pi} \tag{4.8}$$

where a Taylor expansion of the residuals have been used up to first order, and higher orders have been neglected. Introducing Equation 4.8 in Equation 4.7 and identifying $E_t = \left.\frac{\partial\boldsymbol{r}(\boldsymbol{\pi},\boldsymbol{a})}{\partial\boldsymbol{\pi}}\right|_{\boldsymbol{\pi_0}}$, the equation looks as follows:

$$E_t^T V^{-1}\boldsymbol{r_t}(\boldsymbol{\pi_0},\boldsymbol{a}) + E_t^T V^{-1}E_t\delta\boldsymbol{\pi} = 0 \longrightarrow \delta\boldsymbol{\pi} = -(E_t^T V^{-1}E_t)^{-1}E_t^T V^{-1}\boldsymbol{r_t}(\boldsymbol{\pi_0},\boldsymbol{a}) \tag{4.9}$$

The errors of the track parameters can be also determined. The corresponding covariance matrix can be written as:

$$C = (\delta\boldsymbol{\pi})^T(\delta\boldsymbol{\pi}) \quad \longrightarrow \quad C = (E_t^T V^{-1} E_t)^{-1} \tag{4.10}$$

Alignment parameters fit:

Once the track parameters have been calculated, the alignment parameters can be computed. The same approximation is used here: a set of initial parameters is taken ($\boldsymbol{a_0}$) and the goal is to find their corrections ($\delta\boldsymbol{a}$) such that the final alignment parameters ($\boldsymbol{a} = \boldsymbol{a_0} + \delta\boldsymbol{a}$) minimize the χ^2. Using the previous approximation the residuals can be written as:

$$\boldsymbol{r} = \boldsymbol{r}(\boldsymbol{\pi_0}, \boldsymbol{a_0}) + \frac{\partial \boldsymbol{r}}{\partial \boldsymbol{a}}\Big|_{\boldsymbol{a_0}} \delta\boldsymbol{a} \xrightarrow{D=\frac{\partial r}{\partial a}} \boldsymbol{r} = \boldsymbol{r_0} + D\delta\boldsymbol{a} \tag{4.11}$$

Inserting Equation 4.11 in Equation 4.5 and after some algebra, the alignment parameter corrections are given by:

$$\delta\boldsymbol{a} = -\left(\sum_t \left(\frac{d\boldsymbol{r_t}(\boldsymbol{\pi_0}, \boldsymbol{a_0})}{d\boldsymbol{a}}\right)^T V^{-1} \frac{\partial \boldsymbol{r_t}}{\partial \boldsymbol{a}}\Big|_{\boldsymbol{a_0}}\right)^{-1} \left(\sum_t \left(\frac{d\boldsymbol{r_t}(\boldsymbol{\pi_0}, \boldsymbol{a_0})}{d\boldsymbol{a}}\right)^T V_t^{-1} \boldsymbol{r_t}(\boldsymbol{\pi_0}, \boldsymbol{a_0})\right) \tag{4.12}$$

Notice that this equation includes the total derivative of the residuals versus the track parameters, and this term carries a nested dependence of the track and alignment parameters.

$$\frac{d\boldsymbol{r}}{d\boldsymbol{a}} = \frac{\partial \boldsymbol{r}}{\partial \boldsymbol{a}} + \frac{\partial \boldsymbol{r}}{\partial \boldsymbol{\pi}} \frac{d\boldsymbol{\pi}}{d\boldsymbol{a}} \tag{4.13}$$

Therefore, one needs to study how the tracks change when the alignment parameters change ($\frac{d\pi}{da}$). From Equation 4.9:

$$\frac{d\boldsymbol{\pi}}{d\boldsymbol{a}} = -(E_t^T V^{-1} E_t)^{-1} E_t^T V^{-1} \frac{\partial \boldsymbol{r}(\boldsymbol{\pi_0}, \boldsymbol{a_0})}{\partial \boldsymbol{a}} \tag{4.14}$$

Using above relations, the total derivative of the residuals with respect to the alignment parameters times the covariance matrix can be expressed as:

$$\left(\frac{d\boldsymbol{r}}{d\boldsymbol{a}}\right)^T V^{-1} = \left(\frac{\partial \boldsymbol{r}}{\partial \boldsymbol{a}}\right)^T \underbrace{\left[V^{-1} - (V^{-1}E_t)(E_t^T V^{-1} E_t)^{-1}(E_t^T V^{-1})\right]}_{W_t} \tag{4.15}$$

Therefore, the alignment corrections can be written as follows:

$$\delta\boldsymbol{a} = -\left(\sum_t \left(\frac{\partial \boldsymbol{r_t}}{\partial \boldsymbol{a}}\right)^T W_t \frac{\partial \boldsymbol{r_t}}{\partial \boldsymbol{a}}\right)^{-1} \left(\sum_t \left(\frac{\partial \boldsymbol{r_t}}{\partial \boldsymbol{a}}\right)^T W_t \boldsymbol{r_t}\right) \tag{4.16}$$

This equation gives the general solution for the alignment parameters. $\delta\boldsymbol{a}$ represents a set of equations (one for each parameter that have to be determined). In a more compact notation:

$$M = \sum_t \left(\frac{\partial \boldsymbol{r_t}}{\partial \boldsymbol{a}}\right)^T W_t \left(\frac{\partial \boldsymbol{r_t}}{\partial \boldsymbol{a}}\right) \qquad \boldsymbol{\nu} = \sum_t \left(\frac{\partial \boldsymbol{r_t}}{\partial \boldsymbol{a}}\right)^T W_t \boldsymbol{r_t} \tag{4.17}$$

where M is a symmetric matrix with a dimension equally to the number of DoFs to be aligned and $\boldsymbol{\nu}$ is a vector with the same number of components. Therefore the equation can be simply written as:

$$M\delta\boldsymbol{a} + \boldsymbol{\nu} = 0 \longrightarrow \delta\boldsymbol{a} = -M^{-1}\boldsymbol{\nu} \tag{4.18}$$

In order to obtain the alignment corrections, the big matrix M has to be inverted. The structure of this matrix is different depending on the approach used to align the detector:

- **Localχ^2:** the Localχ^2 approach can be considered as a simplified version of the Globalχ^2 where the dependence of the track parameters with respect to the alignment parameters has been considered null ($\frac{d\boldsymbol{\pi}}{d\boldsymbol{a}} = 0$ in Equation 4.6). In this case, the track parameters are frozen and the correlations between different modules are not considered. For the Localχ^2 the big matrix becomes block diagonal. Only the six DoFs in the same module exhibit a correlation. Figure 4.2 (left) shows the Localχ^2 big matrix shape associated to the the silicon system at L1 (alignment levels explained in Section 4.4). Here, the block diagonal associated to the four L1 structures (Pixel, SCT ECC, SCT barrel and SCT ECA) can be clearly seen. Using this method the matrix inversion is not a big challenge since most of its elements are zero. Nevertheless, not taking into account the correlations slows down the convergence of the process and more iterations are needed to get the final alignment corrections.

- **Globalχ^2:** the Globalχ^2 algorithm considers the derivatives of the track parameters respect to the alignment parameters to be non zero. This fact introduces correlations between different module detectors and the matrix elements out of the diagonal are filled. In addition, some track constraints, as a common vertex, can include further relations between different parts of the detector producing a dense populated matrix after few events. The solving of this matrix can represent a big challenge when the alignment is performed for each individual module (detailed information in Section 4.3.3). Besides, singularities may appear and have to be removed (read Section 4.7.1). Figure 4.2 (right) shows a Globalχ^2 big matrix at L1 where almost all boxes are filled indicating a strong correlation between the different regions of the detector. The empty boxes correspond to the SCT end-caps which in general, except for the beam halo events, are not traversed both at the same time.

This section has presented the basics of the Globalχ^2. In addition, the method can accept many extensions and constraints in order to improve the algorithm convergence to the right minimum. The most useful constraints will be described in the following sections. Nevertheless, a more detailed description of the Globalχ^2 formalism can be found in [82].

4.3.1 The Globalχ^2 fit with a track parameter constraint

The Globalχ^2 algorithm can include additional terms in order to accommodate constraints on track parameters. These terms use external information which is confronted with the silicon measurements in order to prevent unrealistic alignment corrections. For example, the momentum of the charged particles obtained with the silicon detector can be constrained to be the same as that measured by the TRT detector. Also the calorimeter and muon spectrometer information can be used to restrict the track parameters

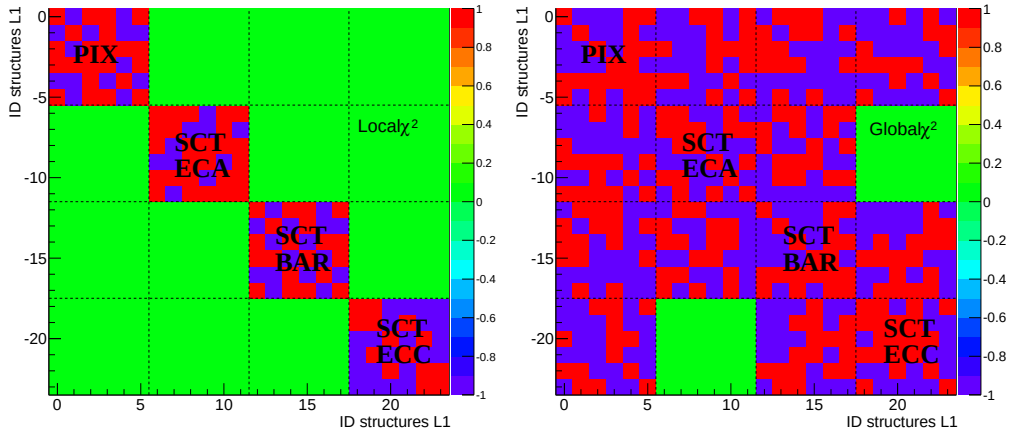

Figure 4.2: Sketch of the alignment matrix in the Localχ^2 (left) and Globalχ^2 (right) approaches for the silicon tracking system devices at L1. The discontinuous lines separate the different L1 structures: Pixel, SCT ECA, SCT barrel and SCT ECC. Taking into account the 6 DoFs of each structure, the dimension of the final matrix is 24×24. The 0, 1, 2, 3, 4 and 5 first bins represent the T_X, T_Y, T_Z, R_X, R_Y and R_Z of the Pixel detector. The other parts of the silicon tracking detector exhibit the same pattern.

reconstructed by the ID. In the same manner, the beam spot (BS) constraint, which coerces the tracks to be originated at the BS, has been extensively used during the ID alignment.

The formalism of the χ^2 including the track parameter constraint looks as follows:

$$\chi^2 = \sum_t \boldsymbol{r_t}(\boldsymbol{\pi}, \boldsymbol{a})^T V^{-1} \boldsymbol{r_t}(\boldsymbol{\pi}, \boldsymbol{a}) + \boldsymbol{R}(\boldsymbol{\pi})^T S^{-1} \boldsymbol{R}(\boldsymbol{\pi}) \tag{4.19}$$

the track constraint is represented by the second term which only depends on the track parameters. The $\boldsymbol{R}(\boldsymbol{\pi})$ vector acts as a residual that contains the track parameter information and S is a kind of covariance matrix which keeps the constraint tolerances. As always, the goal is the minimization of the total χ^2 with respect to the alignment parameters. Therefore:

$$\frac{d\chi^2}{d\boldsymbol{a}} = 0 \longrightarrow \sum_t \left(\frac{d\boldsymbol{r_t}(\boldsymbol{\pi}, \boldsymbol{a})}{d\boldsymbol{a}} \right)^T V^{-1} \boldsymbol{r_t}(\boldsymbol{\pi}, \boldsymbol{a}) + \sum_t \left(\frac{d\boldsymbol{R_t}(\boldsymbol{\pi})}{d\boldsymbol{a}} \right)^T S^{-1} \boldsymbol{R_t}(\boldsymbol{\pi}) = 0 \tag{4.20}$$

The first step is the resolution of the track fit in order to find the track parameters ($\boldsymbol{\pi} = \boldsymbol{\pi_0} + \delta\boldsymbol{\pi}$). Subsequently, the alignment parameters are determined. For the sake of clarity, the details of the mathematical formalism have been moved to Appendix B. The final alignment parameter corrections ($\delta\boldsymbol{a}$) using a track parameter constraint are given by Equation 4.21.

$$\delta\boldsymbol{a} = -\overbrace{\left(\sum_t \left(\frac{\partial \boldsymbol{r_t}(\boldsymbol{\pi_0}, \boldsymbol{a})}{\partial \boldsymbol{a}}\right)^T [I - E_t X']^T V^{-1} \left(\frac{\partial \boldsymbol{r_t}(\boldsymbol{\pi_0}, \boldsymbol{a})}{\partial \boldsymbol{a}}\right)\right)^{-1}}^{M'^{-1}} \cdot \left(\underbrace{-\sum_t \left(\frac{\partial \boldsymbol{r_t}(\boldsymbol{\pi_0}, \boldsymbol{a})}{\partial \boldsymbol{a}}\right)^T [I - E_t X']^T V^{-1} \boldsymbol{r_t}(\boldsymbol{\pi_0}, \boldsymbol{a})}_{\nu'} + \underbrace{\sum_t \left(\frac{\partial r_t(\boldsymbol{\pi_0}, \boldsymbol{a})}{\partial \boldsymbol{a}}\right)^T (Z_t X')^T S^{-1} \boldsymbol{R_t}(\boldsymbol{\pi_0})}_{w}\right) \tag{4.21}$$

Comparing Equation 4.16 and Equation 4.21 the impact of the track parameter constraint in the final alignment corrections can be obviously seen. The big matrix M' includes a new term X' which is built as a function of the covariance matrix V and the derivative of both residual vectors ($\boldsymbol{r}$ and $\boldsymbol{R}$) with respect to the track parameters ($E_t = \frac{\partial \boldsymbol{r}}{\partial \boldsymbol{\pi}}$ and $Z_t = \frac{\partial \boldsymbol{R}}{\partial \boldsymbol{\pi}}$). The big vector $\boldsymbol{\nu'}$ is modified by the same term. Finally a new vector $\boldsymbol{w}$ appears exclusively due to the introduction of the constraint.

In a more compact notation, the final solution can be written as:

$$M'\delta\boldsymbol{a} + \boldsymbol{\nu'} + \boldsymbol{w} = 0 \longrightarrow \delta\boldsymbol{a} = -(M')^{-1}(\boldsymbol{\nu'} + \boldsymbol{w}) \tag{4.22}$$

Beam spot constraint

This constraint serves to ensure that the used tracks were generated in the vicinity of the BS position. At the same time, it is used in order to fix the position of the detector in the transverse plane.

The track parameters can be written as a function of the position of the beam. Therefore, the transverse impact parameter (d_0) can be constrained with its expectation (d_0') from the BS:

$$d_0' = -(x_{BS} + Z_0\alpha_{BS})\sin\phi_0 + (y_{BS} - Z_0\beta_{BS})\cos\phi_0 \tag{4.23}$$

where x_{BS} and y_{BS} are the coordinates of the BS, ϕ_0 the track azimutal angle and the terms $Z_0\alpha_{BS}$ and $Z_0\beta_{BS}$ take into account the tilt of the beam with respect to the Z global axis. The uncertainty which fills the S matrix uses the impact parameter error. The impact of the BS constraint can be seen in Section 4.8.2.

4.3.2 The Globalχ^2 fit with an alignment parameter constraint

In the χ^2 formalism one can also include constraints in the alignment parameters themselves. These constraints can be used to restrict the range of movements of some DoFs which are weakly sensitive. The χ^2 expression including the alignment parameter constraint looks as follows:

$$\chi^2 = \sum_t \boldsymbol{r_t}(\boldsymbol{\pi}, \boldsymbol{a})^T V^{-1} \boldsymbol{r_t}(\boldsymbol{\pi}, \boldsymbol{a}) + \boldsymbol{R}(\boldsymbol{a})^T G^{-1} \boldsymbol{R}(\boldsymbol{a}) \tag{4.24}$$

The constraint has been constructed using a generic residual vector with just an alignment parameter dependence ($\boldsymbol{R} = \boldsymbol{R}(\boldsymbol{a})$) and the corresponding covariance or tolerance matrix (G). Notice that the

conventional χ^2 is evaluated over all tracks while the constrained term is not because the alignment parameters must be the same for the entire set of tracks. Again, the goal is to find the alignment parameters that minimize the χ^2 (Equation 4.24). Therefore:

$$\frac{d\chi^2}{d\boldsymbol{a}} = 0 \quad \rightarrow \quad \sum_t \left(\frac{d\boldsymbol{r_t}(\boldsymbol{\pi}, \boldsymbol{a})}{d\boldsymbol{a}}\right)^T V^{-1} \boldsymbol{r_t}(\boldsymbol{\pi}, \boldsymbol{a}) + \left(\frac{d\mathbf{R}(\mathbf{a})}{d\mathbf{a}}\right)^T G^{-1}\mathbf{R}(\mathbf{a}) = 0 \tag{4.25}$$

The first addend of the equation 4.25 has been solved in Section 4.3. Now, the solution including the second term is going to be explained. The dimension of the $\boldsymbol{R}(\boldsymbol{a})$ depends on the number of used constraints (or residuals in this notation) and G is a square matrix with dimension equal to the number of constraints. As usual, it is convenient to perform a series expansion of the residual $\mathbf{R}$ around a set of initial alignment parameters: $\boldsymbol{a_0}$. This approximation neglects the second derivatives.

$$\mathbf{R} = \mathbf{R}(\mathbf{a}_0) + \left.\frac{\partial \mathbf{R}}{\partial \mathbf{a}}\right|_{\mathbf{a}_0} \delta\mathbf{a} \tag{4.26}$$

Replacing 4.26 in the constrained term, one obtains:

$$\left(\frac{d\boldsymbol{R}(\boldsymbol{a})}{d\boldsymbol{a}}\right)^T G^{-1}\boldsymbol{R}(\boldsymbol{a}) = \left(\left.\frac{\partial \boldsymbol{R}(\boldsymbol{a})}{\partial \boldsymbol{a}}\right|_{a_0}\right)^T G^{-1}\boldsymbol{R}(\boldsymbol{a_0}) + \left(\left.\frac{\partial \boldsymbol{R}(\boldsymbol{a})}{\partial \boldsymbol{a}}\right|_{a_0}\right)^T G^{-1} \left.\frac{\partial \boldsymbol{R}(\boldsymbol{a})}{\partial \boldsymbol{a}}\right|_{a_0} \delta\boldsymbol{a} \tag{4.27}$$

Identifying $D_a = \frac{\partial \boldsymbol{R}(\boldsymbol{a})}{\partial \boldsymbol{a}}\,|_{a_0}$ and using a more compact notation, the above equation can be written as:

$$\left(\frac{d\boldsymbol{R}(\boldsymbol{a})}{d\boldsymbol{a}}\right)^T G^{-1}\boldsymbol{R}(\boldsymbol{a}) = D_a^T G^{-1}\boldsymbol{R}(\boldsymbol{a_0}) + (D_a^T G^{-1} D_a)\delta\boldsymbol{a} = \boldsymbol{\nu_a} + M_a\delta\boldsymbol{a} \tag{4.28}$$

where $\boldsymbol{\nu_a}$ and M_a are the vector and matrix associated to the alignment parameter constraint. This terms has to be added to the general track based alignment equation (Equation 4.18):

$$M\delta\boldsymbol{a} + \boldsymbol{\nu} + M_a\delta\boldsymbol{a} + \boldsymbol{\nu_a} = 0 \tag{4.29}$$

The solving of the alignment equation has the following final expression:

$$\delta\boldsymbol{a} = -(M + M_a)^{-1}(\boldsymbol{\nu} + \boldsymbol{\nu_a}) \tag{4.30}$$

The alignment parameter constraint gives an additional term to the big matrix and also to the big vector. The track parameter constraints can limit the movements of some alignable structures using external position measurements or directly as a sort of penalty term. Both extensions have been implemented in the Globalχ^2 code. An example of these types of constraints is exposed in Section 4.7.3.

Alignment parameter constraint with external position measurements

In order to constrain the alignment corrections, one can write the residuals as a function of the alignment parameters. Therefore, the minimization of the residuals directly imply a straight calculation of these parameters. In that sense, the residual vector $\mathbf{R}(\boldsymbol{a})$ can be written as: $\boldsymbol{R} = C\delta\boldsymbol{a}$, where $\delta\boldsymbol{a}$ is a

vector with the alignment parameter corrections and C represents the lineal combination matrix that can encompass a constraint between different structures and DoFs. Using the above residual, the D_a matrix (4.28) is directly the C matrix and the ν_a is null. Therefore, the final alignment corrections are given by Equation 4.31.

$$\delta\mathbf{a} = -(M + C^T G^{-1} C)^{-1}\boldsymbol{\nu} \tag{4.31}$$

There are different measurements of the detector position done by external systems that could be used to construct the $\boldsymbol{R(a)}$:

- **Survey information:** the position of the module detectors have been determined using optical and mechanical techniques. The data was collected during the different stages of the detector assembly, allowing relative measurements between the module devices [83]. Moreover, position measurements were also done during the detector installation into the ATLAS cavern. The survey information has often been used as starting detector geometry enabling a quick convergence of the track-based alignment algorithms.
- **Frequency Scanning Interferometry (FSI):** the FSI [84] is an optical system installed in the SCT to control the detector movements during the LHC operation. The monitoring of the detector geometry is based on a grid of distances between the nodes installed in the SCT. The grid lines are shined by lasers. This system provides information about the stability of the detector as a function of time and allows the identification of possible detector rotations or radial deformations. Although the FSI has been running during the data taking, its information has not been yet integrated in the alignment chain. Until now, the FSI measurements have been used to cross-check the detector deformations observed by the track-based alignment algorithms.

Alignment parameter constraint as a penalty term

The *SoftModeCut* (SMC) is an alignment parameter constraint added as a penalty term. Basically, it is a simplified version of the previous case where the residuals are just $\boldsymbol{R} = \delta\boldsymbol{a} = (\boldsymbol{a} - \boldsymbol{a_0})$. Here, the D_a simply becomes the identity matrix and the covariance matrix is directly a diagonal matrix with its elements equal to σ^2_{SMC} (resolution of the constrained alignment parameters). Depending of the size of the σ_{SMC} the DoFs will be more or less limited. In this scenario, the final alignment corrections are given by:

$$\delta\boldsymbol{a} = (M + G^{-1}_{SMC})^{-1}\boldsymbol{\nu} \tag{4.32}$$

4.3.3 Globalχ^2 solving

In order to find the alignment parameters (Equation 4.18), the alignment matrix (M) has to be inverted. In general, its inversion is not an easy task since usually it may have a huge size. The size gets bigger for higher alignment levels. Therefore, the solving of the matrix considering every individual module (~35.000 DoFs for the silicon detectors) has been one of the challenging problems for the Globalχ^2 method. The difficulty not only consists in a storage problem but also in the large number of operations that are needed to solve it and the time involved. Many studies were done in order to improve the techniques to invert the matrix [85].

For the alignment constants presented in this thesis, the matrix was inverted using a dedicated machine, called Alineator [86], located at IFIC computing center [87]. This machine is a cluster with two AMD

Dual Core Opteron of 64 bits. It works at 2.6 GHz with 32 GB of memory. A specific protocol (MPI[2]) was used to parallelize the process through the different cores. The matrix was solved using the ScaLAPACK [3] [88] library in order to fully diagonalize it.

Basically, the diagonalization method converts the symmetric, square and dense big matrix in a diagonal one with the same intrinsic information. After diagonalization, the big matrix M looks as follows:

$$M = B^{-1} M_d B \qquad M_d = [diag(\lambda_i)] \tag{4.33}$$

The M_d is the diagonal matrix and B the change of base matrix from the physical DoFs to those sensitive to the track properties. The elements (λ_i) in the diagonal of M_d are called eigenvalues and usually they are written in a increasing order: $\lambda_1 \leqslant \lambda_2 \leqslant ... \leqslant \lambda_{ALIGN}$. The eigenvectors are just the rows of the change of base matrix B. These eigenvectors or eigenmodes represent the movements in the new base.

Errors of the alignment parameters

Beyond the alignment parameters, their accuracy is also an important quantity. The study of the matrix in its diagonal shape allows the recognition of the singularities which are linked with the undefined or weakly determined detector movements. The error of a given alignment parameter, ε_i, is determined by the incrementing of the χ^2 by 1 ($\chi^2 = \chi^2_0 + 1$). The χ^2 in the diagonal base can be expressed as:

$$\chi^2 = \chi^2_0 + \frac{\partial \chi^2}{\partial \boldsymbol{b}} \delta \boldsymbol{b} \tag{4.34}$$

where $\boldsymbol{b}$ represents the alignment parameters in the diagonal base and $\delta \boldsymbol{b}$ theirs associated corrections. The χ^2 derivative with respect to the track parameters can be also calculated in the following way:

$$\frac{\partial \chi^2}{\partial \boldsymbol{b}} = \left(\sum_t \left(\frac{d \boldsymbol{r_t}}{d \boldsymbol{b}} \right)^T V^{-1} \boldsymbol{r_t} \right)^T + \left(\sum_t \boldsymbol{r_t} V^{-1} \frac{d \boldsymbol{r_t}}{d \boldsymbol{b}} \right)^T = 2 \boldsymbol{\nu_b}^T \tag{4.35}$$

where $\boldsymbol{\nu_b}$ is the bigvector in the diagonal base (the local aproximation has been used in order to simplify the calculations). Keeping in mind that the errors are related with the increment of the χ^2 in a unit, one can calculate:

$$\chi^2 = \chi^2_0 + 1 = \chi^2_0 + \frac{\partial \chi^2}{\partial b_i} \varepsilon_i = \chi^2_0 + 2(\nu_b)^T_i \varepsilon_i \tag{4.36}$$

For a given alignment parameter b_i, its associated uncertainty (using the Equation 4.18) is given by:

$$2\varepsilon_i (M_b)_{ii} \varepsilon_i = 2\lambda_i \varepsilon_i^2 = 1 \longrightarrow \varepsilon_i^2 = \frac{1}{2\lambda_i} \tag{4.37}$$

Equation 4.37 shows how the eigenvalues define the precision of the alignment parameters corrections. Therefore, small eigenvalues imply large errors while large eigenvalues are related with small errors and thus, well determined movements. In the extreme case of null eigenvalues (λ_i=0) the matrix becomes singular and the inversion is not possible. The null eigenvalues are usually connected with global movements of the entire system. The study of the matrix in the diagonal base makes easier the identification and rejection of these singularities in order to find a solution for the alignment corrections. Obviously the error on the physical alignment parameters is computed from those in the diagonal base and the change of base matrix B.

[2]Message Passing Interface standards (MPI) is a language-independent communications protocol used to program parallel computers.

[3]ScaLAPACK is a library of high-performance linear algebra routines for parallel distributed memory machines. ScaLAPACK solves dense and banded linear systems, least squares problems, eigenvalue problems and singular value problems [88, 89].

4.3.4 Center of Gravity (CoG)

The function of the Centre-of-Gravity (CoG) algorithm is to correct any change in the center of gravity of the detector as an artefact of the unconstrained global movements. This step is required because in ATLAS the ID provides the reference frame for the rest of the detectors (calorimeters and muon system).

The CoG algorithm is based on the least squares minimization of all detector element distances between their actual positions (κ_{curr}) of their reference one (κ_{ref}). The χ^2 is defined as:

$$\chi^2 = \sum_i \sum_{\kappa=x,y,x} (\Delta\kappa_i)^2 \quad and \quad \Delta\kappa = \kappa_{curr} - \kappa_{ref} \tag{4.38}$$

where the displacement is given in the local frame of the module and the index *i* goes over all detector elements. The Δ's from equation 4.38 can be linearly expanded with respect to the six global transformations of the entire detector system (G_l):

$$\Delta\kappa = \Delta\kappa_0 + \sum_l \frac{\partial\kappa}{\partial G_l}\Delta G_l \quad with \quad G_l \epsilon T_X, T_Y, T_Z, R_X, R_Y, R_Z \tag{4.39}$$

where $\frac{\partial\kappa}{\partial G_l}$ is the Jacobian transformation from the global to the local frame of a module. The χ^2 minimization condition leads to six linear equations with six parameters (T_X, T_Y, T_Z, R_X, R_Y, R_Z). The CoG was used during the commissioning phases and for the cosmic ray runs. Later, it was used with collision data to reinforce the beam spot constraint.

4.4 The ID alignment geometry

The ID alignment is performed at different levels which mimic the steps of the assembly detector process. The alignment proceeds in stages, from the largest (e.g. the whole Pixel detector) to the smallest structures (individual modules). The biggests structures are aligned in order to correct the collective movements. The expected size of the corrections decreases with the size of the alignable objects. By contrast, the statistics required for each level increases with the granularity. The alignment levels are defined as follows:

- **Level 1 (L1):** this level considers the biggest structures. The Pixel detector is taken as a unique body while the SCT and TRT are both split in three structures (one barrel and two end-caps). Generally each structure has 6 DoFs. Although the TRT barrel also has the same DoFs, the position along the wire direction, T_Z is not used in the barrel alignment due to the intrinsic limitations of this sub-detector.
- **Level 2 (L2):** this level subdivides the Pixel and SCT barrel detectors in layers and the TRT barrel in modules. The end-caps of the Pixel and the SCT subsystems are separated in discs and the TRT end-caps in wheels. There are some DoFs that are not used in the alignment because they can not be accurately determined by the algorithm using tracks. For example, the T_Z, R_X and R_Y of the silicon end-caps and the R_X and R_Y for the TRT end-caps.
- **Level 3 (L3):** this level aligns the smallest detector devices. For the silicon tracking system it determines directly the position of the individual modules. For the TRT, the L3 corrects the wire position in the most sensitive DoFs: translations in the straw plane (T_ϕ) and rotations around the axis perpendicular to the straw plane (R_r and R_Z for the barrel and end-cap respectively).

Some intermediate alignment levels were included in the software in order to correct for misalignments introduced during the detector assembly process. For instance, the Pixel barrel was mounted in half-shells and posteriorly they were joined in layers. Taking it into account, the L2 was modified and the three layers of the Pixel detector were accordingly split in six half-shells.

In addition, a new software level, which includes the staves and ring structures, was defined for the silicon detectors (Level 2.5). The Pixel staves are physical structures, composed by 13 modules in the same $R\phi$ position. These structures were assembled and surveyed. By contrast, the SCT modules were not mounted in staves but they were individually placed on the cylindrical structure. Nevertheless, for alignment purposes, the SCT barrel has been also split into rows of 12 modules. The SCT end-cap modules were also mounted individually on the end-cap disks. Nonetheless, in order to correct for some observed misalignments the ring structures were included. Therefore, each SCT end-cap is sorted into 22 rings.

Table 4.4 shows the alignment levels implemented in the Globalχ^2 algorithm for the Pixel, SCT and TRT detectors. Figure 4.3 shows a sketch of the different silicon alignment levels.

Level	Description	Structures	Number of DoFs
1	Whole Pixel detector	1	24
	SCT barrel and 2 end-caps	3	
	TRT barrel	1	18
	TRT end-caps	2	
2	Pixel barrel split into layers	3	186
	Pixel end-caps discs	2×3	
	SCT barrel split into layers	4	
	SCT end-caps split into discs	2×9	
	TRT barrel modules	96	1056
	TRT end-cap wheels	2×40	
2.5	Pixel barrel layers split into staves	112	2028
	Pixel end-cap discs	2×3	
	SCT barrel layers split into rows	176	
	SCT end-cap discs split into rings	2×22	
3	Pixel modules	1744	34992
	SCT modules	4088	
	TRT barrel wires	105088	701696
	TRT end-cap wires	245760	

Table 4.1: Alignment levels implemented for the ID tracking system. The name, a brief description, the number of structures and the total DoFs are reported on the table.

4.5 Weak modes

The Weak Modes are defined as detector deformations that leave the χ^2 of the fitted tracks almost unchanged. The Globalχ^2 method could not completely remove these kind of deformations since they are not detected through the residual analysis. Therefore, these kind of movements (which are really hard

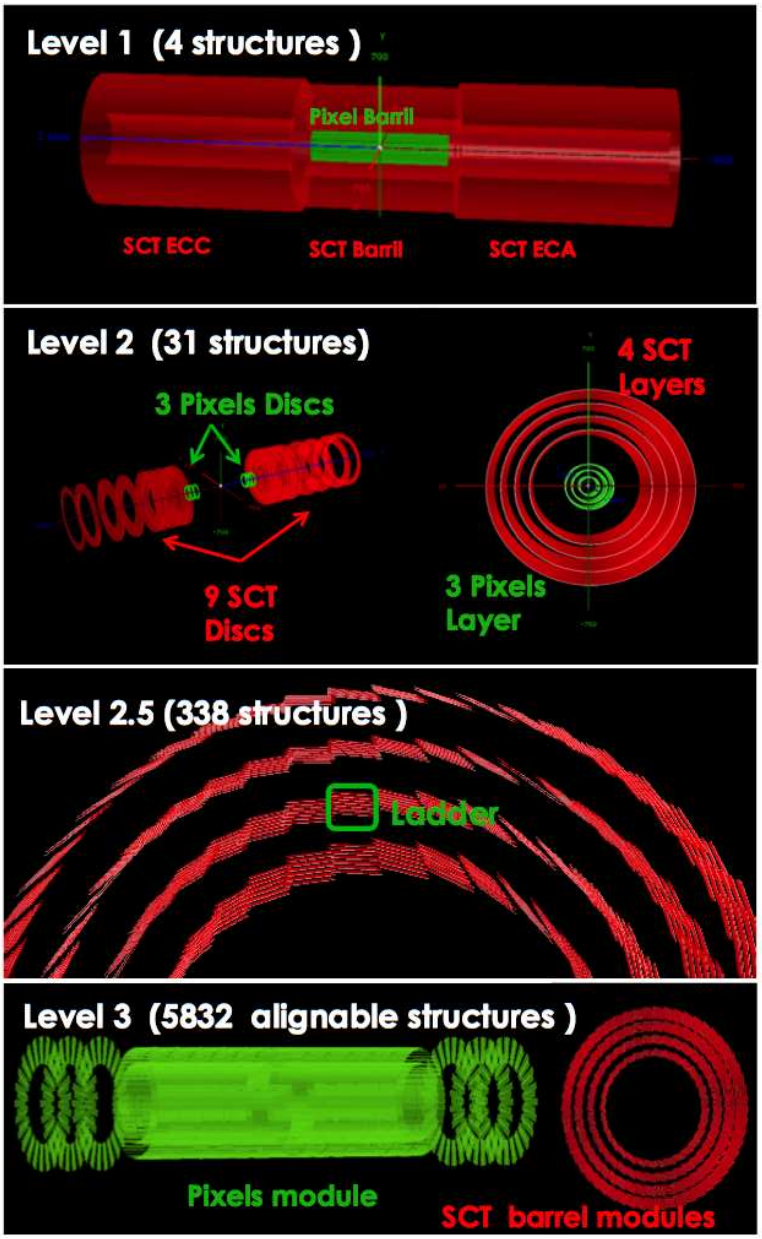

Figure 4.3: Picture of the silicon detector structures for some alignment levels.

to detect and correct) can induce a potential systematic misalignment for the ID geometry compromising the performance of the detector. These movements can be divided in:

- **Global movements:** the absolute position and orientation of the ID inside the ATLAS detector can not be constrained using only reconstructed tracks. In order to detect the ID global movements the use of an external references is needed. The study of the eigenvectors and eigenvalues in the

diagonal base has shown that the global movements have very small or zero associated eigenvalues. In a general situation, where no constraints are included, the global movements associated to the ID are six (three translations and three rotations of the whole system). Nevertheless, depending on the level of alignment and also on the data used, the modes with large errors or weak constrained may change. Moreover, when external constraints are included, the number of global movements is also modified according to the new scenario. Therefore, not always the six first DoFs of the diagonal matrix have to be removed because they can vanish under certain conditions. The number of global movements for different alignment scenarios was indeed studied. The results are presented in Section 4.7.1.

- **Detector deformations:** several MC studies have been done to identify the most important weak modes and their impact on the final physic results [90]. Figure 4.4 introduces some of the potential deformation of the ID geometry. Actually, the picture shows those deformations ΔR, $\Delta\phi$ and ΔZ with module movements along radius (R), azimutal angle (ϕ) or Z direction. The χ^2 formalism allows the addition of constraint terms (Section 4.3.1 and 4.3.2) in order to point the algorithm into the correct direction towards the real geometry. Some of these deformation may be present in the real geometry due to the assembly process. Alternatively, wrong alignment corrections following those patterns can appear as solutions of the alignment equation. In both cases, as said before, it is hard to detect and correct them.

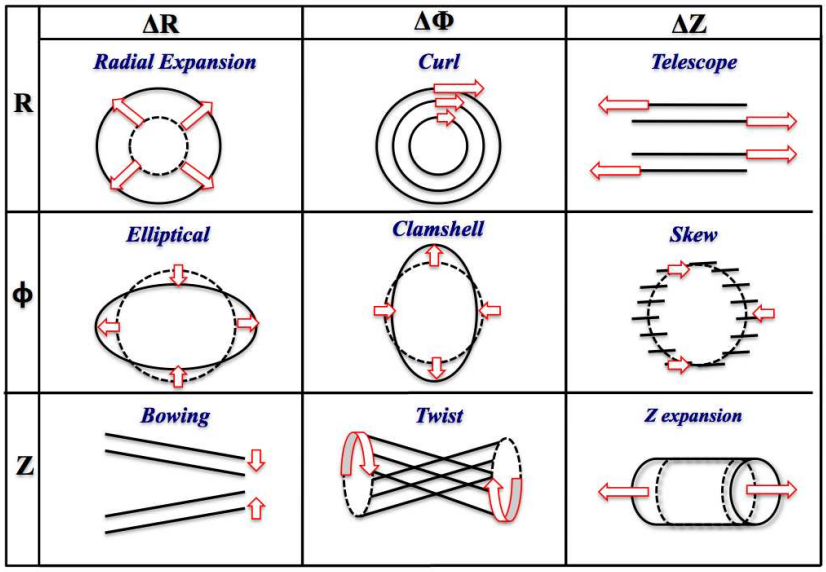

Figure 4.4: Schematic picture of the most important weak modes for the ATLAS Inner Detector barrel.

The alignment strategy has been designed to minimize the pitfalls of the weak modes in the detector geometry during the real data alignment. In that sense, there are different track topologies with different properties that can contribute to the ID alignment. Their combination may mitigate the impact of the weak modes that are not common for all topologies. The used ones for the alignment procedure are the following:

- **Collision data.** The most important sample is formed by the collision events. These ones are produced in the interaction point and the particles are propagated inside out correlating the detectors

radially. The beam spot constraint can be used with these tracks in order to eliminate various weak modes.

- **Cosmic rays data.** These comic ray tracks cross the entire detector connecting the position of the modules in both hemispheres. Due to the nature of the cosmic data, this sample is more useful for the alignment of the barrel part of the detector. Since the cosmics are not affected by the telescope and curl deformations, their combination with collision data allows to fix these weak modes.
- **Overlapping tracks.** Although large data samples are needed, there are special tracks, as those tracks that pass trough the zone where the modules overlap, that can constrain the circumference of the barrel layers and eliminate the radial expansions.
- **Beam halo data:** The beam halo events produce tracks parallel to the beam direction. This sample was proposed as a candidate to improve the alignment of the end-caps. Although, they were not finally used.

4.6 Alignment datasets

Different datasets have been used in order to align the Inner Detector during different data challenges:

- **Multimuons:** the multimuon sample was a specific MC dataset generated primarily for alignment test purposes. This sample consisted in $\sim 10^5$ simulated events. In each event ten muon tracks emerge from the same beam spot. A half of the sample is composed by positively charged particles while the other half consists of negatively charged particles. The transverse momentum of the tracks was generated from 2 GeV to 50 GeV. The ϕ and η presented uniform distributions in the range of $[0, 2\pi]$ and $[-2.7, +2.7]$ respectively. In order to work under realistic detector conditions this sample was generated with the CSC geometry (Section 4.7.2). More information about this sample (track parameters distributions and vertex reconstruction) can be found in the Appendix D.
- **Cosmic Ray Simulation:** the simulation of cosmic ray muons passing though ATLAS is done by running a generator which provides muons at ground level and posteriorly they are propagated within the rock [91]. One of the features of this process is the ability to filter primary muons depending on their direction and energy. For example, those events which do not pass across the ATLAS detector volume are automatically discarded. Moreover, for the ID alignment purposes, the sample has been usually filtered by the TRT volume in order to have a high track reconstruction efficiency. Several cosmic ray samples, filtered using different detector volumes and magnetic field configurations, have been produced [92]. For the first ID alignment tests a sample of 300k events simulated without magnetic field and another one of 100k events with magnetic field were used. Both samples were produced with the CSC geometry (ATLAS-CommNF-02-00-00 and ATLAS-Comm-02-00-00 for magnetic field off and on respectively). The characteristic distributions of the cosmic ray tracks have been included in Appendix E.
- **ID Calibration:** the ID Calibration stream [93] (IDCALIB) was generated for performing the alignment and calibration. This stream provides a high ratio of isolated tracks with a uniform illumination of the detector. During the FDR exercises (Section 4.7.4) an IDCALIB stream composed of isolated pions was used. Their tracks were generated uniformly with a momentum range from 10 to 50 GeV. These single pions were produced with the CSC geometry tag ATLAS-CSC-02-01-00 [94]. The IDCALIB stream has been also used as the main stream for aligning the ID with real data.

- **Cosmic real data 2008 and 2009:** the cosmic real data taking campaigns took place in Autumm 2008 and Summer 2009.
  - 2008 data: during this period around 7 M of events were recorded by the ID using different magnets configuration.
  - 2009 data: the cosmic statistics used to perform the ID alignment with the 2009 cosmic rays were of ~3.2 M of events. An amount of 1.5 M of cosmics were recorded with both magnetic fields, solenoid and toroids, switched on. On the other hand 1.7 M of events were taken without any magnetic field.
- **Collision data at 900 GeV:** millions of collisions, equivalent to a $7\mu b^{-1}$ integrated luminosity, took place during the firsts weeks of operation of the LHC in December 2009. These data were used in order to perform the first alignment of the ID. Straightaway, around ~0.5 M of collision candidate events were recorded with stable beams conditions producing a total of ~380.000 events with all the ID sub-systems fully operational. This set of data was used in order to produce an accurate ID alignment for reconstructing the very first LHC collisions.

4.7 Validation of the *Global*χ^2 algorithm

Prior to the real collision data taking, many studies were performed in order to check the proper behaviour of the alignment algorithms and test the software readiness. This section explains the main ID alignment exercises. Notice that they are not presented in a time sequential line.

4.7.1 Analysis of the eigenvalues and eigenmodes

As stated before, the diagonalization of the alignment matrix can be used to identify the weakly constrained detector movements. During the commissioning of the alignment algorithms different scenarios were studied in order to find out the number of global modes to be removed depending on the running conditions (alignment levels, track topologies, constraints,...). The most common scenarios considered at that time were chosen: only silicon alignment, silicon alignment with BS constraint, silicon alignment with tracks reconstructed using the whole ID and the entire ID alignment (silicon + TRT). The ID geometry used was InDetAlign_Collision_2009_09 and TRTAlign_Collision_2009_04 for the silicon and TRT detectors respectively. The analysis was performed for two different detector geometries (L1 and L2) using two collision data runs (155112, 155634). This section presents the analysis at L1 in detail.

Analysis at L1:

- **Silicon alignment.** In this exercise, only the silicon detector information was used in the track reconstruction. Figure 4.5 (upper left) shows the associated eigenvalue spectrum with a big jump at the seventh eigenvalue. The first six modes are the problematic movements since their low values indicate a not precisely determination by the algorithm. Figure 4.6 shows the first six (1/eigenvalues)×eigenvectors. Each plot presents the twenty-four alignment parameters plotted in the X axis which are separated in four groups of 6 DoFs: first, the pixel detector, after that, the SCT ECA, the SCT barrel and finally the SCT ECC. The eigenvectors correspond to a global T_X and T_Y (modes 0 and 5), a global R_Z (mode 1), a global T_Z (mode 2) and a mixture of global R_X and

R_Y (modes 3 and 4). Therefore, the weakly constrained movements have been found to be indeed the global movements of the entire silicon tracking system inside the ATLAS detector.

- **Silicon alignment with a BS constraint.** A straight forward way to constrain the global translations of the entire system is to use an external reference. A very handy one is the BS. If the tracks are required to have been produced in the vicinity of the BS, then the system as a whole can not depart from that location. Therefore one expects to have just four instead of the six unconstrained movements. This is shown in Figure 4.5 (top right). Figure 4.7 shows the ordered (1/eigenvalues)×eigenvectors: a global R_Z rotation (mode 0), a global T_Z translation (mode 1) and a mixture of global $R_X - R_Y$ (mode 2 and 3). The translations in the transverse plane are not free anymore (global T_X and T_Y movements smaller than 10 μm). In summary, the use of the BS constraint reduces in two the number of modes to be removed of the final alignment solution.

- **Silicon alignment with BS constraint and TRT in the reconstruction.** In this test, the tracks are reconstructed with the full ID (including the TRT). Then, the silicon detectors alignment is attempted adding the BS constraint and keeping the TRT fixed (as an external constraint). Figure 4.5 (bottom left) shows the eigenvalue spectrum where one can see that the numbers of small eigenvalues have been reduced to just one. Figure 4.8 shows the six first (1/eigenvalues)×eigenvectors associated to this scenario. Only the T_Z translation (Mode 0), which is not precisely measured by the TRT, is not well constrained. The other plots display the next modes. Nevertheless, these ones do not correspond to any global mode. Therefore, the use of the TRT in the reconstruction fixes most of the silicon global movements. In this scenario, the number of modes to be removed has been reduced to only one.

- **ID alignment with BS constraint.** The more realistic situation corresponds to the entire ID alignment, where the silicon and the TRT detectors are aligned together. The number of alignable DoFs including the TRT increases to forty-two. The BS constraint is also applied, therefore the global T_X and T_Y are fixed and consequently the number of global movements reduced in two. Figure 4.5 (bottom right) shows the eigenvalue spectrum. Only the first five modes have small eigenvalues. Figure 4.9 displays the associated (1/eigenvalues)×eigenvectors: global T_Z movement of the TRT barrel (mode 0), global R_Z of the whole ID (mode 1), global T_Z excluding the TRT barrel (mode 2) and a $R_X - R_Y$ global rotations (modes 3 and 4). Comparing with the silicon alignment with BS constraint scenario one obtains the same global movements with the addition of the T_Z TRT barrel. Therefore, the number of modes to be removed is equal to five.

Analysis at L2:

The same scenarios were studied at L2. In these tests, the least constrained DoFs of the Pixel and SCT discs (namely T_Z, R_X and R_y) were kept fixed. The constraint of the T_Z, R_X and R_Y of the end-caps were used as a kind of external reference of the entire system and the movements associate to these DoFs disappeared. Therefore, when comparing with the L1 weakly determined modes, the number of global movements was reduced in three for each scenario.

Summary:

The number of modes to be removed at L1 and L2 are summarized in Table 4.2. This table was used during the alignment procedure in order to eliminate the global movements and therefore do not introduce any bias in the final alignment constants.

Alignment Level	Silicon + No BS	Silicon + BS	Silicon + BS + TRT Reco	Silicon + TRT + BS
1	6	4	1	5
2	3	1	0	2

Table 4.2: Number of global movements to be removed depending on the alignment scenario and the detector geometry level.

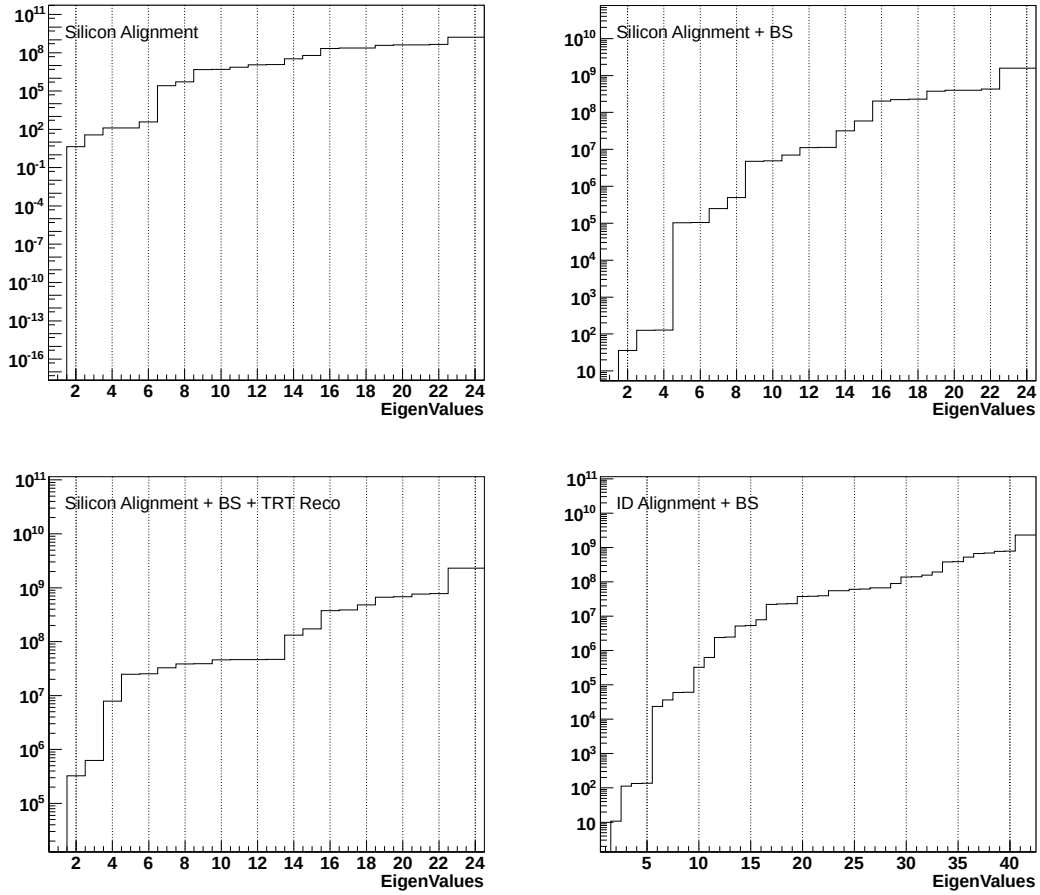

Figure 4.5: Eigenvalue spectrum for the 4 different scenarios aligned at L1: silicon detector (upper left), silicon detector using the BS constraint (upper right), silicon detector using the BS constraint and the TRT in the reconstruction (bottom left) and the ID using the BS constraint (bottom right).

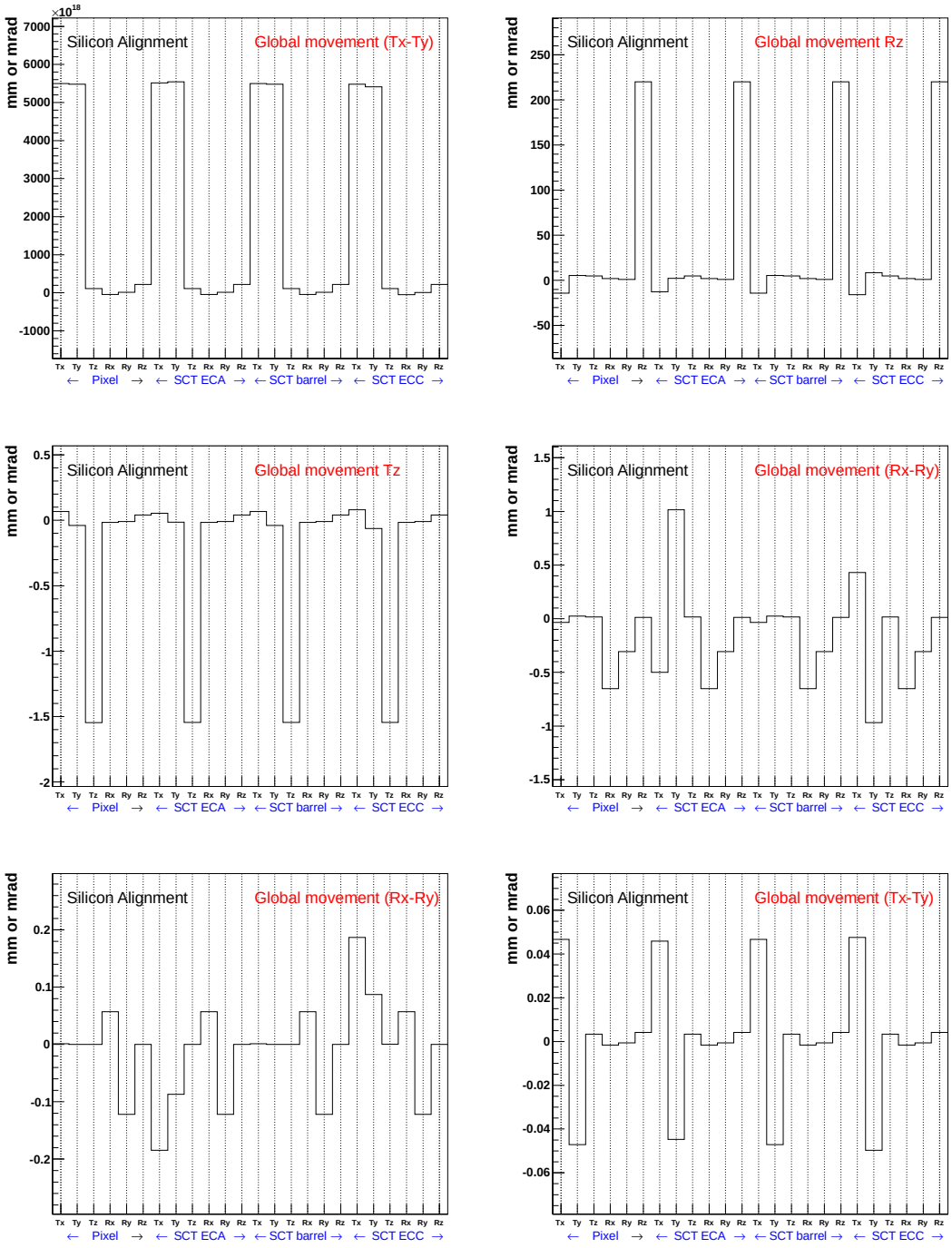

Figure 4.6: First six (1/eigenvalues)×eigenvectors for the silicon tracking detector aligned at L1. The 24 DoFs associated to the four structures at L1 can be seen in the x axis.

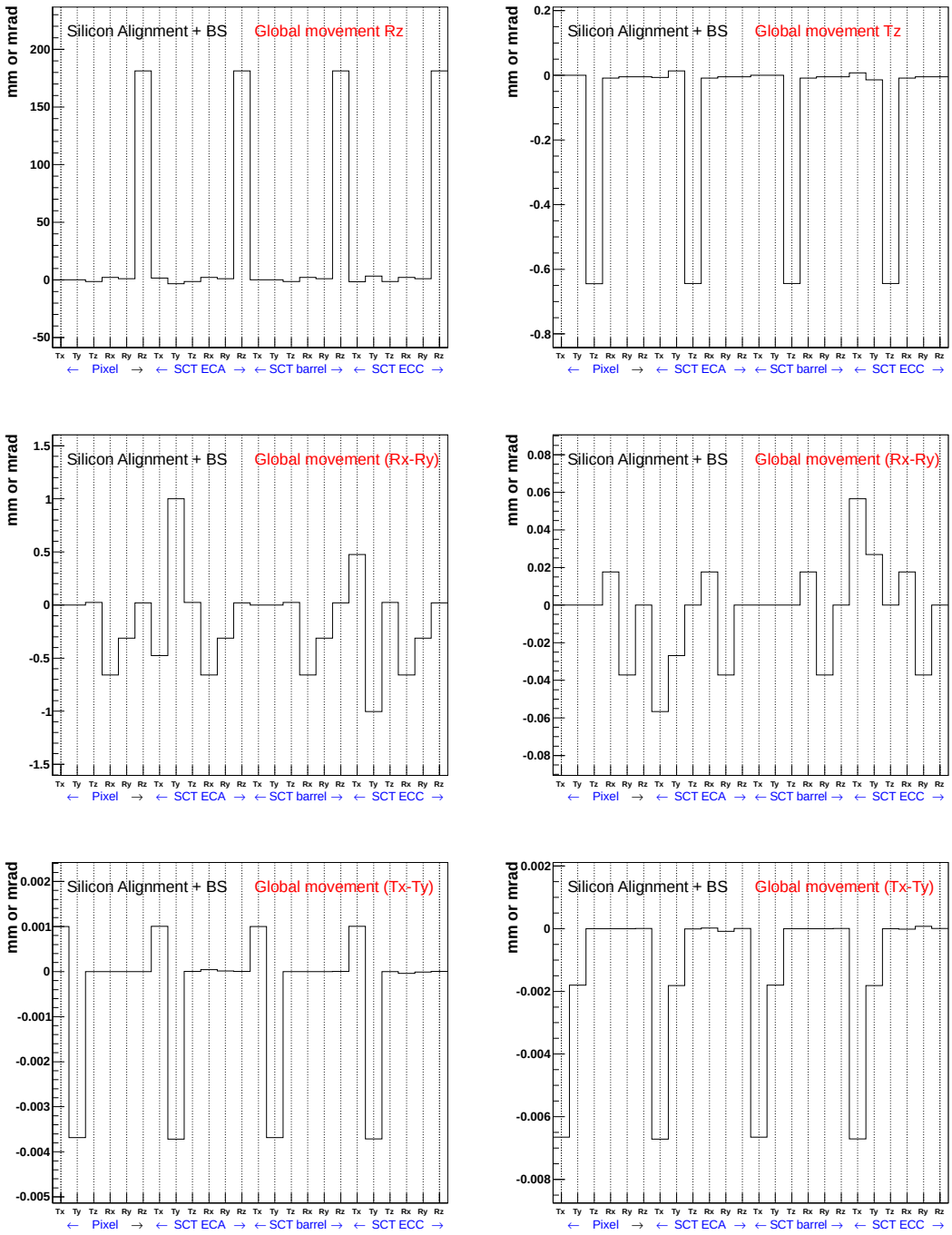

Figure 4.7: First six (1/eigenvalues)×eigenvectors for the silicon tracking detector aligned at L1 using the BS constraint. The 24 DoFs associated to the structures at L1 can be seen in the x axis.

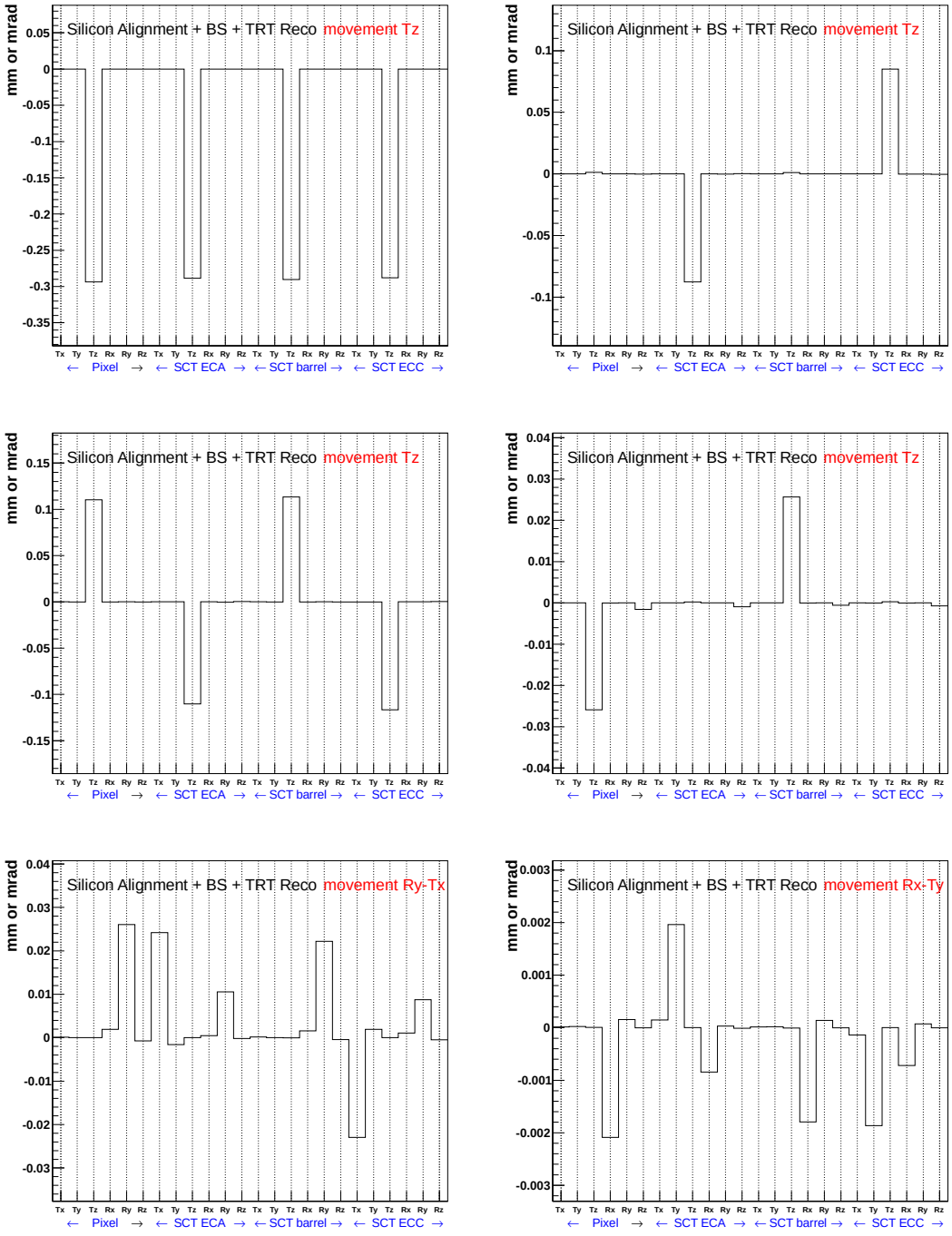

Figure 4.8: First six (1/eigenvalues)×eigenvectors for the silicon detector aligned at L1 using the BS constraint and the TRT in the reconstruction. The 24 DoFs associated to the structures at L1 can be seen in the x axis.

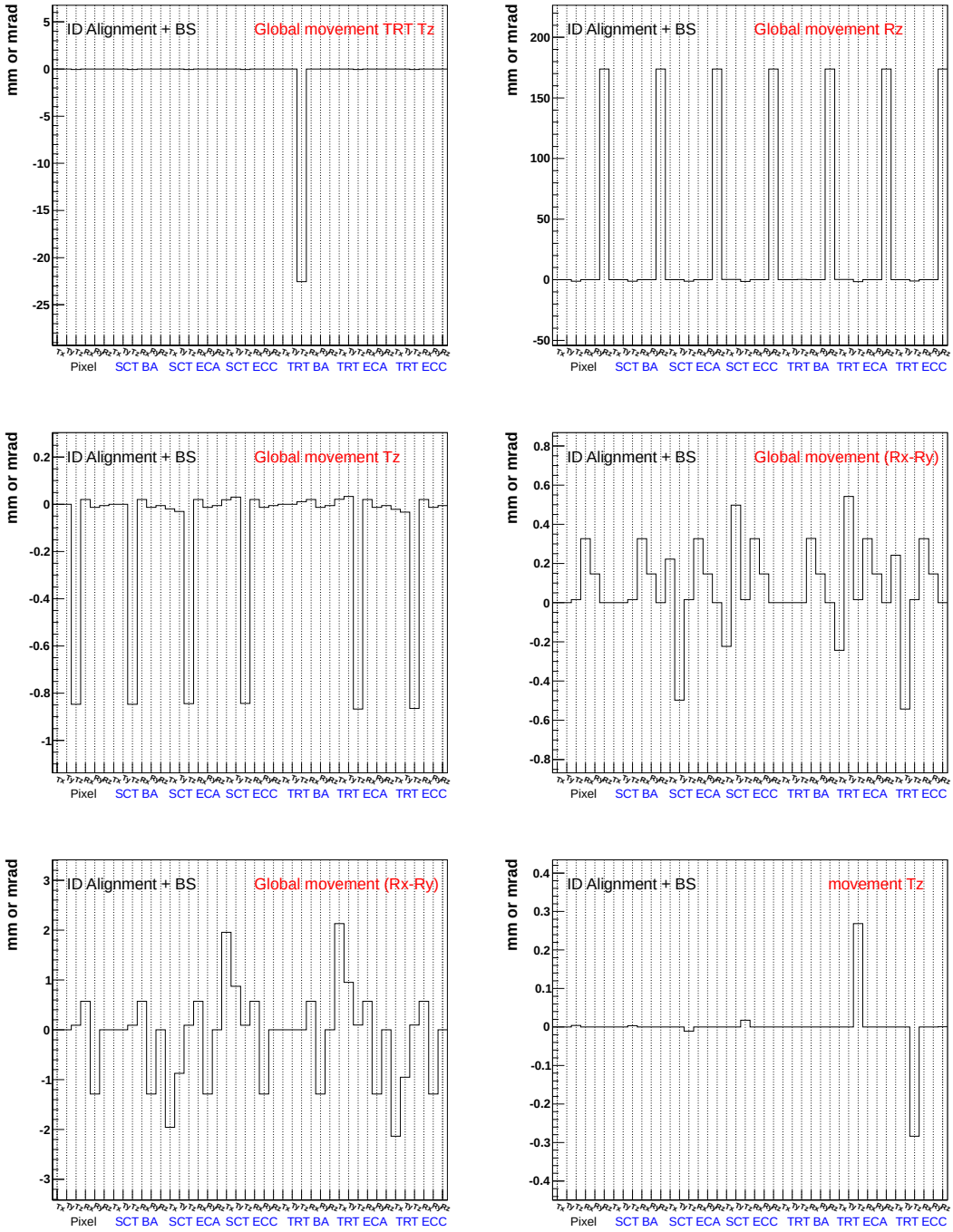

Figure 4.9: First six (1/eigenvalues)×eigenvectors for the ID detector aligned at L1 using the BS constraint. The 42 DoFs associated to the structures at L1 can be seen in the x axis.

4.7.2 Computing System Commissioning (CSC)

The CSC was the first exercise that allowed to test the alignment algorithms under realistic detector conditions [95]. Many simulated samples were produced using a distorted detector geometry, other than the nominal one. The distortions were included taking into account the expected uncertainties observed during the construction of the different parts of the detector. For example, the translation movements in the silicon system range from several mm at L1 to some micrometers at L3. The misaligned geometry also contained some of the ID potential systematic deformation. The curl effect was introduced at L2 by rotating the silicon layers. This deformation caused a bias in the measurement of the particle momentum. The misalignments at L3 were generated randomly and no systematic deformations were introduced at this stage. The detailed CSC misalignments for each DoF of the silicon system at each alignment level are summarized in Appendix C.

The adopted strategy for the CSC exercise [95] consisted in two steps:

- **Silicon alignment:** the alignment of the silicon system was done using the Globalχ^2 algorithm with a BS constraint in order to restrict the detector position in the transverse plane. The multimuon sample was used to perform the alignment at different levels, the DoF corrections at L3 were limited using a *SoftModeCut* (SMC) of tens of microns that avoided big movements inferred by the low statistics. Finally, several iterations were done mixing the cosmic ray and multimuon samples in order to eliminate systematic deformations and verify the convergence of the alignment constants.
- **TRT alignment:** the alignment of the TRT was done using a Localχ^2 approximation. First, an internal TRT alignment with multimuon TRT-only tracks was performed. Then, further iterations at L1 were done in order to align the TRT with respect to the silicon detector.

Once the alignment of the ID was completed, the validation of the results was performed using different figures of merit. The alignment parameters were examined and compared with those distributions obtained using the truth MC information. Moreover, samples as Z$\rightarrow \mu\mu$ were studied to check the impact of the systematic deformations in the physics observables. This exercise was a great success because it provided a perfect scenario to test many of the alignment techniques.

4.7.3 Constraint alignment test of the SCT end-cap discs

The SCT detector is divided in one barrel and two end-caps. Each end-cap is composed by 9 discs extending to cover approximately 2 m long in the beam directions and each disc has a diameter of ~1 m. The discs are not uniformly distributed since their position was optimized in order to every track crosses at least four SCT layers [96]. Figure 4.10 shows one entire SCT end-cap system.

The CSC tests demonstrated that the Globalχ^2 was able to estimate correctly the modules position in the barrel part. Nevertheless, some weakness when finding the corrections for the SCT discs emerged. Figure 4.11 presents the results for the T_Z alignment parameters of the SCT ECA (left) and SCT ECC (right) for an unconstrained alignment at L2. The black circles represent the values of the CSC geometry. The black crosses are the nominal positions of the detectors, which were taken as the starting point of the algorithm. In order to state that the alignment has corrected properly the geometry, the alignment solutions must match the black circles. Green squares and red triangles indicate the alignment corrections obtained by the algorithm at first and seventh iterations at L2 respectively. These results show that the algorithm found the right position of the pixel discs (3 black circles with Z <750 mm) and also for the

first SCT discs (9 discs located at Z >750 mm). Nevertheless, the outermost SCT discs exhibit a problem since their position is not completely recovered.

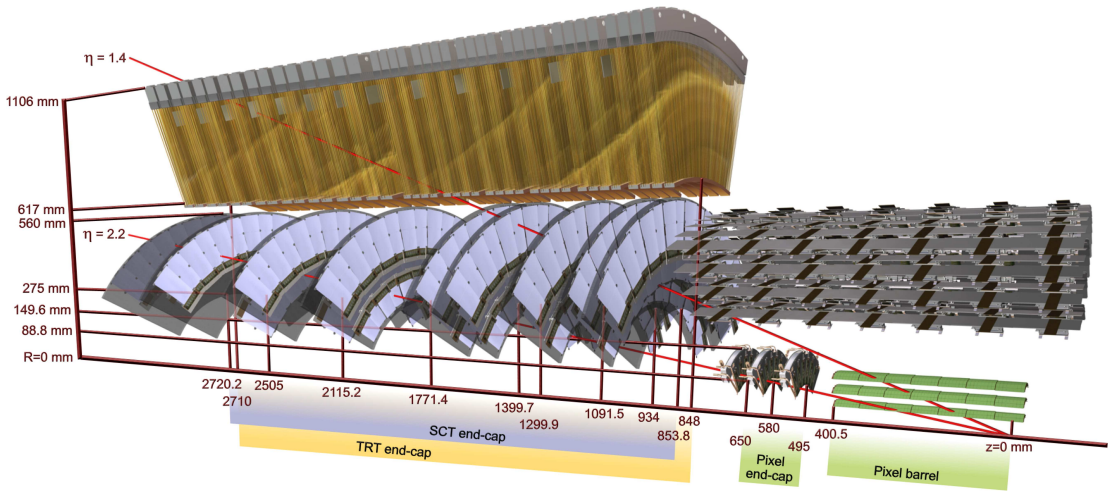

Figure 4.10: An illustration of the structural elements and sensors of the ID end-cap: the beryllium beam-pipe, the three Pixel discs, the nine SCT discs and the forty planes of the TRT wheels. The Pixel and SCT barrel layers are also partially displayed.

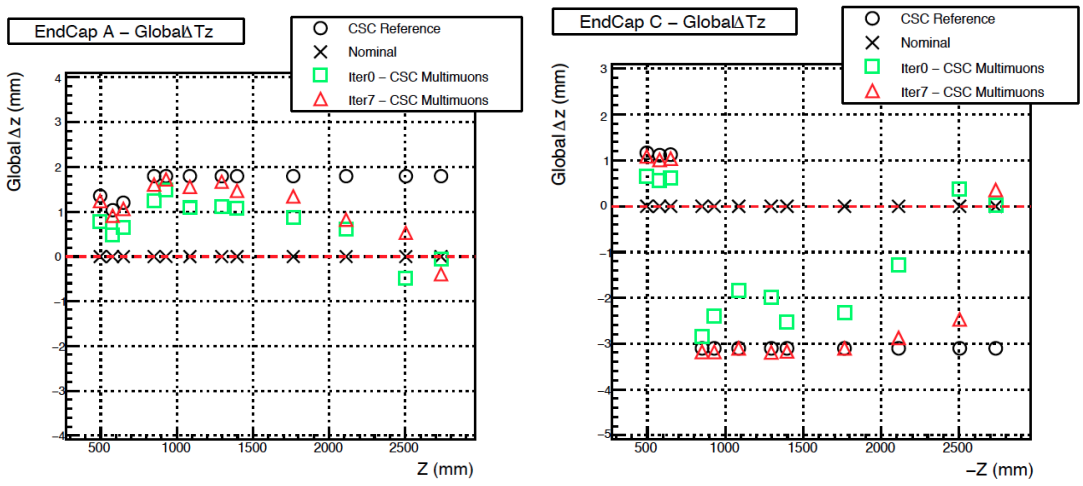

Figure 4.11: T_Z alignment corections for the Pixel and SCT ECA (left) and Pixel and SCT ECC (right) as a function of their distance to the detector center (Z). The disc estimated positions are shown for the first (green squares) and seventh (red triangles) iterations of the Globalχ^2 alignment at L2. The CSC detector position (black circles) and the initial geometry (black crosses) are also drawn.

This was understood as a weak mode. Indeed the eigenmode analysis showed that the T_Z of the end-cap discs was weakly constraint, and expansions of the end-caps were likely to occur. The poorly determined T_Z (even after 7 iterations) for the most external discs, motivated the implementation of an EC alignment parameter constraints to control these kind of movements. In order to illustrate how this EC constraint

was implemented in the Globalχ^2 code the following simple example is depicted. Figure 4.12 shows a sketch of a simple system formed by just three planes that can move only in the Z direction [4].

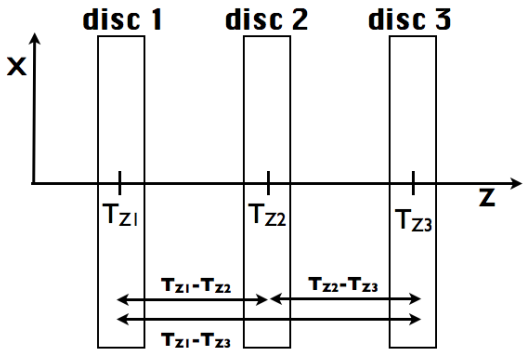

Figure 4.12: Sketch of an alignable system composed by three planes. These structures have to be aligned in the Z coordinate.

In order to avoid the collective expansion deformations of the end-cap discs but allowing a free movement for each individual disc, the residuals are built as a function of the alignment corrections (as explained in Section 4.3.2). The residual were defined as $\boldsymbol{R} = C\boldsymbol{\delta a}$, where $\boldsymbol{\delta a}$ takes into account the difference between the alignment T_Z parameters of each disc ($\delta a = (\delta T_{Z_1}, \delta T_{Z_2}, \delta T_{Z_3})$), the C matrix encompass the relation between the alignment parameters and G is an error diagonal matrix that contains the precision in the measurements. These terms can be seen in Equation 4.40.

$$R = C\delta a = \begin{pmatrix} \delta T_{Z_1} - \delta T_{Z_2} \\ \delta T_{Z_1} - \delta T_{Z_3} \\ \delta T_{Z_2} - \delta T_{Z_3} \end{pmatrix} \; ; \; C = \begin{pmatrix} 1 & -1 & 0 \\ 1 & 0 & -1 \\ 0 & 1 & -1 \end{pmatrix} \; ; \; G = \begin{pmatrix} \sigma_1\sigma_2 & 0 & 0 \\ 0 & \sigma_1\sigma_3 & 0 \\ 0 & 0 & \sigma_2\sigma_3 \end{pmatrix} \tag{4.40}$$

The contribution to the big matrix is done by the term $M_a = D^T G^{-1} D$ (Section 4.3.2). σ_1, σ_2 and σ_3 represent the tolerances in that coordinate for each disk, these ones have been considered to be the same for the three planes. Therefore, the final matrix is shown by equation 4.41.

$$C^T G^{-1} C = \begin{pmatrix} \frac{1}{\sigma_1\sigma_2} + \frac{1}{\sigma_1\sigma_3} & -\frac{1}{\sigma_1\sigma_2} & -\frac{1}{\sigma_1\sigma_3} \\ -\frac{1}{\sigma_1\sigma_2} & \frac{1}{\sigma_1\sigma_2} + \frac{1}{\sigma_2\sigma_3} & -\frac{1}{\sigma_2\sigma_3} \\ -\frac{1}{\sigma_1\sigma_3} & -\frac{1}{\sigma_2\sigma_3} & \frac{1}{\sigma_1\sigma_3} + \frac{1}{\sigma_2\sigma_3} \end{pmatrix} \xrightarrow{(\sigma_1=\sigma_2=\sigma_3)} \begin{pmatrix} \frac{2}{\sigma^2} & -\frac{1}{\sigma^2} & -\frac{1}{\sigma^2} \\ -\frac{1}{\sigma^2} & \frac{2}{\sigma^2} & -\frac{1}{\sigma^2} \\ -\frac{1}{\sigma^2} & -\frac{1}{\sigma^2} & \frac{2}{\sigma^2} \end{pmatrix} \tag{4.41}$$

Of course, this simplified exercise was generalized to be applied for the 9 SCT discs. The matrix (M_a) associated to this constraint can be seen in Figure 4.13 (left). The coloured points marks the filled terms that correspond to the T_Z coordinate of each SCT disc.

The end-cap constraint was tested using different MC samples (multimuons and cosmic rays) as well as real data (cosmic rays). The strategy applied with MC samples was the following: the CSC misalignments were corrected for the big structures and only L2 and L3 misalignments, which are null for the T_Z of the

[4]The planes represent the SCT discs and the free coordinate coincides with the direction of the beam axis (T_Z).

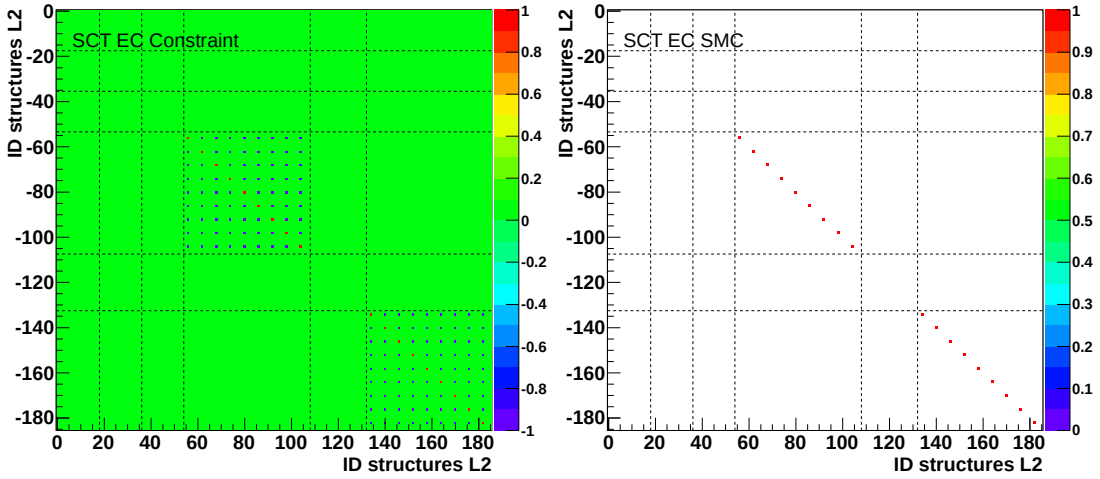

Figure 4.13: The impact of the alignment parameter constraint to the alignment correction enter into the formalism as an extra contribution to the usual big matrix. Left: Survey matrix for the SCT end-cap with a correlated T_Z disc position constraint. Right: SMC matrix for the T_Z DoF of the SCT end-cap discs.

end-caps, remained in the geometry. The Globalχ^2 method ran one iteration at L2 and instead of the likely zero contribution the algorithm provided larger alignment corrections (up to 1 mm). In order to fix these unrealistic movements the end-cap T_Z constraint was applied. The σ_{T_Z} used was of 10 μm. Using this constraint the size of the corrections for the SCT end-cap discs position was reduced. This keeps well under control the relative disc-to-disc alignment, although introduced a small global shift of the full alignment. This shift is understood as an intermediate solution between the alignment corrections of the inner discs and the expansion trend of the outermost ones.

The analysis was also repeated with cosmic ray data. On top of the aligned detector geometry (based on cosmic ray tracks), a L2 alignment of the SCT discs was made. Figure 4.14 shows the corrections obtained for the Globalχ^2 in unconstrained run mode (red points). This result verifies the expansion of the SCT end-cap discs. The end-cap constraint of $\sigma_{T_Z} = 10$ μm was also applied (green points). In the same way as the MC tests, the divergence of the T_Z of the discs was avoided but a small global shift was introduced.

Finally, a SMC technique was also tested to freeze the T_Z position of the SCT discs. Different SMC sizes were used, from few nm until hundred of μm. The size of the σ_{SMC} was chosen in order to obtain the zero corrections as expected from the simulation. For the Cosmic data a SMC of the order of nm was chosen. The results can be seen in Figure 4.14 (blue squares). Although the SMC can not correct the position of the discs, it fixes them to avoid the unreal expansions.

The technique chosen for fixing the position of the SCT discs was the SMC since it avoided the global shifts. Commonly a SMC of $O(nm)$ was applied for the T_Z discs position fixing them completely. In addition also the R_X and the R_Y of the SCT discs were found to be weakly constrained. In the same way, a SMC of $O(\mu rad)$ was introduced. Alternatively, due to the low sensitivity, these DoF can be completely removed from the alignment.

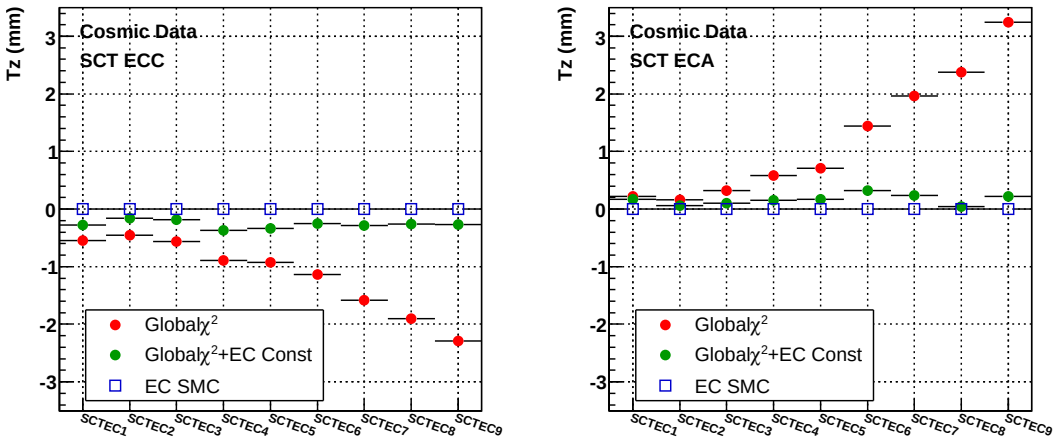

Figure 4.14: T_Z end-cap corrections obtained at L2 with cosmic data for the ECA (right) and ECC (left). Three scenarios are shown: normal alignment algorithm mode where the discs in the SCT end-caps are free (red points), alignment algorithm with a end-cap constraint of 10 μm (green points) and silicon alignment corrections obtained using a SMC of 1 nm for all SCT discs (blue open squares).

4.7.4 Full Dress Rehearsal (FDR)

The FDR was an exercise proposed to test the full ATLAS data taking chain, starting from the EF events stored via sub-farm-output (SFO) at Tier-0 until the physics analysis at Tier-2. Concerning the ID alignment task, the main objective of the FDR exercises was the automation of the full alignment sequence and its integration as a part of the ATLAS chain. The ID alignment has to be updated every 24 hours. This is one of the tighter requirements since within that period not only the alignment constants need to be computed, but also fully validated together with performing a new reconstruction of the beam-spot position.

These exercises used a cosmic ray MC sample and a simulated IDCALIB stream composed by pions (Section 4.6). The collision and cosmic tracks were combined in a single alignment solution. Figure 4.15 shows the different steps of the ID alignment chain developed during the FDR exercises. This chain began with the determination of the BS position which was used to constrict the transverse impact parameter. Straightaway, the silicon alignment constants were obtained. In parallel, the TRT internal alignment was performed using the TRT-only tracks. The center-of-gravity (CoG) (Section 4.3.4) of the system was calculated and subtracted from the alignment constants. This algorithm was used twice, after the silicon alignment and after the full ID alignment (once the TRT was aligned with respect to the silicon detector). Finally, the BS was reconstructed again, but now using the express stream that contains more physics events and it allowed the determination of the BS with its corresponding uncertainties. The express stream was also used for the alignment monitoring tool which displays information about the detector performance and physics observables (invariant mass of resonances, charge momentum asymmetry,...) in order to validate the new sets of constants. The decision of uploading the new alignment constants is taken based on the monitoring results. The tags into the database are then used to reconstruct the physics streams.

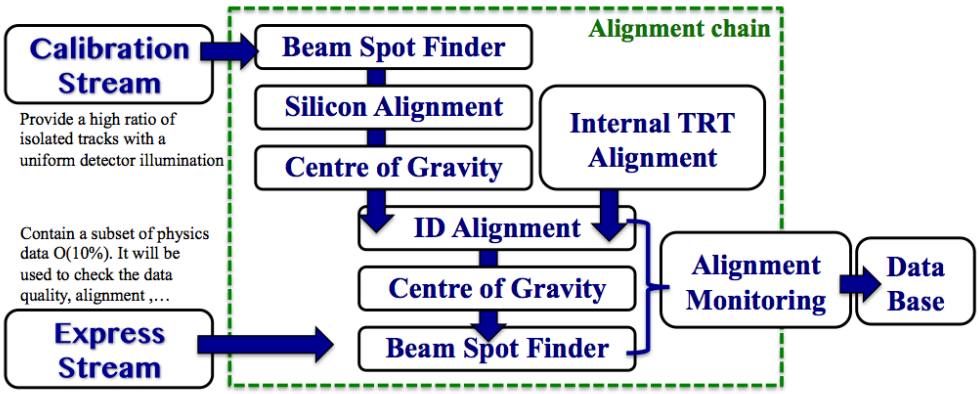

Figure 4.15: Integration of the ID alignment algorithm as part of the ATLAS data acquisition chain. This scheme shows the different steps followed to align the ID during the FDR exercises.

4.8 Results of the *Global*χ^2 alignment algorithm with real data

The ATLAS detector has been recording data since 2008. During the commissioning phases millions of cosmic ray tracks were used to prepare the initial detector geometry for the first LHC collisions. At the end of 2009, the long awaited LHC $p-p$ interactions arrived. Subsequently, the center of mass energy was increased from 900 GeV until 7 TeV. Since then, the LHC has been cumulating more and more data ($\mathcal{L}$=26.5 fb^{-1} combining 7 TeV and 8 TeV runs) which has been used to continuously improve and update the alignment of the Inner Detector.

4.8.1 Cosmic ray data

Cosmic rays were used to test the good operation of the detector as well as the performance of the track reconstruction and alignment algorithms. Figure 4.16 shows two events with a cosmic track crossing the entire ID. The picture on the left represents the straight trajectory of a muon particle through the ID detector without any magnetic field. By contrast, the picture on the right shows how the muon track is bent due to the solenoid magnetic field. The cosmic tracks connect the upper and bottom part of the detector. These correlations are an exclusive feature of the cosmic track topology. On the other hand, the disadvantages of this cosmic topology is the non uniform illumination of the detector. The upper and lower parts, around ϕ= 90° and ϕ=270° respectively, are more populated than the regions in the sides located around ϕ= 0° and ϕ=180°. Moreover, the track statistics in the end-cap is not large enough for the end-cap alignment (characteristic cosmic distributions are shown in Appendix E).

Cosmic ray data 2008

The ID alignment algorithms ran over the sample of cosmic ray tracks collected in the 2008 campaign to produce the first set of alignment constants of the real detector [97, 98]. The alignment was performed for the silicon detector (Pixel + SCT) and TRT separately. The tracks used in the alignment required

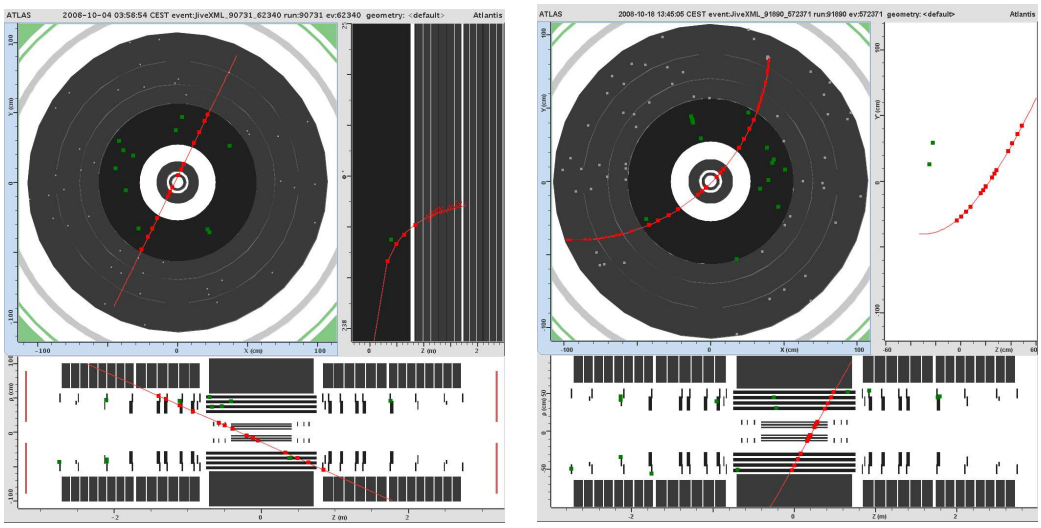

Figure 4.16: Different detector views of a cosmic track crossing the entire ID: Pixel, SCT and TRT detectors. Left: cosmic track without magnetic field. Right: cosmic track with a magnetic field.

hits in the three subsystems: the Pixel, the SCT and the TRT detectors. Moreover a cut in the transverse momentum was also applied: $p_{\mathrm{T}} \geqslant 2$ GeV. Although these requirements reduced the number of tracks considerably (~420 k of tracks kept), the set was large enough to obtain a reasonable good set of alignment constants.

In the first step, alignment corrections up to 1 mm were observed between the Pixel and the SCT detectors in addition to a rotation around the beam axis close to 2 mrad. The rest of the rotations were consistent with zero. In a second step, corrections of the order of hundreds of μm for the barrel layers and up to 1 mm for some SCT end-cap discs were obtained. Afterwards, the alignment of the barrel part was done stave-by-stave. In order to constrain the relative movements between neighbouring staves, at least two overlapping hits were required. Alignment corrections of tens of μm were found for these structures. Finally the alignment at module level was done. In this exercise, only the two degrees of freedom most sensitive to misalignments were aligned: T_x, the translation along the most precise detection, and R_z, the rotation in the module plane. These corrections showed an internal bowed structure in some pixel staves. Figure 4.17 shows the residual distribution of the recorded hits in two different staves as a function of their position along the stave. It is seen that there is no significant dependence on z in the first stave (top) but there is a significant bow with a saggita of ~500 μm in the second one (bottom). These corrections were rather unexpected due to the accuracy of the survey of the pixel staves. However the survey measurements were performed before the assembly of the staves on the half-shells, so this bowing could have been introduced during this process. The SCT staves did not exhibit any particular shape[5], the individual corrections for the modules was around T_X ~30 μm.

Simultaneously to the alignment of the Pixel and SCT detectors, the TRT tracks were used to perform the TRT internal alignment. The size of the corrections were of the order of 200-300 μm with respect to its nominal position. Finally, the TRT detector was aligned with respect to the silicon detectors and the corrections at this level were found to be up to 2 mm.

[5] This is somewhat expected as the SCT modules were not assembled in staves as the pixel modules did, but mounted directly and individually on the barrels.

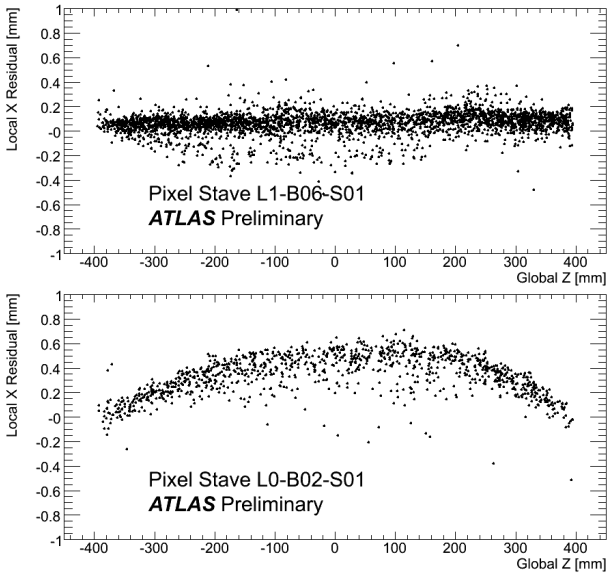

Figure 4.17: Local x residual mean versus the global Z position of the hit for two pixel staves. Top: no residual dependence observed in Z. Bottom: bowed shape seen in the stave.

Study of the alignment performance

The validation of the detector alignment was done using track segments: the cosmic tracks are divided in upper and lower parts taking into account the hits in the top and bottom regions of the ID respectively. These segments are refitted independently and the resultant tracks are called split tracks. The requirements applied to get a good quality of the split tracks are the followings:

- **Hit requirement:** $N_{PIX} \geqslant 2$, $N_{SCT} \geqslant 6$ and $N_{TRT} \geqslant 25$
- **Transverse momentum cut:** $p_{\mathrm{T}} > 1$ GeV
- **Transvere impact parameter cut:** $\mid d_0 \mid < 40$ mm in order to test the impact parameter resolution of the pixel detector.

The expected resolution of the track parameters at the perigee (d_0, z_0, ϕ_0, θ, q/p) for the collisions can be predicted using reconstructed split tracks from cosmic rays. Since both segments come from the same particle, the difference of the track parameters ($\Delta\pi$) must have a variance $\sigma^2(\Delta\pi)$ twice the variance of the track parameters of the entire track. Therefore, the expected resolution for the track parameters is given by $\sigma(\pi) = \sigma(\Delta\pi)/\sqrt{2}$. The measured resolution was compared to the perfect MC expectation. The differences in the performance were attributed to the remaining misalignment. Figure 4.18 (left) shows the transverse impact parameter resolution as a function of the transverse momentum. Three different track collections have been compared: silicon only tracks (tracks using Pixel and SCT detector hits), full ID tracks (tracks refitted using all ID hits) and simulated full ID tracks with a perfect alignment. The d_0 resolution at low p_T is dominated by the MCS. For higher momenta the values rapidly get into an asymptotic limit which is given by the intrinsic detector resolution plus the residual misalignments. Figure 4.18 (right) shows the momentum resolution versus the transverse momentum for the same track

collections. The contribution of the TRT to the momentum resolution can be seen clearly. A precise momentum determination of high momenta particles is a key ingredient for the physics analysis.

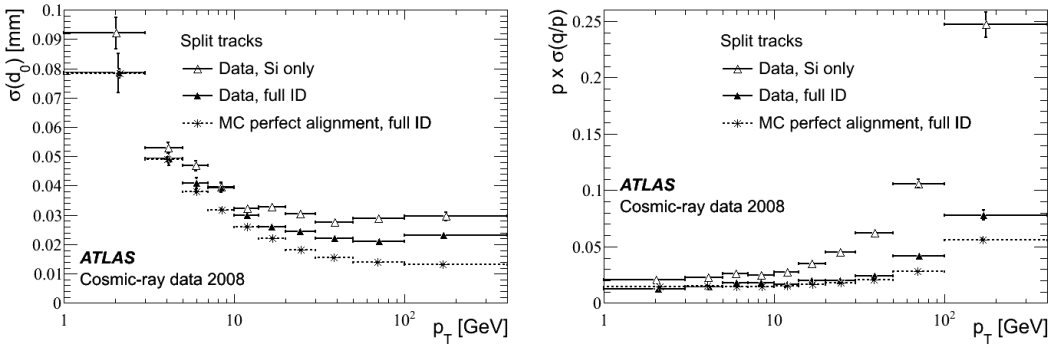

Figure 4.18: Left: transverse impact parameter resolution as a function of the transverse momentum. Right: Momentum resolution as a function of the transverse momentum. The resolution is shown for tracks refitted using all ID hits (solid triangles), silicon only tracks which have been refitted using Pixel and SCT detector hits (open triangles) and simulated full ID tracks with a perfectly aligned detector (stars).

Cosmic ray data 2009

A new ID alignment was performed using the full statistics collected during the 2009 cosmic runs in order to cross-check and improve the detector geometry found in the previous cosmic exercise (Cosmic 2008). Here, the L3 alignment included more DoFs which permitted to obtain a more accurate detector position. Afterwards this geometry was used as starting point for the 900 GeV collision alignment.

A track selection criteria was applied in order to select tracks with certain quality. The requirements varied depending on the dataset and also on the alignment level. The standard selection used was the following:

- **Hit quality requirement:** the InDetAlignHitQuality [99] tool was developed in order to reject potentially problematic hits from the alignment procedure. Among others, the outlier hits, edge channels, gange pixels, large incident angle,... could be identified and removed from the track.

- **Hit requirement:** $N_{SCT} \geqslant 12$. A requirement in the number of pixel hits was not imposed in order to not reduce much the statistics.

- **Transverse momentum cut:** $p_{\mathrm{T}} \geqslant 2$ GeV. The material effects associated to each track were computed according to its momentum. Of course, this cut was not applied for the sample without magnetic field since the momentum can not be measured.

- **Overlap hits:** most of the alignment levels keep the barrel as an entire structure interdicting radial deformations. By contrast, the stave alignment allows possible detector deformations (clamshell, radial or elliptical). Therefore, beyond stave level, at least two overlap hits were required to constrain the radial expansions.

After applying all these requirements the remaining statistics was ~440.000 and ~52.000 tracks without and with magnetic field respectively. Both data sets were used together[6].

The alignment strategy was designed to cover most of the detector misalignments taking into account the available statistics. First, the iterations at L1 were performed in order to correct the big movements of the detector. Figure 4.19 shows the difference between the L1 position of the Pixel and the SCT barrel for all alignment parameters. These results were obtained with different alignment algorithms: Robust (green triangles), Localχ^2 (blue trinagles) and Globalχ^2 (orange squares). In addition, the Globalχ^2 constants obtained for different periods, Cosmic 2008 (grey squares) and Cosmic 2009 (yellow squares), are also plotted. The results indicate a good agreement between all algorithms and also between different datasets. Nonetheless, the rotation around the beam axis exhibits a big discrepancy between the results obtained with and without Pixel survey.

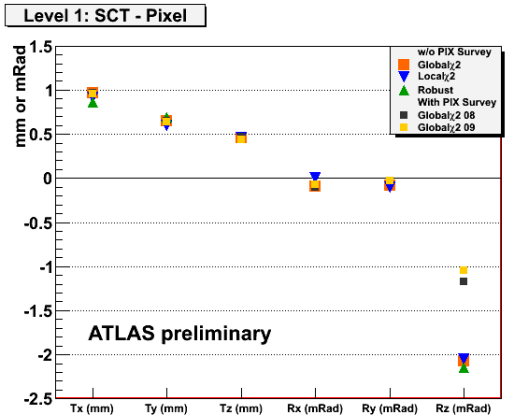

Figure 4.19: Difference between the Pixel and SCT barrel position for each alignment parameter. The results for the Globalχ^2, Localχ^2 and Robust methods are shown. Also the Globalχ^2 results obtained with different cosmic data sets are displayed. Notice that the difference in the R_Z corrections are due to the use of the Pixel detector survey.

After correcting the L1 displacements the alignment of the Pixel half-shells was done. At this level, an ES was used to get a high track hit efficiency (a=0; c=200 μm). The corrections obtained for the Pixel half-shells and for the SCT layers translations were of the order of ~100 μm and rotations, in general, compatibles with zero. On the other hand, the disc alignment was done using only the three more sensitive DoFs while the others were fixed using a strong SMC.

Afterwards, stave alignment was performed (ES of c = 50 μm). At this stage, the requirement of two overlapping hits was imposed in order to maintain under control detector geometry deformations. The corrections obtained were of the order of ~50 μm.

Straightaway, several iterations at L3 were done. Comparing with the Cosmic 2008 alignment strategy, more DoFs were aligned here since T_Y and T_Z were also determined. One important point was the verification of the bowing shape in the $T_X - R_Z$ coordinates. As expected, this pixel stave deformation

[6]Although some detector geometry deformations can be introduced due to the different magnetic field configurations, these deformations are expected to be small compared with the misalignments introduced during the assembly process. Therefore, both samples were combined at this stage of the ID alignment.

was observed again. In addition, a new pixel stave bowing shape was seen in the T_Z coordinate. Figure 4.20 shows a schematic picture of the bow deformations in $R_X - T_Z$ (left) and in T_Z (right). Figure 4.21 presents the local corrections obtained for four different ladders. The two plots in the upper row display the T_X and R_Z local corrections. A clear bowing shape of the order of 250 μm is seen in both Pixel structures. The bottom row shows the T_Z local correction for other two ladders. In this case the observed sagitta is of the order of ~200 μm. On the other hand, the corrections for the individual SCT modules were about ~10 μm.

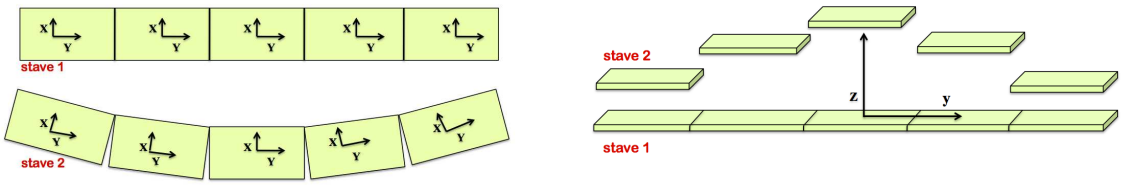

Figure 4.20: Left: Scheme of negative bow in the stave xy local frame. To go from stave 1 to stave 2 geometry a translation in the x direction (T_x) and a rotation in the module plane (R_z) have to be applied. Right: Picture of the positive bow shape in the yz local frame. From stave 1 to stave 2 geometry only a translation in the z direction has to be done.

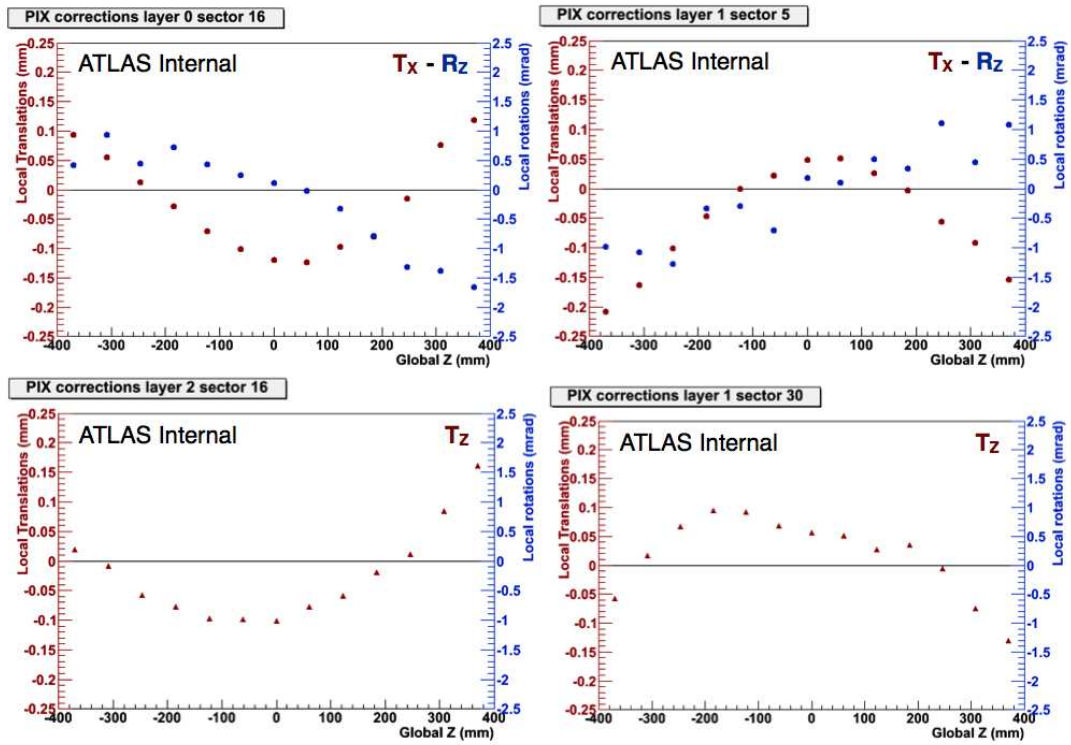

Figure 4.21: Upper row: bowing detector deformation in $T_X - R_Z$ for two different Pixel staves. Bottom row: bowing detector deformation in the T_Z coordinate for other two Pixel staves.

To check the good convergence of the algorithm, several iterations at lower levels were also performed. Therefore, after L3 one iteration at L2.5, followed by other at L2 and finally one at L1 were included. Basically they were done in order to verify that the corrections at highly granular levels didn't introduce movements for the whole structures and the global movements were efficiently removed by the eigenmode analysis. The corrections for these iterations were found to be small. This alignment strategy produced a more accurate ID alignment constants since additional detector deformations, as the T_Z bowing, was corrected.

Figure 4.22 shows the residual maps for the first layer of the Pixel (left) and SCT (right) detectors. These plots show the mean of the residual distribution for each individual module. The Pixel residual map displays huge misalignments since most of the modules have a mean residual of ~100 μm. Moreover the white squares represent mean residual out of scale which means that these structures are heavily affected by large displacements. The SCT residual map also presents large misalignments. Figure 4.23 shows the residual maps for the same layers after the Globalχ^2 alignment. Notice that the scale has been reduced from 100 μm (before alignment) down to 50 μm (after alignment). These residual maps show a uniform distribution around few tens of μm.

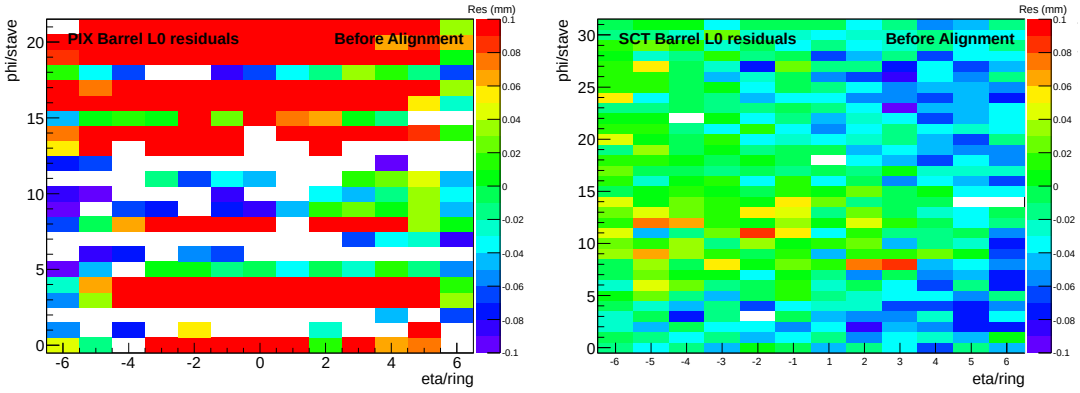

Figure 4.22: Residual maps for the Pixel L0 (left) and SCT L0 (right) before Cosmic ray alignment.

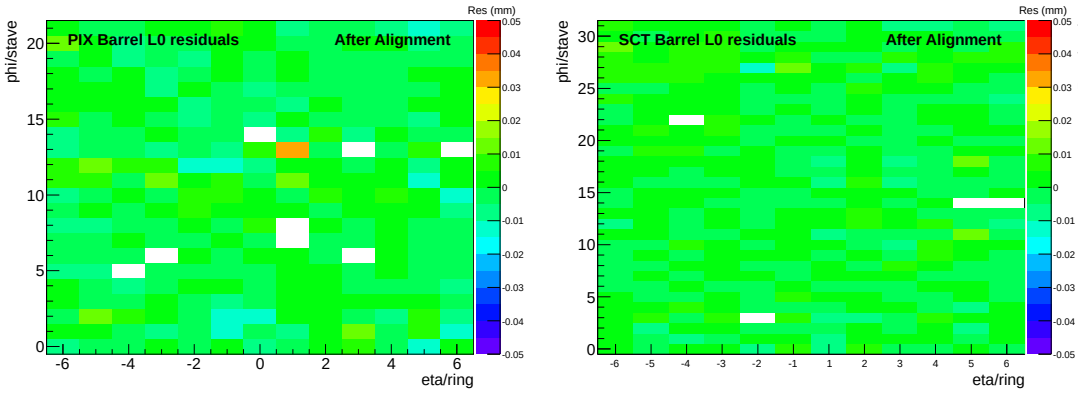

Figure 4.23: Residual maps for the Pixel L0 (left) and SCT L0 (right) after Cosmic ray alignment.

Study of the alignment performance

The resolution of the track parameters can be validated by comparing the parameters of the split tracks (upper and lower segments) at the point of closest approach to the beamline. Both segments were required to have a transverse momentum larger than 2 GeV, more than 1 Pixel hit and at least 6 SCT hits. A transverse impact parameter cut, $|\ d_0\ |< 40$ mm, was also applied. Figure 4.24 and 4.25 show the difference between the track parameters for the upper and lower segments ($\delta\pi$). The resolutions for the impact parameters with magnetic field can be calculated using $\sigma(\pi) = \sigma(\Delta\pi)/\sqrt{2}$ being $\sigma(d_0) \sim 30\ \mu$m and $\sigma(z_0) \sim 117\ \mu$m .

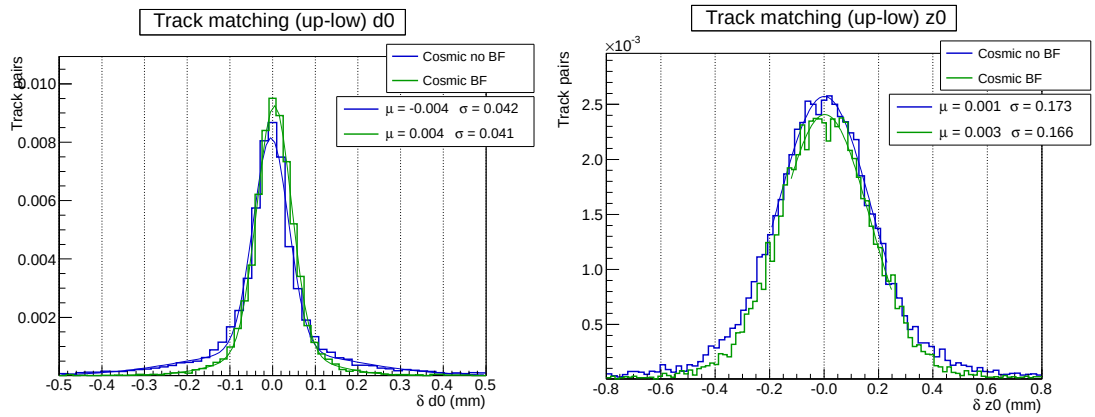

Figure 4.24: Track matching parameter distributions for cosmic ray track segments with and without magnetic field. Left: d_0. Right: z_0.

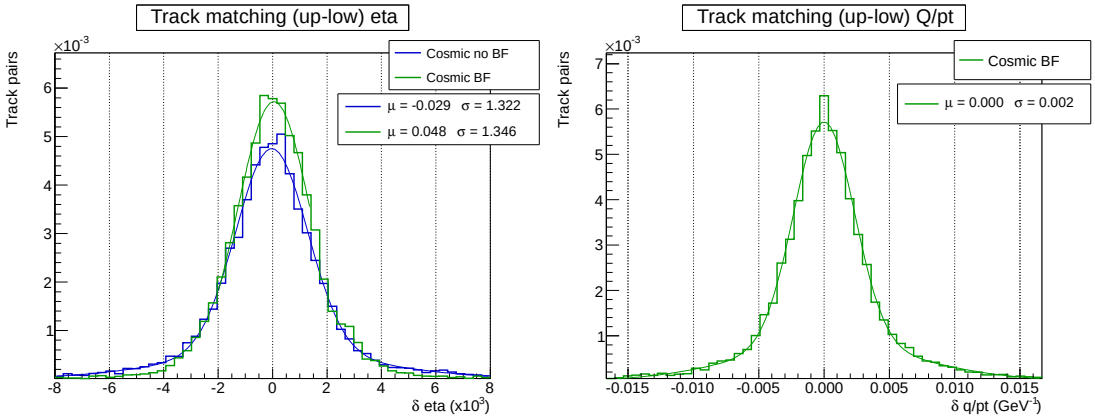

Figure 4.25: Track matching parameter distributions for cosmic ray track segments with and without magnetic field. Right: η. Left: q/p_T.

4.8.2 Collision Data at 900 GeV

The LHC collided proton beams for first time the 29th of November of 2009. The data collected during that pilot run was used for the first ID alignment with real collisions, and later for physics publications using that alignment. Figure 4.26 shows the event displays for two candidate collision events.

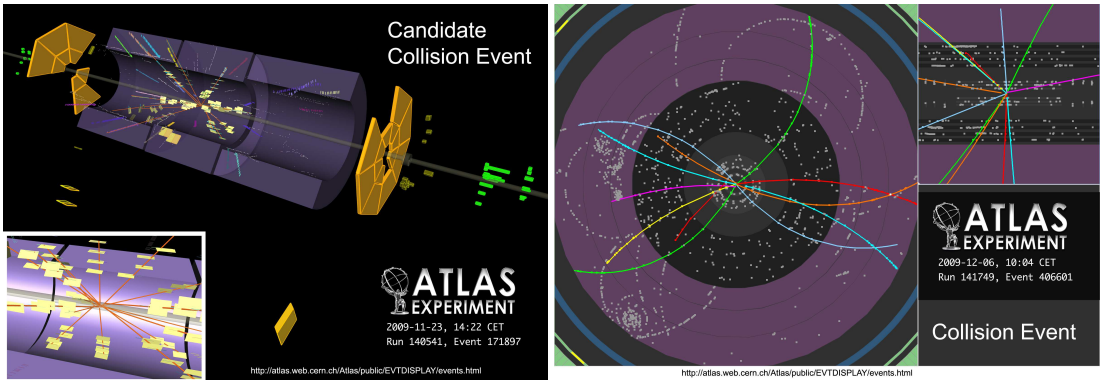

Figure 4.26: Two candidate collision events obtained during the first data taking periods. Left: detector view of the first ever LHC $p-p$ collision event with an ID zoom picture inset. Right: transverse detector view of an early collision event with the full ID.

End-cap alignment with the first collision data

The first events were reconstructed with the available detector geometry obtained from the 2009 Cosmic ray exercise (Section 4.8.1). Whilst the performance in the barrel was acceptable, the reconstruction exhibited some problems in the end-cap regions, as expected, due to the difficulties of aligning properly the end-cap discs with cosmic ray data.

The ID track-hit residual distributions were studied in order to detect the detector misalignments. Figure 4.27 shows the unbiased residual distributions for the Pixel and SCT detectors. The reconstructed residual distributions (black squares) were confronted with those obtained with the perfect detector geometry in MC (blue circles). The first row displays the barrel residuals for the Pixel (left) and SCT (right) detectors. These reconstructed distributions didn't exhibit any bias since they were found to be centred at zero with Gaussian shapes. The second row of Figure 4.27 exhibits the residuals for the Pixel ECA (left) and Pixel ECC (right). The ECA distribution shows a reasonable agreement with the perfect geometry while the ECC showed a wider distribution. Finally, the third row shows the SCT ECA (left) and SCT ECC (right). For both distributions a clear misalignment is visible since the mean of the residuals are not centred at zero ($\mu = -2\mu$m for the ECA and $\mu = -5\mu$m for the ECC). Moreover, wider distributions than for the perfect geometry also indicated the presence of end-cap modules misalignments. The width (σ) of the residual distributions combines the intrinsic resolution of the detector with the uncertainty of the track extrapolation. Therefore, one can assume that the differences between the widths of the reconstructed and the perfect residual distributions are related with the impact of the ID misalignments. Using this assumption, the estimated size of the misalignments were computed as ~70 μm for the SCT ECA and ~113 μm for the SCT ECC. These numbers evidenced the necessity of improving the SCT end-cap alignment.

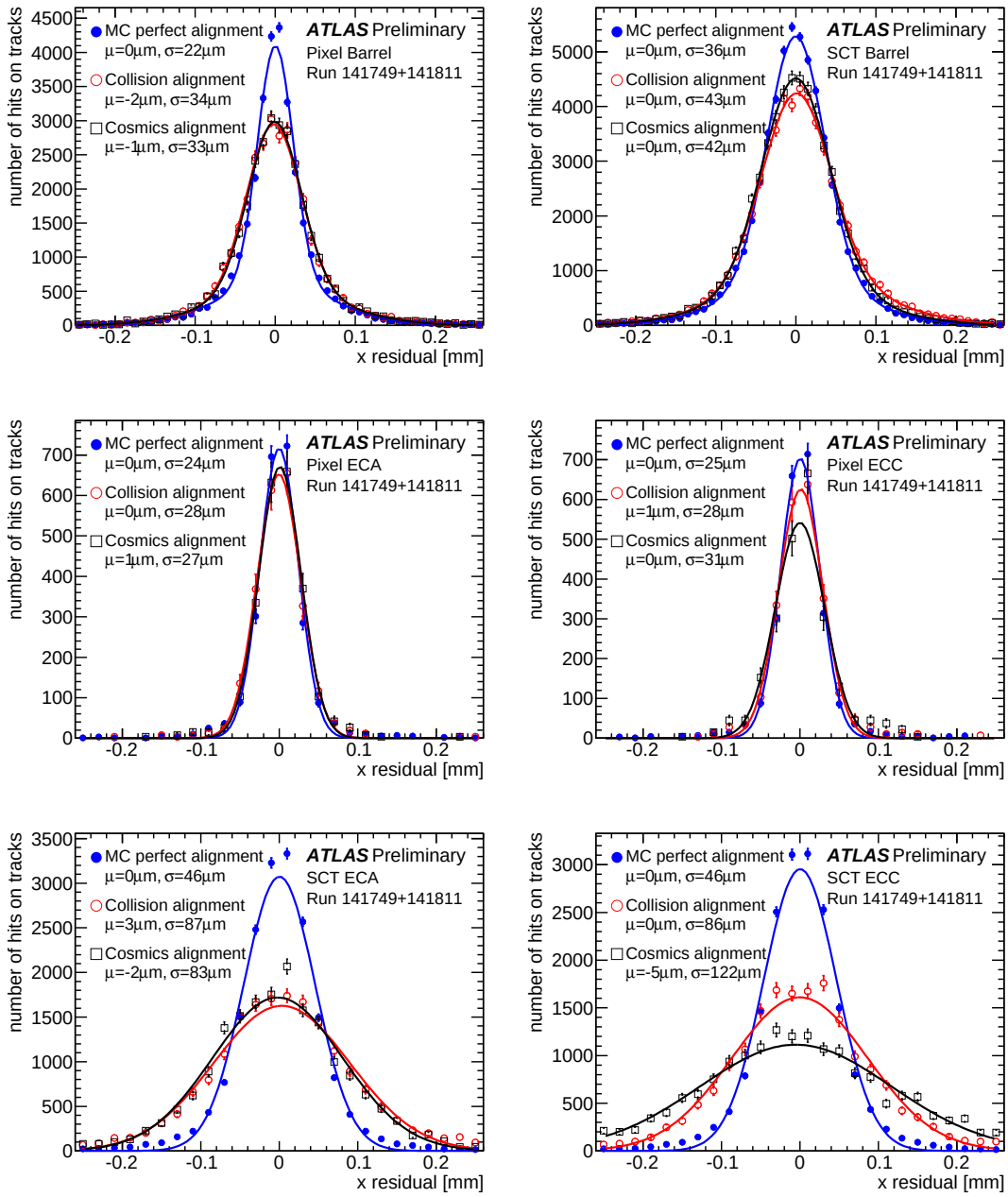

Figure 4.27: Pixel and SCT unbiased residuals with the first LHC collision data. Comparison between perfect MC geometry (blue circles), initial reconstructed geometry based on Cosmic ray (black squares) and reconstructed geometry after end-cap alignment based on Collision09_01 (red circles). First row shows the unbiased barrel residuals for Pixel and SCT detectors and the second and third row present the unbiased residual for ECA and ECC of Pixel and SCT detectors respectively.

The SCT end-cap alignment was performed with the recorded statistics of ~60.000 tracks of minimum bias events. The following track selection criteria was applied:

- **Hit requirement:** $N_{PIX} + N_{SCT} \geqslant 6$.
- **Transverse momentum cut:** $p_{\mathrm{T}} \geqslant 2$ GeV.

The detector alignment tackled only the big structures, whilst module alignment was not attempted as there was not enought statistics. The alignment chain was composed as follows:

- One iteration at L1 was done in order to validate the stability of the ID detector position within ATLAS. The largest corrections obtained at this level were for the SCT ECC with a $T_Z \sim 250\,\mu$m and a R_Z ~0.2 mrad.
- In order to perform a fast SCT disc alignment, the Pixel detector and the barrel part of the SCT, which showed an admissible alignment for the first data taking, were kept fixed. The three more sensitive DoFs of the disc structures were aligned: T_X, T_Y and R_z. Due to the big misalignments observed in some of the SCT end-cap discs an error scaling to inflate the hit error (a=1 and c=200 μm) was used during the first iterations. The biggest misalignments were found for the disc 4 of the ECC with a translation in the X direction of ~105 μm , a translation in the Y direction of ~350 μm and a rotation around the Z axis of ~1.5 mrad.

Figure 4.27 also shows the Pixel and SCT unbiased residual distributions for the collision aligned geometry which was tagged as Collision09_01 (red circles). The improvements observed in the SCT ECC residual was principally due to the L2 alignment corrections. This residual was centred at zero and its width reduced from ~113 μm to ~73 μm. At this stage, both SCT end-caps present similar distributions between them but still far from the perfect geometry. This issue indicated the necessity of a finest granularity alignment.

A closer view of the misalignments of the SCT ECC disc 4 can be seen in Figure 4.28. The left plot illustrates the mean residuals for the initial geometry. The black color indicates residuals out of the scale, thus most of the modules were misaligned by more than 25 μm. The picture on the right, shows the same distributions after the L2 end-cap alignment where the residuals have been significantly reduced. Nevertheless, the misalignments were not totally corrected since the middle ring was systematically shifted around 20 μm. This figure revealed a global distortion at ring level and motivated the necessity of aligning these structures separately. Due to time constraints, this kind of misalignments were not corrected during this exercise, but their correction was postponed to be done in the subsequent ID alignment exercise.

Summing up, the position and orientation of the SCT endcap discs were corrected and the alignment was substantially improved allowing the physics analysis to rely on the track reconstruction. Despite that the most dangerous misalignments were fixed, the study of the final residuals revealed remaining global distortions that had to be eliminated (SCT ring misalignments in Figure 4.28). In that sense, a new accurate alignment was performed. It will be shown in the next subsection.

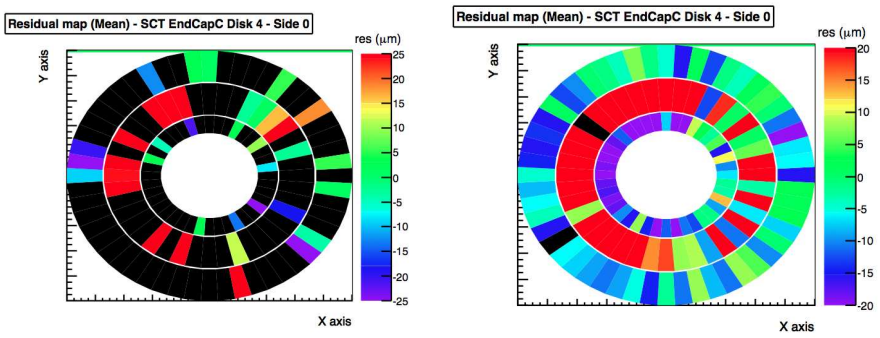

Figure 4.28: Mean residual hitmap before (left) and after (right) alignment. Each cell corresponds with a SCT module.

Accurate alignment with 900 GeV collision data

This alignment was performed using 2009 cosmic ray data (magnetic field on and off) and 900 GeV collision data (datasets explained in Section 4.6). All samples were used simultaneously in order to increase the available statistics[7]. Moreover, the use of different track topologies and the BS constraint helped in the elimination of the weak modes (Section 4.5). During this ID alignment, in addition to the residuals, some physics distributions, as track parameters, transverse momentum, etc, were also monitored. The final alignment constants tagged as InDetCollision_2009_09 were validated using the official ATLAS monitoring software.

Data used

Description of the requirements applied for the samples used:

- **Collision data.** To ensure a good collision track reconstruction the following selection was imposed:
  - **Hit requirement:** $N_{PIX} + N_{SCT} \geqslant 8$ and at least two of them recorded by the Pixel detector ($N_{PIX} \geqslant 2$).
  - **Transverse momentum cut:** $p_T \geqslant 2$ GeV. It was applied in order to reduce the impact of the MCS while preserving enough statistics.
  - **Transverse impact parameter cut:** $d_{0BS} < 4$ mm, this cut in the transverse impact parameter with respect to the beam spot (d_{0BS}) was also applied to select the tracks coming from the BS.
- **Cosmic data.** As the cosmic topology is different from the collision tracks, a distinct track requirement was used:

[7] In general, the datasets collected in different data taking periods could be not compatible if the detector has suffered some hardware changes in between. Nevertheless, as the alignment based on cosmic rays was found to be acceptable for reconstructing the collision events, it was assumed that the shifts were not that big to make the samples incompatible. Therefore both samples were combined to increase the statistics.

– **Hit requirement:** $N_{SCT} \geqslant 12$. For tracks that crossed the Pixel detector at least two Pixel hits were also required.

– **Transverse momentum cut:** $p_T \geqslant 2$ GeV.

After applying all these cuts, the remained statistics was of ~850.000 tracks (60.000 from collision events and 330.000 and 460.000 from cosmic events with and without magnetic field respectively).

Alignment strategy

The starting point for the ID alignment was the geometry obtained with 2009 cosmic data (Section 4.8.1). On top of this, a complete alignment procedure was performed. Moreover, the BS constraint was applied during the whole alignment chain.

Beam Spot Constraint. The beam spot position used in the alignment was read directly from the data base being: $\overline{X}_{BS}$ [8] =-0.19±0.02 mm and $\overline{Y}_{BS}$ = 1.02±0.03 mm. Figure 4.29 shows the X and Y coordinates for the reconstructed BS position with the initial Cosmic geometry (black line) and with the final Collision09_09 constants (red line). The position obtained using the initial Cosmic geometry didn't correspond to the location read from the database[9]. The use of this constraint forced to move the detector globally in order to preserve the BS position. This constraint improved the alignment of the innermost layers of the Pixel detector and also maintained fixed the position of the BS.

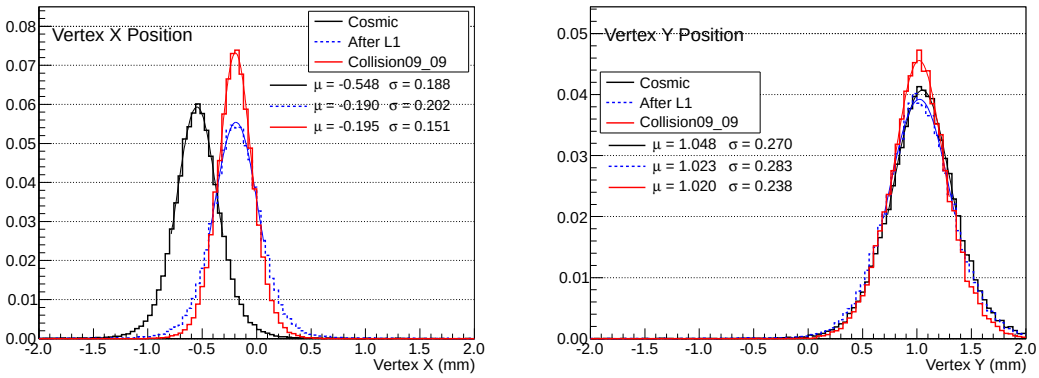

Figure 4.29: X (left) and Y (right) beam spot coordinate position before (black line) and after (red line) alignment. The L1 (blue line) alignment has been also drawn to see its corresponding impact.

Level 1. The L1 corrections for the Pixel detector in the transverse plane where found to be T_X=353.0±0.5 μm and $T_Y = -26.6 \pm 0.5$ m which mainly correspond to the difference between the initial detector geometry and the BS position. Figure 4.29 also shows the L1 alignment (blue line) that presented the major contribution for recovering the BS position. The Z coordinate was also monitored, its value was found to be compatible with its position into the DB: $Z = -8.33$ mm with a width of 41.0 mm.

[8] BS tag: *IndetBeamposr*988*Collision_Robust*_2009_05*v*0.

[9] This mismatch was introduced by using different sets of alignment constants for the on-line and off-line reconstruction.

Level 2. To allow for an efficient track-hit association, the ES technique was applied initially with a constant term c = 200 μm[10], which was subsequently reduced in the following iterations as the quality of alignment improved. Figure 4.30 shows the average number of hits as a function of η for the Pixel (left) and SCT (right) detectors. The distributions are shown for the initial (black points), after L2 (green circles) and for the final detector geometry (red points). These plots show that the barrel region hit efficiency was already high and the big improvement was introduced in the end-caps, specially in SCT ECC. The corrections applied improved the momentum reconstruction in the EC regions.

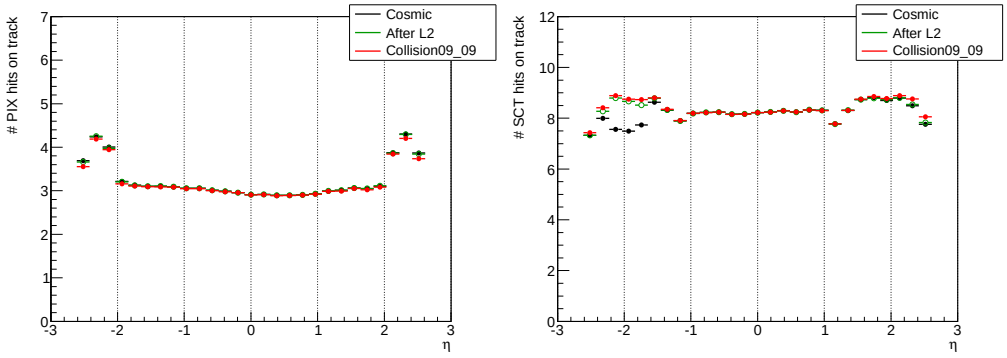

Figure 4.30: Left: Average number of Pixel hits as a function of η. Right: Average number of SCT hits versus η. Different alignment levels are displayed: initial geometry (black points), L2 (green circles) and final detector geometry (red points).

Level 2.5. As usually, for the ladders and rings alignment a requirement in the number of overlapping hits was imposed ($N_{OVER} \geqslant 2$). In order to increase the statistics, the cosmic ray sample with magnetic field was included here. The size of the ladder corrections obtained were $O(20\ \mu\text{m})$ for the Pixel and $O(80\ \mu\text{m})$ for the SCT detectors. The end-cap ring alignment was done and the obtained corrections were up to 20 μm. As an example, Figure 4.31 (left) shows the residual maps associated to the disc 3 of the SCT ECA before the ring alignment, the middle ring exhibits a uniform shift of the residual means of 25 μm. After the ring alignment (right) the global distortion was corrected and the remaining misalignment were amended at L3.

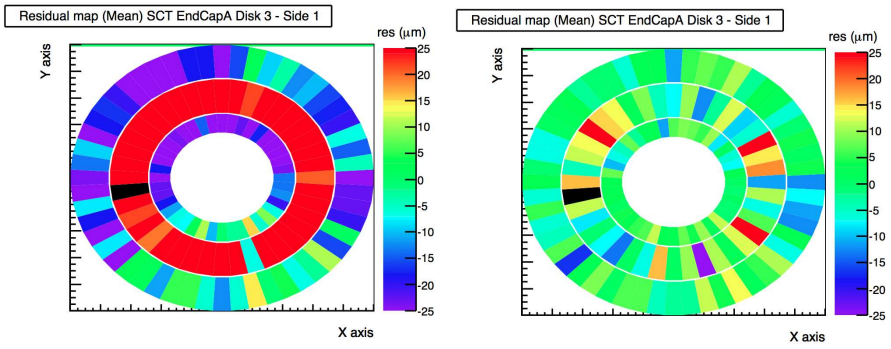

Figure 4.31: Mean residual hitmap for the disc 3 of the SCT ECA before (left) and after (right) the ring alignment. Each cell corresponds with a SCT module.

[10]The ES technique was also applied during the L1 alignment.

Level 3. Finally, some iterations at module level were performed. Therefore, the L3 alignment for the barrel region was attempted using the most sensitive 4 DoFs[11] (T_X, T_Y, T_Z and R_Z) an for the end-cap alignment only the three most precise ones (T_X, T_Y and the R_Z). Even though the number of tracks was quite large, the detector illumination was not uniform and the modules located at large η in the barrel collected ~100 hits while the most illuminated modules had around 5000 hits. Those modules with less than 150 hits were not aligned in order to avoid statistical fluctuations.

Figures 4.32 and 4.33 show the biased residual distributions for the Pixel and SCT detectors. These plots compare the initial "Cosmic" geometry (black line) and InDetCollision09_09 alignment (red line). An improvement in the residuals is shown for both sub-detectors. The widths of the final Pixel barrel rϕ distributions are O(10 μm) and O(16 μm) for the barrel and end-caps respectively. The residuals in the η direction present a width of the O(70 μm) for the barrel and O(108 μm) for the end-caps. The SCT barrel residual distribution has a width of O(13 μm). The biggest improvement can be seen in the SCT end-cap residual distribution. The width of this biased residual was reduced from ~70 μm (before alignment) down to ~17 μm (after alignment).

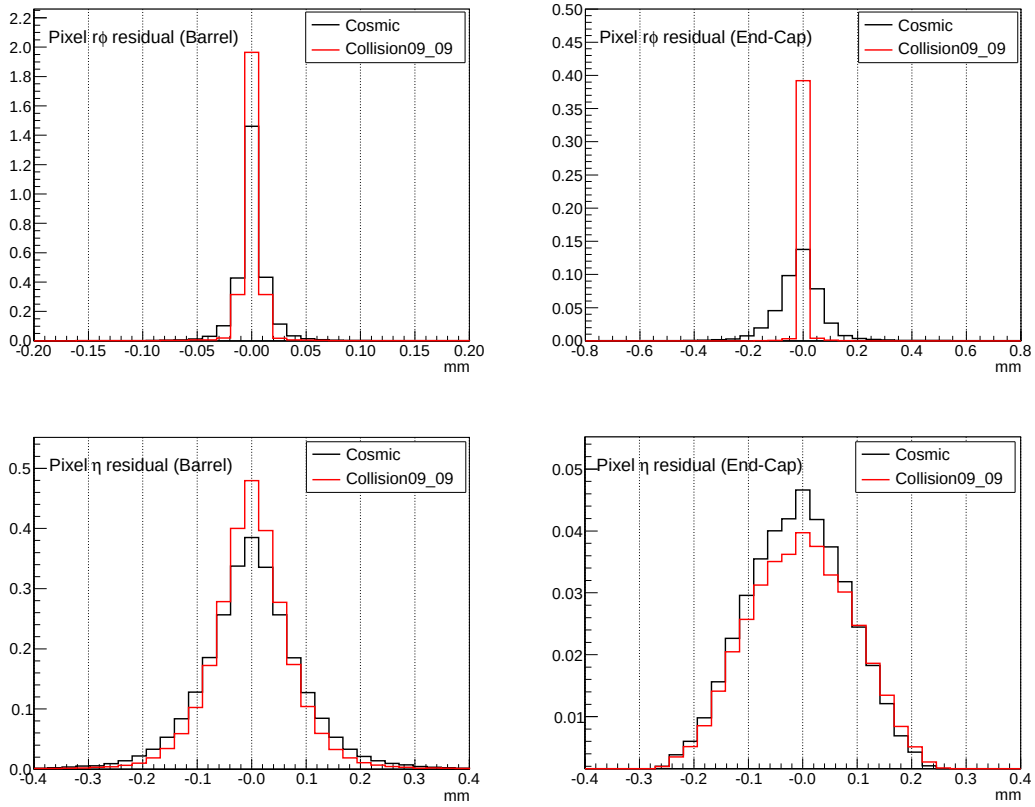

Figure 4.32: Upper row: Pixel biased rϕ residual distributions for barrel (left) and end-caps (right). Bottom row: Pixel biased η residual distributions for barrel (left) and end-caps (right). The distributions are presented for two scenarios: collision data reconstructed with the 2009 Cosmic ray alignment (Cosmic) and with the alignment corrected using collisions data (Collision09_09).

[11] The out of plane rotations (R_X and R_Y) were not used since the statistics were not enough to achieve the desire sensitivity.

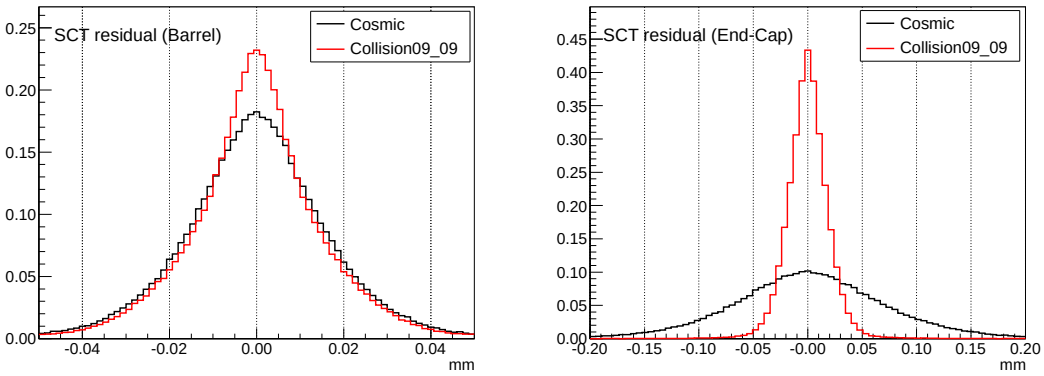

Figure 4.33: SCT biased residual distributions for barrel (left) and end-caps (right). The distributions are presented for the Cosmic ray (Cosmic) and collisions (Collision09_09) alignments.

Study of the alignment performance

After the InDetCollision09_09 alignment, the detector performance was studied in order to validate the goodness of the corrections applied. Many distributions were monitored during and after the alignment to control potential biasing detector deformations and to avoid weak modes. These distributions were studied for the barrel and end-caps separately. As the end-caps suffered the biggest corrections, their distributions were analysed in more detail.

The transverse impact parameter versus the BS position was studied since it can give relevant information about the misalignments of the detector in the transverse plane. Figure 4.34 shows this track parameter at different alignment levels. The reconstructed d_0 distribution using the "Cosmic" alignment (black line) exhibited a non Gaussian shape due to a detector shift with respect to the BS position. Therefore, after correcting this mismatch at L1 (blue line), the Gaussian shape for the d_0 was recovered. Although the BS position was mainly corrected by the L1, the alignment at L2 did a fine tuning and the distribution became a bit narrower. The difference between the initial (black line) and the final (red line) geometry shows the big improvement achieved after the alignment.

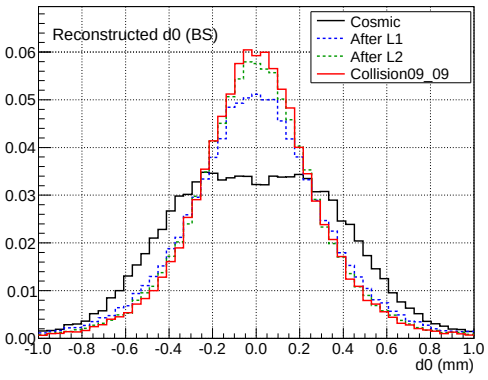

Figure 4.34: d_0 parameter before (black line) and after (red line) alignment. Different levels have been also included to see their corresponding impact: L1 (blue line) and L2 (green line).

Figure 4.35 shows d_0 as a function of η (left) and ϕ_0 (right) of the detector. The d_0 versus η distributions show a flat distribution in most of the detector regions. However, the ECC presented some variations which were largely reduced after the disc alignment (green circles). Of course the ring and module alignment also had a clear impact since the final InDetCollision09_09 distribution (red points) was flatter. On the other hand, the d_0 versus ϕ_0 displays a typical sinusoidal shape for the initial alignment due to the global shift already mentioned. Nevertheless, after L1 (blue circles), when the detector position was corrected to keep the BS, this shape disappeared and the distribution became flat.

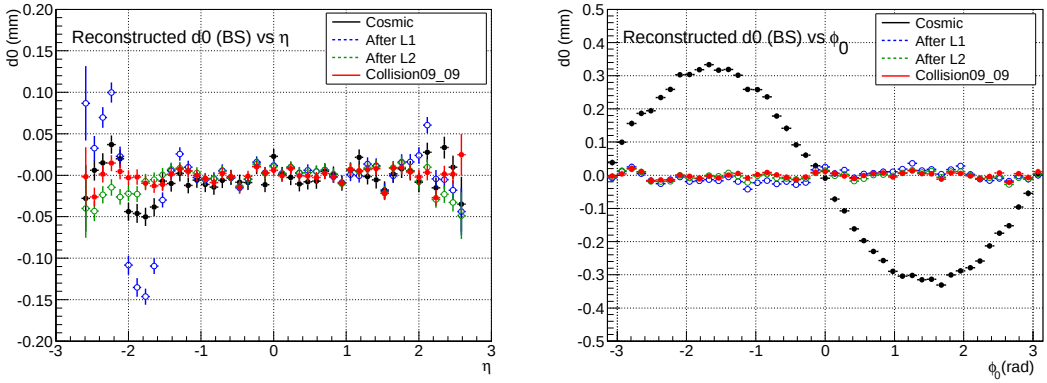

Figure 4.35: Right: d_0 versus η. Left: d_0 versus ϕ_0. Different alignment levels are displayed: initial geometry (black points), L1 (blue circles), L2 (green circles) and final detector geometry (red points).

In order to analyse in more detail the forward regions, the d_0 versus ϕ_0 distribution was drawn for ECA and ECC separately (Figure 4.36). Both display the characteristic sinusoidal shape for the initial geometry (black points). For the ECA the flat distribution was reached after L1 (blue circles). By contrast, the ECC presented a lingering sinusoidal shape which was eliminated after L2 (green circles). For both end-caps the final alignment constants (red points) show a flat distribution around zero for all sectors.

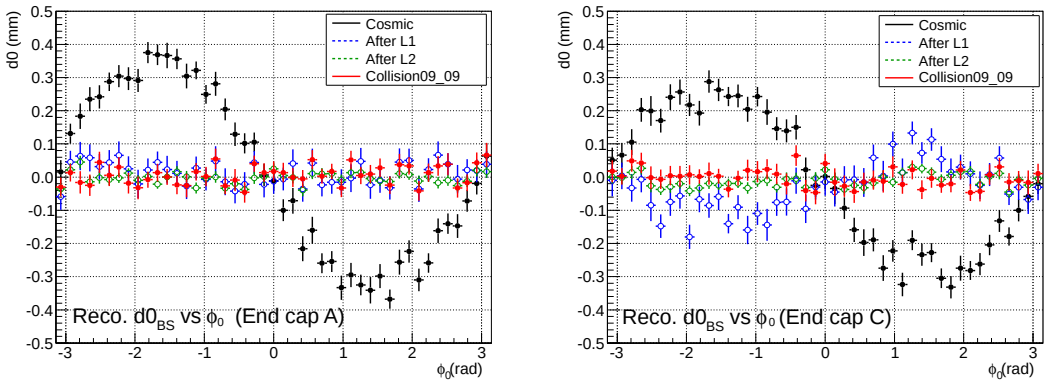

Figure 4.36: d_0 versus ϕ_0 for ECA (left) and ECC (right). Different alignment levels are displayed: initial geometry (black points), L1 (blue circles), L2 (green circles) and final detector geometry (red points).

A crucial aspect for physic analysis is to have a good momentum reconstruction. Figure 4.37 (left) shows the number of positive and negative reconstructed charged tracks by the end-caps using the initial

"Cosmic" geometry . It is known that in $p-p$ collisions there are more positive than negative charge tracks. However this asymmetry should be the same in both end-caps. What was observed initially is that the end-caps did not agree due to the large initial misalignments of the SCT ECC. Figure 4.37 (right) shows the same distribution for Collision09_09 alignment where a clear reduction of this effect can be seen and the track charge distribution is more similar for both end-caps.

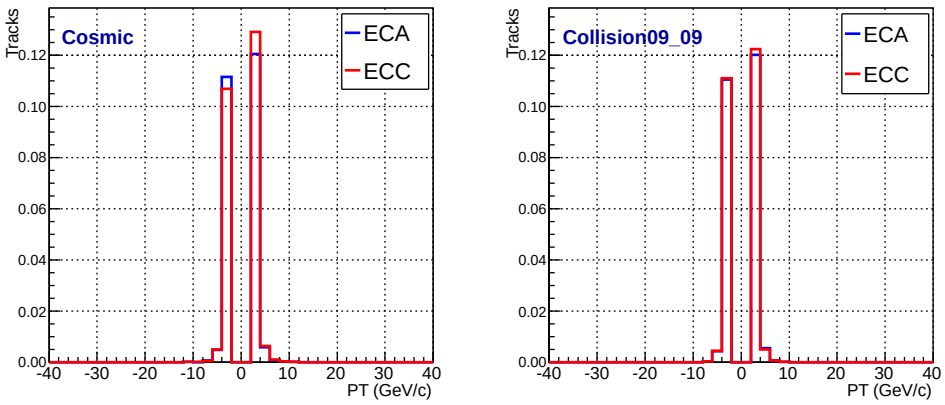

Figure 4.37: Left: Number of positive and negative charged tracks reconstructed for each ECA (blue) and ECC (red) for the initial Cosmic geometry. Right: same distribution reconstructed with the Collision09_09 aligned geometry.

Moreover, Figure 4.38 shows the average charge of the particles as a function of ϕ_0 for ECA and ECC. Distributions for the initial (black points) and the final (red points) geometry are plotted. The SCT ECC exhibits a sinusoidal shape for the "Cosmic" geometry. This asymmetry is unexpected as the number of positive (negative) charged tracks should not depend on ϕ_0. This was interpreted as a kind of curl or saggita distortion. Finally, these deformations were corrected and the final distribution obtained with the InDetCollision09_09 became flat.

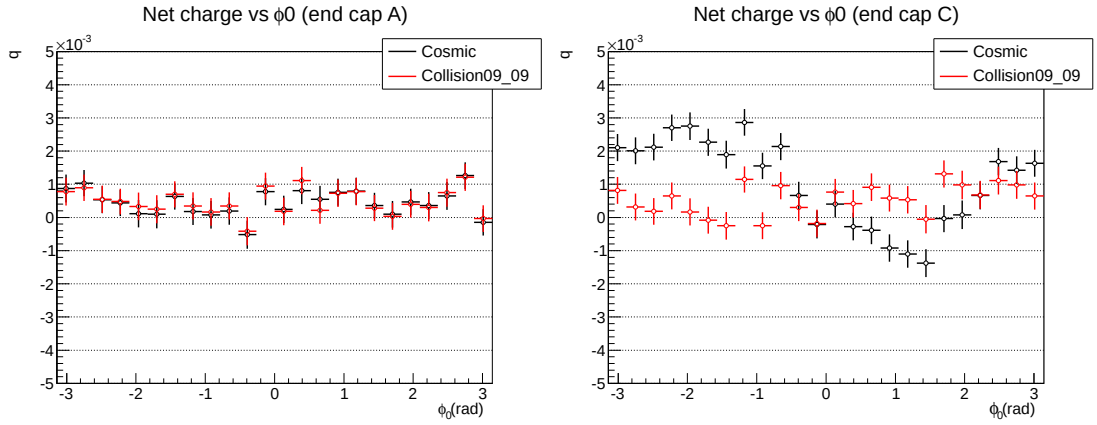

Figure 4.38: Average track charge as a function of the ECA (left) and ECC (right). The initial Cosmic detector geometry is shown by black points while the final Collision09_09 is represented by red points.

In summary, a satisfactory ID performance was achieved using the Collision09_09 geometry for the reconstruction of collision data. Finally the results were validated using the official ATLAS monitoring tool [98].

4.9 Further alignment developments

The alignment of the ATLAS ID has been continuously updated from the first LHC collisions until now. New techniques and larger datasets have been used in order to obtain a more accurate detector description correcting not only the residual misalignments but also those weak modes present in the detector geometry [100, 101]. Special attention has been paid for correcting the momentum of the charge particles since a bias in this parameter affects many physics observables: invariant mass of resonances, charge asymmetries, etc. Moreover, the good reconstruction of the impact parameter (d_0) has been also studied because it influences the vertex fitting and consequently the *b*-tagging performance.

This section presents some of the newer techniques used to align the ID during the Run I:

- **Alignment datasets:** as usual, $p-p$ collision and cosmic ray data have been mixed in order to perform the ID alignment. Newer trigger configurations have allowed the storage of the cosmic tracks simultaneously with collision data taking, just during the periods without proton bunches passing through ATLAS. In this way, the detector geometry and the operation conditions for both samples are exactly the same.

- **New alignment code:** the Pixel, SCT and TRT detectors have been integrated in the same alignment software framework in order to run all sub-detectors at the same time. This software includes both approaches: Localχ^2 and Globalχ^2. In addition, the monitoring tool has been programmed to run automatically after each iteration to check the goodness of the alignment constants.

- **Wire to wire TRT alignment:** in order to get a better detector description, the TRT was aligned using just the two most sensitive degrees of freedom per wire (the translation along ϕ (T_ϕ) and the rotation about r (R_r) and z (R_Z) for the barrel and end-caps respectively). This alignment involves 701696 DoFs. The residual maps exhibited a wheel to wheel oscillatory residual pattern which was identify as an elliptical deformations of the TRT end-cap. This deformation could be explained by the way in which the wheels were assembled. The neighbouring wheels were mounted independently in the same assembly table, and pair of wheels were assembled back to back and stacked to form the end-caps. Therefore, a deformation in the machine table would give rise to the observed misalignments. After the wire-to-wire alignment the detector deformations were corrected and a uniform residuals maps without any significant bias were registered.

- **Study of the deformations within a Pixel module:** the pixel modules were modelled with a distorted module geometry instead of a perfectly flat surface. The deformations were included according to the survey measurements of twist and/or bend of the detector wafers which correspond to out-of-plane corrections of the order of tens of micrometers [102]. These distortions were included into the reconstruction and the measured hit position was corrected accordingly. The alignment of the pixel detector enabling the pixel module distortions showed a big improvement of the pixel alignment. Figure 4.39 shows detailed residual maps of a limited area of the intermediate layer of the barrel pixel detector before (left) and after (right) module alignment. Each pixel module was split into a 4×4 grid and the average residual of the tracks passing through each cell was plotted.

The modules are identified by their position in the layer which is given by their η ring and ϕ sector indices.

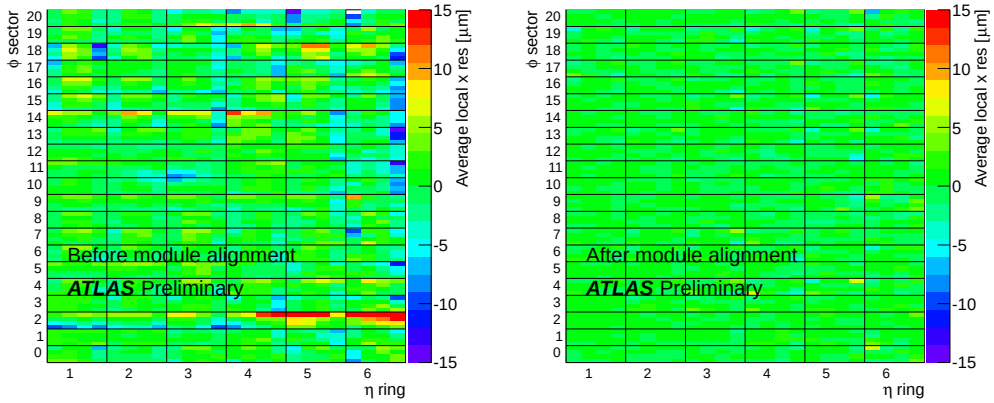

Figure 4.39: Detailed residual maps of the barrel pixel modules (only a subset of the pixel modules of the intermediate pixel barrel layer are shown). Average local x residual before (left) and after (right) module level alignment (including pixel module distortions).

- **Run by run alignment:** the run by run alignment allows the identification of the detector movements prior the data reconstruction. Nowadays the ID alignment has been fully integrated in the 24 hours calibration loop. Therefore the ID track sets are used to perform a couple of L1 iterations to check the stability of the detector. If movements are observed then the higher granularity alignment levels are performed in order to have the best possible geometry description before the data reconstruction. Figure 4.40 shows the global X translations performed on a run by run basis. The large movements of the detector were found after hardware incidents: cooling system failure, power cuts, LHC technical stop, etc. In between these hardware problems small movements (<1μm) are observed indicating that the detector is generally very stable. These run by run corrections were applied during the data reprocessing.

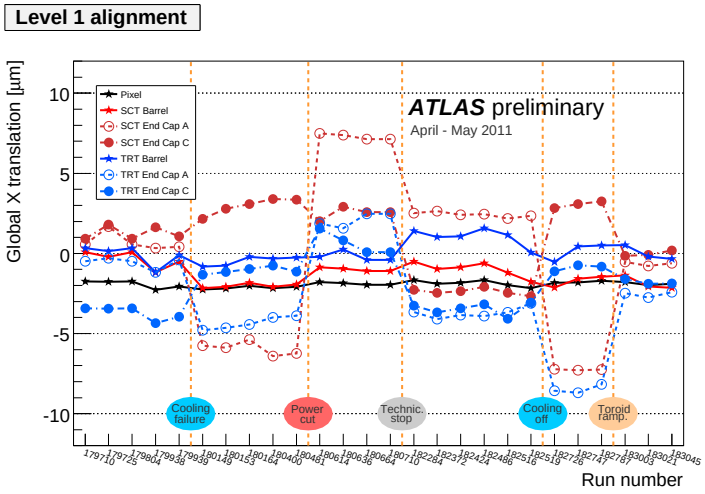

Figure 4.40: Global T_X alignment corrections performed run by run. The large movements of the detector were observed after hardware incidents.

- **Track momentum constraint:** the L2 alignment weak modes can lead to momentum bias. It can be detected using different methods:
  - **Invariant masses of known particles:** violations of the expected symmetries in the reconstructed invariant masses of known particles can be converted into a measurement of the systematic detector deformations. Therefore, scans of these invariant masses as a function of different kinematic quantities are performed for searching the misalignments. For example, particle decaying in one positively and one negatively particle, as $Z \rightarrow \mu^+\mu^-$, must present the same momentum for both particle and any deviation could indicate a momentum bias. Similarly, dependence of the mass on the η of the decay products provide direct sensitivity to the twist.
  - **E/p variable for reconstructed electrons:** as the EM calorimeter response is the same for e^+ and e^-, the E/p technique can be used to detect charge dependent biases of the momentum reconstruction in the ID.

  The momenta of the tracks can be corrected using information from the momentum bias present in the alignment ($\delta_{sagitta}$):

$$q/p_{Corrected} = q/p_{Reconstructed}(1 - qp_T\delta_{saggita}) \tag{4.42}$$

  The sagitta can be estimated using the $Z \rightarrow \mu^+\mu^-$ invariant mass or the E/p method. Both techniques give an independent probe of the alignment performance. Between each iteration the momentum bias is calculated and the new momentum is used in the alignment. The process iterates until convergence. Figure 4.41 shows the saggita map obtained with the $Z \rightarrow \mu^+\mu^-$ invariant mass method before (left) and after (right) alignment with this constraint. The bias in the momentum has been corrected.

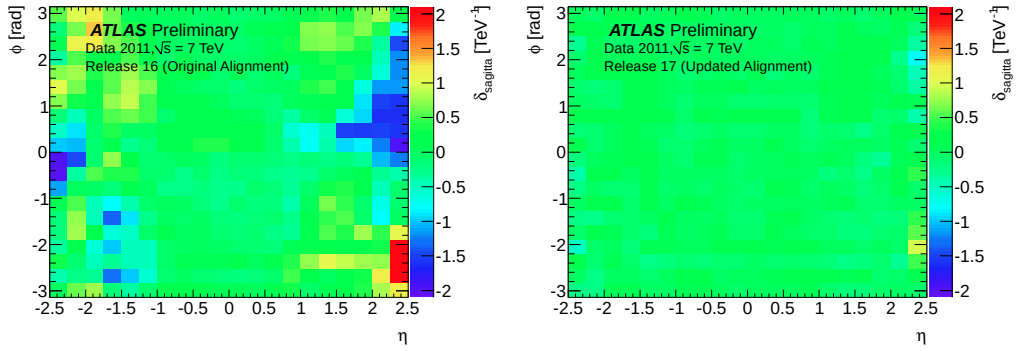

Figure 4.41: Map of $\delta_{sagitta}$ values as extracted from $Z \rightarrow \mu^+\mu^-$ events before (left) and after (right) alignment.

4.10 Impact of the ID alignment on physics

Most of ATLAS physic analyses involve objects reconstructed by the ID, therefore the goodness of the ID performance has a direct impact on the final physics results [103]. The work presented in this thesis was really important for getting the first ATLAS physic paper in which the charged-particle multiplicity and its dependence on transverse momentum and pseudorapidity were measured [104]. In order to obtain

these results, the inner-tracking detector had to be understood with a high precision, and of course, the alignment played an important role.

Figure 4.42 from [104] shows the number of Pixel (left) and SCT (right) hits versus η for data compared with the MC expectation. This figure exhibits a good agreement between data and MC demonstrating the well understanding of the ID.

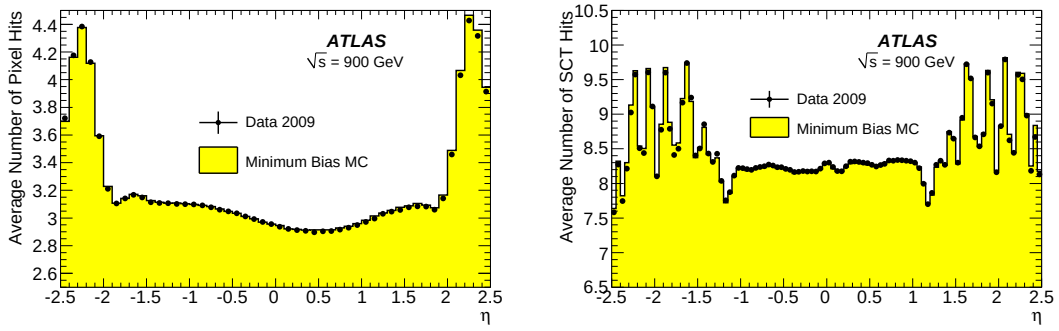

Figure 4.42: Comparison between data (dots) and minimum-bias ATLAS MC simulation (histograms) for the average number of Pixel hits (left) and SCT hits (right) per track as a function of η [104].

An crucial role of the tracking system is the identification of heavy flavour hadrons (*b*-tagging). These particles are involved in many important physics analyses from the re-discovery of the top quark to the Higgs boson and many BSM processes. The capability of the *b*-tagging algorithms rely on the very accurate measurements of the charged track parameters which are provided by the ID. MC studies demonstrated that random Pixel misalignment about 10 μm in the x direction and 30 μm in the y and z direction degraded light jet rejection by a factor 2 for the same *b*-tagging efficiency and even more when including systematic deformations [54]. Among others, the transverse impact parameter (d_0) is a key variable used for the *b*-tagging algorithms in order to discriminate tracks originating from displaced vertices from those originating from the primary vertex. Figure 4.43 from [104] shows the transverse impact parameter (left) and longitudinal impact parameter (right). These distributions also present a good agreement between data and MC. The good shape of the ID alignment at the early stages allowed a satisfactory *b*-tagging performance.

The first measurements arrived from the well known particles, properties as masses, lifetimes, etc, were the goal of the earlier physics analysis. These measurements were also a powerful data-driven tool to demonstrate the good tracking performance of the ID.

Measuring the J/ψ production cross-sections provides sensitive tests of QCD predictions. The J/ψ mass was extracted from the reconstructed di-muon invariant mass spectrum using the muon identification done by the MS and the track parameters determined from the ID [105]. Figure 4.44 shows the reconstructed J/ψ mass, the mass value obtained from the fit was 3.095±0.001 GeV, which is consistent with the the PDG value of 3.096916± 0.000011 GeV [4] within its statistical uncertainty. In addition to the importance of the measurement, this results provided an excellent testing ground for studies of the ID in the region of low transverse momentum and validated the momentum scale determination in the low momentum region.

Decays of the long-lived K^0_S and Λ^0 particles to two charged hadrons can be used to study fragmentation

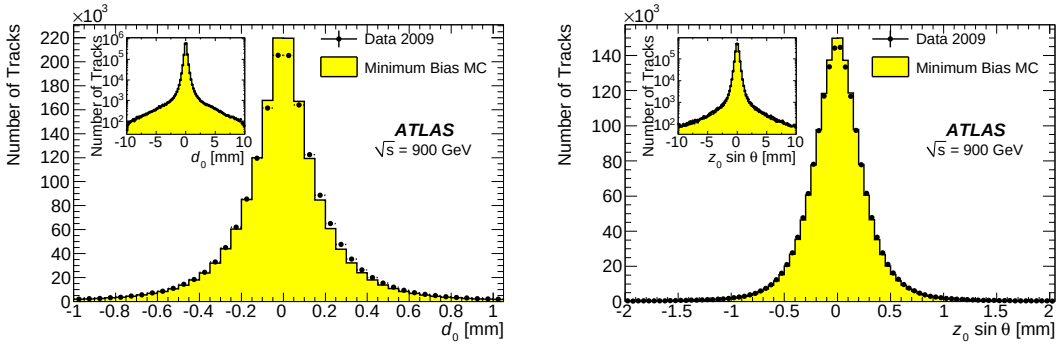

Figure 4.43: The transverse (left) and longitudinal (right) impact parameter distributions of the reconstructed tracks. The Monte Carlo distributions are normalised to the number of tracks in the data. The inserts in the lower panels show the distributions in logarithmic scale [104].

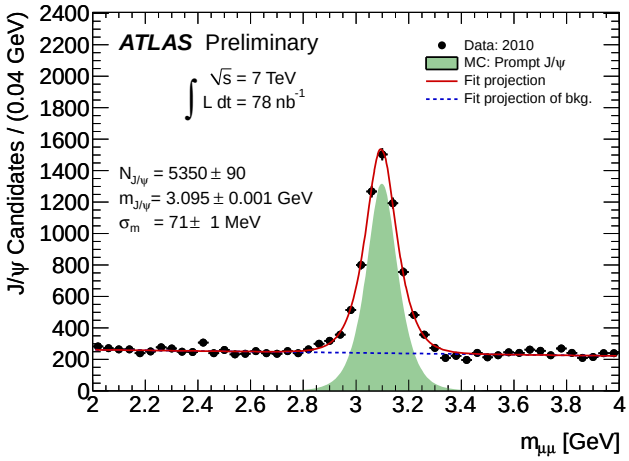

Figure 4.44: The invariant mass distribution of reconstructed $J/\psi \to \mu^+\mu^-$ candidates from data (black points) and MC normalized to number of signal events extracted from the fit to data (filled histogram). The solid line is the projection of the fit to all di-muon pairs in the mass range and the dashed line is the projection for the background component of the same fit [105].

models of strange quarks that are important for modelling underlying-event dynamics, which in turn are a background to high-p_{T} processes in hadron colliders. Roughly 69% of K^0_S mesons decay to two charged pions and 64% of Λ^0 baryons decay to a proton and a pion [106, 107]. The reconstruction of the K^0_S to $\pi^+\pi^-$ decay requires pairs of oppositely-charged particles compatible with coming from a common vertex (secondary vertex displayed more than 0.2 mm from the primary vertex). Figure 4.45 (left) shows the K^0_S invariant mass distribution. The mean and resolution of the mass peak obtained from the fit in data (black points) is consistent with simulation (filled histogram) to a few per cent in most detector regions and with the PDG mass value. Similar results were obtained for the Λ^0 distribution, Figure 4.45 (right). This good agreement demonstrated a high accuracy of the track momentum scale and excellent modelling of the ID magnetic-field.

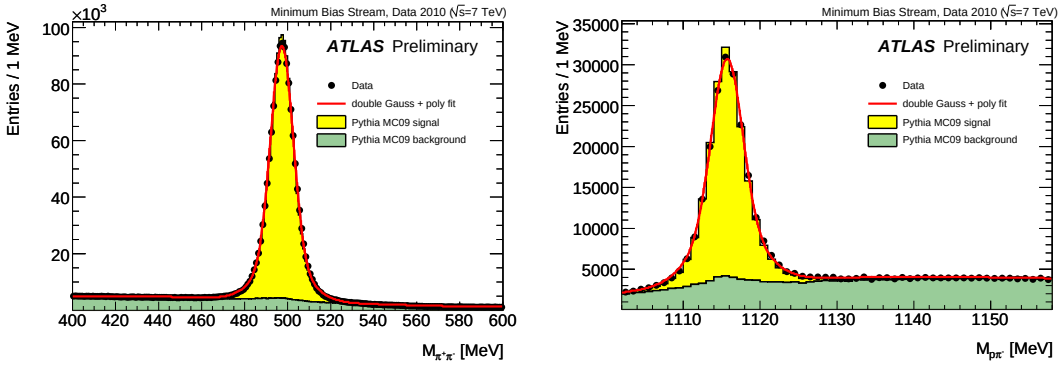

Figure 4.45: The K^0_S (left) and Λ^0 (right) candidate mass distribution using the barrel detector region (both tracks satisfy $|\eta| < 1.2$). The black circles are data, while the histogram shows MC simulation (normalised to data). The red line is the line-shape function fitted to data [107].

In addition to these measurements, many other analysis involving objects chiefly reconstructed by the ID have been published: the mass of the $Z \to \mu^+\mu^-$ and the mass measurement of the Higgs boson in the channel $H \to ZZ \to 4$ leptons (Figure 4.46). Therefore, the importance of the alignment of the Inner Detector for getting precise ATLAS physics results has been thoroughly demonstrated.

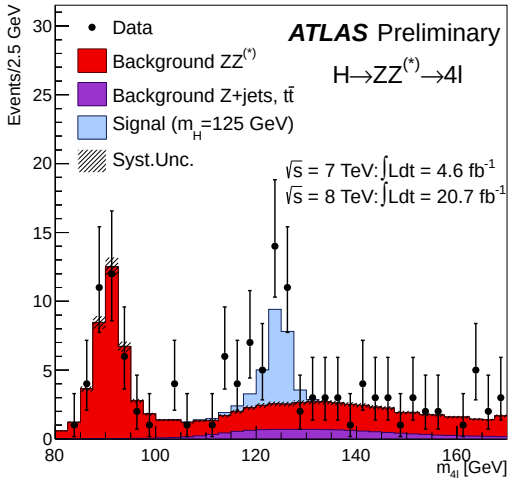

Figure 4.46: The distributions of the four-lepton invariant mass ($m_{4\ell}$) for the selected candidates compared to the background expectation for the combined $\sqrt{s} = 8$ TeV and $\sqrt{s} = 7$ TeV data sets in the mass range of 80-170 GeV. The signal expectation for the m_H=125 GeV hypothesis is also shown.

4.11 ID alignment conclusions

This chapter has presented the exercises performed for preparing, testing and running the Globalχ^2 algorithm.

The CSC distorted geometry was certainly useful to prove the response and convergence of the alignment algorithms under realistic detector conditions. The FDR exercises were used for establishing the steps in the alignment chain and prepare it for the real data taking. During these exercises, special attention were paid for correcting the weak modes and to avoid unconstrained global movements. The study of the eigenmodes and eigenvalues to find the global deformations of the detector for the most typical alignment scenarios were carried through the big matrix diagonalization. All this work has been really important for fixing the basis of the Inner Detector alignment, as it runs today.

This thesis has also presented the first alignment of the ID with real data: cosmic and collisions. Firstly, the cosmic alignment was done using the 2008 and 2009 data recorded by the ATLAS detector during the commissioning phases. The geometry detector was studied in detail, and some unexpected movements (pixel staves bowing shapes, end-cap SCT discs expansion,...) were identified and corrected. This geometry was used as starting point for the first $p-p$ LHC collisions. The $7\mu b^{-1}$ of collisions at $\sqrt{s}$=900 GeV were used to perform the first ID alignment with collision tracks. Here, not only the residuals but also the physics observable distributions were used to control the detector geometry and therefore obtain an accurate ID alignment (residual widths of $O(10\mu\text{m})$ for the barrel pixel and $O(13\mu\text{m})$ for the SCT barrel detectors).

The Inner Detector alignment achieved with the work presented in this thesis was crucial for getting a good initial ID performance and leading to the first ATLAS physic results.

Since then, the ID alignment has been enriched in external constraints tools which have allowed a better reconstruction of the track parameters. Moreover, the establishment of the ID alignment within the calibration loop has permitted to identify and correct the detector movements much faster. Therefore, these new techniques have allowed to obtain a more accurate description of the current ID geometry.

Chapter

5 Top-quark mass measurement with the Globalχ^2

The top-quark is the heaviest fundamental constituent of the SM. Due to its large mass, the top quark may probe the electroweak symmetry breaking mechanism and also may be a handle to discover new physics phenomena BSM.

The first experimental observation of the top quark was done at the Tevatron in 1995 [10, 11]. After its discovery many methods have been developed to measure its mass with high precision. Nowadays, precise measurements of the of the top-quark mass have been provided by the combination of the Tevatron experiments ($m_{\text{top}} = 173.2 \pm 0.9$ GeV[13]) as well as for the combination of the LHC experiments ($m_{\text{top}} = 173.3 \pm 1.0$ GeV[108]).

This chapter presents the measurement of the top-quark mass using an integrated luminosity of $4.7\,fb^{-1}$ of $\sqrt{s} = 7$ TeV collision data collected by the ATLAS detector. The aim of the method is to fully reconstruct the event kinematics and thus compute the top-quark mass from its decay products. The analysis uses the lepton plus jets channel ($t\bar{t} \to \ell$ + jets, where the lepton could be either an electron or a muon). This topology is produced when one of the W bosons decays via $W \to \ell\nu$, while the other decays into hadrons. Thus, the final state is characterized by the presence of an isolated lepton, two light-quark initiated jets, two b-quark jets stemming from the $t \to Wb$ decay and missing transverse energy. The first step of the analysis consists in the reconstruction and identification of all these objects. Once the identification has been done, the Global χ^2 fitting technique is used. This method performs a nested fit where the results of the first (or inner) fit are considered in the second (or global) fit. In the inner fit, the longitudinal component of the neutrino momentum (p_z^ν) is computed, and subsequently fed to the global fit, which obtains the m_{top}. The top-quark mass distribution is filled with the event by event kinematic fit results. Finally, this distribution is fitted with a template method and the top-quark mass value extracted.

The chapter is organized as follows: Section 5.1 gives an overview of the current top-quark mass measurements, Section 5.2 reports the top decay modes and the main physics backgrounds, Section 5.3 summarizes the data and MC samples used in this analysis. Section 5.4 explains the standard event selection for the top-quark analysis while Section 5.5 describes the specific $t\bar{t}$ kinematics exploited by the Globalχ^2. Section 5.6 shows the Globalχ^2 formalism adapted for measuring the top-quark mass. Section 5.7 presents the template method used to extract the m_{top} value. Finally, the systematic uncertainties have been carefully evaluated in section 5.8. In addition, some cross-check tests have been done to validate the final results in Section 5.9 and the top-quark mass conclusions are summarized in Section 5.10.

5.1 Current top-quark mass measurements

The precise determination of the top-quark mass is one of the goals of the LHC experiments. Therefore, different techniques have been developed in order to increasingly getting more accurate top-quark mass measurements:

- **Extraction from cross section:** the top-quark mass can be extracted from the $t\bar{t}$ cross section ($\sigma_{t\bar{t}}$) which has been recently measured with high precision. The comparison of the experimental results with the theoretical predictions allows performing stringent tests of the underlying models as well as constrain some fundamental parameters. The m_{top} is a crucial input for the $\sigma_{t\bar{t}}$ calculation at NNLO order in perturbation theory. Although the sensitivity of the $\sigma_{t\bar{t}}$ to m_{top} might not be strong enough to obtain a competitive measurement with a precision similar to other approaches, this method provides the determination of the m_{top} in a well-defined theoretical scheme (Section 1.2.1). Some of the latest m_{top} results extracted from the $\sigma_{t\bar{t}}$ are reported in [39, 109, 110, 111]. Currently, there are attempts to define a new observable based on the $\sigma_{t\bar{t}+jet}$ able to measure the m_{top} in the $\overline{MS}$ scheme at NLO calculations with better precision [112].

- **Template method:** in these methods the simulated distributions of the m_{top} sensitive observables are confronted with their real data equivalent. The template methods have been continuously improved from the 1-dimensional template fit [113] which used only the m_{top} distribution, passing trough the 2-dimensional template [114] that also determined a global jet energy scale factor (JSF) to the 3-dimensional template [115] where a third variable is used to calculate the global relative b-jet to light-jet energy scale factor (bJSF). Therefore, the systematic error on m_{top} stemming from the uncertainty on the jet energy scale could be considerably reduced, albeit at the cost of an additional statistical uncertainty component. The m_{top} measurement obtained with the template methods corresponds by construction to the mass definition used in the MC generator.

- **Calibration curve:** the calibration curves parametrize the dependence of the top-quark mass with respect to one specific observable. These curves are built using several MC samples generated at different m_{top} values. Therefore, the m_{top} measurement is extracted directly from the curve by comparing with the data observable value. Also in this case, the resulting m_{top} corresponds to the MC mass. Among others, the calibration curves to obtain the m_{top} have been constructed using the top-quark transverse mass m_{T2} [116] and the transverse decay length (L_{xy}) of the b-hadrons between the primary and the secondary vertices [117].

Figure 5.1 shows the evolution of the top-quark mass measurements obtained by the ATLAS and CMS experiments versus time. These measurements have been performed using different techniques and event topologies.

5.2 Topology of the $t\bar{t}$ events

The top quark at LHC is mainly produced in pairs through gluon-gluon fusion processes. Once produced, the top quark decays almost exclusively to a W boson and a b-quark. The b-quark always hadronizes producing at least one jet in the detector while the W boson presents different decay modes. The $t\bar{t}$ events can be divided in three channels depending on the final state objects:

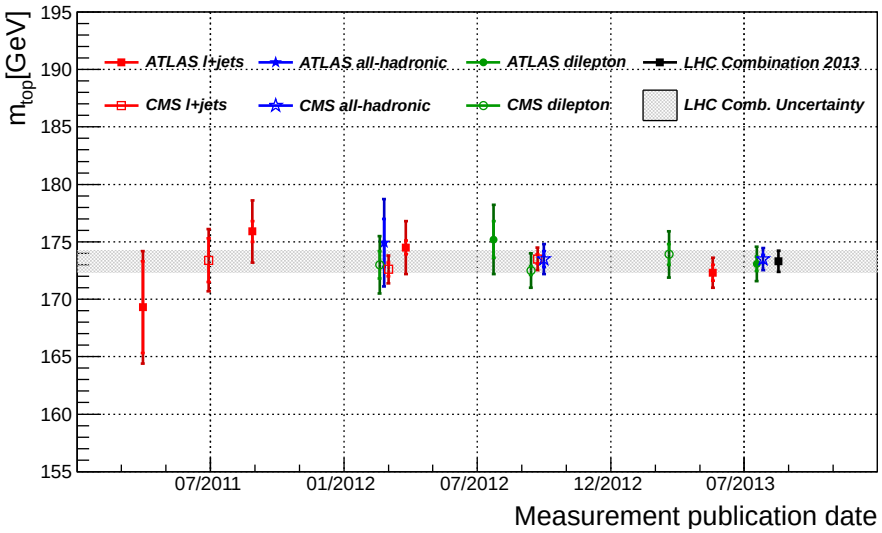

Figure 5.1: Time evolution of the top-quark mass measurements for different techniques and topologies. Different colors indicate the topology used in the analysis: dileptonic (green), l+jets (red) and all-hadronic (blue). Both ATLAS and CMS results have been added in the plots using filled and empty markers respectively.

- **Dilepton channel:** both W bosons decay into lepton plus neutrino: $t\bar{t} \rightarrow W^- b W^+ \overline{b} \rightarrow b\ell^- \overline{\nu_l} \overline{b} \ell^+ \nu_l$ where ℓ corresponds to electron, muon or tau decaying leptonically. Therefore, this channel is characterized by the presence of two b-jets, two high p_T leptons and a big amount of missing transverse energy ($E_{\mathrm{T}}^{\mathrm{miss}}$) coming from the two neutrinos. The existence of two neutrinos associated to the only one $E_{\mathrm{T}}^{\mathrm{miss}}$ leads to an under-constraint system. The presence of the leptons provides a clear signature and the background can be easily rejected. This channel has a branching ratio (BR) of 6.4%.

- **Lepton plus jets channel:** one of the W boson decays leptonically while the other decays hadronically. The final state is characterized by the presence of an isolated lepton in conjunction with $E_{\mathrm{T}}^{\mathrm{miss}}$ due to its undetectable counterpart neutrino, two light jets from the W hadronic decay ($W \rightarrow qq$[1]) and two jets originating from b-quarks ($t \rightarrow Wb$). This channel can be clearly identified by the presence of one isolated high p_T lepton. The BR of this channel is 37.9%

- **All-hadronic channel:** both W bosons decay into quarks with different flavour. This channel is characterized by the presence of only hadronic objects in the final state: four light jets and two b-jets. The final BR is of 55.7%.

To calculate the BR reported above the τ particles have not been treated as a leptons, but their hadronic and leptonic decays are considered to contribute to different channels instead. Figure 5.2 shows the different decay modes and their final objects. The classification of the channels has been done using a LO approximation. Nevertheless, quarks can emit gluons, thus producing more jets in the final state and therefore a more complicated topology.

[1]The hadronic W decay produces a quark and anti-quark of different flavor. Here, $W \rightarrow qq$ is used for simplicity.

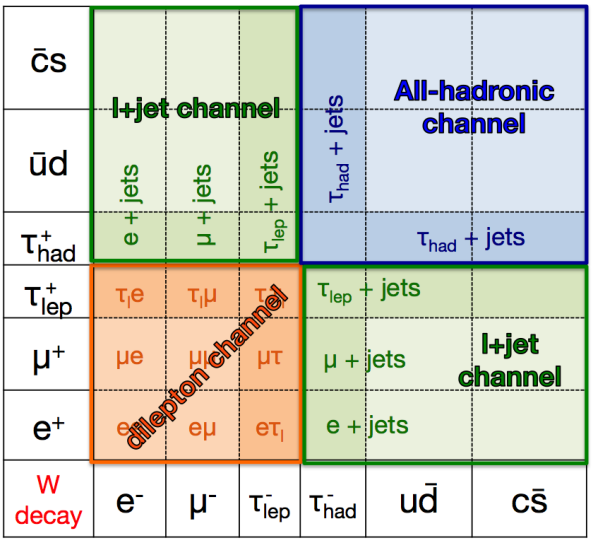

Figure 5.2: Representation of the $t\bar{t}$ decay modes with their final objects.

The top-quark mass analysis presented in this thesis has been performed in the ℓ+*jets* channel ($\ell = e, \mu$) since it has a high enough BR together with a clear signature. Figure 5.3 shows the Feynman diagram associated to the $t\bar{t} \rightarrow \ell$ + jets topology.

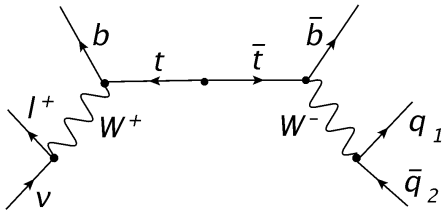

Figure 5.3: Feynman diagram at tree level of the $t\bar{t} \rightarrow \ell$ + *jets* decay mode.

Physics background

In nature, there are physics processes that can be misidentified with the signal under study since they produce similar final states. These processes are called physics backgrounds. For the top-quark mass measurement in the ℓ + *jets* channel there are 5 different SM processes that mimic the same topology:

- **Single top background.** The single top is produced through three different mechanisms: Wt production, s-channel and t-channel. The single top final topology is similar to the $t\bar{t}$ signal and even equal when additional jets are produced by radiation effects. The Feyman diagram of the Wt channel process, which provides the dominant contribution, can be seen in figure 5.4(a).
- **Diboson background.** This background includes processes with a pair of gauge bosons, in particular WW, ZZ and WZ. The Feyman diagram corresponding to this background can be seen in 5.4(b).

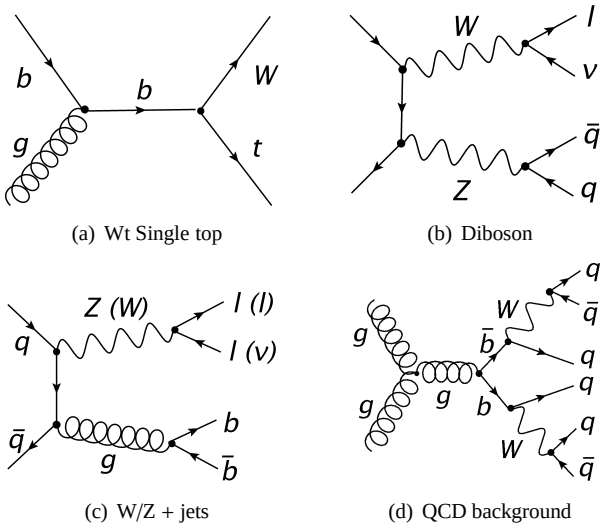

(a) Wt Single top (b) Diboson

(c) W/Z + jets (d) QCD background

Figure 5.4: Feynman diagrams at tree level for the main physical backgrounds.

At LO the topology is not mixed with our signal, but at higher orders extra jets appear therefore resulting in the same final state as with a genuine $t\bar{t}$ event.

- **W+jets background.** This background includes the W boson in association with jets. To mimic the $t\bar{t}$ semileptonic topology the W must decay leptonically (W→lν). A Feyman diagram example can be seen in Figure 5.4(c).

- **Z+jets background.** The Z+jets background may mimic the final signal when it is produced in association with other jets (Figure 5.4(c)).

- **QCD background.** Multijet events (Figure 5.4(d)) become a background of the $t\bar{t}$ events whenever they contain a genuine lepton not coming from the W decay but, for example, from semileptonic decays of some hadrons, which mislead the prompt lepton of the event. In addition, also there are no leptonic particle, like jets, that can mimic the signature of the lepton from the W decay. For the electrons, they may come from the photon conversion and semileptonic decay of the b and c quarks. On the other hand, the muons can arise from the decay of pions and kaons within the tracking volume, punch-through and also from the b and c semileptonic quark decay. These processes happen rarely, however the enormous multijet cross section make them an important source of background.

5.3 Data and MonteCarlo Samples

This analysis has been performed using the $p-p$ collisions recorded by the ATLAS detector during the 2011 LHC run at a center of mass energy of 7 TeV. Only data periods with stable beams and with the ATLAS detector fully operational have been considered. The used data amount to an integrated luminosity of 4.7 fb^{-1}.

MC samples have been used in order to validate the analysis procedure. The $t\bar{t}$ signal sample has been produced with POWHEG [118] with CT10 parton density function (p.d.f.). The parton shower and underlying event has been modelled using PYTHIA [119] with the Perugia 2011C tune [120]. Other MC generators (MC@NLO and ALPGEN), hadronization model (HERWIG) and p.d.f (MSTW2008nlo68cl and NNPDF23_nlo_as_0019) have been also studied and their influence on the m_{top} measurement has been quoted as systematic uncertainty (more information about these variations in Section 5.8).

The baseline sample was generated with $m_{\text{top}} = 172.5$ GeV normalised to a cross-section of 166.8 pb. The value of the total cross section for QCD top-quark pair production in hadronic collision has been calculated using an approximate NNLO calculation from HATHOR [121]. Additional $t\bar{t}$ samples have been produced with different top-quark masses ranging from 165 GeV until 180 GeV. All those samples have been normalized to produce the right cross section at appropriate NNLO precision.

Besides, SM physics backgrounds described in previous section have been simulated to estimate their contribution to the m_{top} measurement. The single top samples have been generated using POWHEG with PYTHIA P2011C tune for s-channel and Wt production while the t-channel uses ACERMC [122] with the same PYTHIA tune. The diboson processes (ZZ/WW/ZW) are produced at LO with lowest multiplicity final state using HERWIG [123] standalone. Finally the Z/W boson in association with jets processes are simulated using the ALPGEN generator interfaced with the HERWIG/JIMMY packages. All these Monte Carlo samples have been generated with multiple $p-p$ interactions. To improve the estimation of the multiple interactions per bunch crossing (pile-up) used in the MC the events need to be re-weighted using the real pile-up conditions as measured in data. All the samples used to perform the analysis can be found in Appendix F.

After event generation, all samples need to pass through the ATLAS detector simulation [124]. It reproduces the response of the ATLAS detector to the passage of particles using GEANT4 [125]. For the sake of the statistical precision of the analysis, it is required that the simulated data sets must be both large and precise, so their production is a CPU-intensive task. ATLAS has developed detector simulation techniques to achieve this goal within the computing limits of the collaboration [126]. Nevertheless, at the analysis time, differences between the full ATLAS simulation (FULL) and faster simulation techniques (AFII) were observed and instead of working with both, only the FULL simulation was used for performing the m_{top} measurement.

5.4 Top-quark event selection

This analysis uses the standard ATLAS selection and calibration performed for the top-quark analyses [64]. A brief description of the involved objects was given in Section 3.3 and the complete list of the software packages used for reconstructing them is given in the Appendix G. The official top-quark event selection consists in a series of requirements to retain an enriched sample of $t\bar{t} \to \ell$ + jets events.

The requirements applied, based on the quality of the events and reconstructed objects, are the followings:

- **Pass trigger selection.** Different trigger chains have been consequently used for the different data periods. The pass of the appropriate single electron or single muon trigger is required. For the e + jets channel the `EF_e20_medium`, `EF_e22_medium` and `EF_e20vh_medium1` with a p_{T} threshold of 20 GeV and 22 GeV are used. In addition, the `EF_e45_medium1` trigger chain is

also used to avoid efficiency losses due to the electrons with high momentum. For the the μ + jets channel, the `EF_mu18` and `EF_mu18_medium`, with a p_{T} threshold of 18 GeV are required.

- **LAr error.** Some flags are filled to indicate dramatic problems with the detectors. The LAr calorimeter suffered some problems during the first periods of 2011 data taking. Those events with data integrity errors in the LAr have been rejected to avert problems in electron, photon or $E_{\mathrm{T}}^{\mathrm{miss}}$ object reconstruction.

- **At least 1 good vertex.** For the cosmic background rejection at least 1 vertex with more than 4 tracks is required.

- **Exactly one isolated lepton with $\mathbf{p}_{\mathrm{T}}$ >25** GeV**.** The isolation variable, defined as the activity around the lepton axis excluding the contribution of the lepton itself, can be used to discern genuine signal leptons from the background (fake leptons). For example, prompt electrons and muons originating from $t\bar{t} \to \ell$ + jets events are relatively well isolated when compared with those leptons emanating from quark heavy flavour decays. Finally, in order to keep those isolated leptons in the analysis, they are required to match with the corresponding trigger object. Only one lepton is required to ensure non overlap with dilepton events.

- **The event is required to have at least 4 jets with $\mathbf{p}_{\mathrm{T}}$ > 25 GeV within** $|\eta|$**< 2.5.** A large number of jets is expected in the $t\bar{t} \to \ell$ + jets topology. This is among the hardest cuts to reduce many of the SM physics backgrounds.

- **Good jet quality criteria.** A jet quality criteria is applied in order to reject jets with bad timing energy deposits in the calorimeter due to hardware problems, LHC beam gas and/or cosmic rays. Different quality levels have been established based on a set of calorimeter variables. Jets with `Loose` [127] quality criteria have been removed.

- **Jet Vertex Fraction (JVF).** The JVF allows for the identification and selection of jets originating in the hard-scatter interaction through the use of tracking and vertexing information. Basically, the JVF variable quantifies the fraction of track p_{T} associated to the jets from the hard scattering interaction [70]. Jet selection based on this discriminant is shown to be insensitive to the contributions from simultaneous uncorrelated soft collisions that occur during pile-up. In this analysis, jets are accepted if $|JVF| > 0.75$.

- $\mathbf{E}_{\mathrm{T}}^{\mathrm{miss}}$ **and** $\mathbf{m}_{\mathrm{T}}(W)$[2]**.** Further selection cuts on the $E_{\mathrm{T}}^{\mathrm{miss}}$ and W transverse mass are applied. For the μ + jets channel: $E_{\mathrm{T}}^{\mathrm{miss}} > 20$ GeV and $E_{\mathrm{T}}^{\mathrm{miss}} + m_{\mathrm{T}}(W) > 60$ GeV are required. Similar cuts are applied in the e + jets channel: $E_{\mathrm{T}}^{\mathrm{miss}} > 30$ GeV and $m_{\mathrm{T}}(W) > 30$ GeV. These cuts help to reduce considerably the QCD multijet background contribution.

- **At least 1** b**-tagged jet.** It is required to have at least 1 b-tagged jet using the MV1 tagger at 70% efficiency.

These selection cuts ensure a good $t\bar{t} \to \ell$ + jets selection with a signal over background factor: S/B$\approx$ 3 for both analysis channels. The main background contributions come from single top, QCD multijets and W+jets. The single top and also the diboson and Z+jets backgrounds have been estimated using MC samples. The contribution of the QCD multijet background has been determined using data driven (DD) methods and the W+jets background has been calculated mixing both, data and MC information.

[2]The W boson transverse mass is defined as follows: $m_{\mathrm{T}}(W) = \sqrt{2p_{\mathrm{T},\ell}\ p_{\mathrm{T},\nu}[1 - cos(\phi_\ell - \phi_\nu)]}$ where the neutrino information is provided by the $E_{\mathrm{T}}^{\mathrm{miss}}$ vector.

QCD multijet background

For the QCD multijet background with fake leptons, the shape and the normalization have been fixed using DD methods. The fake contribution is estimated using matrix methods based on the selection of two categories of events: loose and tight [127]. The matrix methods uses the lepton identification efficiency and the fake efficiency to estimate a final event weight. Those selected events in the analysis are then weighted with the probability of containing a fake lepton. For the $e + jets$ channel the efficiency has been obtained using a tag and probe method over the $Z \rightarrow ee$ sample while the fake efficiency uses a sample with one loose electron and one jet with p_{T} >25 GeV. The $\mu + jets$ channel uses a combination of two alternative matrix methods and the final event weight is obtained as average of both. The first method calculates the muon identification efficiency from $Z \rightarrow \mu\mu$ whilst the fake efficiency is extracted from a specific control region. In the second one, the fake leptons come principally from the heavy flavour quark decays. The signal efficiency is extracted from $t\bar{t}$ sample and the fake efficiency is measured using the impact parameter significance. The QCD estimation methods for both channels are described in reference [64].

W+jets background

The overall normalization of the W+jets background is obtained from the data while the kinematic shape is modelled using the MC information. The W+jets estimation has been performed using the charge asymmetry method based on the fact that the LHC produces more W^+ boson than W^- bosons. This effect is induced for the relative difference between quark and anti-quark parton distribution functions. The W+jets is considered the dominant source of charge asymmetry for high p_{T} leptons in data. The difference between positively and negatively charged W bosons can be calculated as the difference between positive and negative leptons arising from their decay. This quantity together with the well theoretically known ratio $r_{MC} \equiv \frac{\sigma(pp\rightarrow W^+)}{\sigma(pp\rightarrow W^-)}$ are used to estimate the final contributions of the W+jets background. More details about this method are provided in the references [64] and [128].

Figures 5.5, 5.6 and 5.7 present the data vs. MC comparison of some relevant observables for those events satisfying the preliminary $t\bar{t} \rightarrow \ell$ + jets selection stated above. The uncertainty band on the prediction is calculated as the quadratic sum of several contributions: the statistical uncertainty, the b-tagging efficiency uncertainty, the 1.8% uncertainty on the luminosity [129], the 10% on the $t\bar{t}$ cross section, a 24% of uncertainty in the W+jets normalization and a 50% or a 40% on the QCD multijet background normalization in the electron and muon channel respectively. These uncertainties have been applied in all figures.

Table 5.1 quotes the event statistics in the real data, $t\bar{t}$ signal (Powheg+Pythia P2011C tune) samples with a default m_{top} of 172.5 GeV and the expected contributions from the all background sources after the standard top group selection. Beyond these requirements, a specific selection has been implemented for this analysis. Those distinct cuts will be introduced and motivated in the corresponding sections.

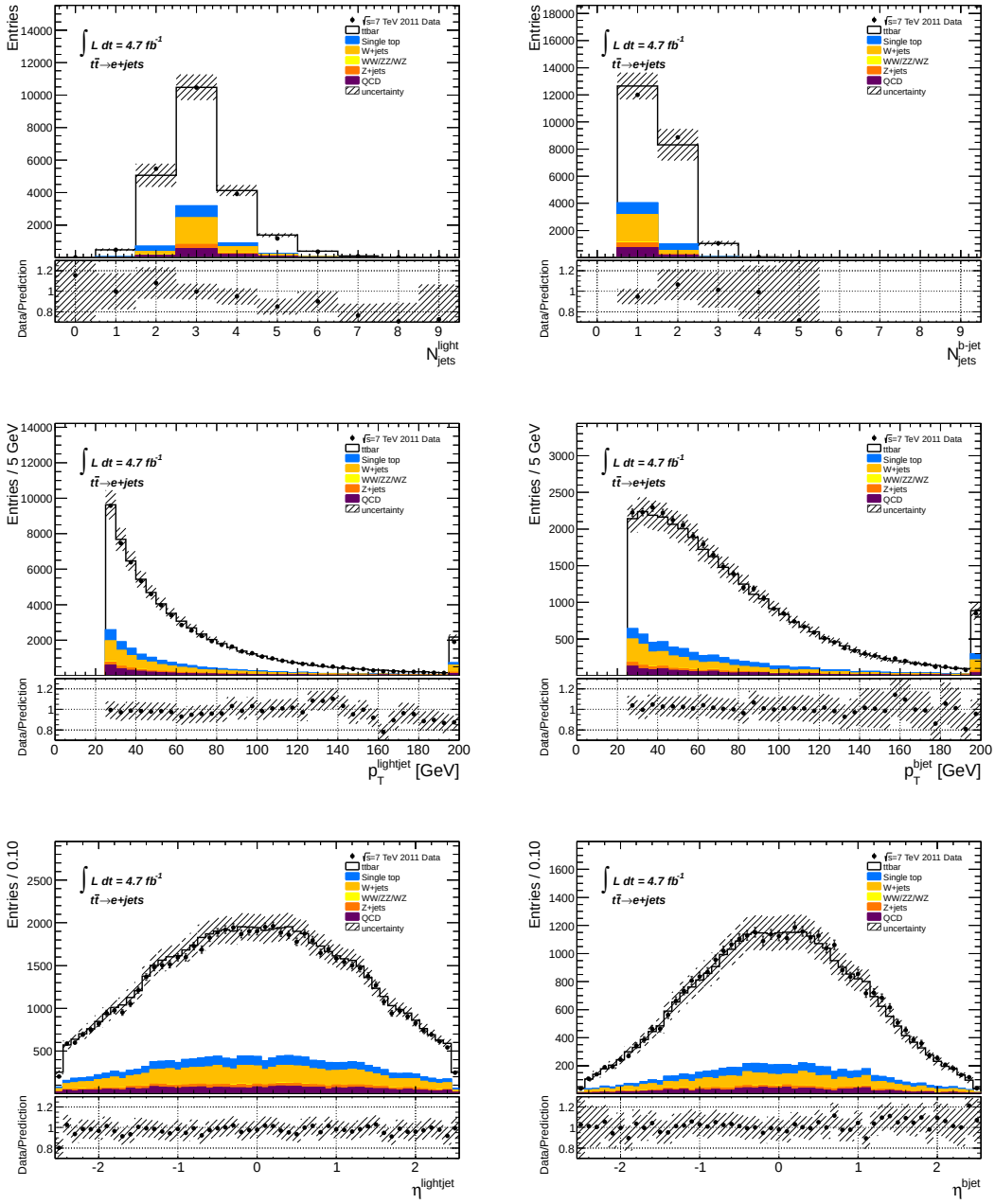

Figure 5.5: Data vs MC comparison of the reconstructed jets in the e + jets channel. Light jets are displayed in the left column whilst b-tagged jets in the right. The shaded area represents the uncertainty on the MC prediction.

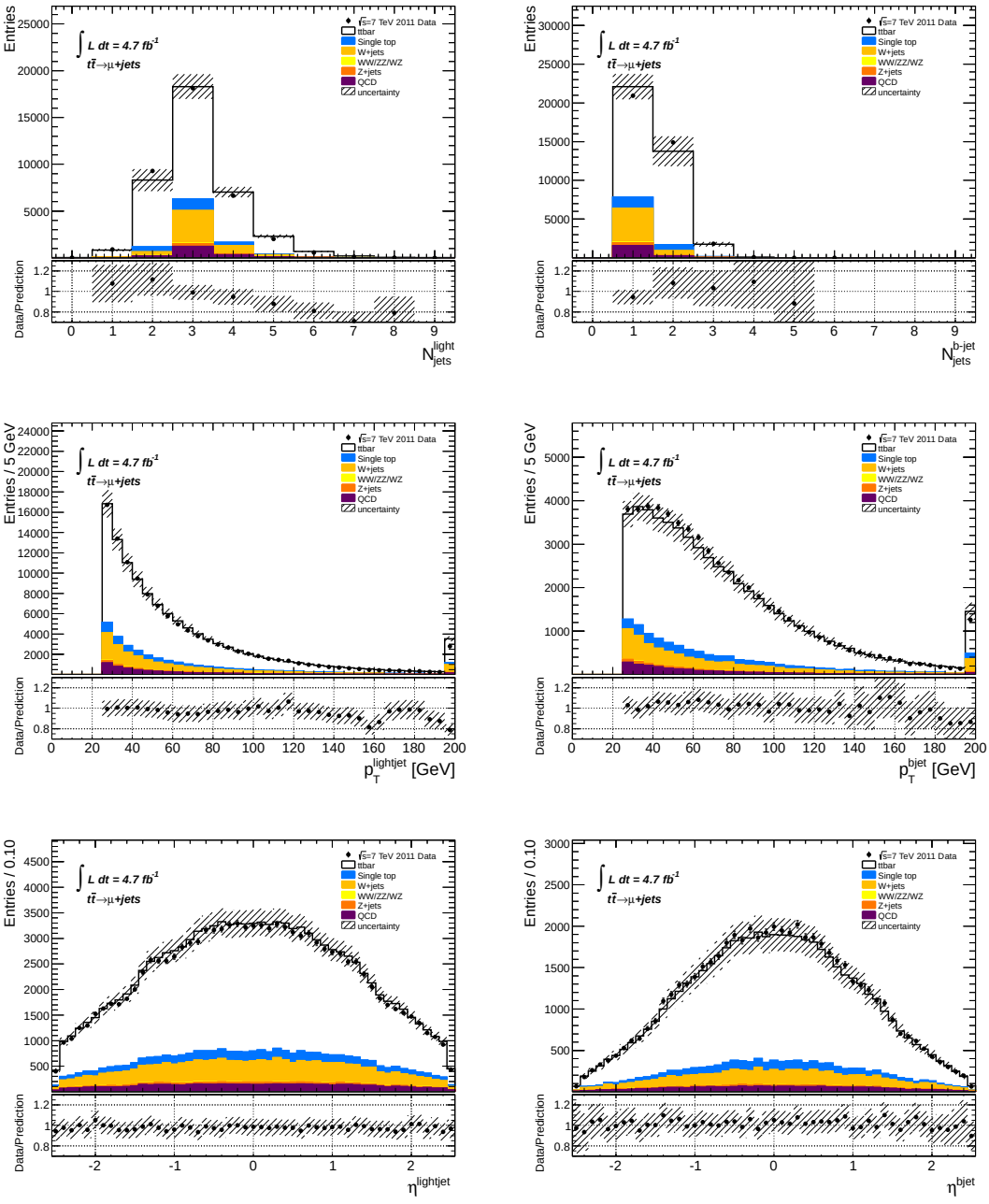

Figure 5.6: Data vs MC comparison of the reconstructed jets in the μ + jets channel. Light jets are displayed in the left column whilst *b*-tagged jets in the right. The shaded area represents the uncertainty on the MC prediction.

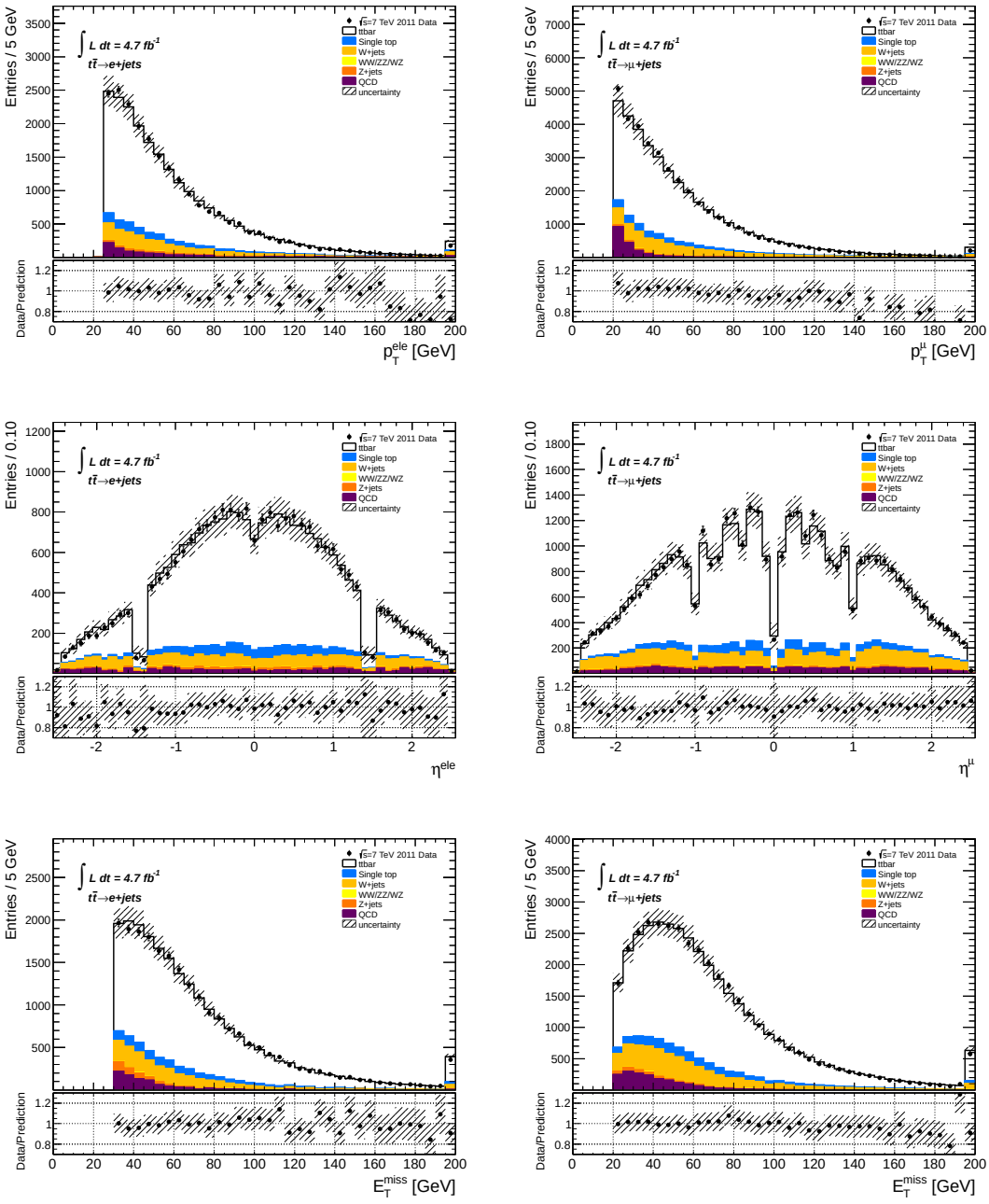

Figure 5.7: Data vs MC comparison of the leptons p_T and η and E_T^{miss}. Left column corresponds to the e + jets channel. Right column displays the μ + jets channel. The shaded area represents the uncertainty on the MC prediction.

Process	e + jets	μ + jets
$t\bar{t}$ signal	17000 ± 1900	28000 ± 3100
Single top	1399 ± 73	2310 ± 120
WW/ZZ/WZ	46.9± 1.4	74.7 ± 2.4
Z+jets	469.5 ± 9.1	453 ± 12
W+jets (data)	2340 ± 450	5000 ± 1100
QCD (data)	890± 450	1820 ± 910
Background	5150 ± 730	9700 ± 1400
Signal+Background	22100 ± 2000	37700 ± 3400
Data	21965	37700

Table 5.1: The observed number of events in data after the standard $t\bar{t}$ event selection. The expected signal and backgrounds correspond to the real data integrated luminosity. The $t\bar{t}$ signal events and the single top background have been estimated with a default m_{top} of 172.5 GeV. The uncertainties include the contribution of statistics, b-tagging efficiency, $t\bar{t}$ normalization, luminosity and QCD and W+jets normalization. The uncertainties have been quoted with two significant digits.

5.5 Kinematics of the $t\bar{t}$ events in the l+jets channel

The full kinematics of a $t\bar{t} \to \ell$+jets event is known once the final state objects are determined: light jets from the hadronic W boson decay, lepton and neutrino from the leptonic W boson decay and b-tagged jet association with its corresponding W to identified the $t \to Wb$ decay. Hence, in order to extract the m_{top} value in each event, one needs to:

- Reconstruct the hadronically decaying W from its jets. Each pair of light jets is confronted with the hypothesis that it emanates from the W hadronic decay. Moreover, the presence of this W is one of the advantages of the lepton+jets topology since it can be used to relate the jet energy scales in data and MC.
- Estimate the p_z component of the neutrino momentum (assuming that $E_{\text{T}}^{\text{miss}}$ provides the p_{T}^{ν}) to reconstruct the leptonically decaying W.
- Match the b-tagged jets to the hadronically and leptonically decaying W bosons.

One of the challenges of the event kinematics reconstruction of the $t\bar{t} \to \ell$ + jets topology is the following: as there are many objects in the final state, one has to ensure a correct matching between the reconstructed objects and that top quark or W boson they meant to represent of the $t\bar{t} \to W^+b\, W^-\bar{b} \to b\bar{b}q\bar{q}\ell\nu$ process. In the $t\bar{t}$ MC, it is possible to evaluate the goodness of the association using the truth information.

Event classification

In the following, a given jet is considered to be initiated by one of the partons stemming from the $t\bar{t}$ decay if their directions match within a $\Delta R < 0.3$ cone (quark-jet association). Although, it may occur that the during parton shower the leading partons change their direction and/or new extra jets may emerge. In the first case, if the direction change is quite abrupt, the quark-jet association may fail. In

the second case, a new jet could probably enter in the event reconstruction, however it is unclear what leading parton (if any) sparked that jet. As a result, one may have to deal with events where all the quark-jet associations are faithful and events where some of the reconstructed jets are unmatched to any leading parton. Consequently, this analysis considers the following type of events:

- Genuine $t\bar{t} \rightarrow \ell$ + jets events with proper object association. All jets matched to a leading parton (light jets to the hadronically decaying W and the b-tagged jets matching well with the b-quarks stemming from the hadronic and leptonic top decay). Hereafter, these events are labelled as *correct*.
- Genuine $t\bar{t} \rightarrow \ell$ + jets events but with defective object association. This is a generic category which involves several subcategories: events where the hadronic W is not correctly matched, events where the b-quark jets were not properly associated to their hadronic or leptonic W companion, no matching between some of the reconstructed jet and a leading parton, etc. This event class contains all the events that fail in at least one of those matchings and no distinction is made between the different subcategories. These events are marked as *combinatorial background.*
- Irreducible physics background. This is composed by SM processes ($t\bar{t}$ excluded) that produce a final event topology similar to the $t\bar{t} \rightarrow \ell$ + jets event topology and satisfy all the triggers plus selection criteria. These processes have been explained in Section 5.2.

Obviously, the *correct* and *combinatorial background* labeling adapts to the kind of study. For the $W \rightarrow qq$ study, it is enough to have a good matching of the light jets for considering an event as *correct* at this stage.

5.5.1 Selection and fit of the hadronic W decay

The identification of the hadronically decaying W from its products helps to characterize the event kinematics.

Preselection of jets

In each event, there is a given number of light jets that fulfill the preselection criteria (Figures 5.5 and 5.6 in Section 5.4). The goal now is to select, among all the possible jet-pair combinations, the pair of jets that can be attributed to the $W \rightarrow qq$[3] decay. Therefore, the viable jet-pairs were selected by testing all possible pairings and retain only those that satisfy the following criteria:

- no b-tagged jets
- Leading jet with $p_{\mathrm{T}} \geqslant 40$ GeV
- Second jet with $p_{\mathrm{T}} \geqslant 30$ GeV
- Radial distance between jets: $\Delta R < 3$
- Reconstructed invariant mass of the jets: $|m_{jj} - M_W^{PDG}| < 15$ GeV

[3] At leading order, the $W \rightarrow qq$ decay will produce two jets. Of course, the quarks can emit hard gluons which their fragmentation may give rise to more jets.

Events with no jet-pair candidates satisfying those criteria were rejected at this stage. Events containing at least one viable jet-pair were considered for the in-situ calibration process.

In order to speed up the analysis, reduce the jet combinatorics, save CPU time and bearing in mind that the final event selection will require exactly two *b*-tagged jets, this restrictive selection cut is already imposed at this stage of the analysis. Therefrom, events enter the in-situ calibration process if, in addition to have at least one viable jet-pair, they contain:

- Exactly two *b*-tagged jets.

All these cuts have been studied with the MC samples and their values have been chosen to reject most of the bad pair combinations (combinatorial background) while retaining enough statistics. Detailed information can be found in Appendix H.

In-situ calibration

The goal of the in-situ calibration is two fold: first to select the jet-pair which will be retained for the analysis, and second to provide a frame to fine-tune the JES separately for real data and MC in $t\bar{t} \to \ell$+jets events.

For every viable jet-pair in the event, a χ^2 fit was performed to compute the jet energy corrections through multiplicative constants. The χ^2 was defined as follows:

$$\chi^2(\alpha_1, \alpha_2) = \left(\frac{E_{j1}(1-\alpha_1)}{\sigma_{E_{j1}}}\right)^2 + \left(\frac{E_{j2}(1-\alpha_2)}{\sigma_{E_{j2}}}\right)^2 + \left(\frac{m_{jj}(\alpha_1, \alpha_2) - M_W^{PDG}}{\Gamma_W^{\text{PDG}} \oplus \sigma_{E_{j1}} \oplus \sigma_{E_{j2}}}\right)^2 \tag{5.1}$$

where E_j and σ_{E_j} are the reconstructed energy of the first and second jet ordered in energy and its uncertainty. α_1 and α_2 are the two in-situ calibration fit parameters. $m_{jj}(\alpha_1, \alpha_2)$ represents the invariant mass of the two jets under test (correcting their energies with the α factors). Γ_W^{PDG} is the width of the W boson as given in the PDG [130].

Amongst all viable jet-pairs in the event, the retained one is that with the lowest χ^2, provided that its $\chi^2 < 20$. Otherwise no jet-pair is accepted and the event is consequently rejected. All the other non light jets in the event which were not retained by this procedure were then discarded for the rest of the analysis. Finally, the energy of the two retained jets is subsequently scaled using the α parameters obtained from the fit (Equation 5.1).

In what concerns the size of the jet energy correction factors (α) obtained during the in-situ calibration, the R.M.S. of the α distributions is below 2% (see Figure 5.8). Figure 5.9 presents the invariant mass of the selected jet pairs (m_{jj}) under two circumstances:

- Using the reconstructed jets as such (plots on the left).
- With the jets energy corrected by the α_1 and α_2 factors extracted from the in-situ calibration (plots on the right).

In these figures one can distinguish the contribution from the *correct* jet-pairs and combinatorial background. These distributions can be also seen separately for both kind of events in Appendix I.

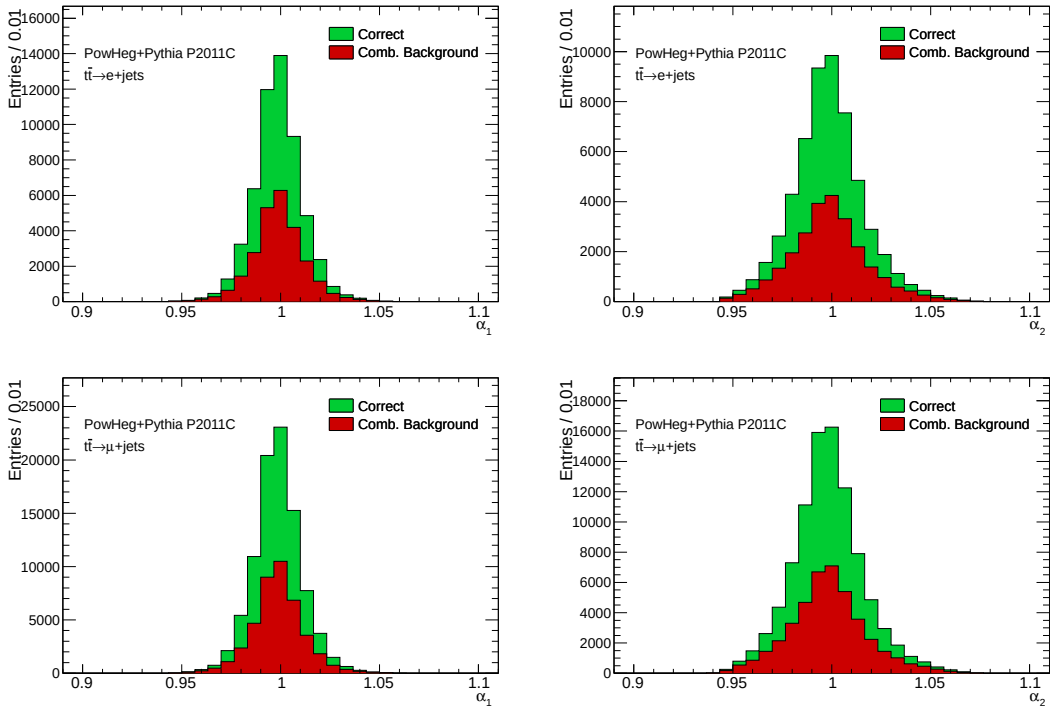

Figure 5.8: MC correction factors α_1 (left) and α_2 (right) obtained from the in-situ calibration fit of the hadronically decaying W for the e + jets channel (upper row) and μ + jets channel (bottom row).

Efficiency and purity of the $W \to qq$ sample

Using the MC $t\bar{t} \to \ell$ + jets sample, the efficiency of this method and the purity of the retained jet-pairs in the $W \to qq$ sample were evaluated. These were defined as:

$$\text{efficiency} = \frac{\text{\# events passing the hadronic } W \text{ fit}}{\text{\# events satisfying the } t\bar{t} \to \ell + \text{jets preselection}}$$

$$\text{purity} = \frac{\text{\# jet pairs with correct matching of the truth hadronic } W \to qq \text{ decay}}{\text{\# events passing the hadronic } W \text{ fit}}$$

The figures found in this analysis were 14% and 54% for efficiency and purity respectively. The relatively low efficiency when compared with those of the $t\bar{t} \to \ell$+jets selection (Section 5.4), is basically due to the tighter jet p_{T} cuts, strong cut in the invariant mass of the jet pair candidate and the requirement of exactly two b-tagged jets (Section 5.5.1).

Table 5.2 quotes the event statistics in MC $t\bar{t} \to \ell$ + jets signal and background processes once the in-situ calibration and its events selection has been applied. Note that the contribution of physics background has been significantly reduced with respect to that of Section 5.4. At this stage it represents $\approx$ 7% of the sample in both channels.

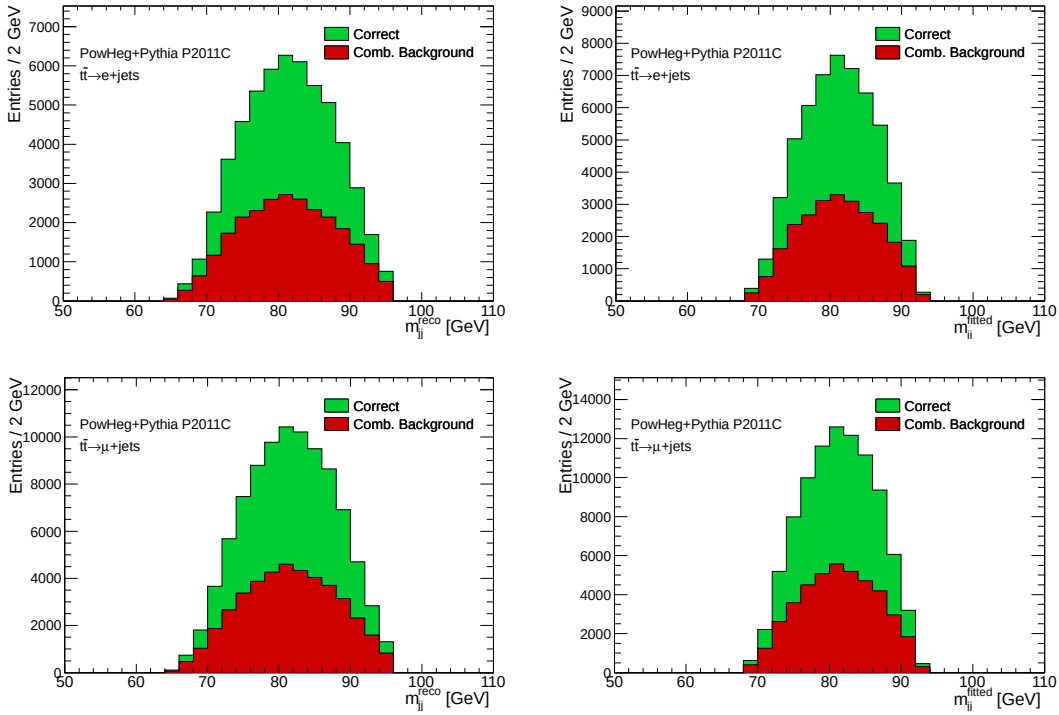

Figure 5.9: MC study of the invariant mass of the jets associated to the hadronically decaying W in the $t\bar{t} \to e+$jets (upper row) and $t\bar{t} \to \mu+$jets (bottom row) channel. Left: with the reconstructed jets before the in-situ calibration. Right: once the jets energy has been corrected with the α factor. Correct jet-pairs are shown in green whilst the combinatorial background jet-pairs are shown in red.

Process	e + jets	μ + jets
$t\bar{t}$ signal	2370 ± 390	3940 ± 520
Single top	111 ± 16	183 ± 27
WW/ZZ/WZ	0.72± 0.16	1.14 ± 0.24
Z+jets	12.4 ± 1.4	6.3 ± 1.1
W+jets (data)	31.2 ± 9.3	70 ± 19
QCD (data)	25 ± 15	39 ± 20
Background	180 ± 24	299 ± 39
Signal+Background	2550 ± 390	4240 ± 520
Data	2674	4603

Table 5.2: Observed number of events in data after hadronic W selection. The expected signal and backgrounds correspond to the real data integrated luminosity. The uncertainties include the contribution of statistics, b-tagging efficiency, $t\bar{t}$ normalization, luminosity and QCD and W+jets normalization. The uncertainties have been quoted with two significant digits.

In-situ calibration with real data

The procedure described above was repeated on the real data sample. Figure 5.10 presents the fitted m_{jj} (therefore applying the α_1 and α_2 factors estimated from data in an event-by-event basis) for real data

compared with the MC expectation. There is a mismatch between both data amd MC m_{jj} distributions because they do not peak at the same value. This unbalance needs to be corrected. Otherwise, having a different jet energy scale factor (JSF) in the MC distributions other than in data, would irremediably bias the top-quark mass measurement with the template method. Table 5.2 quotes the event statistics in real data once the in-situ calibration and its events selection has been applied.

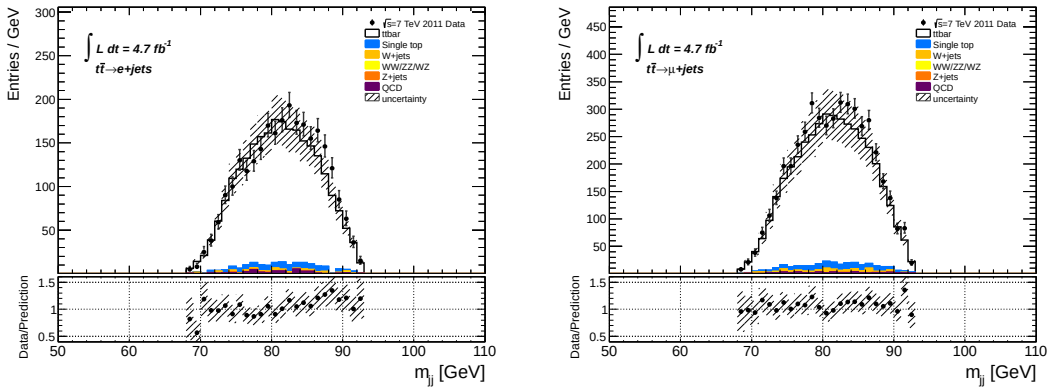

Figure 5.10: Invariant mass (m_{jj}) of the two jets arising from the $W \rightarrow qq$ decay after their correction with α factors extracted from the in-situ calibration. Left: e + jets channel. Right: μ + jets channel.

Determination of the jet energy scale factor (JSF)

In order to tackle this problem, the in-situ calibration needed to be fine tuned, bearing in mind that m_{jj} has to be an observable with the following properties:

- sensitive to the differences in JSF between data and MC.
- independent of the top-quark mass.

To verify this last property, a linearity test of the estimated m_W^{fitted} (from the m_{jj} distribution after in-situ calibration) was performed using different MC samples with varying the m_{top} generated value. The m_W^{fitted} value was calculated as the mean value of the Gauss distribution given by the fit model (details in Appendix J). Figure 5.11 presents the m_W^{fitted} values as a function of the generated top-quark mass for both analysis channels. Consistent values of m_{jj} were found for different m_{top} values and lepton channels, thus discarding any possible dependence of m_{jj} with m_{top}. In MC, the m_{jj} mean values are 81.421 ± 0.031 GeV and 81.420 ± 0.025 GeV for the electron and muon channel respectively.

The same method was used to obtain the m_{jj} with real data. In this case, the fit function was the same but the correlation among some parameters was set to follow that found in the MC (Appendix J). The m_{jj} fitted distribution for real data can be seen in Figure 5.12. The mass values extracted from the fit to data were: 82.12 ± 0.22 GeV and 81.81 ± 0.17 GeV for electron and muon channel respectively.

In order to match the real data and the MC jet energy scales, one should refer the m_{jj} values to the same target. The natural choice is the M_W^{PDG} [130]. Thus the global $\alpha_{\text{JSF}} = M_W^{PDG}/m_{jj}$ factor was introduced. In

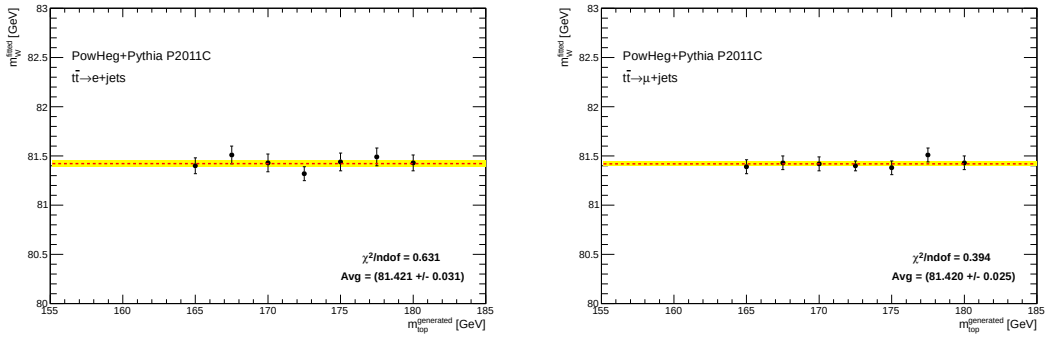

Figure 5.11: Invariant mass of the W jet pair candidate (m_W^{fitted}) versus $m_{\text{top}}^{\text{generated}}$ for the e+jets (left) and μ+jets (right) channels.

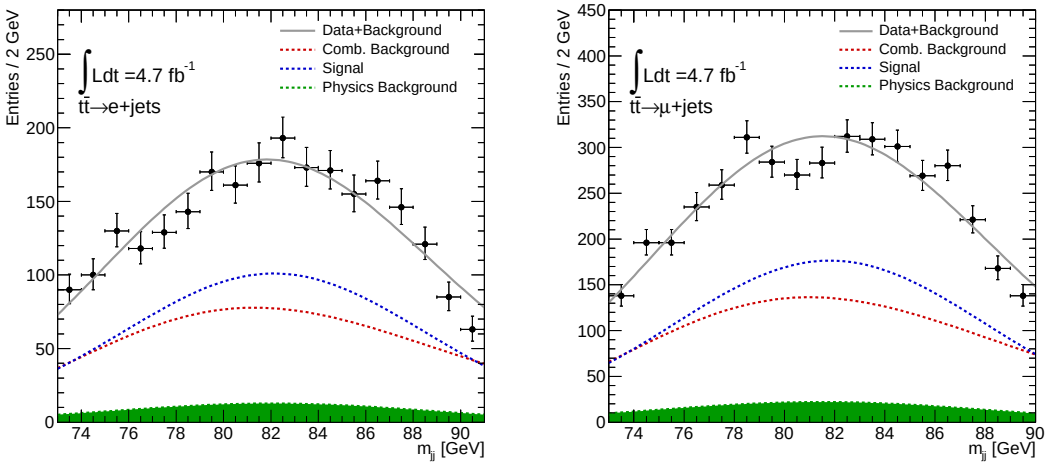

Figure 5.12: Invariant mass of the fitted hadronically decaying W candidate for the e+jets (left) and μ+jets (right) channels. The black points corresponds to the data and the green, red, and blue lines represent the contributions of the physics background, combinatorial background and signal to the final fit (gray line).

a first pass of the analysis, α_{JSF} was computed using the entire sample. Then, in a second pass, that α_{JSF} was subsequently applied to scale the energy of all jets.

The obtained α_{JSF} values in real data and MC are summarized in Table 5.3. The uncertainty on $\alpha_{\text{JSF}}^{\text{MC}}/\alpha_{\text{JSF}}^{\text{data}}$ turns up irremediably as an error on m_{top}. This error will be labelled as the error due to the JSF.

5.5.2 Neutrino p_z and $E_{\text{T}}^{\text{miss}}$

In order to reconstruct the leptonically W boson the p_z^{ν} has to be estimated. The basics math behind the determination of the neutrino p_z can be found in Appendix K. The key ingredient is that the invariant

channel	MC	Real data	$\alpha_{\rm JSF}^{\rm MC}/\alpha_{\rm JSF}^{\rm data}$
e+jets	0.9875 ± 0.0005	0.9791 ± 0.0026	1.009± 0.003
μ+jets	0.9875 ± 0.0004	0.9926 ± 0.0021	1.005± 0.002

Table 5.3: Values of $\alpha_{\rm JSF}$ obtained in each analysis channel (e+jets and μ+jets) and for real data and MC samples. The last column shows the MC to data ratio.

mass of the lepton and neutrino should match M_W^{PDG}. In general this will provide two solutions for p_z^ν. However, it is found that about 35% of the events have complex solutions for the p_z^ν values instead. In order to avoid that problem, a rescaling of the $E_{\rm T}^{\rm miss}$ is then requested. The minimal $E_{\rm T}^{\rm miss}$ rescaling is applied in order to allow a valid p_z^ν.

The performance of the $E_{\rm T}^{\rm miss}$ rescaling has been evaluated in MC by comparing the new computed $E_{\rm T}^{\rm miss}$ with the true $p_{\rm T}^\nu$ of the neutrino stemming from the $W \to \ell\nu$ decay. Figure 5.13 presents the reconstructed $E_{\rm T}^{\rm miss}/p_{\rm T}^{\nu\ \rm true}$ distributions in the e + jets channel for two situations:

- Left: for those events where no rescaling of $E_{\rm T}^{\rm miss}$ is needed (therefore the straight reconstructed[4] $E_{\rm T}^{\rm miss}$ is used).
- Right: for those events where it is necessary to rescale $E_{\rm T}^{\rm miss}$ (and the rescaled $E_{\rm T}^{\rm miss}$ is used). The performance for the same events before the rescaling can be seen in Appendix K where an overestimation of the reconstructed p_T^ν is clearly visible.

As one can see, in both cases the $E_{\rm T}^{\rm miss}/p_{\rm T}^{\nu\ \rm true}$ peaks at 1. Moreover, both cases exhibit a nice $E_{\rm T}^{\rm miss}$ vs $p_{\rm T}^{\nu\ \rm true}$ correlation, even when the rescaled $E_{\rm T}^{\rm miss}$ is below the 30 GeV selection cut (Fig. 5.13 bottom right).

From this study one can conclude that whenever a rescaling is needed and then applied, the new $E_{\rm T}^{\rm miss}$ has a quality as good as the directly reconstructed $E_{\rm T}^{\rm miss}$ (of those events without rescaling need) with the benefit that rescaling the $E_{\rm T}^{\rm miss}$ enables the p_z^ν to be estimated for all events.

5.5.3 b-tagged jet selection

The current implementation of the analysis imposes tighter requirements on the b-tagged jets to enter the analysis (with respect to the selection cuts given in section 5.4). These are the following:

- Exactly two b-tagged jets (although this was already imposed in section 5.5.1).
- b-tagged jet with $p_{\rm T} \geqslant 30$ GeV.

5.5.4 b-tagged jet to W matching and choosing a p_z^ν solution

Now, in order to decide which of the p_z^ν available solutions to use as initial value for the kinematic fit, one has to look as well to which b-tagged jet is matched with either the hadronic or leptonic W decay.

[4]Of course, there is no such a thing like the reconstructed $E_{\rm T}^{\rm miss}$. This is an abuse of language to simplify the notation. The computation of the $E_{\rm T}^{\rm miss}$ was explained in Section 3.3.

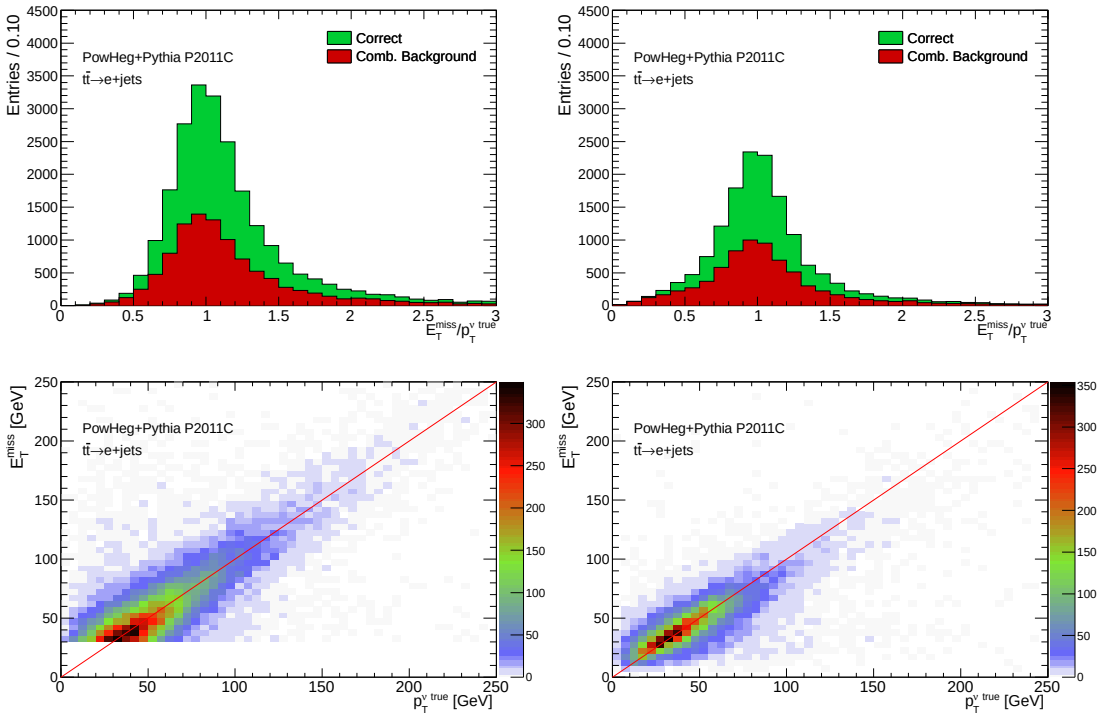

Figure 5.13: $E_{\mathrm{T}}^{\mathrm{miss}}$ related distributions in the MC $t\bar{t} \rightarrow e +$ jets events. Upper row: reconstructed $E_{\mathrm{T}}^{\mathrm{miss}}/p_{\mathrm{T}}^{\nu\ \mathrm{true}}$ for those cases where a valid p_z^{ν} is found (left) and for those cases where $E_{\mathrm{T}}^{\mathrm{miss}}$ was rescaled to obtain at least one p_z^{ν} solution (right). Bottom row: correlation plot between $E_{\mathrm{T}}^{\mathrm{miss}}$ and $p_{\mathrm{T}}^{\nu\ \mathrm{true}}$ for the same cases as above.

There are four possible combinations (2 b-tagged jets $\times$ 2 p_z^{ν} solutions). The used p_z^{ν} solution will regulate the four-momentum of the leptonically decaying W. Moreover, whatever b-tagged jet association to the W's will lead to different raw four-momenta of the triplets representing the top-quarks:

- hadronic part: $p_{\mathrm{top}}^{\mathrm{had}} = p_{jb}^{\mathrm{had}} + p_W^{\mathrm{had}}$ (with $p_W^{\mathrm{had}} = p_{j1} + p_{j2}$).
- leptonic part: $p_{\mathrm{top}}^{\mathrm{lep}} = p_{jb}^{\mathrm{lep}} + p_W^{\mathrm{lep}}$ (with $p_W^{\mathrm{lep}} = p_\ell + p_\nu$).

where p_{jb}^{had} and p_{jb}^{lep} represent the four-momenta of the b-tagged jet associated respectively to the hadronic or leptonic decaying W.

In order to decide which of the four combinations is to be used for the Globalχ^2 fit, the following variable is built and computed for every combination:

$$\varepsilon = |m_t^{\mathrm{had}} - m_t^{\mathrm{lep}}| + 10\left(\sum \Delta R^{\mathrm{had}} + \sum \Delta R^{\mathrm{lep}}\right) \tag{5.2}$$

In this expression m_t^{had} and m_t^{lep} designate the invariant masses of the hadronic and leptonic part of the event (computed from $p_{\mathrm{top}}^{\mathrm{had}}$ and $p_{\mathrm{top}}^{\mathrm{lep}}$ under test). The $\sum \Delta R^{\mathrm{had}}$ and $\sum \Delta R^{\mathrm{lep}}$ terms denote the sum of the distances between all the objects in the same triplet (hadronic: p_{jb}^{had}, p_{j1} and p_{j2}) and (leptonic: p_{jb}^{lep}, p_ℓ and p_ν). The combination providing the lowest ε was afterwards retained for the analysis.

Note that after this stage the fraction of $t\bar{t}$ events with correct matching of both, $W \to qq$ to light jets and the b-tagged jets to the hadronically and leptonically decaying W's, was found to be ≈54%.

Figure 5.14 shows the correlation between the used p_z^ν and its true value (as in MC). Figure 5.14 left exhibits a faint band where the correlation is lost. This is due to those events where the used p_z^ν does not match the true one. Several causes can lead to that: presence of other neutrinos in the event (from B baryons and mesons decays), inaccurate $E_{\mathrm{T}}^{\mathrm{miss}}$, etc. Reference [131] gives further details on how the different contributions to the $E_{\mathrm{T}}^{\mathrm{miss}}$ have an impact in the reconstructed transverse mass of the $W \to \ell\nu$ decays.

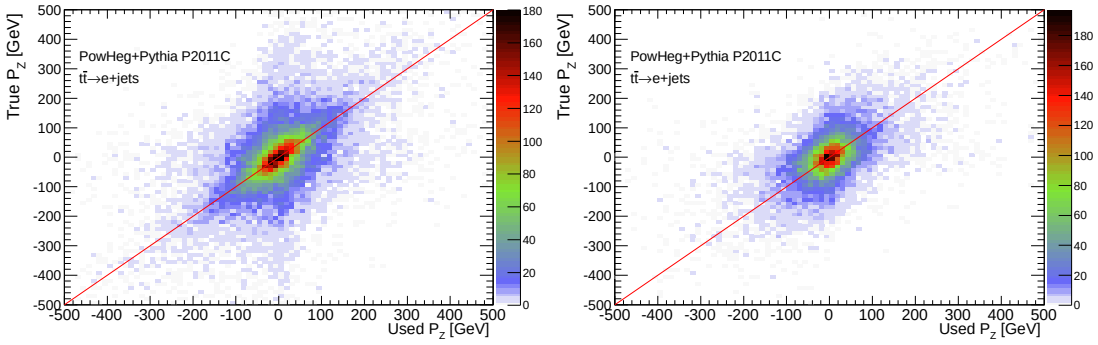

Figure 5.14: MC study of the p_z^ν in the e+jets channel. Correlation found between the computed p_z^ν and the true value. Left: For those cases with 2 p_z^ν solutions. Right: For those cases where $E_{\mathrm{T}}^{\mathrm{miss}}$ was rescaled to find at least one p_z^ν solution.

Reached this point, all the top-quark decay objects have been already selected. Figure 5.15 displays the distributions of the p_{T} and the E of the $t\bar{t}$ system for those events that will enter the top-quark mass fit. These figures show that there is a good data vs MC agreement for observables involving all objects selected with the event kinematics reconstruction.

5.6 Globalχ^2 fit for $t\bar{t}$ events in the ℓ + jets channel

The fitting technique to extract the top-quark mass for each event uses the Globalχ^2 method. The approach has been successfully used for the alignment of the ATLAS Inner Detector tracking system (presented in Chapter 4). The mathematical formalism adapted for the top-quark mass is shown in Appendix L.

As commented before, the Globalχ^2 is a least squares method with two nested fits. Equally than in other fitting procedures, one needs to define observables that depend on the fit parameters and which their values can be confronted with the measured ones. This defines the residuals (in the track-and-alignment fitting jargon) to be minimized. The uncertainty of each observable is then used in the covariance matrix. Both, residuals and uncertainties, will be explained in Section 5.6.1 and 5.6.2 respectively.

The full kinematics of the event will be determined once m_{top} and p_z^ν are known (plus of course all the jet and lepton energy measurements). Therefore those are the fit parameters: p_z^ν acts as local parameter (in the inner fit of the Globalχ^2) and m_{top} as global parameter. The initial values of the fit parameters are

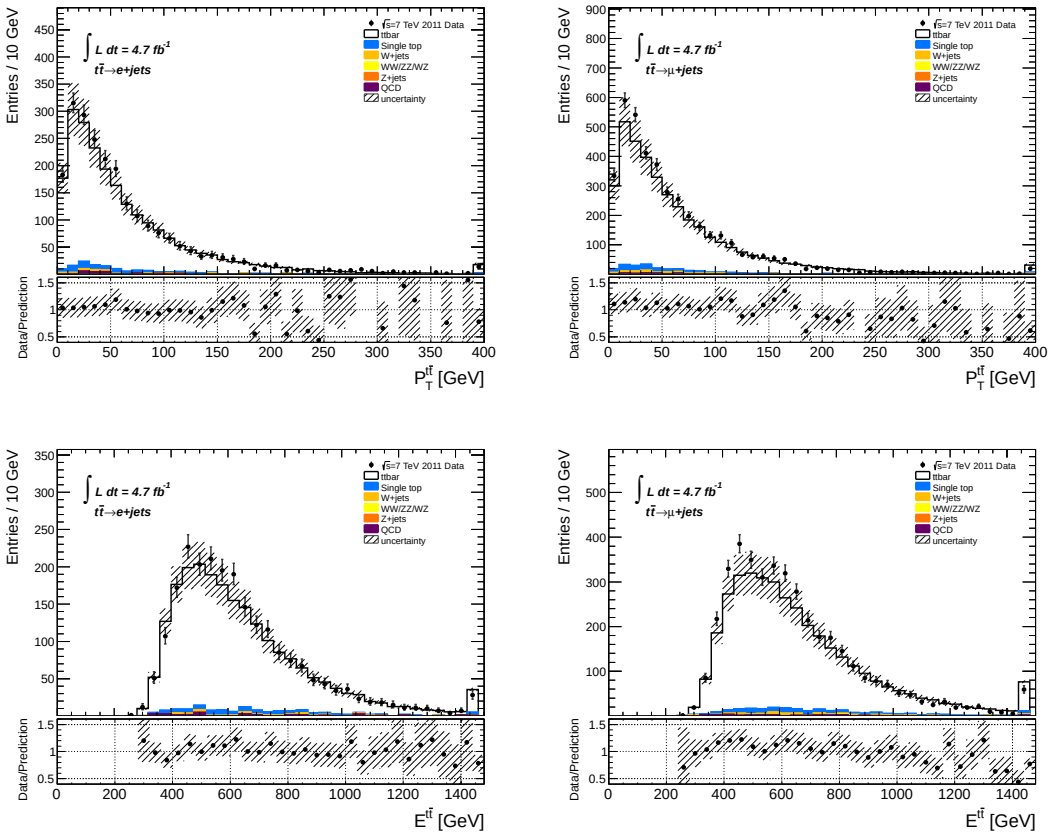

Figure 5.15: Data vs MC comparison of some relevant properties for the events satisfying all the selection requirements to enter the Globalχ^2 fit. Upper row shows the p_T of the $t\bar{t}$ system. Bottom row shows the E of the $t\bar{t}$ system. Left (right) hand plots display those distributions for the events selected in the e + jets (μ + jets) channel.

taken as follows:

- p_z^ν takes the value as explained in section 5.5.4.
- m_{top} is initialized with a value of 175 GeV.

5.6.1 Observables definition for the Globalχ^2 fit

In the current fit implementation, the used observables exploit the rest frame information of each top-quark in the event in two different ways:

- First, in the top-quark rest frame, the kinematics of the $t \rightarrow Wb$ is that of a two-body decay. In that rest frame, the energy and momentum of the W and b quark depend just on: m_W, m_b and, of course,

m_{top} (which is among the fit parameters). The four-momenta of the W boson and b-jet, initially given in the top-quark rest frame are afterwards boosted to the lab frame. It is in this latter frame where the comparison between the measured observables and their expectations are done.

- Second, the momentum conservation law imposes that in the top-quark rest frame, the net momentum of the decay products must be null. Therefore the reconstructed objects (light-jets, b-jets, lepton and neutrino[5]) are boosted to their corresponding top-quark rest frame (using the test m_{top} value as hypothesis). In the rest frame of each top-quark, a check is performed to verify that the sum of their momenta is null (Figure 5.16).

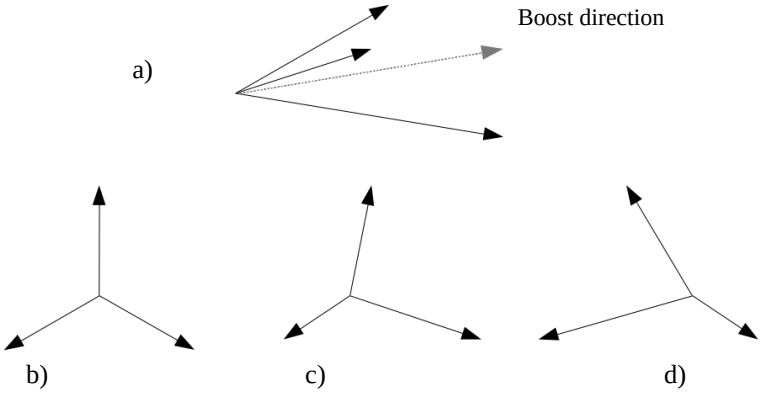

Figure 5.16: Example of boosting three jets to a common rest frame. a) The three jets are reconstructed in the lab frame. The boost direction is obtained from the sum of the three jets four momenta. b), c) and d) depict the three jets after the attempt of boosting them to the common rest frame. b) The boost is correct and the sum of the momenta of the 3 jets is null. c) The boost was too short and there is a net component of the momentum in the boost direction. d) The boost was too large and there is a net component of the momentum in the opposite direction.

In what follows, for those observables in which a boost of a four-momentum vector must be performed, the boost is conducted along the flying direction of the reconstructed top-quark to which the object belongs. In order to estimate the boost magnitude to be used during the fit procedure, bearing in mind that m_{top} is a fit parameter, the following protocol is adopted:

- the four-momentum of the top quark is computed from the reconstructed four-momenta of the objects in the triplet.
- the energy and direction of the reconstructed top are preserved.
- the hypothesis is made that the m_{top} takes the value under test.

List of observables

The observables used by the Globalχ^2 fit (which act as residual vector, $\boldsymbol{r}$, in Equation L.1) are detailed below and summarized in Table 5.4.

[5]Just to remind that the ν four-momentum is built assuming it is the responsible of the $E_{\text{T}}^{\text{miss}}$ in the event and its p_z is computed according to prescriptions given in section 5.5.2.

1. **Invariant mass of the leptonically decaying W.**
   This term acts as constraint for the p_z^ν. The neutrino four-momentum is built from the $E_{\mathrm{T}}^{\mathrm{miss}}$, its direction ($\phi_{E_{\mathrm{T}}^{\mathrm{miss}}}$) and the initial p_z^ν: $p_\nu = (E_{\mathrm{T}}^{\mathrm{miss}} \cos\phi_{E_{\mathrm{T}}^{\mathrm{miss}}}, E_{\mathrm{T}}^{\mathrm{miss}} \sin\phi_{E_{\mathrm{T}}^{\mathrm{miss}}}, p_z^\nu, 0)$ (neglecting the tiny neutrino mass). The four-momentum of the leptonically decaying W is thus: $p_{W_\ell} = p_\ell + p_\nu$. Obviously, its invariant mass is just $m^2_{W_\ell} = (p_\ell + p_\nu)^2$. This residual is defined as:

$$r_1 = m_{W_\ell} - M_W^{PDG} \tag{5.3}$$

2. **Energy of the hadronicaly decaying W.**
   First, the W four-momentum vector is built in the top-quark rest frame. Its energy and momentum are taken in accordance with those from the two body decay of an object with a mass of m_{top} (test value). Then, the computed four-momentum of the W is boosted to the lab frame. The resulting energy ($E_{W_h}^{\mathrm{test}}$) is compared with the reconstructed one ($E_{W_h}^{\mathrm{reco}}$) from the pair of the selected light jets (section 5.5.1):

$$r_2 = E_{W_h}^{\mathrm{reco}} - E_{W_h}^{\mathrm{test}} \tag{5.4}$$

3. **Energy of the leptonically decaying W.**
   In order to compute this residual, the same procedure as for the hadronically decaying W is followed. Only this time: $p_{W_l} = p_\ell + p_\nu$. Therefore this residual depends on both fit parameters: m_{top} and p_z^ν. The four-momentum built in the top-quark rest frame is boosted to the lab frame. The comparison is made between the W computed energy ($E_{W_\ell}^{\mathrm{test}}$) and its reconstructed one ($E_{W_\ell}^{\mathrm{reco}}$):

$$r_3 = E_{W_\ell}^{\mathrm{reco}} - E_{W_\ell}^{\mathrm{test}} \tag{5.5}$$

4. **Energy of the b-jet in the hadronic part.**
   This residual is computed in a similar manner, but now the b-tagged jet associated to the hadronically decaying W is handled. The four-momentum of the jet in the top quark rest frame acquires the energy and momentum in accordance with the two body decay expressions with m_{top} as hypothesis. Then the resulting four momentum is boosted to the lab frame, where its energy ($E_{b_h}^{\mathrm{test}}$) is compared with the reconstructed one ($E_{b_h}^{\mathrm{reco}}$):

$$r_4 = E_{b_h}^{\mathrm{reco}} - E_{b_h}^{\mathrm{test}}$$

5. **Energy of the b-jet in the leptonic part.**
   Exactly the same procedure as above is repeated for the b-tagged jet associated to the leptonically decaying W. Its computed energy ($E_{b_\ell}^{\mathrm{test}}$) is confronted with its reconstructed one ($E_{b_\ell}^{\mathrm{reco}}$):

$$r_5 = E_{b_\ell}^{\mathrm{reco}} - E_{b_\ell}^{\mathrm{test}} \tag{5.6}$$

6. **Sum of the momenta in the rest frame of the objects in the hadronic part.**
   The four-momenta of the reconstructed objets in the hadronic triplet: light-quark jets (from the hadronically decaying W) plus their associated b-tagged jet (p_{j_1}, p_{j_2} and p_{b_h} respectively) are boosted to the top-quark rest frame ($p^\star_{j_1}$, $p^\star_{j_2}$ and $p^\star_{b_h}$). In this frame, if the boost factor (which depends on the m_{top} under test) were right, one would expect that the sum of their boosted momenta ($\vec{p}^{\,\star}_{j_1}$, $\vec{p}^{\,\star}_{j_2}$ and $\vec{p}^{\,\star}_{b_h}$) to be null. The quantity to minimize is then $\left|\vec{p}^{\,\star}_{j_1} + \vec{p}^{\,\star}_{j_2} + \vec{p}^{\,\star}_{b_h}\right|$. Still, there is the sign to be defined. The sign is defined according to the angle between the resulting momentum vector $\vec{p}^{\,\star}_{\mathrm{had}} = \vec{p}^{\,\star}_{j_1} + \vec{p}^{\,\star}_{j_2} + \vec{p}^{\,\star}_{b_h}$ and the boost direction (Fig 5.16).

$$r_6 = \cos\left(\mathrm{angle}(\vec{p}^{\,\star}_{\mathrm{had}},\ \vec{p}^{\,\mathrm{had}}_{\mathrm{top}})\right)\left|\vec{p}^{\,\star}_{j_1} + \vec{p}^{\,\star}_{j_2} + \vec{p}^{\,\star}_{b_h}\right| \tag{5.7}$$

7. **Sum of the momenta in the rest frame of the objects in the leptonic part.**
   An analogue test to the above one is performed with the leptonic triplet of the event. Now, the lepton, the neutrino and their associated *b*-tagged jet are used. Their reconstructed four momenta are boosted to the top-quark rest frame. This time the boost factor depends on m_{top} and p_z^ν. The sum of their momenta in the top-quark rest frame ($\vec{p}^{\,\star}_{\text{lep}} = \vec{p}^{\,\star}_{\ell} + \vec{p}^{\,\star}_{\nu} + \vec{p}^{\,\star}_{b_l}$) is then computed. Its sign is defined in a similar manner with respect to the boost direction:

$$r_7 = \cos\left(\text{angle}(\vec{p}^{\,\star}_{\text{lep}},\ \vec{p}^{\,\text{lep}}_{\text{top}})\right)\left|\vec{p}^{\,\star}_{\ell} + \vec{p}^{\,\star}_{\nu} + \vec{p}^{\,\star}_{b_\ell}\right| \tag{5.8}$$

Table 5.4: List of residuals, their uncertainties and their dependence on the two fit parameters.

Residual	Expresion	Uncertainty	p_z^ν	m_{top}
r_1	$m_{W_\ell} - M_W^{PDG}$	$\sigma_{E_\ell} \oplus \sigma_{E_{\text{T}}^{\text{miss}}} \oplus \Gamma_W^{\text{PDG}}$	$\surd$	
r_2	$E_{W_h}^{\text{reco}} - E_{W_h}^{\text{test}}$	$\sigma_{E_{j_1}} \oplus \sigma_{E_{j_2}}$		$\surd$
r_3	$E_{W_l}^{\text{reco}} - E_{W_l}^{\text{test}}$	$\sigma_{E_\ell} \oplus \sigma_{E_{\text{T}}^{\text{miss}}}$	$\surd$	$\surd$
r_4	$E_{b_h}^{\text{reco}} - E_{b_h}^{\text{test}}$	$\sigma_{E_{j_b}^{\text{had}}}$		$\surd$
r_5	$E_{b_l}^{\text{reco}} - E_{b_l}^{\text{test}}$	$\sigma_{E_{j_b}^{\text{lep}}}$	$\surd$	$\surd$
r_6	$\cos\left(\text{angle}(\vec{p}^{\,\star}_{\text{had}},\ \vec{p}_{\text{top}})\right)\left\vert\vec{p}^{\,\star}_{j_1} + \vec{p}^{\,\star}_{j_2} + \vec{p}^{\,\star}_{b_h}\right\vert$	$\sigma_{E_{j_1}} \oplus \sigma_{E_{j_2}} \oplus \sigma_{E_{j_b}^{\text{had}}}$		$\surd$
r_7	$\cos\left(\text{angle}(\vec{p}^{\,\star}_{\text{lep}},\ \vec{p}_{\text{top}})\right)\left\vert\vec{p}^{\,\star}_{\ell} + \vec{p}^{\,\star}_{\nu} + \vec{p}^{\,\star}_{b_\ell}\right\vert$	$\sigma_{E_\ell} \oplus \sigma_{E_{\text{T}}^{\text{miss}}} \oplus \sigma_{E_{j_b}^{\text{lep}}}$	$\surd$	$\surd$

5.6.2 Globalχ^2 residual uncertainties

The uncertainties of the residuals must be fed to the fitting algorithm. These fill the covariance matrix used in the χ^2 (Equation L.1). The residual uncertainties are obviously derived from the corresponding uncertainties of the measured (reconstructed) observables. When several of them need to be accounted together, these are just added quadratically. Whenever the lepton uncertainty had to be combined with other jets or E_T^{miss} uncertainty, the lepton one was not consider since it is negligible compared with the others.

The uncertainties that were introduced in the diagonal elements of the covariance matrix are detailed in Table 5.4. As the uncertainties of each of the reconstructed object varies from one event to another, the covariance matrix was computed in an event by event basis.

The possible correlation between the observables may be also introduced in the covariance matrix as off-diagonal elements. Though the Globalχ^2 fitting technique computes itself the correlations of those observables affected by the inner (local) fit. Still the possibility that some of the observables that depend only on m_{top} were correlated. The size of the possible correlations were studied by means of a toy MC test where the kinematics of the $t \to Wb$ decay was reproduced. The conclusions of the toy MC test were:

- the sum of the momenta in the rest frame of the objects in the hadronic (leptonic) part had a -0.13 correlation with the energy of the hadronic (leptonic) W.
- The same residual had a -0.09 correlation with the energy of the associated *b*-tagged jet.
- No correlation was present between the residuals of the hadronic and leptonic triplet.

Moreover, as in the ideal case (when m_{top} takes its true value, and there are no reconstruction errors) the correlations are null, no off-diagonal terms were introduced in the Globalχ^2 covariance matrix.

5.6.3 Globalχ^2 fit results

The Globalχ^2 kinematic fit was applied on all the real data and MC events that satisfied the whole set of selection criteria. In each iteration, the inner fit computes p_z^ν, as it depends on the m_{top}. Its result (p_z^ν value as well as all the derivatives and correlations matrices) are fed to the outer fit, which computes m_{top}. After the Globalχ^2 fit, a final event selection was applied to reject those events where the fit did not convege or it was poor ($\chi^2 > 20$). The final event statistics is given in Table 5.5, which already reflects this last selection cut. Notice that at this point, the background has been reduced considerably, representing now the 5.5% for the e+jets channel and 4.7% for the μ+jets channel.

Process	e+jets	μ+jets
$t\bar{t}$ signal	1540 ± 210	2530 ± 350
Single top	45.4 ± 6.3	78 ± 11
WW/ZZ/WZ	0.22 ± 0.09	0.46 ± 0.12
Z+jets	3.16 ± 0.67	2.51 ± 0.65
W+jets (data)	12.5 ± 4.4	23 ± 14
QCD (data)	24 ± 14	17.1 ± 8.9
Background	85 ± 16	120 ± 20
Signal+Background	1630 ± 210	2650 ± 350
Data	1656	2943

Table 5.5: Event statistics satisfying the full selection and corresponding to the entire 2011 sample at 7 TeV (4.7 fb^{-1}). Expected figures are given from MC expectations for signal events and physics backgrounds. The number of the selected real data events is also provided.

The distributions of the two fitted parameters (p_z^ν and m_{top}) are displayed in Figures 5.17 and 5.18 respectively. In those figures, the real data outcome of the Globalχ^2 fit of the event kinematics is compared with the SM expectation.

A reasonable data-MC agreement is seen for both parameters[6]: p_z^ν and m_{top}. Likewise, the resulting distributions of those parameters agree well in both channels (e + jets and μ + jets). That being the case, and for the sake of accumulating as much statistics as possible, the outcome of both channels has been added together in one single distribution. The joint distributions are also presented in previous figures.

5.7 Extracting m_{top} with a template fit

As explained in previous Section, for each event entering the Globalχ^2 fit, the fit returns values for p_z^ν and m_{top}. The distribution of each of the observables has contributions from the distinct type of events: correct, combinatorial background and irreducible physics background events (all of them explained in Section 5.5).

[6] Although there is a small deficit of MC events in the μ + jets channel which could be introduced by the requirement of having exactly two b-tagged jets, Figure 5.6.

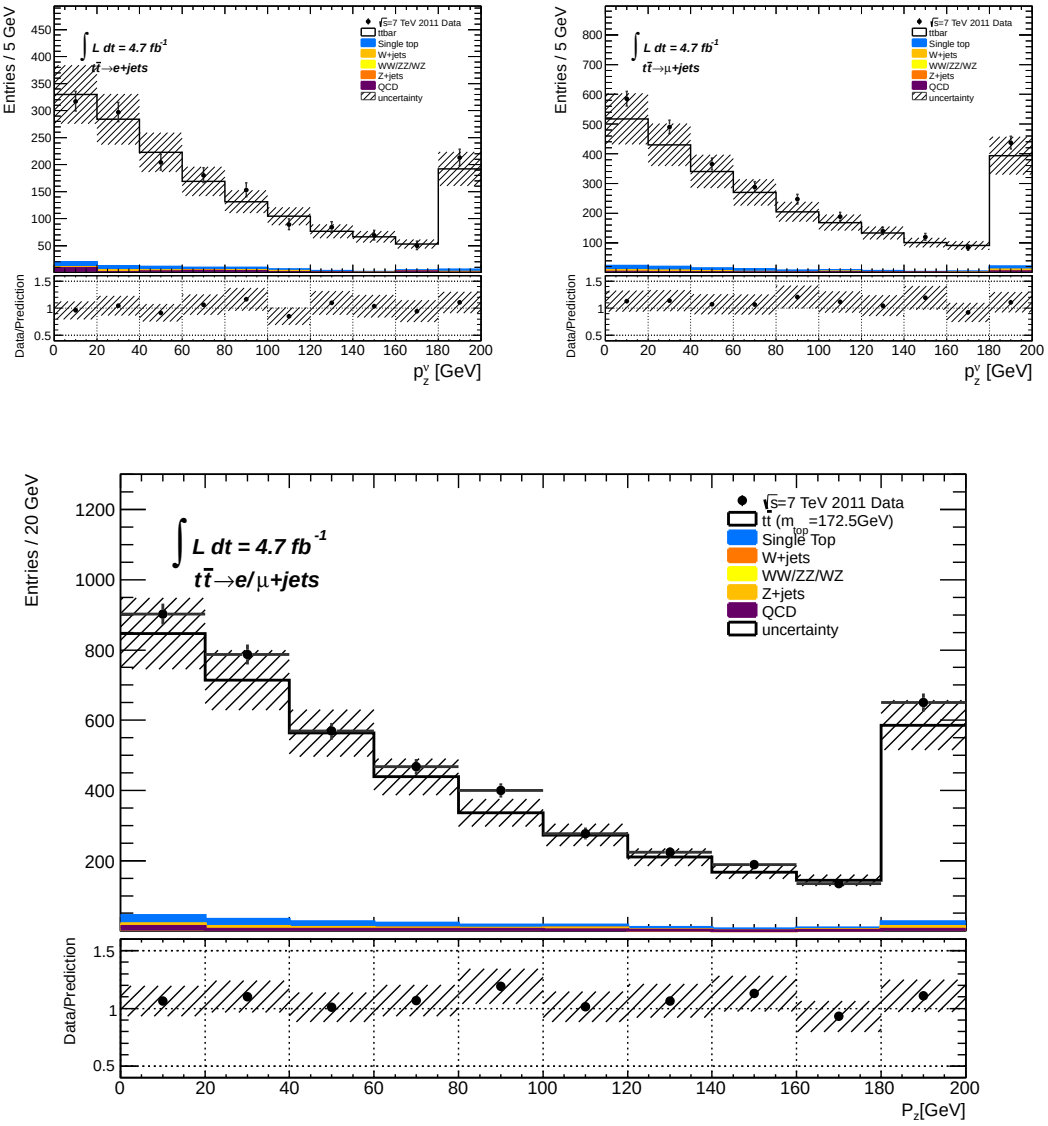

Figure 5.17: Distribution of the p_z^ν parameter after the Globalχ^2 fit. Real data is compared with the SM expectation (which includes the $t\bar{t} \to \ell$+jets signal and the sources of the irreducible background). Upper left: $t\bar{t} \to e$ + jets channel. Upper right: $t\bar{t} \to \mu$ + jets channel. Bottom plot: joined distribution for both analysis channels.

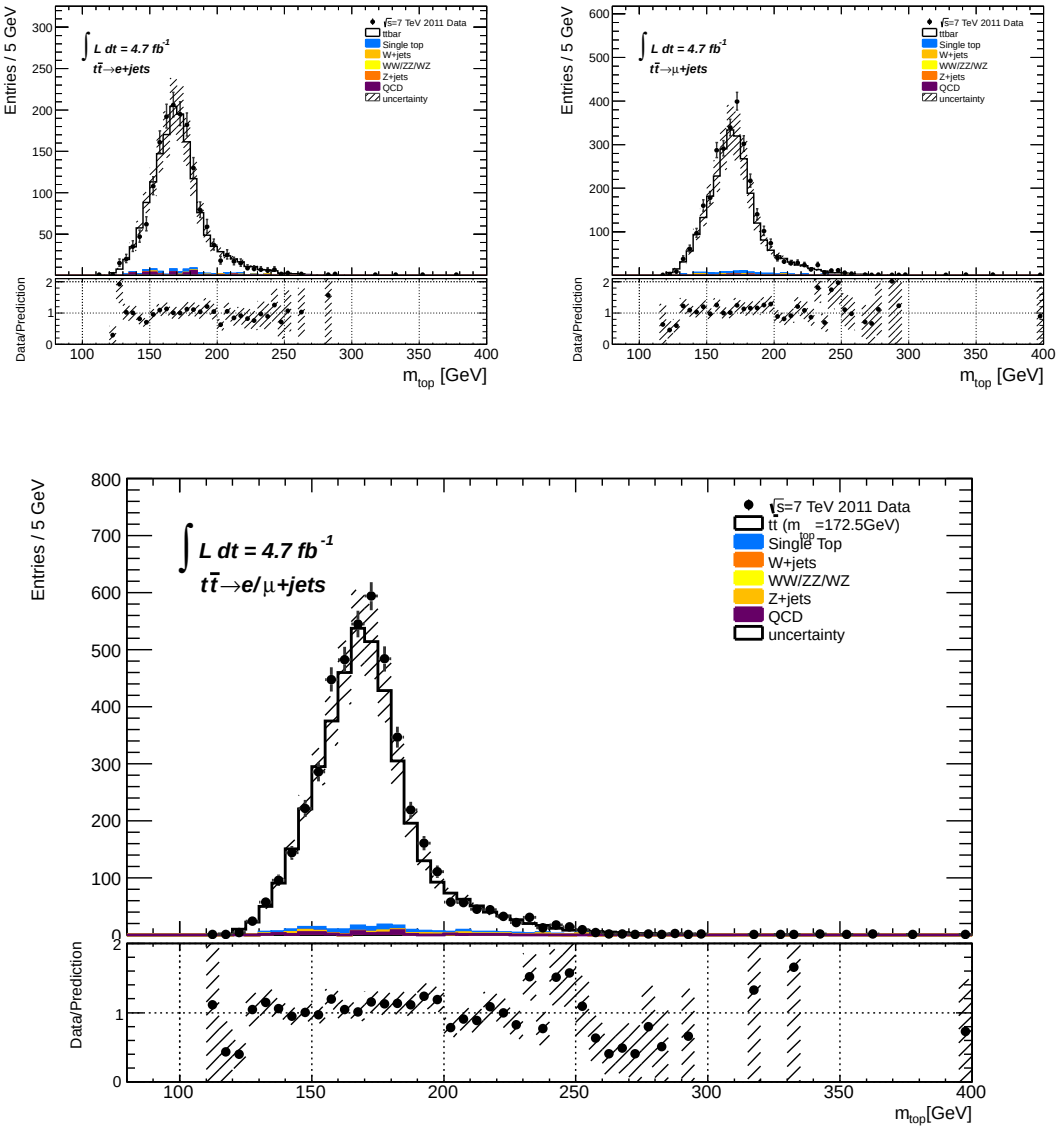

Figure 5.18: Distribution of the m_{top} parameter after the Globalχ^2 fit. Real data is compared with the SM expectation (which includes the $t\bar{t} \to \ell$ + jets signal and the sources of the irreducible background). The $t\bar{t}$ signal assumes a mass of 172.5 GeV. Upper left: $t\bar{t} \to e$ + jets channel. Upper right: $t\bar{t} \to \mu$ + jets channel. Bottom plot: joined distribution for both analysis channels.

5.7.1 Test with $t\bar{t}$ MC samples

Using the MC sample of $t\bar{t} \to \ell$ + jets it is possible to foresee the contribution of each type of events to the m_{top} distribution. Figure 5.19 presents the resulting m_{top} MC distributions for both analysis channels. As anteriorly mentioned, these distributions contain two event classes: correct combinations (in green) and combinatorial background (in red). Each category contributes in a different manner to the overall distribution.

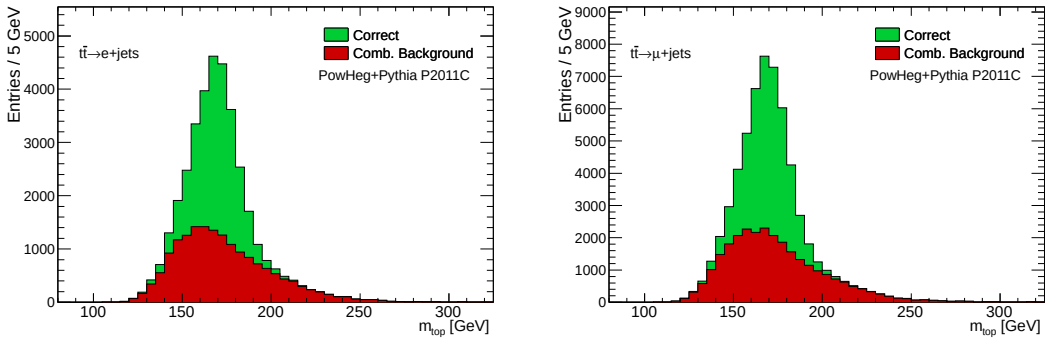

Figure 5.19: Distribution of the fitted m_{top} as it comes from the Globalχ^2 fit using $t\bar{t} \to e$ + jets (left) and $t\bar{t} \to \mu$ + jets (right) MC samples. The green area corresponds to the events with correct object association and the reddish area with the combinatorial background events.

The distribution of the correct combinations alone is displayed separately in Figure 5.20. It is worth noticing that the m_{top} input value of that MC sample was 172.5 GeV. As one can see, this distribution presents two important features:

- Although it looks nearly Gaussian, the tails are asymmetric (larger tail towards lower values).
- The distribution does not peak at nominal m_0=172.5 GeV. Instead it peaks at a lower mass value. Therefore the most probable value is not the nominal mass (as one would naively expect).

The description of this shape made here can be done as follow: the raw mass distribution has a maximum value (m_0) with an exponential tail (λ) towards lower values. In addition, the mass distribution is also subject to the detector resolution (σ) (convolution with a Gaussian) which casts its final shape.

These features are well modeled by the probability density function of the lower tail exponential with resolution model. The characteristics of this function are specified in Appendix M.

On the other hand, the shape of the combinatorial background event category can be well modeled by a Novosibirsk distribution (Apendix M). The Novosibirsk probability density function has the following parameters: μ (most probable value), σ (width) and Λ (tail).

Thereafter, fits of the m_{top} distribution in the MC $t\bar{t} \to \ell$ + jets are performed using the following model:

- a lower tail exponential distribution with resolution model, for the peaking part of the distribution (fed with the correct combinations, Figure 5.19),

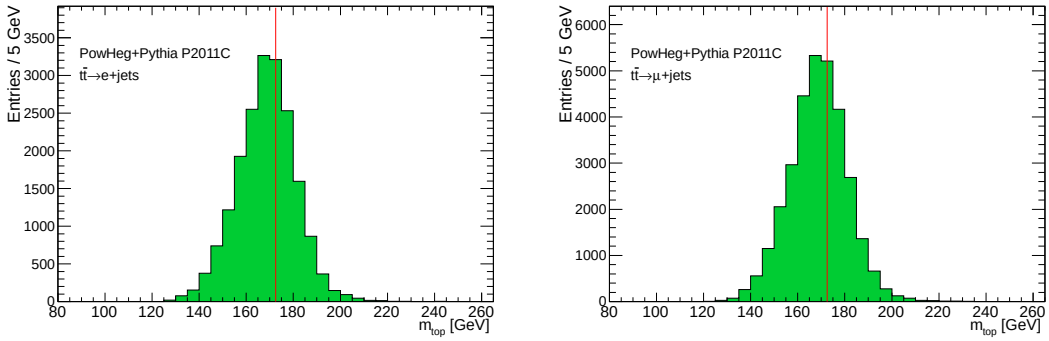

Figure 5.20: Distribution of the fitted m_{top} as it comes from the Globalχ^2 fit using $t\bar{t} \to e$ + jets (left) and $t\bar{t} \to \mu$ + jets (right) MC samples and only for the correct combinations. The red line highlights the nominal m_{top} value (172.5 GeV).

- plus a Novosibirsk distribution (which determines the contribution of the combinatorial background).

This distribution has in total 7 parameters to describe its full shape:

1. m_0 as the mass of the object being measured.
2. λ as the lower tail of the peak distribution.
3. σ as the experimental resolution on m_0.
4. μ_{bkg} as the most probable value of the combinatorial background.
5. σ_{bkg} as the width of the combinatorial background.
6. Λ_{bkg} as the parameter describing the combinatorial background tail.
7. ϵ as the fraction of the events entering the peaking distribution (correct combinations). Of course $1 - \epsilon$ is the fraction of combinatorial background events.

MC samples with different m_{top} values

Several MC samples were available that are identical except for the m_{top} value used in the event generator and its consequences. The set of masses used in the simulation was: 165, 167.5, 170, 172.5, 175, 177.5, and 180 GeV.

Corresponding top-quark mass distributions were obtained for each of the MC samples with varying m_{top} and apliying the same Globalχ^2 kinematic fit (described in Section 5.6). Those distributions were successfully fitted with the model given in the previous section and the values of the parameters of probability density function were extracted. Though in each fit, m_0 was fixed to the input m_{top}. This technique allowed to derive the dependence of each of the parameters with respect to the true m_{top} as depicted in

Figure 5.21 for the λ, σ, μ_{bkg}, σ_{bkg}, Λ_{bkg} and ϵ respectively. As it is seen in those figures all parameters exhibit a linear dependence with the true m_{top} (at least in the range under study).

One can express then each of the parameters of the distribution as a linear function of the m_0. For example, λ can be expressed as:

$$\lambda(m) = \lambda_{172.5} + \lambda_s \Delta m \tag{5.9}$$

with $\Delta m = m_0 - 172.5$ (in GeV) and $\lambda_{172.5}$ is the linear fit result of λ when $m_0 = 172.5$ GeV. λ_s is the resulting slope of the λ linear fit. The dependence with m_{top} of the rest of the parameters was formulated in a similar manner.

A template fit was then prepared, where the reconstructed top-quark mass distribution is confronted with the model given by the parametrization. The result will provide our measurement of m_{top}.

There are few important remarks:

- The σ of the resolution model still exhibits a linear dependence on m_{top} (Figure 5.21.b). Although this was expected, as larger m_{top} values will produce more energetic jets and their energy uncertainty is also bigger.

- Figure 5.21.c depicts the evolution of the combinatorial background most probable value (μ_{bkg}) with m_{top}. Actually some dependence of μ_{bkg} with m_{top} was naively expected, as the energy of the jets in those combinatorial background events depends on the input m_{top} value. So larger m_{top} will produce larger μ_{bkg}.

- The fraction of correct combinations (ϵ) and combinatorial background is almost independent of the input m_{top} (Figure 5.21.f.) In what follows this is assumed to be constant and equal to 54.6%.

Now, m_{top} can be determined by fitting the joined distribution (Figure 5.18). In this study, this is achieved by using the template method which uses the linear parametrization of all the parameters (except m_0) describing the m_{top} shape as given in section 5.7.1. This approach assumes that the MC describes well the dependence of the probability density function parameters with generated m_{top}. From now on, the results extracted using this method will be referred as *template* results.

5.7.2 Linearity test

The linearity of the template method with respect to the generated top-quark mass has been validated using pseudoexperiments. At each mass point 500 pseudoexperiments have been performed, each randomly filled using the content of the top-quark mass histogram for the nominal MC sample with the same number of entries. The physics background has not been included in this study as its distribution is independent of m_{top} (see Appendix N). The figure 5.22 (left) shows the difference between the fitted top-quark mass versus the generated top-quark mass (true value). It presents an average offset of (0.138±0.035) GeV. This offset will be later included in the calibration systematic uncertainty. The pull distributions are produced and fitted with a Gaussian. The width of the pull distribution as a function of the top-quark mass generated is shown in Figure 5.22 right. The average value is close to unity (1.001±0.016) which indicates a proper estimation of statistical uncertainty.

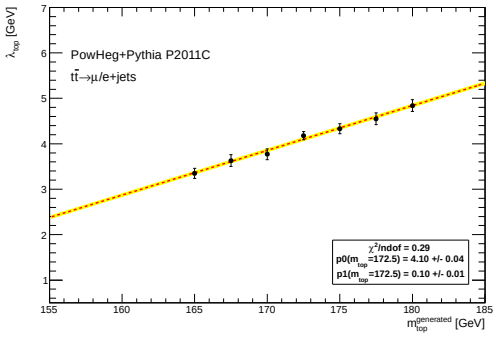

(a) λ fit parameter dependence.

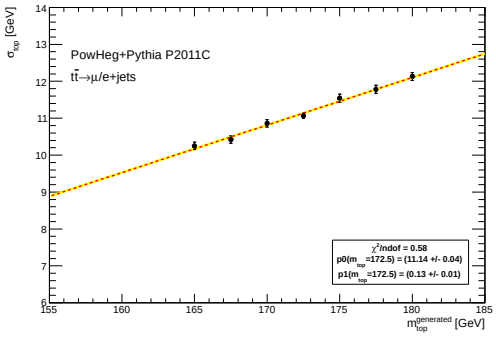

(b) σ (resolution) fit parameter dependence.

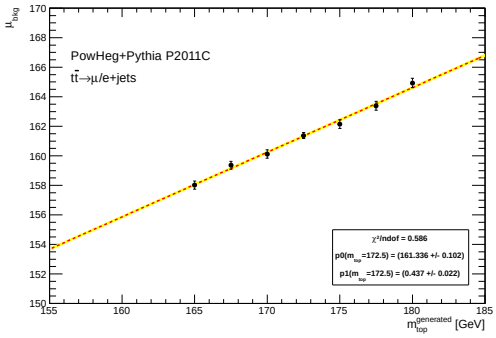

(c) μ_{bkg} (background mean) fit parameter dependence.

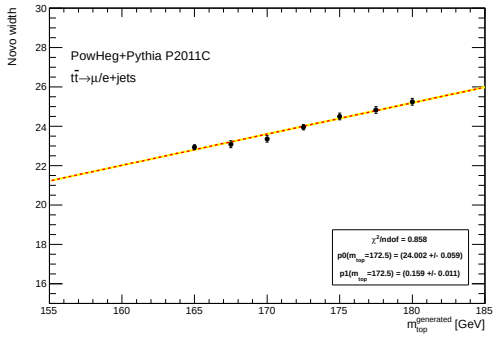

(d) σ_{bkg} (background width) fit parameter dependence.

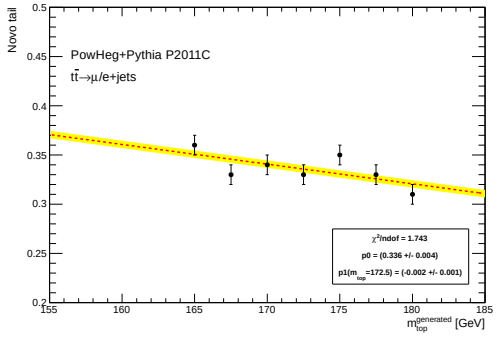

(e) Λ_{bkg} (background tail) fit parameter dependence.

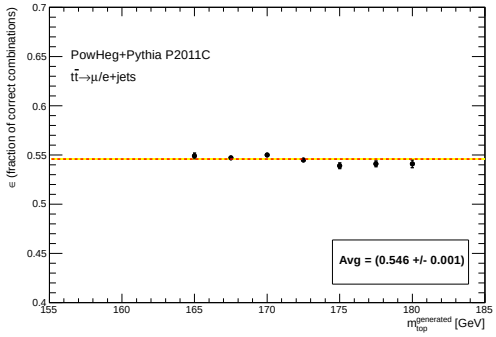

(f) ϵ (correct combinations fraction) dependence.

Figure 5.21: Dependence of each fit parameter versus the input m_{top} value for the combined channel (e + jets plus μ + jets).

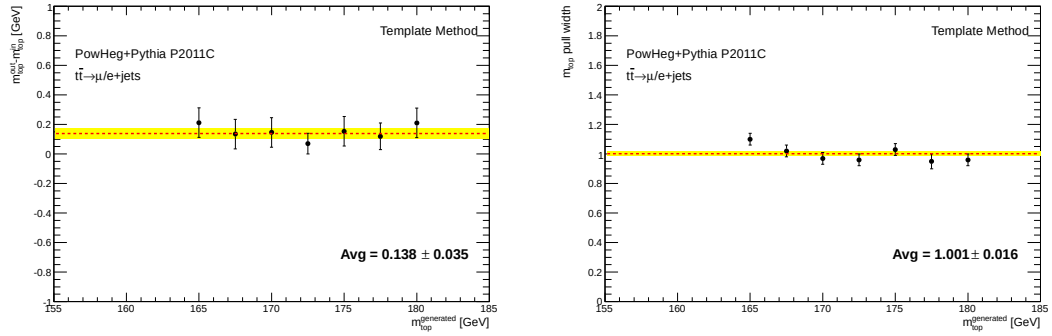

Figure 5.22: Left: difference between the fitted top-quark mass and the generated mass as a function of the true mass. Right: Width of the pull distribution as a function of the true top-quark mass.

5.7.3 Template fit results on real data

The template fitted distribution of the split and combined channels is presented in Figure 5.23. The extracted value of m_{top} using the real data gives:

$$m_{\text{top}} = 173.22 \pm 0.32\ (\text{stat.}) \pm 0.42\ (\text{JSF})\ \text{GeV}$$

the error quotes the statistics plus the associated to the jet scale factor (JSF) which comes from the $\alpha_{\text{JSF}}^{\text{MC}}/\alpha_{\text{JSF}}^{\text{data}}$ uncertainty (Table 5.3 in Section 5.5.1). The split m_{top} results by channel and also the rest of the parameters can be consulted in Table 5.6.

Parameter	ℓ + *jets*	e + *jets*	μ + *jets*
m_{top}	173.22 ± 0.32	173.44 ± 0.58	173.08 ± 0.48
σ (*GeV*)	11.23± 0.06	11.32 ± 0.10	11.16 ± 0.08
λ	4.17± 0.05	4.29 ± 0.09	4.07 ± 0.07
μ_{bkg} (*GeV*)	161.62±0.18	161.46 ± 0.33	161.74 ± 0.24
σ_{bkg} (*GeV*)	24.12± 0.08	24.17 ± 0.15	24.09 ± 0.11
Λ_{bkg}	0.33± 0.01	0.34 ± 0.01	0.33 ± 0.01

Table 5.6: Parameter values extracted in the template method fit. The fraction of combinatorial events has been fixed to 54.6% in all cases. The errors only account for the statistical uncertainty of the fit.

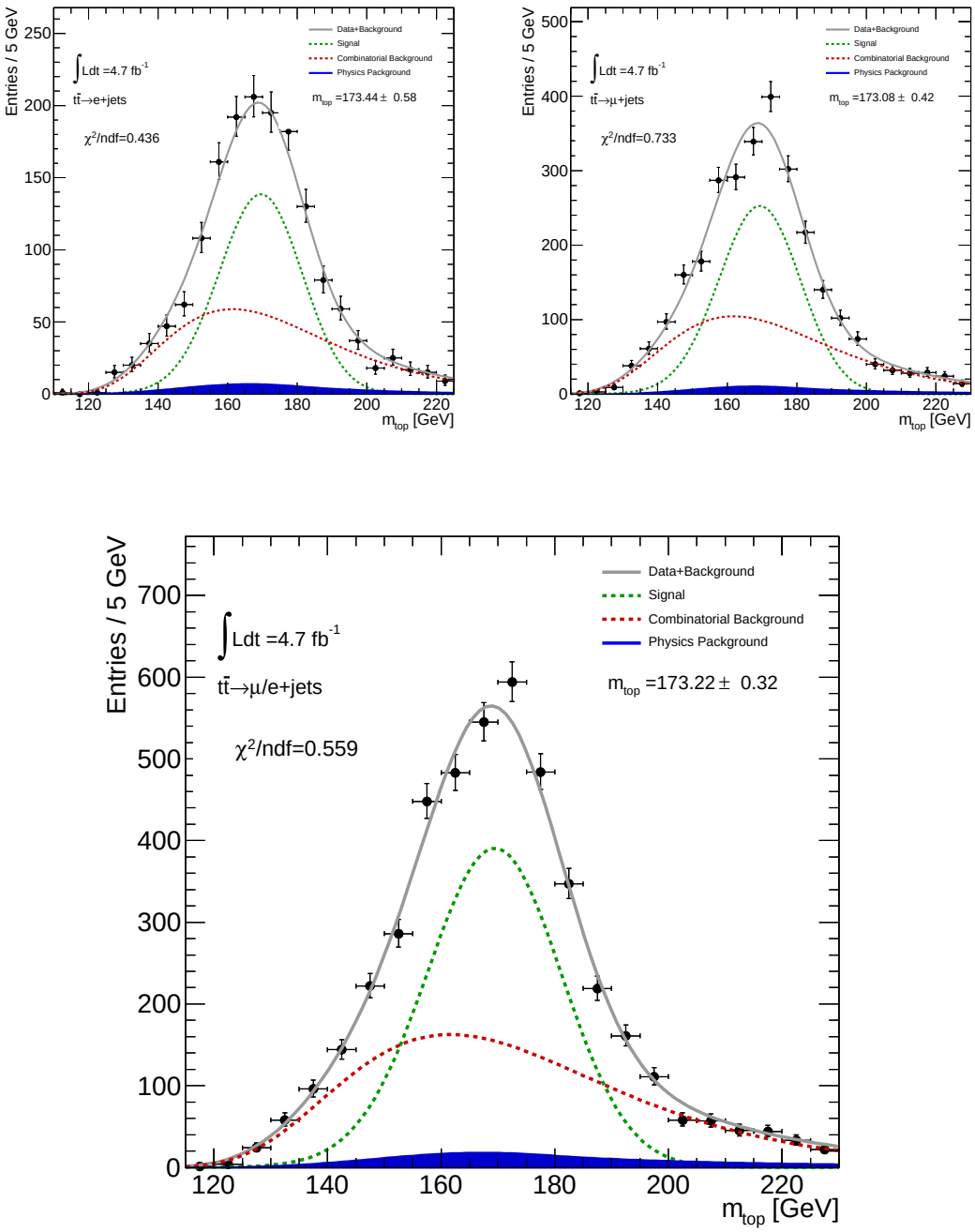

Figure 5.23: Distribution of the m_{top} parameter after the Globalχ^2 fit using the template method. Upper right presents the results in the e + jets channel and upper left in the μ + jets one. Bottom plot: the distributions of the e + jets and μ + jets are added together. The real data distribution has been fitted (drawn as a solid gray line) to a lower tail exponential distribution with resolution model (for the correct combinations, drawn as green dashed line) plus a Novosibisrk function (to account for the combinatorial background, drawn as a red dashed line). All the contributions to the irreducible physics background are added together (blue area).

5.8 Evaluation of systematic uncertainties on $m_{\mathbf{top}}$

This section discusses the systematic error sources considered in this analysis and how each of them has been evaluated. There are different procedures to compute the systematic uncertainties. Usually the quantities associated with the error source are varied ±1 standard deviation (σ) with respect to the default value. Nonetheless, there are some systematic variations, related with the generation process, that can not be figured out in this way. In such cases specific MC samples are required. More detailed information about the reconstruction packages and samples used to compute these uncertainties are summarized in Appendix G and F.

The full analysis has been repeated for each systematic variation: the event selection, JSF determination and Globalχ^2 fit. The JSF values obtained for each systematic error are reported in Table 5.7. Those systematic variations unconnected from the jet reconstruction have a JSF compatible with the one used in the main analysis. On the other hand, the systematic samples affected by the jet reconstruction present differences in the JSF (as expected).

Once the variation has been applied, 500 pseudo-experiments are performed using MC events. The final MC top-quark mass distribution is used to generate 500 compatible distribution within statistical errors. Then, the template fit is repeated. This produces 500 m_{top} values which in their turn are used to fill histogram of results. That histogram is fitted with a Gaussian function and its mean is taken as the top-quark mass systematic-source dependent value. Generally, the full m_{top} difference between the varied and default sample is quoted as the systematic uncertainty.

A brief description of each systematic error source considered in this analysis is given in the following:

Template method calibration: the precision of the template fits is limited by the available MC statistics. This is translated into an error in the probability density function of the fit parameters. This systematic also includes the shift of 0.138 GeV obtained in the linearity test (Figure 5.22).

MC Generator: this takes into account the choice of a specific generator program. The ATLAS MC $t\bar{t} \to \ell$ + jets samples have been produced alternatively with PowHeg [118] and MC@NLO [132] (both using the Herwig program to perform the hadronization), generated at m_{top}=172.5 GeV. These generators produce different jet multiplicity in the ℓ+jets channel [133]. Initially, the Alpgen generator program was also considered, nevertheless due to its poor agreement with data it was discarded. Figure 5.26(a) shows the obtained m_{top} distributions for PowHeg (black) and MC@NLO (red) MC generators. The systematic uncertainty is computed as the full difference between both m_{top} values.

Parton shower fragmentation (hadronization model): the MC generators make use of perturbative calculations either at LO or NLO. This produces just a limited number of particles (partons at this stage) in the final state. On the other hand, the detector registers several dozens of them. What happens in between is a non perturbative QCD process: the *hadronization*, where quarks and gluons form themselves into hadrons. Although this process modifies the outgoing state it occurs to late to modify the probability for the event to happen. In other words, it does not affect the cross section but it shapes the event as seen by the detector. The two main models are:

- the string model [134] used in Pythia [119]: this model considers the colour-charged particles to be connected by field lines which are attracted by the gluon self-interaction. These strings are associated to the final colour-neutral hadrons.

Source	M_{jj} [GeV]		JSF	
	e + *jets*	μ + *jets*	e + *jets*	μ + *jets*
Data	82.12 ± 0.22	81.81 ± 0.17	0.979 ± 0.003	0.992 ± 0.002
$t\bar{t}$ Signal (from individual sample)	81.32 ± 0.07	81.40 ± 0.05	0.9887 ± 0.0009	0.9877 ± 0.0007
$t\bar{t}$ Signal (from linear fit)	81.42 ± 0.03	81.42 ± 0.02	0.9875 ± 0.0005	0.9875 ± 0.0005
Signal MC generator (PowHeg)	81.26 ± 0.07	81.31 ± 0.05	0.9894 ± 0.0009	0.9888 ± 0.0007
Signal MC generator (MC@NLO)	81.21 ± 0.06	81.24 ± 0.05	0.9900 ± 0.0009	0.9897 ± 0.0007
Hadronization model (Herwig)	81.26 ± 0.07	81.31 ± 0.05	0.9894 ± 0.0009	0.9888 ± 0.0007
Hadronization model (Pythia)	81.09 ± 0.07	81.13 ± 0.05	0.9915 ± 0.0009	0.9910 ± 0.0007
Underlying event (Nominal)	81.05 ± 0.06	81.04 ± 0.05	0.9920 ± 0.0008	0.9921 ± 0.0007
Underlying event (mpiHi)	81.01 ± 0.07	81.10 ± 0.05	0.9925 ± 0.0008	0.9914 ± 0.0007
Color reconnection (Nominal)	81.05 ± 0.06	81.04 ± 0.05	0.9920 ± 0.0008	0.9921 ± 0.0007
Color reconnection (no CR)	81.03 ± 0.06	81.10 ± 0.05	0.9922 ± 0.0008	0.9914 ± 0.0007
ISR (signal only)	80.63 ± 0.07	80.50 ± 0.05	0.9971 ± 0.0009	0.9988 ± 0.0007
FSR (signal only)	81.69 ± 0.05	81.71 ± 0.04	0.9842 ± 0.0007	0.9840 ± 0.0006
Jet Energy Scale (Up)	81.92 ± 0.07	81.98 ± 0.05	0.9814 ± 0.0009	0.9807 ± 0.0007
Jet Energy Scale (Down)	80.73 ± 0.07	80.90 ± 0.05	0.9959 ± 0.0009	0.9938 ± 0.0007
b-tagged Jet Energy Scale (Up)	81.92 ± 0.07	81.98 ± 0.05	0.9814 ± 0.0009	0.9807 ± 0.0007
b-tagged Jet Energy Scale (Down)	80.73 ± 0.07	80.90 ± 0.05	0.9959 ± 0.0009	0.9938 ± 0.0007
Jet energy resolution	81.34 ± 0.07	81.35 ± 0.06	0.9884 ± 0.0009	0.9883 ± 0.0008
Jet reconstruction efficiency	81.31 ± 0.07	81.39 ± 0.05	0.9888 ± 0.0009	0.9878 ± 0.0007
b-tagging efficiency Up	81.32 ± 0.07	81.40 ± 0.05	0.8997 ± 0.0009	0.9877 ± 0.0007
b-tagging efficiency Down	81.30 ± 0.07	81.38 ± 0.05	0.9889 ± 0.0010	0.9880 ± 0.0007
c-tagging efficiency Up	81.32 ± 0.07	81.40 ± 0.05	0.9887 ± 0.0009	0.9877 ± 0.0007
c-tagging efficiency Down	81.31 ± 0.07	81.39 ± 0.05	0.9888 ± 0.0009	0.9878 ± 0.0007
mistag rate efficiency	81.31 ± 0.07	81.39 ± 0.05	0.9888 ± 0.0009	0.9878 ± 0.0007
mistag rate efficiency	81.32 ± 0.07	81.39 ± 0.05	0.9887 ± 0.0009	0.9878 ± 0.0007
Lepton energy scale Up	81.32 ± 0.07	81.39 ± 0.05	0.9887 ± 0.0009	0.9878 ± 0.0007
Lepton energy scale Down	81.32 ± 0.07	81.39 ± 0.05	0.9887 ± 0.0009	0.9877 ± 0.0007
Missing transverse energy Up	81.32 ± 0.07	81.39 ± 0.05	0.9887 ± 0.0009	0.9878 ± 0.0007
Missing transverse energy Down	81.32 ± 0.07	81.40 ± 0.05	0.9887 ± 0.0009	0.9877 ± 0.0007

Table 5.7: JSF values determined for data, nominal $t\bar{t}$ MC and for each systematic source. The pdf, pile-up, calibration method and physics background systematics are not reported in the table since they are the same as the default $t\bar{t}$ sample.

- the cluster model used in Herwig [123]: the colour-charged quarks and gluons form color-neutral clusters. These clusters are comparable to massive colour-neutral particles which decay into known hadrons.

This systematic is evaluated using samples with the same generator (PowHeg) and different hadronisation models: Pythia with P2011C tune and Herwig. The corresponding m_{top} distributions for both models can be seen in Figure 5.26(b). The size of the systematic is taken as the full difference between the m_{top} of both samples.

Underlying event (UE): the UE in $p-p$ collisions is associated with all particles produced in the interaction excluding the hard scatter process. The properties of the objects entering this analysis can be altered if part of the UE gets clustered in to the used jets and it may translate into a faint change of the m_{top}

distribution shape. This uncertainty is computed by comparing the results obtained for m_{top} when using PowHeg+Pythia samples with different underlying event parameter settings [120]. The full difference between the default Perugia 2011C and the mpiHi tunes [120] is taken as the systematic uncertainty. The m_{top} distributions associated to these variations are shown in Figure 5.26(c).

Color Reconnection: quarks carry color charge, however hadrons are color singlets. Therefore when the $t\bar{t}$ quarks arise from the collision, the color charge flow has to be such that has to produce the final colorless hadrons. This rearrangement of the color structure of the event is known as *color reconnection*. The evaluation of this systematic uncertainty is performed by simulating $t\bar{t} \rightarrow \ell$ + jets events with PowHeg+Pythia and using different color reconnection settings of the Perugia 2011C tuning [120]. Figure 5.26(d) shows the impact of these settings in the final m_{top} distribution. The full difference between both variations is taken as systematic uncertainty.

Initial and Final State Radiation (ISR and FSR): the amount of radiation in the initial and/or final state may affect the number of jets in the event as well as their energies (as more or less energy can leak out of the jet cone). Consequently, the ISR and FSR may affect to all jets in the event. Thus, both: the hadronic W (section 5.5.1) and the m_{top} fit may be sensitive to the amount of ISR and FSR. In order to estimate the size of this uncertainty, two samples generated with AcerMC but differ in the amount of initial and final state radiation were used. Figure 5.26(e) displays the m_{top} distribution for more (black) and less (red) amount of radiation. The systematic uncertainty is taken as a half of the difference between both samples.

Proton pdfs: the Parton Distribution Function represents the probability of finding a parton (quark of gluon) carrying a fraction x of the proton momentum for a hard interaction energy scale fixed. Usually, the pdfs are determined by a fit to data from experimental observables. The proton pdf functions affect not only the cross section of the process but also the final event shape. The $t\bar{t}$ signal has been generated with CT10 pdf. In addition, the NNPDF23 and the MSTW2008 have been considered to evaluate the systematic uncertainty. Each pdf is accompanied by a set of uncertainties (20 for MSTW2008, 26 for CT10 and 50 for NNPDF23). The variations up and down of these uncertainties are transformed in an event weight. To evaluate the impact of using different pdf sets, the events generated with PowHeg+Pythia P2011C are reweigthed and the resultant m_{top} distributions fitted. Figure 5.24 shows the obtained m_{top} for different pdf sets. The final uncertainty is calculated taking into account both, the uncertainty within each pdf and also between different pdf sets.

Irreducible Physics background: the amount of physics background in the final sample is known with a given precision. Some channels (QCD, W + jets) are evaluated with data driven methods. The single top events are also considered as a source of background. In this category the impact of the normalization of the background on the m_{top} is evaluated. Actually, the fraction of physics background has been varied 10% up and down.

Jet Energy Scale (JES): the calibration of the jet energy was briefly summarized in section 3.3. Besides that, this analysis performs an in-situ jet energy calibration by fitting the W mass of the hadronic part in the event (section 5.5.1). However the JES determination [69] still has an intrinsic uncertainty which may have a subsidiary impact on the m_{top}. Although thanks to the in-situ calibration its repercussion is reduced. The JES was altered by plus (up) or minus (down) its uncertainty. The largest difference with respect to the nominal was taken as systematic error of the Jet Energy Scale. Figure 5.27(a) shows the m_{top} distribution for the default sample (black) and up (red) and down (blue) variations.

***b*-tagged Jet Energy Scale (*b*JES)**: as a consequence of the B hadrons decay, b-quark initiated jets have a larger multiplicity than light-quark initiated jets. Therefore, the b-tagged jets carry another energy scale

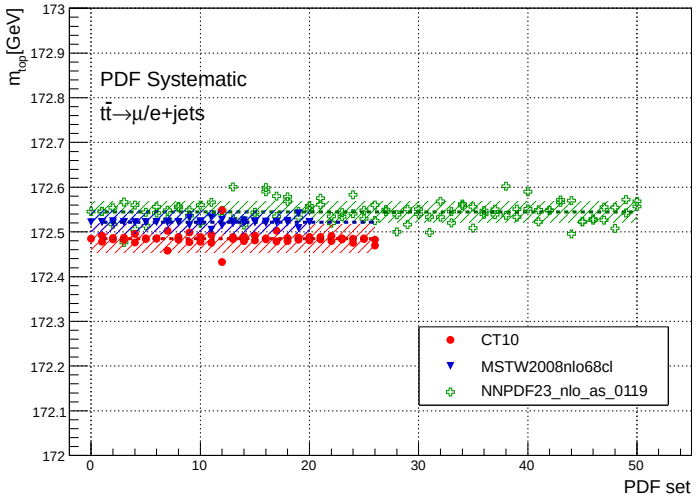

Figure 5.24: m_{top} measurement for different pdf sets: CT10, MSTW2008 and NNPDF23. The lines represent the central value of each pdf and the error bands are the associated uncertainties.

uncertainty that the light jets. The *b*-JES uncertainty has been one of the dominant systematic errors in the m_{top} measurement, therefore it has been extensively studied (a *b*-JES validation study using tracks is shown in Appendix P). In this analysis, the *b*JES has been accounted in top of the JES. Thereupon, the reference MC sample was reprocessed with varying *b*JES (up or down) by its uncertainty (Figure 5.27(b)). The worse scenario was considered. That means, the *b*JES uncertainty was added on top of the JES-up case (hereafter *b*JES-up) and subtracted to the JES-down case (hereafter *b*JES-down). Also here, the largest difference with respect to the nominal was taken as *b*JES systematic error.

Jet energy resolution (JER): this systematic quantifies the impact of the jet energy resolution uncertainty on the measurement. Before performing the analysis, the energy of each jet is smeared by a Gaussian function with a width closer to the jet resolution uncertainty. It may affect the event kinematics as well as the event selection. The analysis is repeated with the smeared jets and the difference to the default top-quark mass fitted value is taken as a systematic uncertainty. Figure 5.26(f) shows the top-quark mass distribution for the reference (black) and varied (red) sample. The JER variation gets a wider distribution. Consequently, its effect in the σ parameter of the template (Section 5.7.1) seems to have a sizable impact on the m_{top} measurement.

Jet reconstruction efficiency: this systematic analyses the impact of the jet reconstruction inefficiency in the final measurement. In ATLAS, the reconstruction efficiency for the calorimeter jets is derived by matching the jets reconstructed from tracks to the calorimeter base jets. The extracted MC reconstruction efficiency is compared to those extracted from data getting a good agreement [69]. Nevertheless some small inefficiencies observed in the comparison need to be apply to the MC jets. These inefficiencies are found to be at most 2.7% for jets with p_{T} lower than 20 GeV, few per mile for jets with a p_{T} between 20 GeV and 30 GeV and fully efficient for the rest. To compute this systematic a probability to be a badly reconstructed jet is associated to each jet and when this probability is reached the jet is drop from the event. The jets involved in the analysis have a p_{T} higher than 30 GeV, so the effect of the jet reconstruction inefficiency is expected to be very small (Figure 5.27(c)). The systematic value is taken as the difference

divided by two.

***b*-tagging efficiency and mistag rate:** scale factors (SF) are needed to be applied on MC samples in order to match the real data *b*-tagging efficiency and mis-tag rates. These SF have been calculated for the MV1 *b*-tagging algorithm working at 70% of efficiency. The systematic uncertainty is computed by changing the scale factor value by $\pm 1\sigma$ and repeat the analysis. The *b*-tagging, *c*-tagging and the mistag rate SF are varied independently. Figure 5.27(d), 5.27(e) and 5.27(f) show the m_{top} distributions for each flavour variation separately. The size of the total *b*-tagging uncertainty is calculated as the quadratic sum of the three contributions.

Lepton momentum: the lepton energy must be scaled to restore the agreement between the data and MC. These SF are accompanied by their uncertainties which are applied in the MC sample to compute the systematic uncertainty. The full difference between the modified and nominal sample is taken as the systematic uncertainty (Figure 5.28(b)).

Transverse Missing Energy: any possible mis-calibration of the $E_{\text{T}}^{\text{miss}}$ can affect the final measurement since the $E_{\text{T}}^{\text{miss}}$ is used in the event selection and also to perform the Globalχ^2 kinematic fit. There are two main types of uncertainties that enter into the $E_{\text{T}}^{\text{miss}}$ calculation: the impact of the pile-up and those uncertainties related with the reconstructed objects. The pile-up effect has been considered separately. On the other hand, the $E_{\text{T}}^{\text{miss}}$ uncertainties associated with electron, muons and jet variations are considered for each separate object and only the uncertainties associated to the Cell Out and SoftJets terms are evaluated here. Since these two terms are 100% correlated, they have to be varied together. The uncertainty due to the mis-calibration is propagated into the analysis by changing the terms of the $E_{\text{T}}^{\text{miss}}$ one sigma up and down and a half of the difference is taken as the systematic error (Figure 5.28(a)).

Pile-up: additional $p-p$ interactions may happen per beam cross. The presence of other objects in the event originated in the extra interactions may affect the measurement and reconstructions of the genuine objects from the $pp \to t\bar{t}$ interaction. The pile-up systematic uncertainty has been treated as follows: the number of primary vertex (N_{vtx}) and the average of interactions per bunch crossing ($\langle\mu\rangle$) distributions have been divided in three bins and the m_{top} has been calculated for each interval. The intervals have been chosen to maintain the same statistics. Figure 5.25 shows the m_{top} values obtained for MC (black) and data (blue) in each N_{vtx} interval (left) and $\langle\mu\rangle$ region (right).

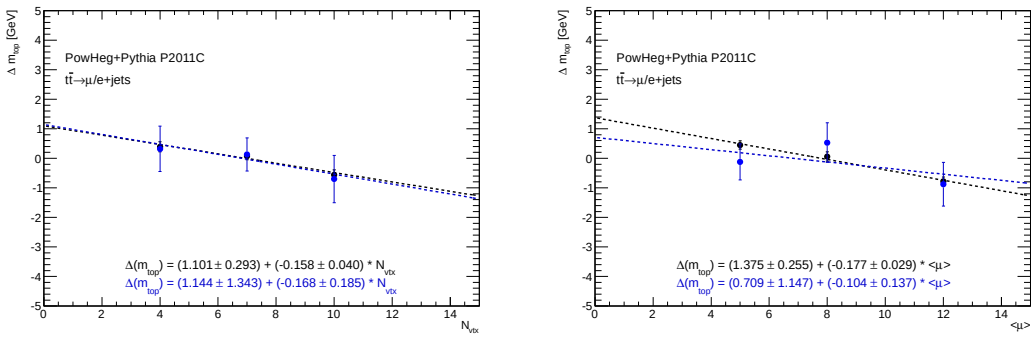

Figure 5.25: Left: Δm_{top} value calculated for each N_{vtx} interval. Right: Δm_{top} value calculated for each $\langle\mu\rangle$ interval. Results are shown for MC (black) and data (blue) samples.

The relation between the Δm_{top} and N_{vtx} has been used to get the final m_{top} as a weighted sum of $m_{\text{top}}[i]$ where i corresponds to each N_{vtx} bin. This has been calculated for data and MC and the difference has been quoted as 0.007 GeV. The same procedure has been applied for $\langle\mu\rangle$ and the difference has been found to be 0.016 GeV. Both quantities have been added in quadrature to determine the pile-up systematic uncertainty.

Table 5.8 lists the studied sources of systematic uncertainties and their corresponding size. The total uncertainty is calculated as the quadratic sum of the individual contributions. The m_{top} distribution for each source of systematic uncertainty is compared with the default sample in Figures 5.26, 5.27 and 5.28.

Table 5.8: Systematic errors of the m_{top} analysis with the template method.

Source of error	Error (GeV)
Method Calibration	0.17
Signal MC generator	0.17
Hadronization model	0.81
Underlying event	0.09
Color reconection	0.24
ISR & FSR (signal only)	0.05
Proton PDFs	0.07
Irreducible physics background	0.03
Jet Energy Scale (JES)	0.59
b-tagged Jet Energy Scale (bJES)	0.76
Jet energy resolution	0.87
Jet reconstruction efficiency	0.09
b-tagging efficiency	0.54
Lepton Energy Scale	0.05
Missing transverse energy	0.02
Pile-up	0.02
Total systematic uncertainty	1.67

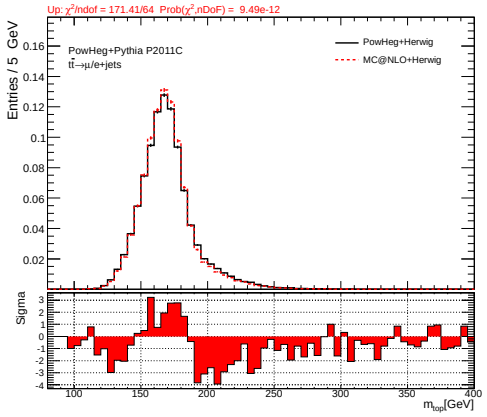

(a) MC generator.

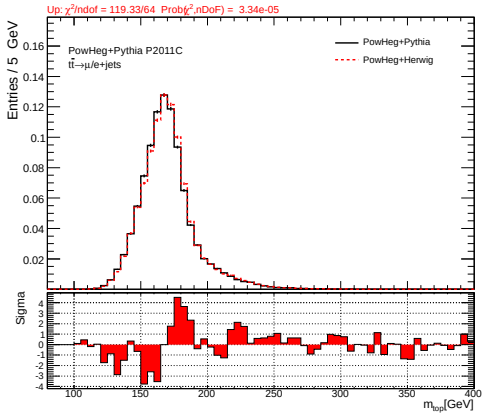

(b) Hadronization model.

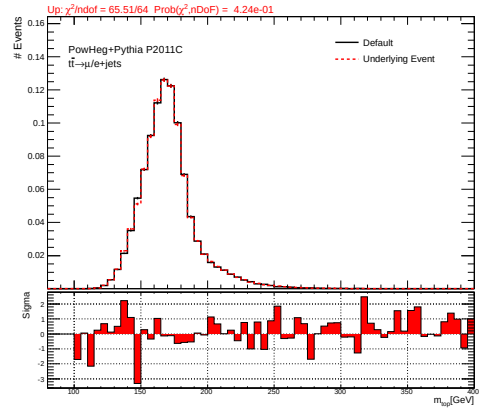

(c) Underlying event.

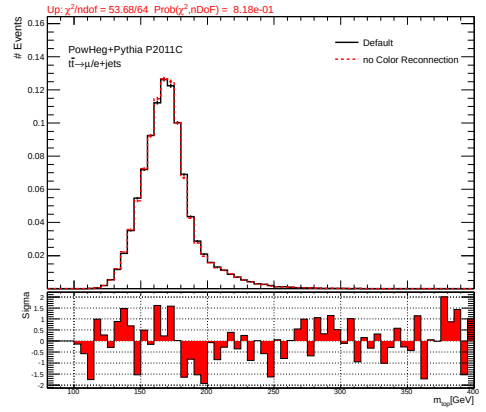

(d) Color reconnection.

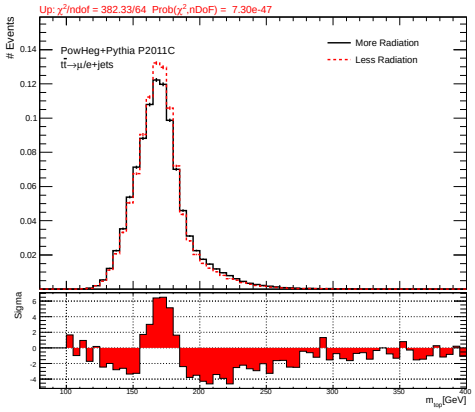

(e) Initial and Final state radiation.

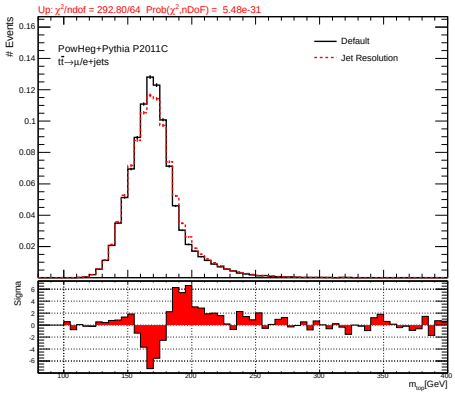

(f) Jet resolution.

Figure 5.26: m_{top} distributions for $t\bar{t}$ default sample and systematic variation.

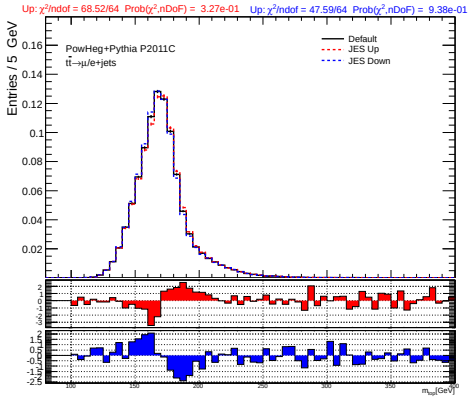

(a) Jet energy scale.

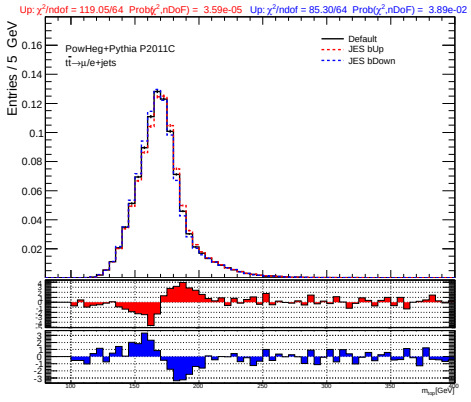

(b) *b*-jet energy scale.

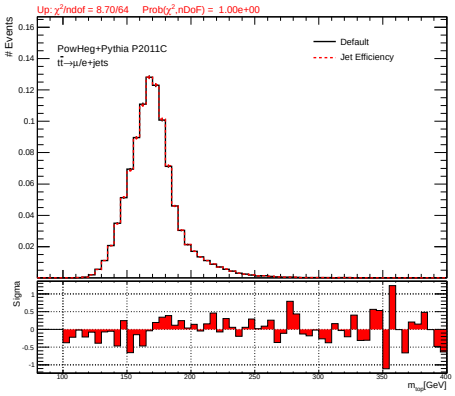

(c) Jet efficiency.

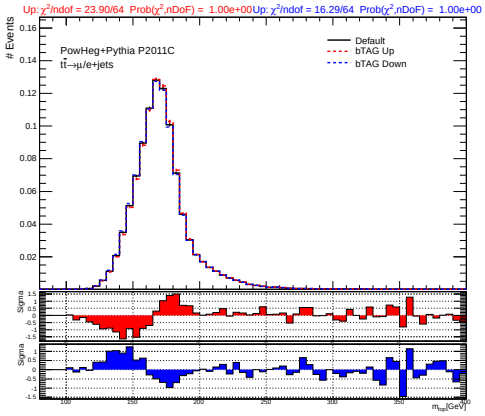

(d) *b*-tagging efficiency.

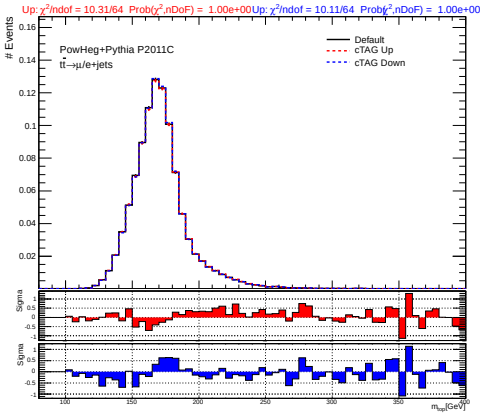

(e) *c*-tag efficiency.

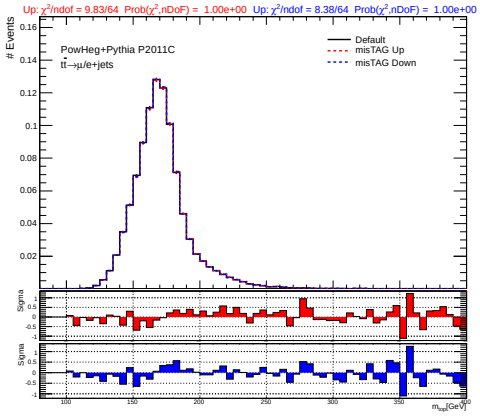

(f) miss-tag efficiency.

Figure 5.27: m_{top} distributions for $t\bar{t}$ default sample and systematic variations.

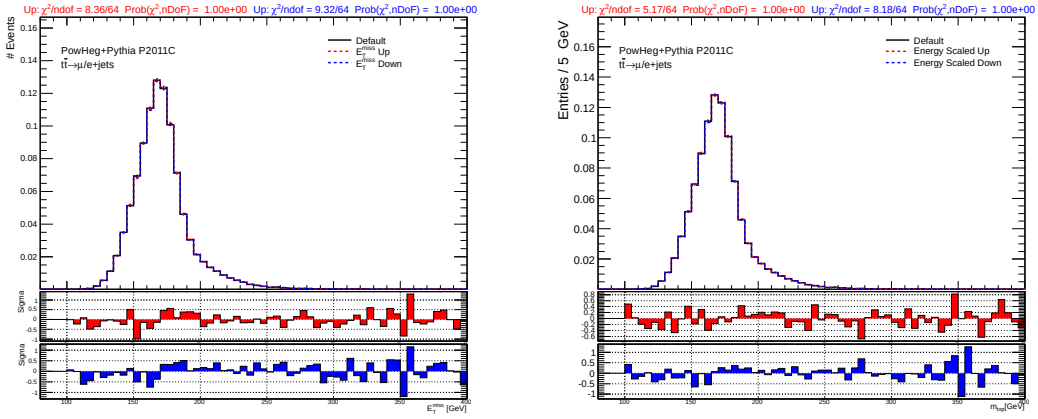

(a) Missing transverse energy:$E_{\mathrm{T}}^{\mathrm{miss}}$.

(b) Lepton energy/momentum scale.

Figure 5.28: m_{top} distributions for $t\bar{t}$ default sample and systematic variations.

5.9 Crosschecks

Alternative methods to extract m_{top} from its distribution (Figure 5.18) have been attempted. The goal is to test the robustness of the template method explained above.

5.9.1 Mini-template method

This section explains a simplified template method to extract the m_{top}. The goal is to perform the fit of the m_{top} distribution (Figure 5.29) using the function given in Section 5.7 but with as many free parameters as possible. The idea is to avoid possible MC malfunctions[7], as for example different jet energy resolution.

In the current implementation all the parameters are left free except λ, which took the same parametrization as in the template method, and ϵ, which takes its constant value. Hereafter, this method and their results will be labelled as *mini-template*. The linearity of the mini-template has been also studied and the results are shown in Appendix O.

When fitting the combined distribution with the mini-template technique the extracted top-quark mass value is:

$$m_{\mathrm{top}} = 174.18 \pm 0.50\ (\mathrm{stat.}) \pm 0.42\ (\mathrm{JSF})\ \mathrm{GeV}$$

the error quotes the statistics plus the jet scale factor uncertainties. All fit parameters split by channel can be consulted in Table 5.9.

The m_{top} value obtained with the template and mini-template methods are just above 1 standard deviation from each other. Moreover, it is worth to compare the fitted value for σ in the mini-template method (10.74 ± 0.34 (stat.) GeV) with its counterpart in the template fit (11.23 ± 0.09 (stat.) GeV). The σ values

[7] It is already proven that the JES is different between data and MC as shown in Table 5.3.

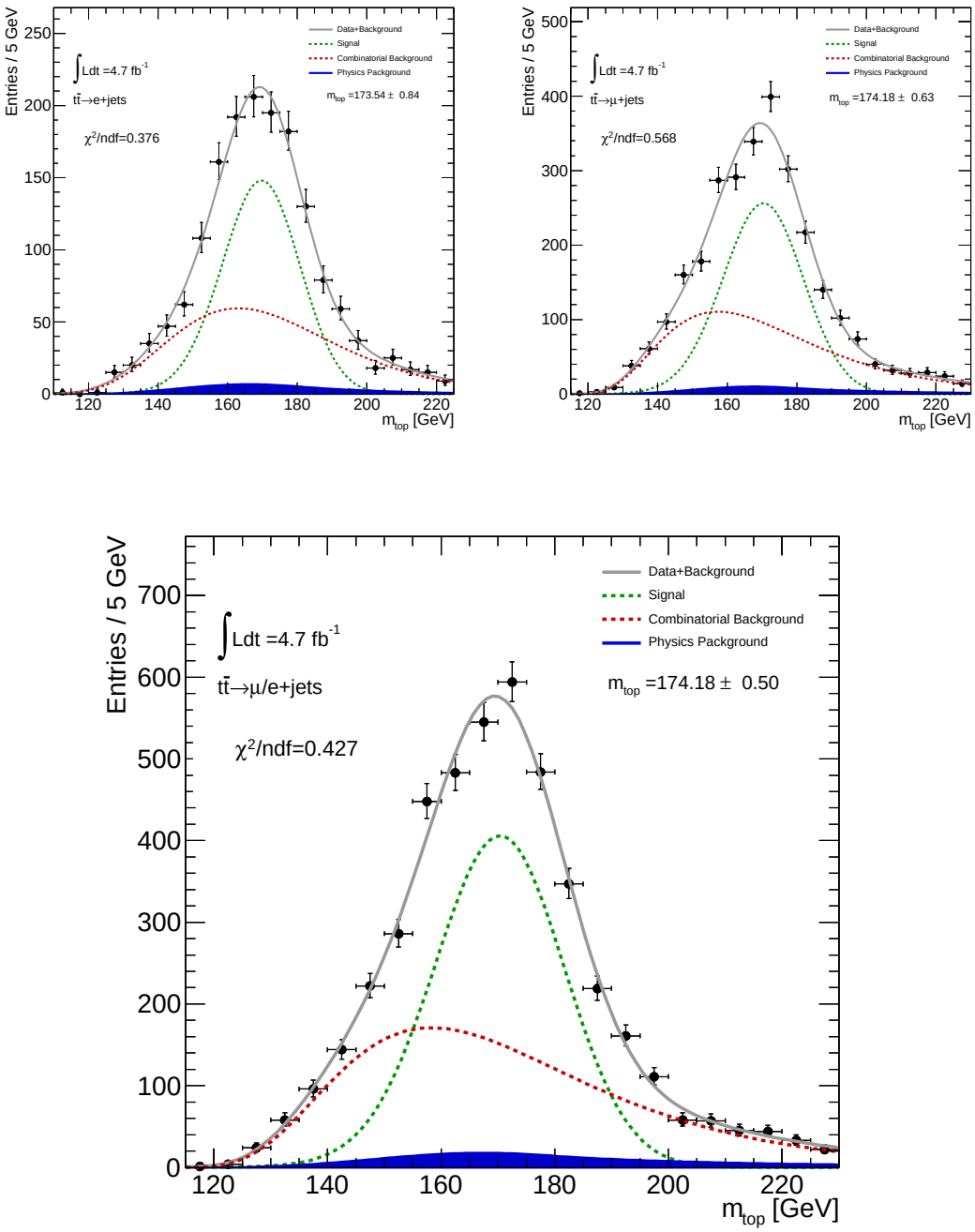

Figure 5.29: Distribution of the m_{top} parameter after the Globalχ^2 fit using the *mini – template* method. Upper right presents the results in the e + jets channel and upper left in the μ + jets one. Bottom plot: the distributions of the e + jets and μ + jets are added together. The real data distribution has been fitted (drawn as a solid gray line) to a lower tail exponential distribution with resolution model (for the correct combinations, drawn as green dashed line) plus a Novosibisrk function (to account for the combinatorial background, drawn as a red dashed line). All the contributions to the irreducible physics background are added together (blue area).

Parameter	ℓ + *jets*	e + *jets*	μ + *jets*
m_{top}	174.18 ± 0.50	173.54 ± 0.84	174.18 ± 0.63
σ (*GeV*)	10.74 ± 0.34	10.51 ± 0.55	10.96 ± 0.44
λ	4.27± 0.06	4.30 ± 0.09	4.17 ± 0.07
μ_{bkg} (*GeV*)	158.34 ± 1.51	163.03 ± 2.80	157.37 ± 1.89
σ_{bkg} (*GeV*)	22.65 ± 0.68	23.81 ± 1.15	22.39 ± 0.88
Λ_{bkg}	0.41 ± 0.05	0.26 ± 0.08	0.44 ± 0.06

Table 5.9: Parameter values extracted with the mini-template method fit. The fraction of combinatorial events has been fixed to 54.6% in both methods. The errors only account for the statistical uncertainty of the fit.

obtained from the two fits are 1.4 standard deviations away from each other. Although that difference is not significant yet, it may suggest a slightly different jet energy resolution in data and MC.

The systematic uncertainties for the mini-template method have been also computed. Table 5.10 quotes the results for each individual systematic source and also for the total systematic uncertainty. These uncertainties were evaluated following the same prescription given in Section 5.8. Notice that the JER systematic uncertainty, one of the dominant errors for the template method, has been considerably reduced. This could be understood since the mini-template leaves the σ as a free parameter and therefore it can absorb the impact of the JER as already highlited in the paragraph above. Nonetheless, the final systematic uncertainty was found to be larger than in the template method.

Table 5.10: Systematic errors of the m_{top} analysis with the mini-template method.

Source of error	Error (GeV)
Method Calibration	0.21
Signal MC generator	0.49
Hadronization model	1.04
Underlying event	0.19
Color reconection	0.05
ISR & FSR (signal only)	0.38
Proton PDFs	0.04
Irreducible physics background	0.05
Jet Energy Scale (JES)	0.73
b-tagged Jet Energy Scale (bJES)	0.87
Jet energy resolution	0.09
Jet reconstruction efficiency	0.09
b-tagging efficiency	0.54
Lepton Energy Scale	0.11
Missing transverse energy	0.02
Pile-up	0.11
Total systematic uncertainty	1.76

This method represents an attempt to understand the shape of the m_{top} distribution with a minimal MC input. If for some reason, data and MC had different behaviour, the template will irremediable bias the m_{top} measurement. By contrast, the mini-template method could avoid this kind of problems.

5.9.2 Histogram comparison

The m_{top} distribution extracted from data has been compared with those extracted from $t\bar{t}$ MC samples at different m_{top} generated points. These histograms have been contrasted with the expected hypotheses that both represent identical distributions. The Chi2TestX ROOT [135] routine has been used to perform this cross-check.

The test has been done for signal events only. Therefore the physics background contribution has been subtracted from the data histogram. The $\chi 2$/nDoF values for each $t\bar{t}$ MC samples compared with data can be seen in Figure 5.30. The results for the electron, muon and combined channel have been separately fitted with a parabolic function in order to obtain their minima. The final values, reported below, agree with the template m_{top} result within their uncertainties.

$$m_{\text{top}}(e/\mu + jets) = 173.1 \pm 0.4 \text{ GeV}$$
$$m_{\text{top}}(e + jets) = 173.5 \pm 0.7 \text{ GeV}$$
$$m_{\text{top}}(\mu + jets) = 173.1 \pm 0.4 \text{ GeV}$$

The aim of using this method has only been a cross-check and the systematic uncertainties have not been evaluated.

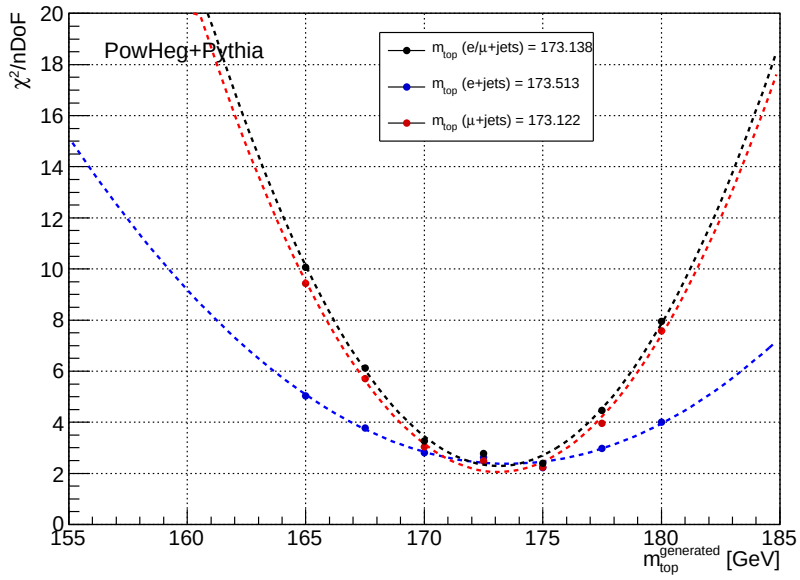

Figure 5.30: Parabolic function describing the χ^2/nDoF versus generated m_{top} for electron, muon and combined channel.

5.10 Conclusions of the $m_{\mathbf{top}}$ measurement

The top-quark mass has been measured using 4.7 fb^{-1} of data collected by ATLAS during the 7 TeV LHC run of 2011.

The measurement has been performed in the $t\bar{t} \rightarrow \ell$ + jets channel (ℓ was either an electron or a muon). In order to get an enriched sample different requirements were imposed. First of all, the standard $t\bar{t}$ selection was applied. In addition, only those events with two b-tagged jets were kept. Moreover, the hadronically decaying W boson reconstruction introduced several cuts to remove most of the combinatorial background while keeping enough statistics. After this selection the physics background was considerable reduced. The W boson allowed for an in-situ calibration of the jet energy as well as to determine a global jet energy scale factor.

For each event, the m_{top} is evaluated with the Globalχ^2 kinematics fit. This method exploits the full kinematics in the global rest frame of each top quark (including the estimation of the p_z^ν). Finally, the m_{top} distribution was fitted using a template method. In this template the correct jet combinations are cast to a lower tail exponential with resolution model probability density function. The combinatorial background is described with a Novosibirsk distribution. The physics background contribution to the $t\bar{t} \rightarrow \ell$ + jets of the final sample is about 5%.

The extracted value for m_{top} is:

$$m_{\text{top}} = 173.22 \pm 0.32 \text{ (stat.)} \pm 0.42 \text{ (JSF)} \pm 1.67 \text{ (syst.) GeV}$$

where the errors are presented separately for the statistics, the jet energy scale factor and systematic contributions. Its precision is limited by the systematic uncertainties of the analysis. The main contributors are the uncertainty due to the hadronization model (0.81 GeV), jet energy resolution (0.87 GeV) and the b-tagged jet energy scale (0.76 GeV). The result of this analysis is compatible with the recent ATLAS and CMS combination [14].

An alternative template fit, where many of the parameters that describe the m_{top} probability distribution function were left free, was also attempted. This mini-template approach could be used to detect data-MC mismatch effects blinded for the template method. In addition, a cross-check based on a χ^2 histogram comparison has been also performed and the obtained results are compatible with the m_{top} value from the template method.

Chapter

6 Conclusions

This thesis is divided in two parts: one related with the alignment of the ATLAS Inner Detector tracking system and other with the measurement of the top-quark mass. Both topics are connected by the Globalχ^2 fitting method.

In order to measure the properties of the particles with high accuracy, the ID detector is composed by devices with high intrinsic resolution. If by any chance the position of the modules in the detector is known with worse precision than their intrinsic resolution this may introduce a distortion in the reconstructed trajectory of the particles or at least degrade the tracking resolution. The alignment is the responsible of determining the location of each module with high precision and avoiding therefore any bias in the physics results. My contribution in the ID alignment has been mainly related with the developing and commissioning of the Globalχ^2 algorithm. During the commissioning of the detector, different alignment exercises were performed for preparing the Globalχ^2 algorithm: the CSC exercise allowed to work under realistic detector conditions, whilst the FDR exercises were used for integrating and running the ID alignment software within the ATLAS data taking chain. In addition, special studies were continuously done for maintaining the weak modes under control. At the same time, the ATLAS detector was collecting million of cosmic rays which were used to align the modules with real data. The alignment with cosmic rays provided a large residual improvement for the barrel region producing therefore a good detector description for the first LHC collisions. Subsequently, the data collected during the pilot runs was used for performing the first ID alignment with real collisions. Here, not only the residuals but also physics observable distributions were used to monitor the detector geometry and therefore obtain a more accurate ID alignment (specially in the end-cap region). The Inner Detector alignment achieved with the work presented in this thesis was crucial for fixing the basis of the ID alignment, getting a good initial ID performance and leading to the first ATLAS physic paper [104].

The physics analysis part of this thesis is focused on measuring the top-quark mass with the Globalχ^2 method. This measurement is important since the top quark is the heaviest fundamental constituent of the SM and may be a handle to discover new physics phenomena BSM. The analysis used the 4.7 fb^{-1} of data collected by ATLAS during the 7 TeV LHC run of 2011 in order to obtain a m_{top} measurement with real data. This measurement has been performed in the $t\bar{t} \to \ell$ + jets channel with two b-tagged jets in the event. This topology contains a W boson decaying hadronically which is used to determine the global jet energy scale factor for this kind of events. This factor helps to reduce the impact of the Jet Energy Scale uncertainty in the final measurement. For each event the m_{top} is evaluated from a Globalχ^2 fit which exploits the full kinematics in the global rest frame of each top. Finally, the m_{top} distribution has been extracted using a template method and the obtained m_{top} value is:

$$m_{\text{top}} = 173.22 \pm 0.32\ (\text{stat.}) \pm 0.42\ (\text{JSF}) \pm 1.67\ (\text{syst.})\ \text{GeV}$$

The total uncertainty is dominated by the systematic contribution. The result of this analysis is compatible with the recent ATLAS and CMS combination [14].

CHAPTER

7 Resum

El Model Estàndard (SM) de la física de partícules és la teoria que descriu els constituents fonamentals de la matèria i les seves interaccions. Aquest model ha sigut una de les teories científiques amb més èxit construïdes fins ara, degut tant, al seu poder descriptiu com també predictiu. Per exemple, aquest model permeté postular l'existència dels bosons $W^{\pm}$ i Z^0 i del quark *top* abans de la seva confirmació experimental. Malgrat que, en general, aquest model funciona extremadament bé, hi ha certs problemes teòrics i observacions experimentals que no poden ser correctament explicats. Davant d'aquest fet, s'han desenvolupat extensions del SM així com també noves teories.

Actualment, la física d'altes energies s'estudia principalment mitjançant els acceleradors de partícules. El Gran col·lisionador d'hadrons (LHC) [40], situat al CERN [41], és l'accelerador més potent que tenim avui en dia. Aquesta màquina ha sigut dissenyada per fer xocar feixos de protons a una energia de 14 TeV en centre de masses. En l'anell col·lisionador hi ha instal·lats quatre detectors qué permeten estudiar i analitzar tota la física que es produeix al LHC. ATLAS [44] és un detector de propòsit general construït per realitzar tant mesures de precisió com recerca de nova física. Aquest gran detector està format per diferents subsistemes els quals s'encarreguen de mesurar les propietats de les partícules. Generalment, després del muntatge i instal·lació del detector, la localització de cadascun dels seus mòduls de detecció es coneix amb una precisió molt pitjor que la seua pròpia resolució intrínseca. L'alineament s'encarrega d'obtenir la posició i orientació real de cadascuna d'aquestes estructures. Un bon alineament permet una bona reconstrucció de les trajectòries de les partícules i evita un biaix dels resultats físics. D'entre totes les partícules produïdes en les col·lisions del LHC, el quark *top*, degut a les seves propietats (gran massa i desintegració ràpida), és de gran importància en la validació de models teòrics i també en el descobriment de nova física més enllà del SM.

7.1 El model estàndard

El SM intenta explicar tots els fenòmens físics mitjançant un grup reduït de partícules i les seves interaccions. Avui en dia les partícules elementals, i com a tals sense estructura interna, es poden classificar en tres grups: leptons, quarks i bosons. Els leptons i els quarks són fermions, partícules d'espín 1/2, mentre que els bosons, partícules mediadores de les forces, son partícules d'espín enter. Aquestes partícules interaccionen a través de quatre forces fonamentals: la força electromagnètica, que és la responsable de mantenir els electrons lligats als àtoms; la força dèbil, que és l'encarregada de la desintegració radioactiva d'alguns nuclis; la força forta, la qual manté els protons i neutrons en el nucli, i finalment la força gravitatòria. Actualment, el SM només descriu tres d'aquestes quatre forces, però hi ha noves teories que intenten explicar la unificació de totes elles.

El SM es pot escriure com una teoria gauge local basada en el grup de simetria $SU(3)_C \otimes SU(2)_L \otimes$

$U(1)_Y$, on $SU(3)_C$ representen la interacció forta, $SU(2)_L$ la dèbil i $U(1)_Y$ l'electromagnètica. El lagrangià del SM descriu la mecànica i la cinemàtica de les partícules fonamentals i de les seves interaccions. La inclusió dels termes de massa dels bosons $W^{\pm}$ i Z^0 viola automàticament la invariància gauge local. Aquest problema es resol mitjançant la ruptura espontània de simetria (mecanisme de Higgs) el qual genera massa per als bosons $W^{\pm}$ i Z^0 mentre que manté el fotó i el gluó com partícules de massa nul·la. Aquest mecanisme introdueix una nova partícula fonamental: el bosó de Higgs. Recentment, en els experiments ATLAS i CMS del LHC, s'ha descobert una partícula amb una massa de 126 GeV i propietats compatibles amb les del Higgs del SM [6]. Aquest descobriment és el resultat d'un gran esforç teòric i experimental per entendre quin és el mecanisme que dona massa a les partícules.

La majoria de les observacions experimentals realitzades fins al moment presenten un bon accord amb les prediccions del SM. No obstant, hi ha alguns problemes pendents, com per exemple: com s'unifiquen les forces? com es resol el problema de la jerarquia? que es la matèria fosca? com es genera l'asimetria matèria-antimatèria? etc. Una de les teories més populars per resoldre aquests problemes es la supersimetria. Aquesta teoria incorpora partícules supersimètriques amb propietats similars a les del model estàndard però amb diferent espín. D'acord amb la versió més comuna d'aquesta teoria, la desintegració d'una partícula supersimètrica produeix almenys una altra partícula supersimètrica en l'estat final i les més lleugeres són estables. Així doncs, en cas d'existir, deuria haver un espectre de superpartícules detectables al LHC. Totes les noves teories deuen ser validades experimentalment i es ací on el quark *top* juga un paper fonamental.

Física del quark top

El quark *top* fou descobert l'any 1995 en l'accelerador Tevatron en Chicago (USA). El seu descobriment fou un gran èxit per al model estàndard perquè confirmà l'existència de la parella d'isospín del quark bellesa (quark b). En els col·lisionadors hadrònics, el quark *top* es produeix principalment a través de la interacció forta i es desintegra ràpidament sense hadronitzar (casi exclusivament a través de $t \to Wb$). Segons el SM el quark *top* es un fermió amb càrrega elèctrica de 2/3 la càrrega de l'electró i es transforma sota el grup de color $SU(3)_C$. Durant el primer període de funcioament del LHC, ATLAS ha recollit més de 6 milions de parelles $t\bar{t}$. Aquesta gran quantitat de dades ha servit per mesurar les propietats del quark *top* amb una alta precisió (secció eficaç [15, 16] , càrrega elèctrica [20], asimetria de càrrega [23], espín [24], acoblaments estranys [25, 26], ressonàncies [29],...). A més a més, també s'ha mesurat la seva massa (m_{top}) [14], la qual és important per ser un dels paràmetres fonamentals de la teoria així com també per tenir una alta sensibilitat a la física més enllà del SM.

La massa del quark *top* depén de l'esquema de renormalització i per tant només té sentit dintre d'un model teòric. Aquesta no és una propietat exclusiva de la massa del quark *top*, sinó comuna a tots els paràmetre del model estàndard (masses i constants d'acoblament). En contraposició a les masses dels leptons, la definició de massa d'un quark té algunes limitacions intrínseques ja que els quarks són partícules amb color i no apareixen en estats asímptoticament lliures. Hi ha diferents definicions de massa: la massa pol (definida en l'esquema de renormalització *on-shell* on s'assumeix que la massa de la partícula correspon al pol del propagador) i la massa *running* (massa definida en l'esquema de renormalització de mínima sostracció ($\overline{MS}$) on els paràmetres del lagrangià esdevenen dependents de l'escala d'energies a la qual es treballa). Experimentalment, malgrat no estar teòricament ben definida, també s'utilitza la massa cinemàtica què correspon a la massa invariant dels productes de la desintegració del quark *top*. La majoria de les anàlisis que utilitzen la massa cinemàtica empren un mètode de patrons (*template method*). Així doncs el paràmetre m_{top} mesurat correspon a la massa generada en el Monte-Carlo (MC) la qual s'espera que diferisca aproximadament de la massa pol en un GeV [32, 33].

7.2 L'accelerador LHC i el detector ATLAS

El LHC, amb un perímetre de 27 Km i situat a 100 m sota la superfície del CERN, és l'accelerador de partícules més gran del món. Aquest potent accelerador guia dos feixos de protons (també pot treballar amb ions de plom) en direccions oposades i els fa col·lidir en els punts de l'anell on estan instal·lats els detectors. L'alta lluminositat de disseny del LHC ($\mathcal{L} = 10^{34}$ cm^{-2} s^{-1}) permet estudiar processos físics interessants malgrat tenir una secció eficaç menuda. Per estudiar la física del LHC hi ha 4 grans experiments: ATLAS, CMS [45], LHCb [46] i ALICE [47]. ATLAS i CMS són dos detectors de propòsit general els quals permeten realitzar un estudi ampli de tota la física que es produeix, tant mesures de precisió com nova física. L'existència de dos detector de característiques similars és necessari per comprovar i verificar els descobriments realitzats. El LHCb és un espectròmetre dissenyat per a estudiar la física del quark *b* i ALICE és un detector construït per treballar principalment amb ions de plom i estudiar les propietats del plasma de quarks i gluons.

El detector de partícules ATLAS

El detector ATLAS pesa 33 tones i té 45 m de llarg i 22 m d'alt. Està format per diferents subdetectors instal·lats al voltant del tub del feix. En general tots presenten la mateixa estructura, capes concèntriques al voltant del tub en la zona central (zona barril) i discs perpendiculars al feix en la zona de baix àngle cap endavant i cap a darrere (zona *forward* o *backward*). Aquesta estructura proporciona una cobertura hermètica i facilita una reconstrucció completa de cada esdeveniments. La Figura 7.1 mostra un dibuix esquemàtic de la geometria del detector. ATLAS está format per tres subdetectors, cadascun dels quals construït per desenrotllar una determinada funció:

- **Detector intern (ID):** és el detector responsable de la reconstrucció de les trajectòries de les partícules, la mesura del seu moment i la reconstrucció dels vèrtexs primaris i secundaris. Aquest detector, format per detectors de silici i tubs de deriva, està envoltat per un solenoide que genera un camp magnètic de 2 T i corba les trajectòries de les partícules carregades.
- **Calorímetres:** són els detectors encarregats de la mesura de l'energia de les partícules. El calorímetre electromagnètic, amb una geometria d'acordió, mesura l'energia dels electrons, positrons i fotons. Tot seguit tenim el calorímetre hadrònic format per teules espurnejadores què mesuren l'energia depositada pels hadrons.
- **Espectròmetre de muons:** aquest detector s'encarrega principalment de la identificació i mesura del moment dels muons. És el detector més extern d'ATLAS i es combina amb un sistema de toroides que generen el camp magnètic necessari per corbar la trajectòria dels muons.

També cal comentar l'importància del sistema de *trigger* que s'encarrega d'identificar i seleccionar els esdeveniments interessants produïts en les col·lisions. Mitjançant tres nivells de selecció aquest sistema redueixen en un factor 10^5 el nombre d'esdeveniments que cal emmagatzemar.

Per últim la distribució de dades d'ATLAS, basada en tecnologies grid, ha estat dissenyada per cobrir les necessitats de la col·laboració. Bàsicament aquest model permet guardar, accedir i anal·litzar ràpidament la gran quantitat de dades que genera el LHC.

Gràcies al bon funcionament del LHC i ATLAS, els quals han treballat amb una alta eficiencia de producció i recol·lecció, s'ha aconseguit una lluminositat integrada de $26.5\ fb^{-1}$ en la primera etapa de

presa de dades (*Run* I).

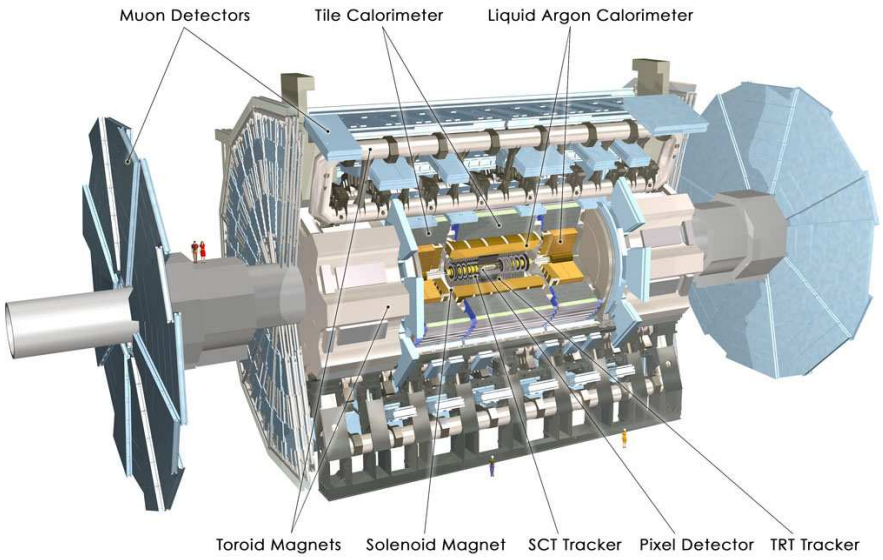

Figura 7.1: Dibuix esquemàtic de la geometria del detector ATLAS.

El Detector Intern

El ID és el detector més intern del sistema de reconstrucció de traces d'ATLAS. Aquest detector, amb una geometria cilíndrica al voltant del feix de 7 m de longitud i un diàmetre de 2.3 m, està compost per tres subdetectors: el detector de Píxels, el detector de micro-bandes (SCT) i el detector de tubs de deriva (TRT).

El principal objectiu del detector de Píxels és determinar el paràmetre d'impacte de la trajectòria de les partícules i reconstruir els vèrtexs primaris i secundaris. Aquest detector está format per 1744 mòduls de píxels de silici (amb una grandària de 50 μm×400 μm) distribuïts en tres capes concèntriques al voltant del feix i tres discs perpendiculars al feix en les zones end-cap. Aquest geometria produeix com a mínim tres mesures (*hits*) per traça. La resolució intrínseca del detector és de 10 μm en la direcció més precisa del mòdul (rϕ) i 115 μm en la direcció perpendicular.

L'SCT s'encarrega de la mesura del moment de les partícules. Els seus mòduls estan formats per dos detectors de micro-bandes (distancia entre bandes de 80 μm) pegats esquena amb esquena i rotats 40 mrad un respecte a l'altre. El SCT està format per 4088 modules instal·lats en 4 capes cilíndriques al voltant del feix i nou discs perpendiculars en cada end-cap. La geometria del SCT proporciona com a mínim 4 hits per traça. La resolució intrínseca d'aquest detector és de 17 μm en la direcció rϕ (perpendicular a les bandes) i de 580 μm en la direcció de les bandes.

El TRT s'encarrega de la identificació de les partícules i també intervé en la mesura del moment. Aquest detector produeix en mitja 30 hits per traça. Està format ~300.000 tubs de deriva amb un diàmetre de 4 mm i una longitud variable depenent de la zona del detector. La seva resolució intrínseca és de 130 μm en la direcció perpendicular al fil del tub de deriva.

7.3 Alineament del Detector Intern d'ATLAS

El ID és un ingredient crucial en les anàlisis de física ja que molts del algoritmes de reconstrucció d'objectes utilitzen la seva informació (traces, vèrtex, identificació de partícules,...). Les prestacions d'aquest detector es poden veure compromeses per una incorrecta descripció del camp magnètic, desconeixement del material i per suposat d'un alineament erroni. Els desalineaments dels mòduls degraden la reconstrucció de les trajectòries de les partícules, cosa que afecta inevitablement als resultats de física. Per assolir els objectius d'ATLAS, l'alineament del ID no deu introduir una degradació dels paràmetres de les traces en més d'un 20% de la seva resolució intrínseca. Els estudis realitzats amb mostres simulades exigeixen una resolució de 7 μm per als píxels, 12 μm per al SCT (ambdós en la direcció rϕ) i 170 μm per al TRT. No obstant hi ha escenaris més ambiciosos que requereixen conèixer les constants d'alineament amb una precisió de l'ordre del micròmetre en el plànol transvers del detector.

L'algoritme Globalχ^2 s'ha utilitzat per a alinear el sistema de silici del ID. Aquest sistema consta de 5832 mòduls (1744 del Píxel i 4088 del SCT). Cadascuna d'aquestes estructures té 6 graus de llibertat: tres translacions (T_X, T_Y, T_Z) i tres rotacions (R_X, R_Y, R_Z). Així doncs, el repte de l'alineament és determinar ~35.000 graus de llibertat amb la precisió requerida.

L' algoritme d'alineament Globalχ^2

Els algoritmes d'alineament utilitzen les trajectòries de les partícules per estudiar les deformacions del detector. Idealment, en un detector perfectament alineat, la posició del *hit* deu coincidir amb la posició de la traça extrapolada. Per altra banda, en un detector desalineat aquests punts són diferents. La distància entre ambdues posicions s'anomena residu i està definida com:

$$r = (\boldsymbol{m} - \boldsymbol{e}\,(\boldsymbol{\pi}, \boldsymbol{a})) \cdot \boldsymbol{u} \tag{7.1}$$

on $\boldsymbol{e}(\boldsymbol{\pi}, \boldsymbol{a})$ representa la posició de la traça extrapolada en el detector i depèn dels paràmetres de les traces ($\boldsymbol{\pi}$) i dels d'alineament ($\boldsymbol{a}$). $\boldsymbol{m}$ dona la posició del *hit* i $\boldsymbol{u}$ és un vector unitari que indica la direcció de mesura.

Dintre del software d'ATLAS s'han testejat diferents algoritmes d'alineament:

- **Robust** [77]: és un mètode iteratiu que utilitza els residus calculats a les zones de solapament. Aquests residus permeten correlacionar la posició dels mòduls dintre d'un *stave* o *ring* i identificar més facilment les deformacions radials. Aquest algoritme només permet alinear les direccions més sensibles (coordenades x i y locals).
- **Localχ^2 [78] i Globalχ^2 [79]**: són algoritmes iteratius basats en la minimització d'un χ^2. El Globalχ^2 utilitza residus definits dintre de la superficie planar del detector. Per altra banda, la implementació del Localχ^2 utilitza residus en tres dimensions (DOCA). Les diferencies del formalisme matemàtica entre els dos algoritmes s'explica més endavant.

L'algoritme Globalχ^2 calcula les constants d'alineament a partir de la minimització del següent χ^2:

$$\chi^2 = \sum_t \boldsymbol{r}\,(\boldsymbol{\pi}, \boldsymbol{a})^T\, V^{-1}\, \boldsymbol{r}\,(\boldsymbol{\pi}, \boldsymbol{a}) \tag{7.2}$$

on $\boldsymbol{r}(\boldsymbol{\pi},\boldsymbol{a})$ són els residus i V la matriu de covariàncies. Aquesta matriu conté principalment les incerteses o erros dels hits. Si no tenim en compte les correlacions entre els mòduls, la matriu V és diagonal. Per

contra, si s'inclou la dispersió Coulombiana (MCS) o qualsevol altre efecte que connecte diferents mòduls s'omplin els termes fora de la diagonal.

El χ^2 té un mínim per a la geometria real. Així doncs, per trobar la posició correcta dels mòduls es minimitza l'Equació 7.2 respecte a les constants d'alineament:

$$\frac{d\chi^2}{d\boldsymbol{a}} = 0 \longrightarrow \sum_t \left(\frac{d\boldsymbol{r_t}(\boldsymbol{\pi}, \boldsymbol{a})}{d\boldsymbol{a}}\right)^T V^{-1}\boldsymbol{r_t}(\boldsymbol{\pi}, \boldsymbol{a}) = 0 \tag{7.3}$$

Els residus poden calcular-se per a un conjunt de paràmetres inicials ($\boldsymbol{r_0}$=$\boldsymbol{r}$($\boldsymbol{\pi_0}$,$\boldsymbol{a_0}$)) i poden ser introduïts en el formalisme del Globalχ^2 mitjançant un desenvolupament en serie al voltant d'aquests valors:

$$\boldsymbol{r} = \boldsymbol{r}(\boldsymbol{\pi_0}, \boldsymbol{a_0}) + \left[\frac{\partial \boldsymbol{r}}{\partial \boldsymbol{\pi}}\frac{d\boldsymbol{\pi}}{d\boldsymbol{a}} + \frac{\partial \boldsymbol{r}}{\partial \boldsymbol{a}}\right]\delta\boldsymbol{a} \tag{7.4}$$

La clau del Globalχ^2 es considerar que els paràmetres de les traces depenen dels paràmetres d'alineament i per tant la derivada de $\boldsymbol{\pi}$ respecte a $\boldsymbol{a}$ no és nul·la. Açò pot ser fàcilment entès ja que la posició dels mòduls (donada per les constants d'alineament) s'utilitza en la reconstrucció de les trajectòries i per tant en la determinació dels paràmetres de les traces. Degut a l'aproximació lineal utilitzada, el mètode necessitarà iterar abans de convergir al resultat correcte. Introduint l'equació anterior en l'Equació 7.3 i després d'alguns càlculs s'obté la sol·lució general per a les constants d'alineament:

$$\delta\boldsymbol{a} = -\left(\sum_t \left(\frac{\partial \boldsymbol{r_t}}{\partial \boldsymbol{a}}\right)^T W_t \frac{\partial \boldsymbol{r_t}}{\partial \boldsymbol{a}}\right)^{-1}\left(\sum_t \left(\frac{\partial \boldsymbol{r_t}}{\partial \boldsymbol{a}}\right)^T W_t \boldsymbol{r_t}\right) \tag{7.5}$$

En una notació més compacta podem identificar el primer terme de la part dreta de l'igualtat com una matriu simètrica (M) amb una dimensió igual al nombre de graus de llibertat que estem alineant i el segon terme com un vector amb el mateix nombre de components:

$$M = \sum_t \left(\frac{\partial \boldsymbol{r_t}}{\partial \boldsymbol{a}}\right)^T W_t \left(\frac{\partial \boldsymbol{r_t}}{\partial \boldsymbol{a}}\right) \quad \boldsymbol{\nu} = \sum_t \left(\frac{\partial \boldsymbol{r_t}}{\partial \boldsymbol{a}}\right)^T W_t \boldsymbol{r_t} \tag{7.6}$$

De manera simplificada, l'equació 7.5 es pot escriure com:

$$M\delta\boldsymbol{a} + \boldsymbol{\nu} = 0 \longrightarrow \delta\boldsymbol{a} = -M^{-1}\boldsymbol{\nu} \tag{7.7}$$

Per obtenir les constants d'alineament necessitem invertir la matriu M. L'estructura d'aquesta matriu depèn de l'algoritme d'alineament amb el que treballem:

- Localχ^2: aquest algoritme es pot considerar un cas particular del Globalχ^2 on la dependència dels paràmetres de les traces respecte als paràmetres d'alineament es considera nul·la (dπ/da=0 en l'equació 7.4). Aquesta aproximació calcula els paràmetres de les traces sense tenir en compte les seves correlacions. El resultat és una matriu diagonal de blocs 6×6 perquè només els graus de llibertat dintre de cada estructura estan correlacionats. Aquesta matriu pot diagonalitzar-se fàcilment ja que la majoria dels elements són zero.

- Globalχ^2 : aquest algoritme calcula la derivada dels paràmetres de les traces respecte als paràmetres d'alineament. Aquest fet introdueix una correlació entre estructures i ompli els termes fora de la diagonal. A més a més, aquesta aproximació permet incloure restriccions en els paràmetres de les traces i d'alineament, produint d'aquesta manera, una matriu totalment poblada.

La inversió de la matriu *M* esdevé un problema quan alineem els mòduls de manera individual (~35.000 graus de llibertat). La dificultat no només radica en l'emmagatzemament d'una matriu enorme, sinó també en el gran nombre d'operacions que han d'executar-se per trobar la sol·lució de tots els graus de llibertat del sistema. S'han realitzat molts estudis per determinar i millorar la tècnica d'inversió de la matriu. És possible obtenir la matriu inversa a través del mètode de diagonalització què converteix una matriu quadrada simètrica en una matriu diagonal què conté la mateixa informació. Així doncs la matriu es pot escriure com:

$$M = B^{-1} M_d B \qquad M_d = [diag(\lambda_i)] \tag{7.8}$$

n M_d es la matriu diagonal i B la matriu canvi de base. Els elements de la diagonal (λ_i) de la matriu M_d s'anomenen valors propis o *eigenvalues* i apareixen en la diagonal ordenats de manera ascendent $\lambda_1, \lambda_2, ...\lambda_N$. Per altra banda els vectors propis o *eigenvectors* són les files de la matriu canvi de base. Estos valors i vectors propis representen els moviments del sistema en la nova base.

El formalisme del Globalχ^2 permet introduir termes per constrenyir els parmetres de les traces (utilitzant la posició del feix, la posició dels vèrtex primaris o la reconstrucció invariant d'algunes masses) com també els parmetres d'alineament (utilitzant informació mesurada en la fase d'instal·lació, del sistema de làsers del SCT,...). La inclusió d'aquests termes modifica l'estructura interna tant de la matriu com del vector d'alinemanet.

Weak modes

Els *weak modes* es defineixen com deformacions del detector què mantenen invariant el χ^2 de les traces. L'algoritme Globalχ^2 no els pot eliminar completament ja que no poden ser detectades mitjançant l'anàlisi dels residus. Estes deformacions poden ser font d'errors sistemàtics en la geometria del detector i comprometre el bon funcionament del ID.

Aquestes deformacions poden dividir-se en dos grups:

- **Moviments globals**: la posició absoluta del ID dintre d'ATLAS no ve fixada per l'alineament amb traces. Per tal de controlar aquesta posició necessitem incloure referencies externes al sistema. L'estudi dels valors i vectors propis indica quins són els moviments menys restringits del sistema i permet eliminar-los. En general el sistema presenta sis moviments globals: tres translacions i tres rotacions. Per altra banda, l'ús de diferents col·leccions de traces, configuracions, etc pot modificar/eliminar aquests modes globals.

- **Deformacions del detector**: s'han realitzat estudis amb mostres simulades per tal d'identificar aquelles deformacions del detector que no modifiquen el χ^2 i tenen un gran impacte en els resultats físics (Figura 4.4 del Capítol 4). El Globalχ^2 pot incloure restriccions en els paràmetres de les traces així com també en els paràmetres d'alineament per tal de dirigir l'algoritme cap al mínim correcte i evitar que apareguen aquests tipus de deformacions en la geometria final.

L'estratègia d'alineament s'ha dissenyat per eliminar els *weak modes*. S'han desenrotllat diferents tècniques per poder controlar aquest tipus de deformacions durant la presa de dades reals. A més s'ha estudiat que la combinació de diferents topologies pot mitigar l'impacte d'aquells *weak modes* que no són comuns a totes les mostres. Per això, l'alineament del ID s'ha realitzat utilitzant raigs còsmics i col·lisions al mateix temps.

Nivells d'alineament

D'acord amb la construcció i el muntatge del detector s'han definit diferents nivells d'alineament que permeten determinar la posició de les estructures més grans (corregint moviments col·lectius dels mòduls) com també de les més petites (mòduls individuals). Aquests nivells són:

- Nivell 1 (L1): alinea el Píxel sencer com una estructura i divideix el SCT en tres parts (un barril i dos end-caps).
- Nivell 2 (L2): corregeix la posició de cada una de les capes i dels discs del detector.
- Nivell 3 (L3): determina la posició de cada mòdul individual.

A més d'aquests nivells, s'han definit nivells intermedis que permeten corregir desalineaments introduïts durant la fase de construcció del detector. Per exemple, els píxels es montaren en tires de 13 mòduls (*ladders*) i foren instal·lats en estructures semi-cilindriques (*half-shells*) les quals porteriorment foren ensamblades de dos en dos per formar les capes completes. Per tant, aquestes estructures mecàniques utilitzades en la construcció del detector foren definides com nous nivells d'alineament i s'alinearen de manera independent. Per altra banda, les rodes del SCT (*rings*) també foren alineades per separat.

Desenvolupament i validació de l'algoritme Globalχ^2

Préviament a l'arribada de les col·lisions es realitzaren molts estudis per comprovar i validar el correcte funcionament dels algoritmes d'alineament. Alguns dels exercicis més rellevants foren:

Anàlisi de la matriu d'alineament
Quan resolem l'alineament del detector intern amb el Globalχ^2, es pot utilitzar la diagonalització de la matriu per identificar els moviments globals del sistema menys constrets (els quals estan associats a valors propis nuls). La grandària dels valors propis depèn de la configuració del sistema (si s'utilitzen restriccions en els paràmetres de les traces o d'alineament) així com també de la topologia de les traces utilitzades (raigs còsmics, col·lisions,...). Per tal d'identificar i eliminar els modes globals de cada sistema s'analitzaren les matrius dels escenaris d'alineament més utitzats: alineament del detector de silici, alineament del detector de silici amb la posició del feix fixada, alineament del detector de silici utilitzant la posició del feix i el TRT en la reconstrucció de les traces i alineament de tot el detector intern amb la posició del feix fixada. L'estudi es realitzà a nivell 1 i a nivell 2. Els resultats obtinguts permeteren conèixer el nombre de moviments globals de cadascun d'aquests escenaris (Taula 4.2 del Capítol 4). Aquests modes foren eliminats de la matriu i no computaren per a l'obtenció de les constants d'alineament, evitant d'aquesta manera, una possible deformació en la descripció geomètrica del detector que podria produir un biaix en els paràmetres de les traces.

CSC
L'exercici d'alineament CSC (sigles del nom en anglès *Computing System Commissioning*) permeté per primera vegada treballar amb una geometria distorsionada del detector. La geometria inicial es generà d'acord amb la posició dels mòduls mesurada en la fase d'instal·lació. Sobre aquestes posicions s'inclogueren desalineaments aleatoris per a cadascun dels mòduls així com també deformacions sistemàtiques (rotació de les capes del SCT). Aquest exercici fou realment important ja que permeté treballar amb una geometria més similar a la real i comprovar el comportament dels algoritmes d'alineament front a deformacions aleatòries i sistemàtiques del detector.

FDR
Els exercicis FDR (de les sigles en anglès de *Full Dress Rehearsal*) serviren per comprovar el correcte funcionament de la cadena d'adquisició de dades d'ATLAS. Dintre d'aquesta cadena el calibratge i l'alineament del detector intern deu realitzar-se en menys de 24 hores. La cadena d'alineament integrada en el software d'ATLAS té diferents passes: reconstrucció de la posició del feix, alineament dels detectors de silici i el TRT (primer per separat i després un respecte a l'altre) i reconstrucció de la posició del feix amb la nova geometria. Aquestes constants foren validades amb el monitor oficial d'ATLAS i en cas de millorar la geometria inicial introduides a la base de dades per ser utilitzades en posteriors reprocessats. Els exercicis FDR es repetiren al llarg de l'etapa de preparació del detector per tal de dissenyar i comprovar l'automatització de la cadena d'alineament i el seu correcte funcionament.

Restricció dels moviments dels discs del detector SCT
La convergència de l'algoritme Globalχ^2 s'estudià utilitzant mostres simulades. El Globalχ^2 treballà amb una geometria perfecta (no inclou cap distorsió del detector) i realitzà unes quantes iteracions per analitzar la grandària i la tendència de les constants d'alineament. En principi les constants d'alineament deurien ser nul·les ja que partim d'una geometria perfectament alineada. No obstant, s'observà una divergència de la posició dels discs del SCT en la direcció Z (paral·lela al feix). Després d'alguns estudis detallats, l'expansió dels discs s'identificà com un *weak mode*. Per tal de controlar-la es desenvoluparen diferents tècniques:

- Restricció relativa dels discs del SCT: l'evolució de les constants d'alineament per als discs del SCT mostrava un comportament divergent molt més pronunciat per als discs externs que interns. Així doncs, es fixà la posició dels discs externs respecte als interns utilitzant les distàncies mesurades durant la instal·lació del detector i s'alinearen només els discs més pròxims a la zona barril.
- SMC (de les sigles en anglès de *Soft Mode Cut*): aquesta tècnica introdueix un factor de penalització en la matriu d'alineament què desfavoreix grans moviments dels mòduls.

El comportament de les constants d'alineament fou estudiat utilitzant ambdues estratègies. Els resultats mostraren que, malgrat la reducció dels desplaçaments dels discs utilitzant la primera tècnica, no obtenien les correccions correctes. Així doncs, s'escollí la tècnica de SMC per a fixar els graus de llibertat dels discs del SCT menys constrets.

Alineament del detector intern amb dades reals

El detector ATLAS ha estat prenent dades des del 2008. Durant l'etapa de calibratge i comprovació del funcionament del detector es recolliren milions de raigs còsmics. Aquestes dades foren utilitzades

per obtenir la geometria inicial del detector. Seguidament arribaren les primeres col·lisions les quals s'utilitzaren per corregir la posició dels mòduls, sobretot en la zona end-cap. Des d'aleshores el continu funcionament del LHC ha permès recollir una gran quantitat de dades què han sigut utilitzades per millorar la descripció geomètrica del detector intern de manera continuada.

Raigs còsmics

Els esdeveniments de còsmics tenen una característica molt interessant: connecten la part de dalt i de baix del detector establint una bona correlació entre ambdues regions. Per contra, la il·luminació del detector no és uniforme ja que les parts situades al voltant de ϕ=90° i ϕ=270° estan més poblades que les regions situades en ϕ=0° i ϕ=180° les quals estan pràcticament desertes.

Els còsmics recol·lectats durant el 2008 i el 2009 s'empraren per obtenir el primer alineament del ID amb dades reals. L'estratègia d'alineament utilitzada intentà corregir la majoria de les deformacions del detector. Primer s'alinearen les grans estructures (L1), seguidament els nivells intermedis (capes, discs, anells, *ladders*,...) i finalment la posició de cada modul individual. Degut a l'estadística només s'alinearen els graus de llibertat més sensibles: T_X, T_Y, T_Z i R_Z. Durant l'alineament de L3 es van detectar deformacions sistemàtiques dintre d'alguns *ladders* del detector de Píxels. Concretament, aquestes estructures presentaren una forma arquejada en la direcció $T_X - R_Z$ i en T_Z.

La Figura 7.2 mostra els mapes de residus per a una de les capes del SCT abans (esquerra) i després (dreta) de l'alineament. Cada quadre representa un modul del SCT i el color indica el tamany dels residus en eixe mòdul. L'estudi i correcció d'aquestes deformacions permeté obtenir un bona reconstrucció de les primeres col·lisions del LHC.

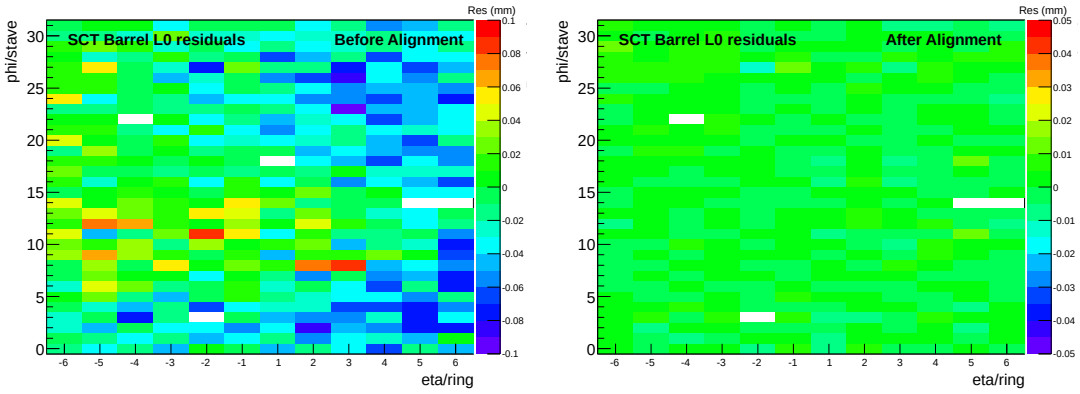

Figura 7.2: Mapa de residus per a la capa més interna del SCT abans (esquerra) i després (dreta) de l'alineament amb raigs còsmics.

Col·lisions

En Novembre del 2009 arribaren les primeres col·lisions del LHC. La reconstrucció d'aquests esdeveniments mostrà un alineament acceptable de la zona barril mentre que la zona *forward* exhibí alguns

problemes. Els desalineaments en els end-caps, degut principalment a la impossibilitat d'alinear-los amb raigs còsmics, foren ràpidament corregits amb les dades recol·lectades durant les dos primeres setmanes. Una vegada millorada l'eficiència de reconstrucció dels end-caps es realitzà un alineament complet del detector (zona barril i zona *forward*). Aquest exercici d'alineament utilitzà no només les distribucions de residus, sinò també distribucions d'observables físics que permeteren monitoritzar la geometria del detector i corregir/evitar l'aparició de *weak modes*. A més s'imposà una restricció en la localització del feix que permeté fixar la posició del ID dintre d'ATLAS així com també millorar la resolució del paràmetre d'impacte transversal. La Figura 7.3 mostra la distribució de residus per al barril i end-cap del SCT abans (negre) i després (roig) de l'alineament. L'amplada de les distribucions dels end-caps, de 70 μm abans i de 17 μm després d'alinear, mostra la millora considerable de l'alineament en aquesta zona.

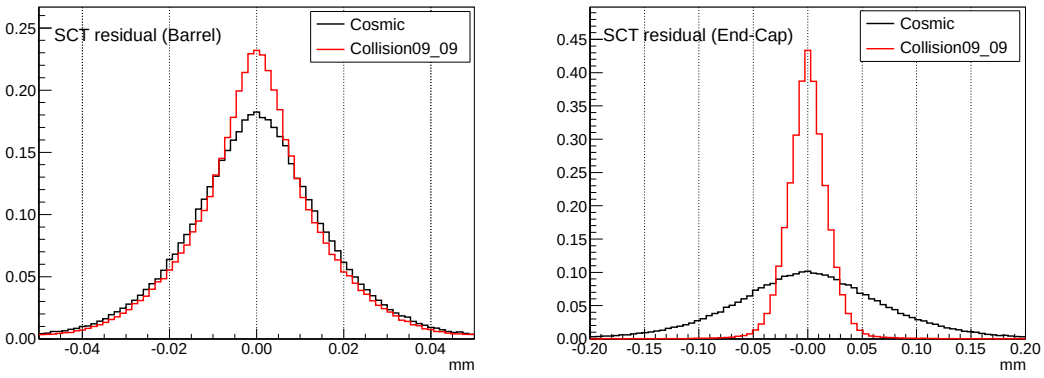

Figura 7.3: Distribució de residus del SCT per a la zona barril (esquerra) i end-cap (dreta) abans (negre) i després (roig) de l'alinemanet amb col·lisions.

En resum, l'alineament del detector intern amb els primers 7 μb^{-1} de col·lisions corregí els desalineaments de la zona *forward* i millorà l'alineament de la zona barril. Aquest exercici permeté reconstruir els posteriors esdeveniments de manera molt més eficient.

Millores tècniques de l'alineament

L'alineament del detector Intern d'ATLAS ha estat millorant-se contínuament. Després de l'alineament del ID amb les primeres col·lisions s'han anat desenvolupant noves tècniques per obtenir una descripció més acurada de la geometria del detector. Algunes d'aquestes tècniques són:

- **Combinació de còsmics i col·lisions:** paral·lelament a les col·lisions s'han recol·lectat raigs còmics. Aquest fet ha permés, no tant sols augmentar l'estadística de les dades, sinó també treballar amb diferents topologies reconstruïdes sota les mateixes condicions d'operació i geometria del detector.

- **Estudi de les deformacions internes dels píxels:** en la fase de construcció del detectors de píxels es realitzaren estudis de qualitat de cadascun dels mòduls que mostraren algunes deformacions internes. Aquestes distorsions s'han introduït en la geometria del ID i han sigut corregides per l'alineament.

- **Millora de l′ alineament del TRT:** s′ha implementat el *software* necessari per corregir la posició dels fils del TRT. L′alineament d′aquestes estructures en la direcció més sensible ha permés corregir deformacions sistemàtiques del detector.

- **Alineament dels detector *Run* a *Run*:** l′alineament de cada *Run* per separat permet corregir i detectar més ràpidament els canvis en la geometria del detector. S′ha observat un canvi notable en les constants d′alineament després d′algunes incidències en l′operació del detector, com ara: conectar o desconectar l′alt voltatge, el sistema de refredament, el camp magètic, etc.

- **Anàl·lisi de la reconstrucció del moment de les partícules:** la correcta reconstrucció del moment de les partícules és molt important per a les anàl·lisis de física. Així doncs, s′ha estudiat els possibles biaixos d'aquest paràmetre degut a les distorsions en la geometria del detector i les tècniques per resoldre′ls. Bàsicament tenim dos mètodes: un basat en la reconstrucció de la massa invariant de partícules conegudes ($Z \rightarrow \mu^+\mu^-$) i altre basat en la comparació de la informació del ID i el calorímetre (E/p). Tots dos mètodes permeten corregir i validar la geometria del detector.

7.4 Mesura de la massa del quark *top*

El quark *top* és la partícula més massiva del SM. En l′actualitat, la seva massa s′ha mesurat amb una alta precisió tant en Tevatron (m_{top}=173.2±0.9 GeV) [13] com en el LHC (m_{top}=173.2±1.0 GeV) [108].

En aquesta tesi s′ha mesurat la massa del quark *top* amb les col·lisions del LHC a 7 TeV (lluminositat integrada de 4.7 fb^{-1}). El mètode utilitzat reconstrueix completament la cinemàtica de l′esdeveniment i calcula la m_{top} a partir dels productes de la seva desintegració. L′anàlisi s′ha realitzat en el canal de ℓ + *jets* ($\ell = e, \mu$). Aquest canal està caracteritzat per la presencia d′un bosó W que es desintegra en leptó i neutrí mentre que l′altre ho fa hadrònicament. Així doncs, l′estat final presenta un leptó aïllat, dos *light-jets*, dos $b-$ *jets* que emanen directament de la desintegració del *top* ($t \rightarrow Wb$) i energia transversal faltant ($E_{\text{T}}^{\text{miss}}$). Una vegada s′han identificat i reconstruït tots aquest objectes s′introdueixen a l′ajust del Globalχ^2 . Aquest mètode té un primer fit (o fit intern) que calcula els paràmetres locals (p_z^ν) i un segon fit (o fit global) que determina la massa del quark *top*. Finalment la distribució de la m_{top} obtinguda amb els resultats del Globalχ^2 es fita amb un *template method* i d′aquesta manera s′extrau el valor de la massa.

Dades reals i mostres simulades

Aquesta anàlisi ha utilitzat les dades de col·lisions de protons a una energia de 7 TeV en centre de masses recollides per ATLAS durant l′any 2011.

Per altra banda les mostres simulades s′utilitzen per validar l′anàlisi. La mostra de referencia de $t\bar{t}$ s′ha generat amb el programa POWHEG [118] amb una massa de 172.5 GeV normalitzada a una secció eficaç de 166.8 pb. La funció de distribució de partons (pdf) utilitzada en la simulació és CT10. La cascada de partons i els processos subjacents produïts en una col·lisió (*underlying event*) s′han modelitzat amb PYTHIA [119] Perugia 2011C. A més a més de la mostra de referencia s′han produït altres mostres de MC amb les mateixes caracterśtiques però amb diferents masses de generació: de 165 GeV fins 180 GeV.

Hi ha esdeveniments que malgrat no ser $t\bar{t}$ deixen en el detector una signatura molt similar. Aquests processos, anomenats fons físic, han sigut simulats per tal d′estimar la seva contribució en la mesura final de m_{top}. Les mostres de *single-top* s′han generat amb POWHEG+PYTHIA PC2011C per al canals s

i Wt, mentre que el canal t utilitza AcerMC [122] +Pythia. Els processos dibosonics (ZZ/WW/ZW) s'han produït utilitzant Herwig [123]. Els processos de Z/W associats a jets han sigut generats amb Alpgen+Herwig/Jimmy. Totes aquestes mostres inclouen múltiples interaccions per a cada encreuament de feixos (*pile-up*) per tal d'imitar les condicions reals del detector.

Selecció estàndard del quark top

Totes les anàlisis d'ATLAS relacionades amb el quark *top* apliquen una mateixa selecció estàndard. Aquesta selecció consisteix en una serie de talls, basats en la qualitat dels esdeveniments i propietats dels objectes reconstruïts, que permeten obtenir una mostra enriquida en processos $t\bar{t} \rightarrow \ell + jets$:

- L'esdeveniment deu passar el trigger del leptó aïllat.
- Els esdeveniments deuen tenir només un leptó aïllat amb p_{T} >25 GeV.
- Es requereix un vèrtex amb més de 4 traces per tal de rebutjar processos de raigs còsmics.
- Almenys 4 jets amb p_{T} >25 GeV i $|\eta|$ <2.5.
- S'exigeix una bona qualitat dels jets reconstruïts. S'eliminen jets relacionats amb zones sorolloses del detector o processos del feix (*beam gas, beam halo*),...
- Es seleccionen només jets originats en el procés principal i no degut a efectes de *pile-up*.
- S'imposa un tall en la $E_{\mathrm{T}}^{\mathrm{miss}}$ i la m_w per reduir la contribució del fons de multi-jets.
- L'esdeveniment deu tenir almenys 1 jet identificat com a *b* (a partir d'ara els jets identificats com a *b* s'anomenaran directament *b-jets*) .

La taula 7.1 resumeix l'estadística obtinguda per a la senyal i cadascun dels fons. El factor de senyal sobre fons (S/B) es de l'ordre de 3. Els principals fons són *single top*, QCD multi-jet i Z+jets. Les figures 5.5, 5.6 i 5.7 del Capítol 5 mostren la comparació de dades i MC d'alguns observables importants per al canal e + jets i μ + jets.

Process	e + jets	μ + jets
$t\bar{t}$ signal	17000 ± 1900	28000 ± 3100
Single top	1399 ± 73	2310 ± 120
WW/ZZ/WZ	46.9± 1.4	74.7 ± 2.4
Z+jets	469.5 ± 9.1	453 ± 12
W+jets (data)	2340 ± 450	5000 ± 1100
QCD (data)	890± 450	1820 ± 910
Background	5150 ± 730	9700 ± 1400
Signal+Background	22100 ± 2000	37700 ± 3400
Data	21965	37700

Taula 7.1: Estadística de dades i MC després de la selecció estàdard. La senyal i els fons físics esperats corresponen a una lluminositat integrada de $4.7\,fb^{-1}$. La incertesa inclou els següents errors: estadístic, efficiència de *b*-tagging, normalització de $t\bar{t}$, lluminositat i normalització de QCD i W+jets.

Cinemàtica dels esdeveniments $t\bar{t}$ en el canal $\ell + jets$

Per tal d'obtenir la massa del quark top en cada esdeveniment necessitem:

- Reconstruir el bosó W que es desintegra hadrònicament a partir dels seus jets lleugers ($W \to q\overline{q}$). A més a més, la presència del W pot ser utilitzada per establir una relació entre l'escala d'energies dels jets en dades i en MC.
- Estimar la p_z del neutrí (assumint que la $E_{\mathrm{T}}^{\mathrm{miss}}$ correspon al moment transvers del neutrí) per reconstruir el W leptònic.
- Associar els *b-jets* a la part leptònica o hadrònica de l'esdeveniment.

Un dels reptes de l'anàlisi és la correcta identificació dels objectes. En les mostres simulades podem accedir a la informació vertadera i, per tant, comprovar que la reconstrucció i associació s'ha realitzat correctament. Quan els objectes reconstruïts no són correctament associats al seu parell vertader parlem de fons combinatorial. Així doncs, els esdeveniments de l'anàlisi poden dividir-se segons les seves característiques en: esdeveniments $t\bar{t}$ correctament associats (*correct*), esdeveniments $t\bar{t}$ on l'associació ha fallat (*combinatorial background*) i fons físic irreductible (*physics background*).

Selecció del W hadrònic

L'objectiu d'aquesta secció és seleccionar d'entre totes les possibles combinacions, el parell de jets associats al W hadrònic. La parella de jets seleccionada deu complir les següents condicions:

- Cap dels jets deu ser un *b-jet*.
- El moment transvers del jet més energètic de la parella deu ser major de 40 GeV i el del segon jet major de 30 GeV.
- La distancia radial entre els dos jets $\Delta\mathrm{R}(j_1, j_2) < 3$.
- La massa invariant reconstruïda deu estar dintre de la finestra de masses: $|m_{jj} - M_W^{PDG}| < 15$ GeV.

Per tal d'agilitzar l'anàlisi i ja que la selecció final requereix dos *b-jets*, s'eliminen també tots aquells esdeveniments que no compleixin aquesta condició.

Calibratge in-situ

El calibratge in-situ es realitza amb una doble finalitat: seleccionar el parell de jets correcte i corregir l'escala d'energies dels jets tant per a dades com per a MC. Per a cadascun del parells de jets seleccionats calculem el següent χ^2:

$$\chi^2(\alpha_1, \alpha_2) = \left(\frac{E_{j1}(1-\alpha_1)}{\sigma_{E_{j1}}}\right)^2 + \left(\frac{E_{j2}(1-\alpha_2)}{\sigma_{E_{j2}}}\right)^2 + \left(\frac{m_{jj}(\alpha_1, \alpha_2) - M_W^{PDG}}{\Gamma_W^{\mathrm{PDG}} \oplus \sigma_{E_{j1}} \oplus \sigma_{E_{j2}}}\right)^2 \tag{7.9}$$

on $E_{1,2}$ i $\sigma_{1,2}$ són l'energia del jet i la seva incertesa. α_1 i α_2 són els paràmetres del fit. m(α_1, α_2) representa la massa invariant del parell que testem i Γ_W^{PDG} és l'amplada del bosó W tabulada en el PDG. L'energia dels jets seleccionats s'escala amb els factors de calibratge α_1 i α_2.

Si un esdeveniments té més d'un parell de jets viable s'escull el de menys χ^2. A més a més, només els esdeveniments amb un χ^2 menor de 20 s'utilitzen per a la posterior anàlisi. L'eficiència i la puresa de la mostra després d'aquesta selecció correspon al 14% i 54% respectivament.

Per a dades reals s'utilitza el mateix procediment. Cal notar que la contribució dels fons de processos físics després de la selecció del W hadronic es redueix considerablement (essent un 7% del total). La Figura 7.4 mostra la distribució de la massa invariant del parell de jets (m_{jj}) en el canal e + jets i μ + jets.

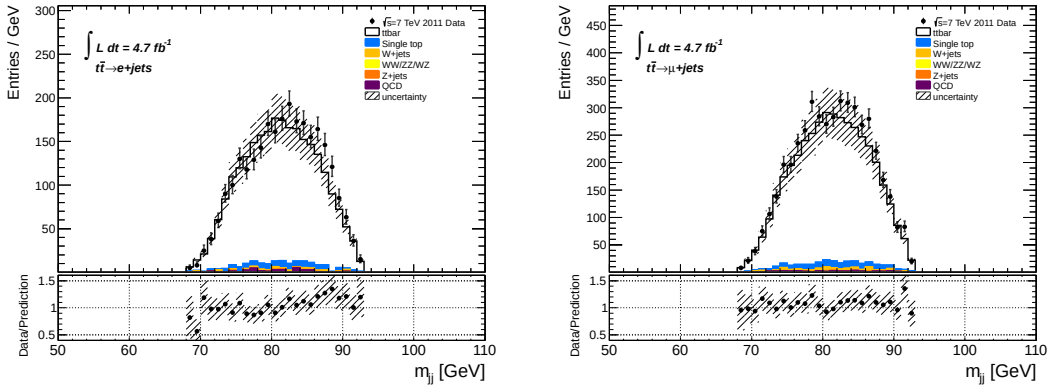

Figura 7.4: Massa invariant del parell de jets associat al bosó W hadrònic per a dades i MC en el canal e + jets (esquerra) i μ + jets (dreta).

La figura anterior mostra que la distribució de m_{jj} obtesa amb dades i MC no pica per al mateix valor. Aquesta diferència (associada a una escala d'energies diferent per als jets de les dades i del MC) necessita corregir-se per no introduir un biaix en la mesura final de m_{top}. Per tal de corregir aquesta diferència es defineix el següent factor: $\alpha_{JSF} = M_W^{PDG}/M_{jj}$. Els valors obtinguts poden consultar-se en la Taula 5.3 del Capítol 5. Aquest factor es calcula utilitzant tota la mostra i s'aplica a tots els jets que intervenen en el càlcul de la m_{top}.

Neutrí p_z i $E_{\text{T}}^{\text{miss}}$

Per reconstruir el W leptònic necessitem estimar la p_z del neutrí. L'ingredient essencial és exigir que la massa invariant del leptó i el neutrí siga la massa del bosó W. El desenvolupament matemàtic es troba en l'Apèndix K. En general, aquesta equació proporciona dos solucions per a la p_z i n'hem d'escollir una. No obstant, el 35% de les vegades l'equació no té una solució real. En aquests casos es realitza un reescalat de la $E_{\text{T}}^{\text{miss}}$ per trobar almenys una solució real. La tècnica de reescalat ha sigut validada comparant la $E_{\text{T}}^{\text{miss}}$ reconstruïda i la vertadera (informació MC). Les distribucions de l'Apèndix K mostren que el reescalat es apropiat, la qual cosa permetet treballar amb tota l'estadística.

Selecció dels *b-jets*

En aquesta secció s'exigeix que els dos *b-jets* seleccionats anteriorment tinguen un p_T >30 GeV. En cas contrari l'esdeveniment no s'utilitzarà en l'anàlisi.

b-jet i selecció de la p_z del neutrí

Per escollir la p_z del neutrí i associar els *b-jets* a la part hadrònica i leptònica de l'esdeveniment s'utilitza el següent criteri:

$$\varepsilon = |m_t^{\text{had}} - m_t^{\text{lep}}| + 10\left(\sum \Delta R^{\text{had}} + \sum \Delta R^{\text{lep}}\right) \tag{7.10}$$

on m_t^{had} i m_t^{lep} designen la massa invariant de la part hadrònica i leptònica i $\sum \Delta R^{\text{had}}$ i $\sum \Delta R^{\text{lep}}$ descriuen la distància dels objectes dintre dels triplets. Després d'aquesta selecció la puresa de la mostra és del 54%.

Algoritme Globalχ^2 per a la mesura de la m_{top}

En l'actual implementació del fit Globalχ^2, els observables utilitzats exploten la informació de l'esdeveniment en el centre de masses de cada quark *top*:

- **Cinemàtica dels dos cossos ($t \to Wb$):** l'energia i el moment del bosó W i del quark *b* en el centre de masses depenen de les seves masses així com també de m_{top} (paràmetre del fit). Aquestes magnituds es calculen en el centre de masses i es transporten al sistema de laboratori on es comparen amb les magnituds mesurades directament pel detector.
- **Conservació de moment:** la suma del moment dels productes de la desintegració del quark *top* en el seu centre de masses deu ser nul·la. Així doncs, els objectes reconstruïts en el sistema de referència de laboratori són traslladats al sistema en repós on es calcula la suma de moments i s'exigeix que siga nul·la.

La llista de residus i les seves incerteses es poden veure en la Taula 7.2. També es mostra la dependència de cada residu amb el paràmetre local o global. Per tal d'eliminar esdeveniments divergents o amb una mala reconstrucció s'aplica un tall en el χ^2 (χ^2 <20). La distribució final de la massa del quark top en el canal combinat pot veure's en la Figura 7.5. El fons físic s'ha reduït fins a un ∼5% de l'estadística total.

Obtenció de la massa del *top* amb el mètode de patrons

Com s'ha explicat anteriorment, per a cada esdeveniment que entra al fit del Globalχ^2 obtenim un valor de p_z i de m_{top}. Aquestes distribucions tenen diferents contribucions: esdeveniments correctes, fons combinatorial i fons físic. Utilitzant la informació del MC és possible separar cadascuna d'aquestes contribucions i analitzar el seu impacte en la forma final de la distribució.

La distribució de m_{top} obtinguda només amb les combinacions correctes (Figura 5.20 del Capítol 5) presenta les següents propietats: és una distribució quasi Gaussiana amb caiguda asimètrica per la dreta i esquerra i a més no pica en el seu valor nominal (m_{top}=172.5 GeV) sinó a un valor inferior. Per descriure correctament les característiques d'aquesta distribució s'ha utilitzat una Gaussiana convolucionada amb

Taula 7.2: Llista de residus, incerteses i dependència amb els paràmetres local i global.

Residual	Expresion	Uncertainty	p_z^ν	m_{top}
r_1	$m_{W_\ell} - M_W^{PDG}$	$\sigma_{E_\ell} \oplus \sigma_{E_{\text{T}}^{\text{miss}}} \oplus \Gamma_W^{\text{PDG}}$	√	
r_2	$E_{W_h}^{\text{reco}} - E_{W_h}^{\text{test}}$	$\sigma_{E_{j_1}} \oplus \sigma_{E_{j_2}}$		√
r_3	$E_{W_l}^{\text{reco}} - E_{W_l}^{\text{test}}$	$\sigma_{E_\ell} \oplus \sigma_{E_{\text{T}}^{\text{miss}}}$	√	√
r_4	$E_{b_h}^{\text{reco}} - E_{b_h}^{\text{test}}$	$\sigma_{E_{j_b}^{\text{had}}}$		√
r_5	$E_{b_l}^{\text{reco}} - E_{b_l}^{\text{test}}$	$\sigma_{E_{j_b}^{\text{lep}}}$	√	√
r_6	$\cos\left(\text{angle}(\vec{p}_{\text{had}}^{\,\star}, \vec{p}_{\text{top}})\right)\left\lvert\vec{p}_{j_1}^{\,\star} + \vec{p}_{j_2}^{\,\star} + \vec{p}_{b_h}^{\,\star}\right\rvert$	$\sigma_{E_{j_1}} \oplus \sigma_{E_{j_2}} \oplus \sigma_{E_{j_b}^{\text{had}}}$		√
r_7	$\cos\left(\text{angle}(\vec{p}_{\text{lep}}^{\,\star}, \vec{p}_{\text{top}})\right)\left\lvert\vec{p}_{\ell}^{\,\star} + \vec{p}_{\nu}^{\,\star} + \vec{p}_{b_\ell}^{\,\star}\right\rvert$	$\sigma_{E_\ell} \oplus \sigma_{E_{\text{T}}^{\text{miss}}} \oplus \sigma_{E_{j_b}^{\text{lep}}}$	√	√

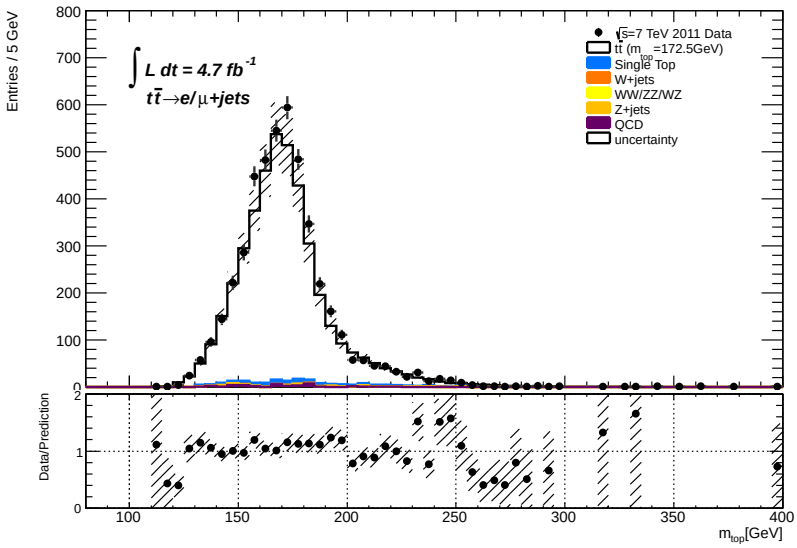

Figura 7.5: Distribució del paràmetre m_{top} obtingut amb el Globalχ^2 per al canal combinat. Les dades reals es comparen amb el MC.

una distribució exponencial amb caiguda negativa. Per altra banda la contribució del fons combinatorial (distribució roja de la Figura 5.19) està ben descrita per una funció Novosibirsk. Així doncs, la distribució final s'obté de la suma de ambdues funcions i té 7 paràmetres:

- m_0: és la massa de l'objecte a mesurar.
- λ: caiguda negativa del pic de la distribució.
- σ: resolució experimental en m_0.
- μ_{bkg}: valor més probable de la distribució de fons combinatorial.

- σ_{bkg}: amplada de la distribució de fons combinatorial.
- Λ_{bkg}: caiguda de la distribució de fons combinatorial.
- ϵ: fracció d'esdeveniments correctes.

El mètode de patrons utilitza les mostres de MC generades per a diferents masses del quark *top*. L'anàlisis es repeteix per a cada una d'aquestes mostres i la distribució final es fita amb la funció anteriorment comentada. En cada fit, m_0 es fixa a la massa de generació i s'extrauen la resta de paràmetres. Està tècnica permet calcular la dependència de cadascun del paràmetres en funció de la massa de generació. La figura 5.21 del capítol 5 mostra les distribucions dels paràmetres per al canal combinat. Podem expressar cada paràmetre de la distribució com una combinació lineal de m_0, per exemple el paràmetre λ es pot escriure com:

$$\lambda(m) = \lambda_{172.5} + \lambda_s \Delta m \tag{7.11}$$

D'igual manera es parametritzen tota la resta. Així doncs, quan obtenim la distribució de dades finals la comparem amb el model donat per la parametrització i obtenim la massa del quark *top*. La distribució 7.6 mostra la distribució de m_{top} fitada. La funció blava representa el fons físic, la roja el fons combinatorial i la verda les combinacions bones. El valor obtés de m_{top} amb dades reals és:

$$m_{\text{top}} = 173.22 \pm 0.32 \text{ (stat.)} \pm 0.42 \text{ (JSF) GeV}$$

on l'error correspon a la suma de l'error estadístic i l'error associat a l'escala d'energies del jets (JSF).

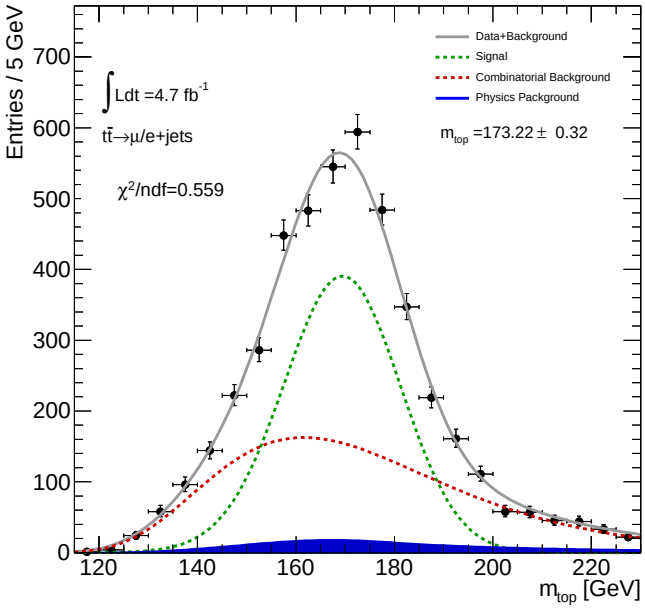

Figura 7.6: Distribiució del paràmetre m_{top} obtingut amb el Globalχ^2 amb dades. La distribució mostra el resultat del fit per al canal combinat.

Errors sistemàtics

Els errors sistemàtics s'han avaluat seguint les prescripcions oficials del grup del *top*. Cada una de les variacions sistemàtiques s'aplica a la mostra i es repeteix l'anàlisi: la preselecció, el càlcul del JSF i el fit Globalχ^2. La distribució final de MC s'utilitza per generar 500 pseudo-experiments. Utilitzant el mètode de patrons s'obtenen 500 mesures de m_{top} amb les quals s'ompli un histograma. La distribució resultant s'ajusta a una Gaussiana i la mitja s'agafa com a valor m_{top} de la mostra modificada. Generalment l'error sistemàtic es calcula com la diferència entre el valor de la mostra de referència i la mostra on s'ha aplicat la variació. La taula 7.3 mostra els resultats dels errors sistemàtic avaluats en aquesta anàlisi així com també la combinació total.

Taula 7.3: Errors sistemàtics de m_{top} obtesos amb el mètode de patrons.

Font d'error	Error (GeV)
Mètode de Calibració	0.17
Generador de MC	0.17
Model d'hadronització	0.81
Underlying event	0.09
Color reconection	0.24
Radiació d'estat inicial i final	0.05
pdf	0.07
Fons físic irreductible	0.03
Escala d'energies dels jets (JES)	0.59
Escala d'energies dels *b*-jets (bJES)	0.76
Resolució de l'energia dels jets	0.87
Eficiència de reconstrucció de jets	0.09
Efficiència de *b*-tagging	0.54
Escala d'energies dels leptons	0.05
Energia transversa faltant	0.02
Pile-up	0.02
Incertesa sistemàtica final	1.67

7.5 Conclusions

Aquesta tesi està dividida en dos parts: la primera relacionada amb l'alineament del detector intern d'ATLAS i la segona amb la mesura de la massa del quark *top*. Tots dos temes estan connectats per l'algoritme Globalχ^2.

Per mesurar les propietats de les partícules amb una alta precisió, el ID està format per unitats de detecció amb resolucions intrínseques molt menudes. Normalment, la localització d'aquests dispositius es coneix amb una resolució pitjor que la pròpia resolució intrínseca i açò pot produir una distorsió de la trajectòria de les partícules. L'alineament és el responsable de la determinació de la posició i orientació de cada mòdul amb la precisió requerida. Durant l'etapa d'instal·lació i comprovació del detector se realitzaren diferents exercicis per tal de preparar el sistema d'alineament per a l'arribada de les dades reals: l'exercici CSC permeté treballar sota condicions reals del detector, el FDR s'utilitzà per automatitzar la cadena d'alineament i integrar-la dintre de la cadena de presa de dades d'ATLAS. A més a més, s'ha

desenvolupat un treball continu per a l'estudi i correcció dels *weak modes* del detector. En paral·lel a tots aquests exercicis ATLAS estigué prenent dades de raigs còsmics els qual s'utilitzaren per determinar la geometria real del detector. Finalment arribaren les primeres collisions i amb elles es tornà a alinear el detector. En aquest exercise d'alineament no només es monitoritzaren les distribucions de residus sinó també les distribucions d'observables físics per tal d'evitar i eliminar els possibles *weak modes*. Açò permeté obtenir un alineament molt més precís del detector (millora notable en els end-caps). El treball presentat en aquesta tesi serví per fixar les bases de l'alineament del detector intern, obtenir una descripció acurada de la seva geometria i contribuir de manera significativa als primeres articles de física publicats per ATLAS.

La segona part de la tesi descriu l'anàlisi realitzada per mesurar la massa del quark *top*. El quark *top* és una de les partícules fonamentals de la matèria i la seva gran massa li confereix propietats importants en la física més enllà del model estàndard. Per tant, és important obtenir una mesura precisa de la seva massa. Aquesta anàl·lisi ha utilitzat 4.7 fb^{-1} de dades de col·lisions a 7 TeV en centre de masses recol·lectades per ATLAS en el 2011. L'anàlisi s'ha realitzat en el canal de ℓ + *jets* amb esdeveniments que tenen dos *b-jets*. Esta topologia conté un W que es desintegra hadrònicament i s'utilitza per obtenir un factor de correcció de l'escala d'energies dels jets (JSF). Amb el mètode d'ajust Globalχ^2 s'obté una mesura de m_{top} per a cada esdeveniment. Finalment la distribució de m_{top} es fita utilitzant el mètode de patrons i s'obté el resultat final:

$$m_{\text{top}} = 173.22 \pm 0.32\ (\text{stat.}) \pm 0.42\ (\text{JSF}) \pm 1.67\ (\text{syst.})\ \text{GeV}$$

La incertesa de la mesura està dominada per la contribució de l'error sistematic. Els resultats d'aquesta anàlisi són compatibles en els recents resultats d'ATLAS i CMS.

Appendices

Appendix

A Lepton and Quark masses

The SM is a renormalizable field theory, meaning that definite predictions for observables can be made beyond the tree level. The predictions are made collecting all possible loop diagrams up to a certain level, although unfortunately many of these higher contributions are often ultraviolet divergent [1]. The regularization method [136], which is a purely mathematical procedure, is used to treat the divergent terms. Once the divergent integrals have been made manageable, the renormalization process [136] subtracts their divergent parts. The way the divergences are treated affects the computation of the finite part of the parameters of the theory: the couplings and the masses. Therefore, any statement about the quantities must be made within a theoretical framework.

For an observable particle such as the e^-, the definition of its physical mass corresponds to the position of the pole in the propagator. The computation of its mass needs to include the self-interaction terms which takes into account the contribution of the photon loop to the electron propagator. Some of these diagrams are shown in the Figure A.1.

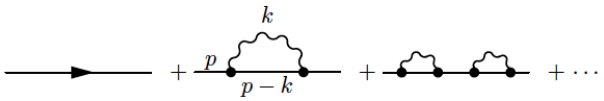

Figure A.1: Self-energy contributions to the electron propagator at one and two loops. The p and k are the four-momentum vector of the electron and photon respectively.

The propagator of the electron, $S(p) = \frac{1}{\not{p}-m}$ will have a new contribution due to the higher order loop corrections $\Sigma(p)$:

$$iS'(p) = \frac{i}{\not{p} - m - \Sigma(p)} \tag{A.1}$$

The pole of the propagator is not m anymore but rather the loop corrected mass m'=m+$\Sigma(p)$. The $\Sigma(p)$ is the self-energy contribution to the electron mass. Its calculation at one loop is logarithmically divergent, so a regularization and a renormalization scheme have to be introduced. There are different renormalization methods depending on how the divergences are subtracted out. One of the common approaches is the on-shell scheme, which assumes that the renormalized mass is the pole of the propagator. Another used technique is the modified minimal subtraction scheme ($\overline{MS}$). Here, the renormalized parameters are energy dependent and commonly called running parameters. The running mass is not the pole mass but reflects the dynamics contribution of the mass to a given process. The relation between the

[1] Ultraviolet divergences in the loop corrections usually stem from the high momentum limit of the loop integral.

pole mass and the running mass can be calculated as a perturbative series of the coupling constants α_Q[2].

Table A.1 shows the electron and top-quark masses calculated with both methods, on-shell scheme ($M_{l/q}$) and $\overline{MS}$ renormalization scheme at different energies (m_c (c-quark mass), m_W and m_{top}). The electron exhibits small differences between both masses ($O(10^{-2})$ MeV). The effects of the renormalitzation in QED are almost negligible due to the small value of α_e [4]. Detailed calculations have shown that after four loop corrections, the value of the mass converges and higher orders do not have any additional contribution. On the other hand, the quarks exhibit a different behaviour since they are always confined into hadrons. The QCD coupling constant (α_s) increases when decreasing the energy so the quark pole mass is affected by infrared divergences [3] giving a non negligible contribution for higher order corrections. The top-quark mass in different schemes can differ up to 10 GeV, and that is way the mass of the quarks has to be always given within a certain renormalization scheme.

Energy Scale (μ)	$m_e(\mu)$ (MeV)	$m_{top}(\mu)$ (GeV)
$m_c(m_c)$	0.495536319±0.000000043	$384.8^{+22.8}_{20.4}$
M_W	0.486845675±0.000000042	173.8±3.0
$m_{top}(m_{top})$	0.485289396±0.000000042	162.9±2.8
$M_{l/q}$	0.510998918±0.000000044	172.5±2.7

Table A.1: Running electron and top-quark masses at different energies $\mu = m_c$, $\mu = M_W$ and $\mu = m_{top}$ and their pole masses $M_{l/q}$. The values shown in the table are taken from [137] where the masses for all leptons and quarks are reported.

[2] α_Q symbol refers QCD coupling (α_s) as well as QED coupling (α_e).

[3] Infrared divergencies are generated by massless particles involved in the loop quantum corrections at low momentum.

Appendix

B

Globalχ^2 fit with a track parameter constraint

The χ^2 equation including a track parameter constraint looks as follows:

$$\chi^2 = \sum_t \boldsymbol{r_t}(\boldsymbol{\pi}, \boldsymbol{a})^T V^{-1} \boldsymbol{r_t}(\boldsymbol{\pi}, \boldsymbol{a}) + \boldsymbol{R}(\boldsymbol{\pi})^T S^{-1} \boldsymbol{R}(\boldsymbol{\pi}) \tag{B.1}$$

The second term, which only depends on the track parameters, represents the track constraint. The $\boldsymbol{R}(\boldsymbol{\pi})$ vector acts as the track parameter residuals and S is a kind of covariance matrix that keeps the tolerances. As always, the goal is the minimization of the total χ^2 with respect to the alignment parameters. Therefore:

$$\frac{d\chi^2}{d\boldsymbol{a}} = 0 \longrightarrow \sum_t \left(\frac{d\boldsymbol{r_t}(\boldsymbol{\pi}, \boldsymbol{a})}{d\boldsymbol{a}}\right)^T V^{-1} \boldsymbol{r_t}(\boldsymbol{\pi}, \boldsymbol{a}) + \sum_t \left(\frac{d\boldsymbol{R_t}(\boldsymbol{\pi})}{d\boldsymbol{a}}\right)^T S^{-1} \boldsymbol{R_t}(\boldsymbol{\pi}) = 0 \tag{B.2}$$

Track fit:

In order to find the solution for the track parameters, the minimization of the χ^2 with respect to the track parameters needs to be calculated:

$$\frac{d\chi^2}{d\boldsymbol{\pi}} = 0 \quad \longrightarrow \quad \left(\frac{d\boldsymbol{r_t}(\boldsymbol{\pi}, \boldsymbol{a})}{d\boldsymbol{\pi}}\right)^T V^{-1} \boldsymbol{r_t}(\boldsymbol{\pi}, \boldsymbol{a}) + \left(\frac{d\boldsymbol{R_t}(\boldsymbol{\pi})}{d\boldsymbol{\pi}}\right)^T S^{-1} \boldsymbol{R_t}(\boldsymbol{\pi}) = 0 \tag{B.3}$$

The track-hit residuals are computed for an initial set of alignment parameters ($\boldsymbol{\pi_0}$) which enter in the Globalχ^2 expression via Taylor expansion (as in Equation 4.8). The second derivatives are considered equal to zero. Inserting these expanded residuals in Equation B.3 and identifying $E_t = \partial \boldsymbol{r_t}/\partial \boldsymbol{\pi} \,|_{\pi=\pi_0}$ and $Z_t = \partial \boldsymbol{R_t}/\partial \boldsymbol{\pi} \,|_{\pi=\pi_0}$ one obtains the track parameter corrections:

$$\delta\boldsymbol{\pi} = -(E_t^T V^{-1} E_t + Z_t^T S^{-1} Z_t)^{-1} (E_t^T V^{-1} \boldsymbol{r_t}(\boldsymbol{\pi_0}, \boldsymbol{a}) + Z_t^T S^{-1} \boldsymbol{R_t}(\boldsymbol{\pi_0})) \tag{B.4}$$

Alignment parameters fit:

Once the track parameters have been calculated ($\boldsymbol{\pi} = \boldsymbol{\pi_0} + \delta\boldsymbol{\pi}$) the alignment parameters must be computed by minimizing the χ^2 (Equation B.2). The key of the Globalχ^2 lies in the total residual derivatives

since the dependence of the track parameters with respect to the alignment parameters is considered not null. Therefore, the $d\boldsymbol{\pi}/d\boldsymbol{a}$ has to be evaluated:

$$\frac{d\boldsymbol{\pi}}{d\boldsymbol{a}} = -(E_t^T V^{-1} E_t + Z_t^T S^{-1} Z_t)^{-1} (E_t^T V^{-1} \cancel{\frac{d\boldsymbol{r_t}(\boldsymbol{\pi_0}, \boldsymbol{a})}{d\boldsymbol{a}}}^{\frac{\partial \boldsymbol{r}(\boldsymbol{\pi_0}, \boldsymbol{a})}{\partial \boldsymbol{a}}} + Z_t^T S^{-1} \cancel{\frac{d\boldsymbol{R_t}(\boldsymbol{\pi_0})}{d\boldsymbol{a}}}^{0}) \tag{B.5}$$

Including B.5 in B.2, one obtains:

$$\begin{aligned} \sum_t \left(\frac{\partial \boldsymbol{r_t}(\boldsymbol{\pi_0}, \boldsymbol{a})}{\partial \boldsymbol{a}} - E_t (E_t^T V^{-1} E_t + Z_t^T S^{-1} Z_t)^{-1} E_t^T V^{-1} \frac{\partial \boldsymbol{r_t}(\boldsymbol{\pi_0}, \boldsymbol{a})}{\partial \boldsymbol{a}} \right)^T V^{-1} \boldsymbol{r_t}(\boldsymbol{\pi_0}, \boldsymbol{a}) \\ + \sum_t \left(-Z_t (E_t^T V^{-1} E_t + Z_t^T S^{-1} Z_t)^{-1} E_t^T V^{-1} \frac{\partial \boldsymbol{r_t}(\boldsymbol{\pi_0}, \boldsymbol{a})}{\partial \boldsymbol{a}} \right)^T S^{-1} \boldsymbol{R_t}(\boldsymbol{\pi_0}, \boldsymbol{a}) = 0 \end{aligned} \tag{B.6}$$

In order to simplify the equation one can defined $X' = (E_t^T V^{-1} E_t + Z_t^T S^{-1} Z_t)^{-1} E_t^T V^{-1}$. Therefore:

$$\sum_t \left(\frac{\partial \boldsymbol{r_t}(\boldsymbol{\pi_0}, \boldsymbol{a})}{\partial \boldsymbol{a}} \right)^T [I - E_t X']^T V^{-1} \boldsymbol{r_t}(\boldsymbol{\pi_0}, \boldsymbol{a}) - \sum_t \left(\frac{\partial \boldsymbol{r_t}(\boldsymbol{\pi_0}, \boldsymbol{a})}{\partial \boldsymbol{a}} \right)^T (Z_t X')^T S^{-1} \boldsymbol{R_t}(\boldsymbol{\pi_0}) = 0 \tag{B.7}$$

Now, calculating the residuals for an initial set of alignment parameters ($\boldsymbol{a_0}$) using again a Taylor expansion ($\boldsymbol{r} = \boldsymbol{r_0} + \frac{\partial \boldsymbol{r}}{\partial \boldsymbol{a}} \delta \boldsymbol{a}$) , the expression looks as follows:

$$\begin{aligned} \overbrace{\sum_t \left(\frac{\partial \boldsymbol{r_t}(\boldsymbol{\pi_0}, \boldsymbol{a})}{\partial \boldsymbol{a}} \right)^T [I - E_t X']^T V^{-1} \left(\frac{\partial \boldsymbol{r_t}(\boldsymbol{\pi_0}, \boldsymbol{a})}{\partial \boldsymbol{a}} \right)}^{M'} \delta \boldsymbol{a} + \overbrace{\sum_t \left(\frac{\partial \boldsymbol{r_t}(\boldsymbol{\pi_0}, \boldsymbol{a})}{\partial \boldsymbol{a}} \right)^T [I - E_t X']^T V^{-1} \boldsymbol{r_t}(\boldsymbol{\pi_0}, \boldsymbol{a})}^{\nu'} \\ \underbrace{- \sum_t \left(\frac{\partial \boldsymbol{r_t}(\boldsymbol{\pi_0}, \boldsymbol{a})}{\partial \boldsymbol{a}} \right)^T (Z_t X')^T S^{-1} \boldsymbol{R_t}(\boldsymbol{\pi_0})}_{\boldsymbol{w}} = 0 \end{aligned} \tag{B.8}$$

The impact of the track parameter constraint in the final alignment corrections is clearly seen. The big matrix M' includes a new term X' which is built as a function of the covariance matrix V and the partial derivatives of both residual vectors ($\boldsymbol{r_t}$ and $\boldsymbol{R_t}$) with respect to the track parameters. The big vector $\boldsymbol{\nu'}$ is modified by the same term. Finally a new vector $\boldsymbol{w}$ appears exclusively due to the introduction of the constraint term.

In a more compact notation, the final solution can be written as:

$$M' \delta a + \nu' + w = 0 \longrightarrow \delta a = -M'(\nu' + w) \tag{B.9}$$

APPENDIX

C CSC detector geometry

The Computing System Commissioning (CSC) provided the optimal framework to test the ATLAS physics, calibration and alignment algorithms with a realistic (distorted) detector geometry. Concretely, for the ID, this geometry included misalignments of different sub-systems as expected from the parts assembly accuracy (*as-built* geometry), different amounts of ID material and different distorted magnetic field configurations [95].

The ID CSC geometry was generated at different levels (L1, L2 and L3) in order to mimic the real detector misalignments observed during the construction of the detector components. Generally, these displacements were computed in the global reference frame, except for the L3 where the local reference frame was used (Section 3.1). In addition to these misalignments, the CSC geometry also contains some systematic deformations: a curl distortion was included by rotating the SCT barrel layers and a kind of telescope effect was introduced due to the SCT layers translations in the beam direction. These detector distortions affect the track parameters of the reconstructed particles leading to systematic biases.

Level 1

Table C.1 shows the size of the misalignments applied for the Pixel and SCT sub-detectors at L1.

Level 2

The misalignments applied at L2 are displayed in Table C.2. For the Pixel discs, the misalignments were generated as follows: from a flat distribution of width of [-150, +150] μm for the X and Y displacements and [-200, +200] μm in the Z direction and the rotations around the axis (α, β and γ) from a flat distribution of width [-1, +1] mrad.

Level 3

The L3 misalignments have been applied for each Pixel and SCT module. The misalignments have been generated using flat distributions with their widths defined by the numbers quoted in Table C.3.

System	T_X (mm)	T_Y (mm)	T_Z (mm)	α (mrad)	β (mrad)	γ (mrad)
Pixel Detector	+0.60	+1.05	+1.15	-0.10	+0.25	+0.65
SCT ECC	-1.90	+2.00	-3.10	-0.10	+0.05	+0.40
SCT Barrel	+0.70	+1.20	+1.30	+0.10	+0.05	+0.80
SCT ECA	+2.10	-0.80	+1.80	-0.25	0	-0.50

Table C.1: L1 as built positions for the Pixel and SCT detectors.

System	Layer/Disc	T_X (mm)	T_Y (mm)	T_Z (mm)	α (mrad)	β (mrad)	γ (mrad)
Pixel Barrel	L0	+0.020	+0.010	0	0	0	+0.6
	L1	-0.030	+0.030	0	0	0	+0.5
	L2	-0.020	+0.030	0	0	0	+0.4
SCT Barrel	L0	0	0	0	0	0	-1.0
	L1	+0.050	+0.040	0	0	0	+0.9
	L2	+0.070	+0.080	0	0	0	+0.8
	L3	+0.100	+0.090	0	0	0	+0.7
SCT ECA	D0	+0.050	+0.040	0	0	0	-0.1
	D1	+0.010	-0.080	0	0	0	0
	D3	-0.050	+0.020	0	0	0	0.1
	D4	-0.080	+0.060	0	0	0	0.2
	D5	+0.040	+0.040	0	0	0	0.3
	D6	-0.050	+0.030	0	0	0	0.4
	D7	-0.030	-0.020	0	0	0	0.5
	D8	+0.060	+0.030	0	0	0	0.6
	D9	+0.080	-0.050	0	0	0	0.7
SCT ECC	D0	+0.050	-0.050	0	0	0	+0.8
	D1	0	+0.080	0	0	0	0
	D3	+0.020	+0.010	0	0	0	+0.1
	D4	+0.040	-0.080	0	0	0	-0.8
	D5	0	+0.030	0	0	0	+0.3
	D6	+0.010	+0.030	0	0	0	-0.4
	D7	0	-0.060	0	0	0	+0.4
	D8	+0.030	+0.030	0	0	0	+0.6
	D9	+0.040	+0.050	0	0	0	-0.7

Table C.2: L2 as built positions for the layers and discs of the Pixel and SCT detectors.

Module Type	T_X (mm)	T_Y (mm)	T_Z (mm)	α (mrad)	β (mrad)	γ (mrad)
Pixel Barrel	0.030	0.030	0.050	0.001	0.001	0.001
Pixel End-cap	0.030	0.030	0.050	0.001	0.001	0.001
SCT Barrel	0.150	0.150	0.150	0.001	0.001	0.001
SCT end-cap	0.100	0.100	0.150	0.001	0.001	0.001

Table C.3: L3 as built positions for the modules of the Pixel and SCT detectors.

APPENDIX

D Multimuon sample

One of the goals of the multimuon sample was to commission the calibration and alignment algorithms. This sample consists in $\sim 10^5$ simulated events with the following properties:

- Each event contains ten particles which properties are given below.
- Half of the sample is composed by positive charged particles and the other half by negative charged particles.
- All tracks are generated to come from the same vertex which has been simulated using a Gaussian function centred at zero and a width of $\sqrt{2}\times 15$ μm in the transverse plane and $\sqrt{2}\times 56$ mm in the longitudinal plane.
- The transverse momentum of the tracks ranges from 2 GeV to 50 GeV.
- The ϕ presents a uniform distributions in the range of $[0 - 2\pi]$.
- The η has a uniform distributions in the range of $[-2.7, +2.7]$.

Some of the characteristic distributions for the multimuon sample reconstructed with a perfect knowledge of the detector geometry (CSC geometry, Appendix C) are shown in this appendix.

Number of silicon hits:

Figure D.1 shows the number of reconstructed hits per track for the Pixel (left) and SCT (right) detectors. The hits per track mean values are ~3 and ~8 for the Pixel and SCT detectors respectively. These numbers agree with the expected ones since each track produced at the beam spot usually crosses three Pixel layers and four SCT layers.

Hit maps:

The muon tracks have been generated to be uniformly distributed in the detector without any preferred direction. Figure D.2 shows the hit maps for the four SCT layers. Each module is identified by its ring and sector position. The Z axis indicates the number of reconstructed hits per module (the exact number is written on each module).

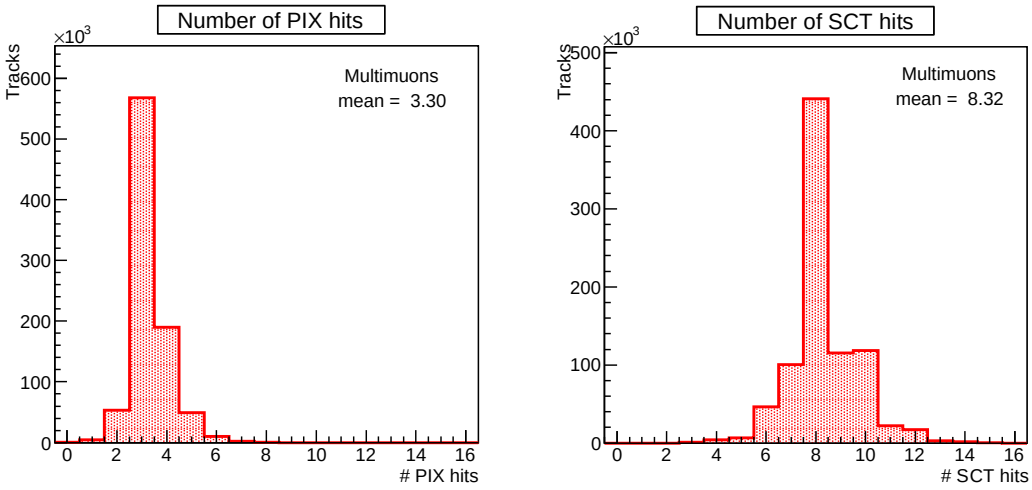

Figure D.1: Number of reconstructed Pixel (left) and SCT (right) hits.

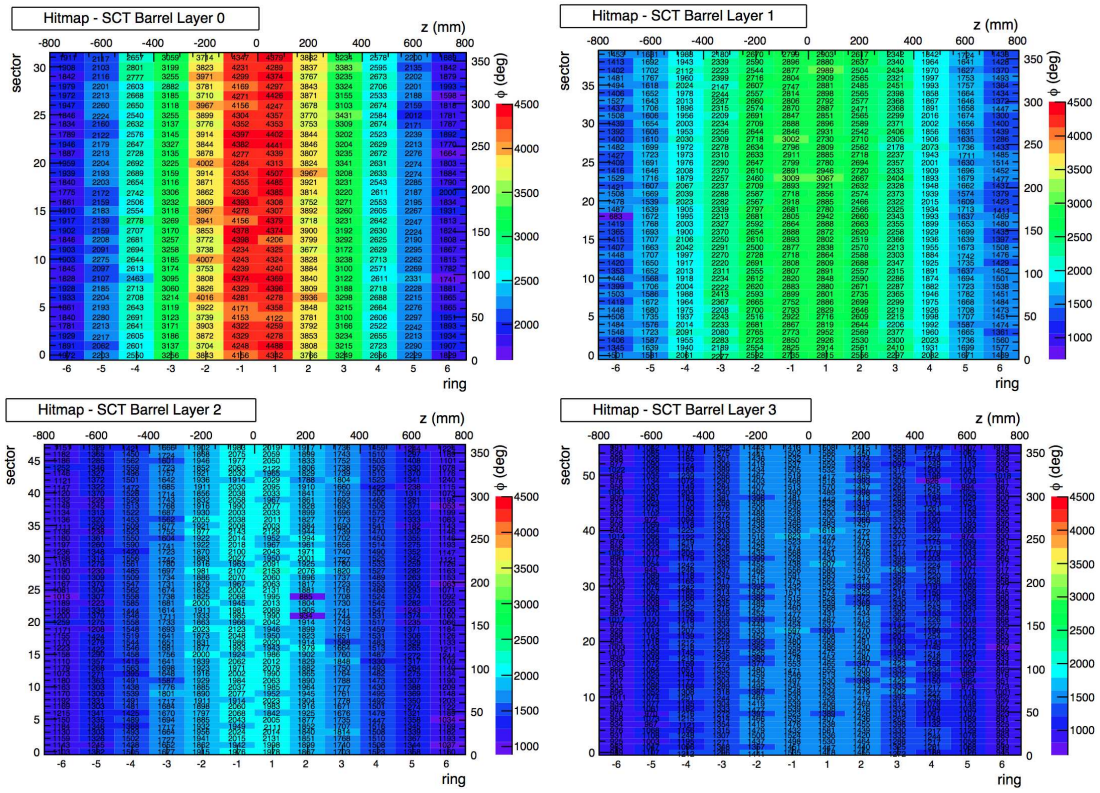

Figure D.2: Hit maps for the SCT layers. The numbers of the layers are ordered for inside to outside of the SCT detector.

Track parameters:

The track parameter distributions can be used to check the correct track reconstruction. Any deviation from their expected shapes could point out the presence of detector misalignments. Figure D.3 displays the impact transverse parameter (d_0) (left) and the longitudinal impact parameter (z_0) (right). Both distributions present a Gaussian shape with a resolution of 22.9 μm and 79.3 mm for d_0 and z_0 respectively.

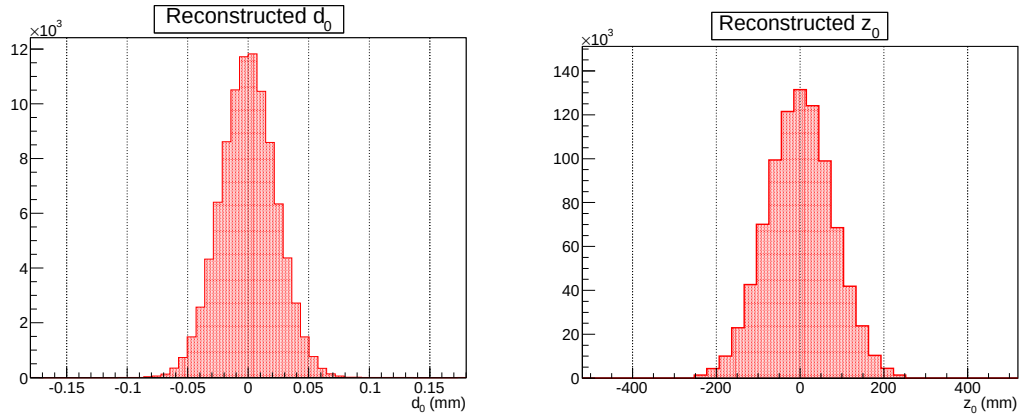

Figure D.3: Left: reconstructed d_0 distribution. Right: reconstructed z_0 distribution.

Figure D.4 shows the polar angle (θ_0) (left) and the pseudorapidity (η[1]) (right). Due to the detector acceptance, the θ_0 covers a region between [0.16, 2.98] rad and according to this the η range goes from $[-2.5, +2.5]$.

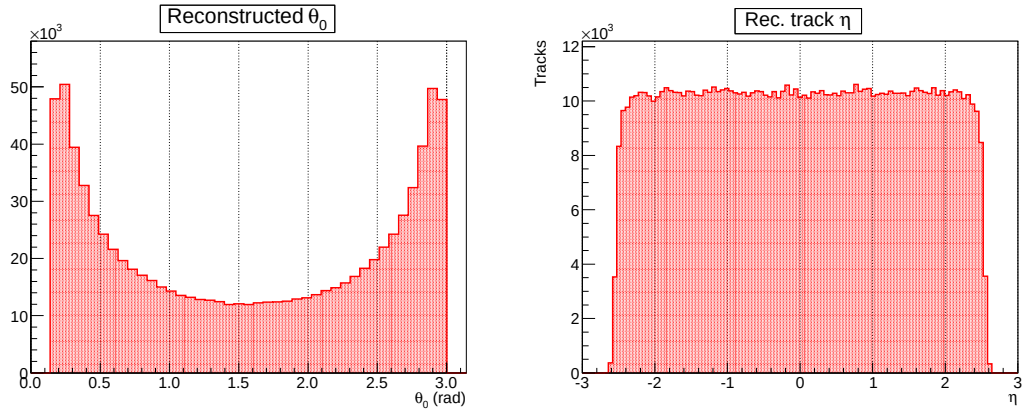

Figure D.4: Left: reconstructed θ_0 distribution. Right: reconstructed η distribution.

Finally, Figure D.5 shows the reconstructed azimutal angle (ϕ_0) (left) and the transverse momentum distribution multiplied by the charge of each particle ($q \cdot p_T$) (right). The ϕ_0 presents a flat behaviour

[1]The pseudorapidity is defined as: $\eta = -ln\ tan(\theta_0/2)$

between $[0, 2\pi]$. The $q \cdot p_T$ distribution exhibits the same quantity of positive and negative muon tracks, as expected.

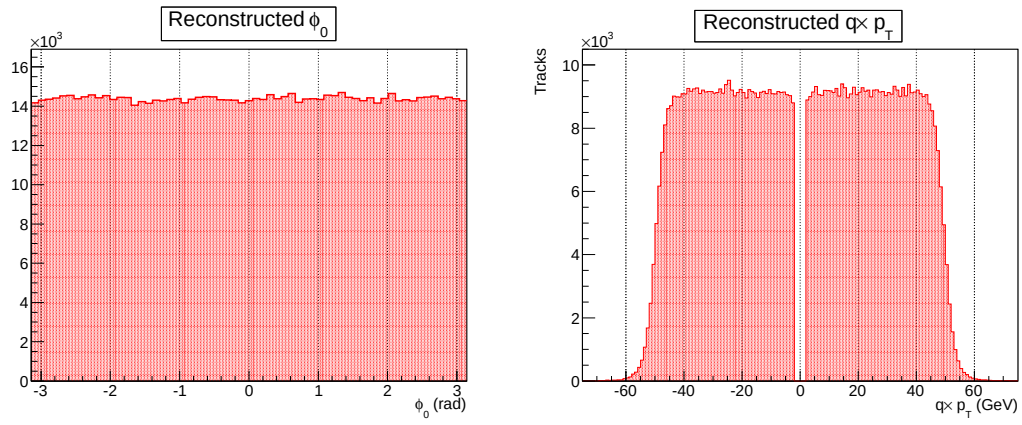

Figure D.5: Left: reconstructed ϕ_0 distribution. Right: reconstructed $q \cdot p_T$ distribution.

Vertex:

The primary vertex profiles for the transverse and longitudinal planes can be seen in Figure D.6. Their position and resolution agree with the simulated values.

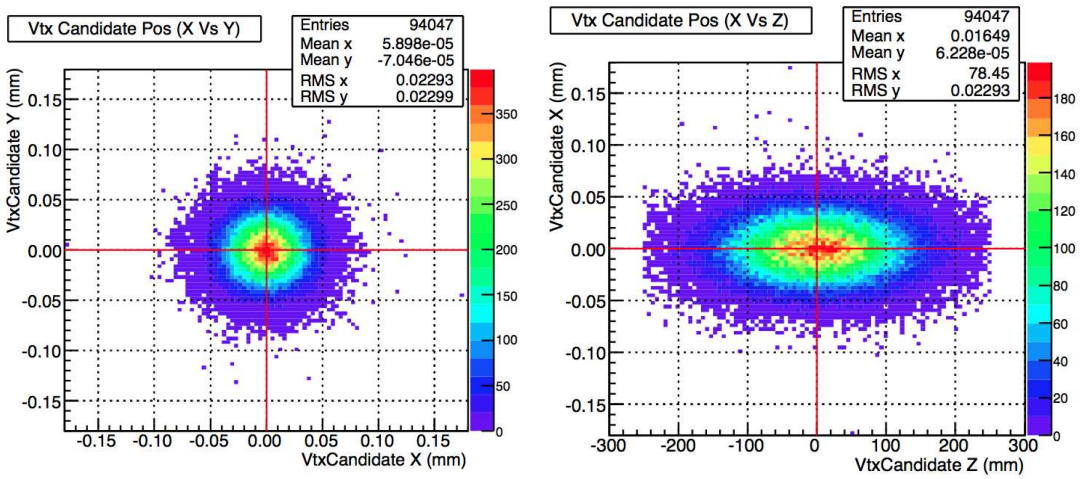

Figure D.6: Generated primary vertex distribution for the multimuon sample.

APPENDIX

E Cosmic rays samples

The cosmic rays, natural source of real data, were extensively used during the detector commissioning in order to improve the alignment, calibration and track reconstruction algorithms.

The cosmic ray sample is basically composed of muons that cross the entire detector. According to their nature, the simulation of the cosmic muons passing though ATLAS is done by running a generator which provides muons at ground level and posteriorly they are propagated within the rock [91].

Some of the characteristic distributions for the cosmic ray sample are shown in this appendix. The sample used to produce these distributions consists in ~100 k simulated events filtered for the innermost ID volume with the magnetic fields switched on. The perfect CSC geometry has been used in the reconstruction.

Number of hits:

Figure E.1 shows the number of reconstructed hits per track for the Pixel (left) and SCT (right) detectors. A track-hit requirement in the number of SCT hits has been imposed in order to improve the cosmic track reconstruction ($N_{SCT} \geqslant 10$). This requirement selects tracks that pass at least through three layers of the SCT. Therefore, the number of Pixel hits per track can be zero. Actually, the most probable value of the reconstructed hits per track for the Pixel detector is 0 as only few tracks cross the Pixel detector volume. For the SCT the most probable value is 16, which corresponds to the tracks crossing the four SCT layers.

Hit maps:

The cosmic ray tracks are not equally along the detector but there are privileged regions. Figure E.2 shows the hitmaps for the four SCT layers where the non-uniformity illumination can be seen. The upper and bottom parts of the detector, corresponding to ϕ=90° and ϕ=270° respectively, are more populated since the cosmic particles come from the surface. In addition, one can also notice that the number of hits is also lower at large η regions due to the difficult reconstruction of the cosmic rays in the end-caps. Each module is identified by its ring and sector position. The Z axis measures the number of reconstructed hits per module (the exact number is written on each module).

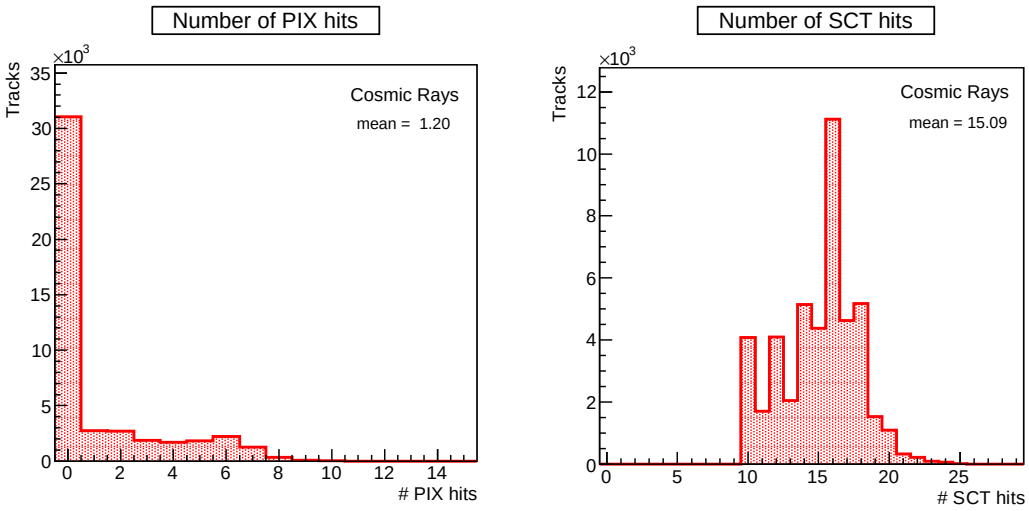

Figure E.1: Number of reconstructed Pixel (left) and SCT (right) hits .

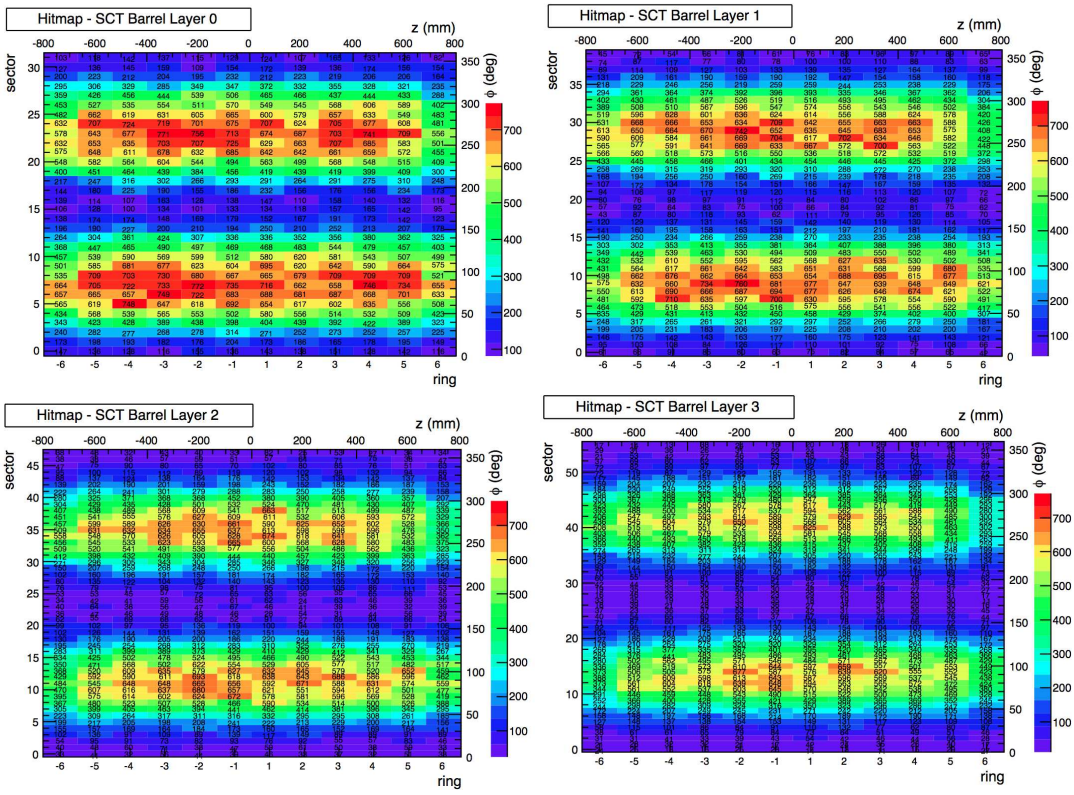

Figure E.2: Hit maps for the SCT layers. The numbers of the layers are ordered for inside to outside of the detector.

Track parameters:

Figure E.3 displays the impact transverse parameter (d_0) (left) and the longitudinal impact parameter (z_0) (right). Both parameters present flat distributions due to the flux distribution of the cosmic rays trough the detector. The shape of the d_0 can be understood since the generated sample was filtered to cross the innermost ID volume. The range of the z_0 distribution is mainly limited by the length of the SCT barrel detector (~850 mm).

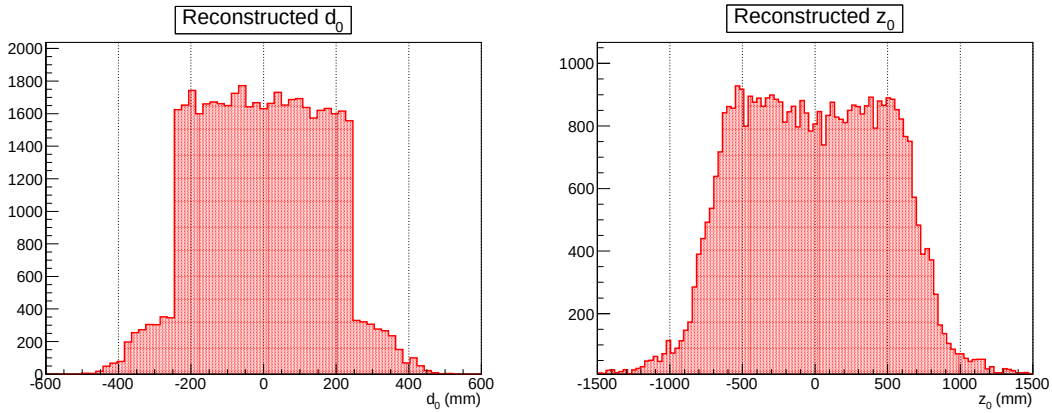

Figure E.3: Left: reconstructed d_0 distribution. Right: reconstructed z_0 distribution.

Figure E.4 shows the polar angle (θ_0) (left) and the pseudorapidity (η) (right). The two peaks present in both distributions correspond to the position of the cavern shafts and reflect the fact that particles could enter into the ATLAS cavern through the access of shafts more easily than through the rock.

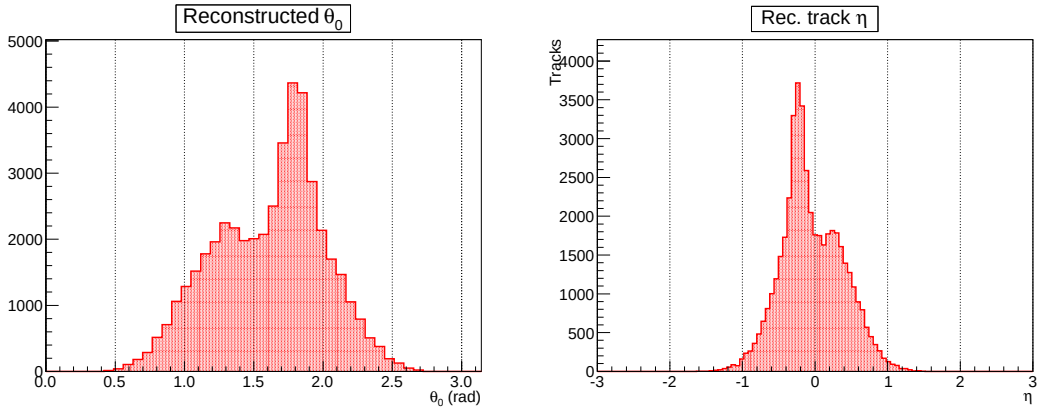

Figure E.4: Left: reconstructed θ distribution. Right: reconstructed η distribution.

Figure E.5 displays the reconstructed azimutal angle (ϕ_0) distribution (left) and the transverse momentum distribution multiplied by the charge of each particle ($q \cdot p_T$) (right). The ϕ_0 presents only one peak at -$\pi/2$ since the cosmic rays comes from the surface. The $q \cdot p_T$ distribution exhibits a μ^+/μ^- asymmetry

as expected since this ratio has been measured by other experiments [4]. Nevertheless, this asymmetry is higher in the low momentum bins due to the toroid deflecting μ^- coming from the shafts away from the ID.

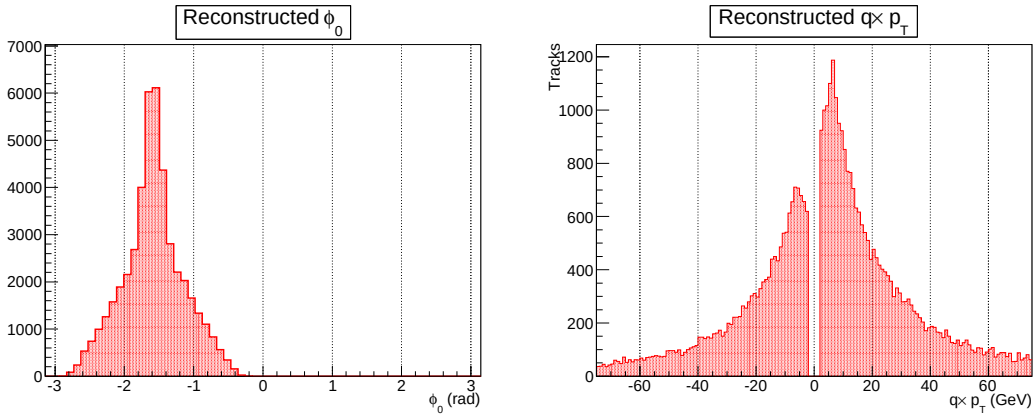

Figure E.5: Left: reconstructed ϕ_0 distribution. Right: reconstructed $q \cdot p_T$ distribution.

APPENDIX

F Top data and MC samples

This appendix summarizes the data and the MC samples used to perform the top-quark mass measurement presented in Chapter 5.

Data samples

The top-quark mass analysis has been done with the LHC data collected during 2011 at center of mass energy of 7 TeV. The used data amount to an integrate luminosity of 4.7 fb^{-1}. The official data files have been grouped according to the different data taking periods.

Electron data:

```
user.moles.DataContainer.data11_7TeV.periodBD.physics_Egamma.merge.NTUP_TOPEL.p937.v1
user.moles.DataContainer.data11_7TeV.periodEH.physics_Egamma.merge.NTUP_TOPEL.p937.v1
user.moles.DataContainer.data11_7TeV.periodI.physics_Egamma.merge.NTUP_TOPEL.p937.v1
user.moles.DataContainer.data11_7TeV.periodJ.physics_Egamma.merge.NTUP_TOPEL.p937.v1
user.moles.DataContainer.data11_7TeV.periodK.physics_Egamma.merge.NTUP_TOPEL.p937.v1
user.moles.DataContainer.data11_7TeV.periodLM.physics_Egamma.merge.NTUP_TOPEL.p937.v1
```

Muon data:

```
user.moles.DataContainer.data11_7TeV.periodBD.physics_Muons.merge.NTUP_TOPMU.p937.v1
user.moles.DataContainer.data11_7TeV.periodEH.physics_Muons.merge.NTUP_TOPMU.p937.v1
user.moles.DataContainer.data11_7TeV.periodI.physics_Muons.merge.NTUP_TOPMU.p937.v1
user.moles.DataContainer.data11_7TeV.periodJ.physics_Muons.merge.NTUP_TOPMU.p937.v1
user.moles.DataContainer.data11_7TeV.periodK.physics_Muons.merge.NTUP_TOPMU.p937.v1
user.moles.DataContainer.data11_7TeV.periodLM.physics_Muons.merge.NTUP_TOPMU.p937.v1
```

$t\bar{t}$ signal MC samples

The baseline $t\bar{t}$ sample has been produced with full mc11c simulation at m_{top}=172.5 GeV with a statistics of 10 M of events. It has been generated with POWHEG with CT10 pdf. The parton shower and underlying event has been modelled using PYTHIA with the Perugia 2011C tune. The dataset name corresponds to:

```
mc11_7TeV.117050.TTbar_PowHeg_Pythia_P2011C.merge.NTUP_TOP.e1377_s1372_s1370_r3108_r3109_p937/
```

Additional $t\bar{t}$ samples have been produced with different top-quark masses ranging from 165 GeV until 180 GeV. All those samples have been also generated with PowHeg+Pythia with Perugia P2011C tune. The statistics is about 5 M of events per sample. These ones can be identified as:

```
mc11_7TeV.117836.TTbar_MT1650_PowHeg_Pythia_P2011C.merge.NTUP_TOP.e1736_s1372_s1370_r3108_r3109_p937/
mc11_7TeV.117838.TTbar_MT1675_PowHeg_Pythia_P2011C.merge.NTUP_TOP.e1736_s1372_s1370_r3108_r3109_p937/
mc11_7TeV.117840.TTbar_MT1700_PowHeg_Pythia_P2011C.merge.NTUP_TOP.e1736_s1372_s1370_r3108_r3109_p937/
mc11_7TeV.117842.TTbar_MT1750_PowHeg_Pythia_P2011C.merge.NTUP_TOP.e1736_s1372_s1370_r3108_r3109_p937/
mc11_7TeV.117844.TTbar_MT1775_PowHeg_Pythia_P2011C.merge.NTUP_TOP.e1736_s1372_s1370_r3108_r3109_p937/
mc11_7TeV.117846.TTbar_MT1800_PowHeg_Pythia_P2011C.merge.NTUP_TOP.e1736_s1372_s1370_r3108_r3109_p937/
```

Background MC samples

Different SM physics backgrounds have been simulated to estimate their contribution in the final m_{top} measurement:

Single top

The single top samples have been generated using PowHeg+Pythia with Perugia P2011C tune for s-channel and Wt production while the t-channel has used Alpgen with Pythia P2011C tune. They are identified as:

```
mc11_7TeV.110101.AcerMCPythia_P2011CCTEQ6L1_singletop_tchan_lept.merge.NTUP_TOP.e1682_a131_s1353
_a145_r2993_p937/
mc11_7TeV.110119.st_schan_Powheg_Pythia_P2011C.merge.NTUP_TOP.e1778_s1372_s1370_r3108_r3109_p937/
mc11_7TeV.110140.st_Wtchan_incl_DR_PowHeg_Pythia_P2011C.merge.NTUP_TOP.e1778_s1372_s1370_r3108_
r3109_p937/
```

The single top mass variation samples have been produced using AFII mc11c and the m_{top} ranging from 165 GeV until 180 GeV. The corresponding identifiers are the following:

```
ntuple_mc11_7TeV.110123.st_schan_PowHeg_Pythia_P2011C_mt_165.merge.NTUP_TOP.e1778_a131_s1353_a145
_r2993_p937
ntuple_mc11_7TeV.110125.st_schan_PowHeg_Pythia_P2011C_mt_167p5.merge.NTUP_TOP.e1778_a131_s1353_a145
_r2993_p937
ntuple_mc11_7TeV.110127.st_schan_PowHeg_Pythia_P2011C_mt_170.merge.NTUP_TOP.e1778_a131_s1353_a145
_r2993_p937
ntuple_mc11_7TeV.110129.st_schan_PowHeg_Pythia_P2011C_mt_175.merge.NTUP_TOP.e1778_a131_s1353_a145
_r2993_p937
ntuple_mc11_7TeV.110131.st_schan_PowHeg_Pythia_P2011C_mt_177p5.merge.NTUP_TOP.e1778_a131_s1353_a145
_r2993_p937
ntuple_mc11_7TeV.110133.st_schan_PowHeg_Pythia_P2011C_mt_180.merge.NTUP_TOP.e1778_a131_s1353_a145
_r2993_p937
mc11_7TeV.110113.AcerMCPythia_P2011CCTEQ6L1_singletop_tchan_lept_mt165GeV.merge.NTUP_TOP.e1682_a131
_s1353_a145_r2993_p937
mc11_7TeV.110114.AcerMCPythia_P2011CCTEQ6L1_singletop_tchan_lept_mt167p5GeV.merge.NTUP_TOP.e1682_a131
_s1353_a145_r2993_p937
mc11_7TeV.110115.AcerMCPythia_P2011CCTEQ6L1_singletop_tchan_lept_mt170GeV.merge.NTUP_TOP.e1682_a131
_s1353_a145_r2993_p937
mc11_7TeV.110116.AcerMCPythia_P2011CCTEQ6L1_singletop_tchan_lept_mt175GeV.merge.NTUP_TOP.e1682_a131
_s1353_a145_r2993_p937
mc11_7TeV.110117.AcerMCPythia_P2011CCTEQ6L1_singletop_tchan_lept_mt177p5GeV.merge.NTUP_TOP.e1682_a131
_s1353_a145_r2993_p937
mc11_7TeV.110118.AcerMCPythia_P2011CCTEQ6L1_singletop_tchan_lept_mt180GeV.merge.NTUP_TOP.e1682_a131
_s1353_a145_r2993_p937
mc11_7TeV.110124.st_Wtchan_incl_DR_Powheg_Pythia_P2011C_mt_165.merge.NTUP_TOP.e1778_a131_s1353_
a145_r2993_p937
mc11_7TeV.110126.st_Wtchan_incl_DR_Powheg_Pythia_P2011C_mt_167p5.merge.NTUP_TOP.e1778_a131_s1353_
```

```
a145_r2993_p937
mc11_7TeV.110128.st_Wtchan_incl_DR_Powheg_Pythia_P2011C_mt_170.merge.NTUP_TOP.e1778_a131_s1353_
a145_r2993_p937
mc11_7TeV.110130.st_Wtchan_incl_DR_Powheg_Pythia_P2011C_mt_175.merge.NTUP_TOP.e1778_a131_s1353_
a145_r2993_p937
mc11_7TeV.110132.st_Wtchan_incl_DR_Powheg_Pythia_P2011C_mt_177p5.merge.NTUP_TOP.e1778_a131_s1353_
a145_r2993_p937
mc11_7TeV.110134.st_Wtchan_incl_DR_Powheg_Pythia_P2011C_mt_180.merge.NTUP_TOP.e1778_a131_s1353_
a145_r2993_p937
```

Diboson

The diboson processes (ZZ/WW/ZW) are produced at LO with lowest multiplicity final state using HERWIG standalone.

```
mc11_7TeV.105985.WW_Herwig.merge.NTUP_TOP.e825_s1310_s1300_r3043_r2993_p937/
mc11_7TeV.105986.ZZ_Herwig.merge.NTUP_TOP.e825_s1310_s1300_r3043_r2993_p937/
mc11_7TeV.105987.WZ_Herwig.merge.NTUP_TOP.e825_s1310_s1300_r3043_r2993_p937/
```

Z+jets

The Z boson production in association with jets is simulated using ALPGEN generator interfaced with HERWIG/JIMMY.

```
mc11_7TeV.107650.AlpgenJimmyZeeNp0_pt20.merge.NTUP_TOP.e835_s1299_s1300_r3043_r2993_p937
mc11_7TeV.107651.AlpgenJimmyZeeNp1_pt20.merge.NTUP_TOP.e835_s1299_s1300_r3043_r2993_p937
mc11_7TeV.107652.AlpgenJimmyZeeNp2_pt20.merge.NTUP_TOP.e835_s1299_s1300_r3043_r2993_p937
mc11_7TeV.107653.AlpgenJimmyZeeNp3_pt20.merge.NTUP_TOP.e835_s1299_s1300_r3043_r2993_p937
mc11_7TeV.107654.AlpgenJimmyZeeNp4_pt20.merge.NTUP_TOP.e835_s1299_s1300_r3043_r2993_p937
mc11_7TeV.107655.AlpgenJimmyZeeNp5_pt20.merge.NTUP_TOP.e835_s1299_s1300_r3043_r2993_p937
mc11_7TeV.107660.AlpgenJimmyZmumuNp0_pt20.merge.NTUP_TOP.e835_s1299_s1300_r3043_r2993_p937
mc11_7TeV.107661.AlpgenJimmyZmumuNp1_pt20.merge.NTUP_TOP.e835_s1299_s1300_r3043_r2993_p937
mc11_7TeV.107662.AlpgenJimmyZmumuNp2_pt20.merge.NTUP_TOP.e835_s1299_s1300_r3043_r2993_p937
mc11_7TeV.107663.AlpgenJimmyZmumuNp3_pt20.merge.NTUP_TOP.e835_s1299_s1300_r3043_r2993_p937
mc11_7TeV.107664.AlpgenJimmyZmumuNp4_pt20.merge.NTUP_TOP.e835_s1299_s1300_r3043_r2993_p937
mc11_7TeV.107664.AlpgenJimmyZmumuNp4_pt20.merge.NTUP_TOP.e835_s1299_s1300_r3043_r2993_p937
mc11_7TeV.107665.AlpgenJimmyZmumuNp5_pt20.merge.NTUP_TOP.e835_s1299_s1300_r3043_r2993_p937
mc11_7TeV.107670.AlpgenJimmyZtautauNp0_pt20.merge.NTUP_TOP.e835_s1299_s1300_r3043_r2993_p937
mc11_7TeV.107671.AlpgenJimmyZtautauNp1_pt20.merge.NTUP_TOP.e835_s1299_s1300_r3043_r2993_p937
mc11_7TeV.107672.AlpgenJimmyZtautauNp2_pt20.merge.NTUP_TOP.e835_s1299_s1300_r3043_r2993_p937
mc11_7TeV.107673.AlpgenJimmyZtautauNp3_pt20.merge.NTUP_TOP.e835_s1299_s1300_r3043_r2993_p937
mc11_7TeV.107674.AlpgenJimmyZtautauNp4_pt20.merge.NTUP_TOP.e835_s1299_s1300_r3043_r2993_p937
mc11_7TeV.107675.AlpgenJimmyZtautauNp5_pt20.merge.NTUP_TOP.e835_s1299_s1300_r3043_r2993_p937
mc11_7TeV.109300.AlpgenJimmyZeebbNp0_nofilter.merge.NTUP_TOP.e835_s1310_s1300_r3043_r2993_p937
mc11_7TeV.109301.AlpgenJimmyZeebbNp1_nofilter.merge.NTUP_TOP.e835_s1310_s1300_r3043_r2993_p937
mc11_7TeV.109302.AlpgenJimmyZeebbNp2_nofilter.merge.NTUP_TOP.e835_s1310_s1300_r3043_r2993_p937
mc11_7TeV.109303.AlpgenJimmyZeebbNp3_nofilter.merge.NTUP_TOP.e835_s1310_s1300_r3043_r2993_p937
mc11_7TeV.109305.AlpgenJimmyZmumubbNp0_nofilter.merge.NTUP_TOP.e835_s1310_s1300_r3043_r2993_p937
mc11_7TeV.109306.AlpgenJimmyZmumubbNp1_nofilter.merge.NTUP_TOP.e835_s1310_s1300_r3043_r2993_p937
mc11_7TeV.109307.AlpgenJimmyZmumubbNp2_nofilter.merge.NTUP_TOP.e835_s1310_s1300_r3043_r2993_p937
mc11_7TeV.109308.AlpgenJimmyZmumubbNp3_nofilter.merge.NTUP_TOP.e835_s1310_s1300_r3043_r2993_p937
mc11_7TeV.109310.AlpgenJimmyZtautaubbNp0_nofilter.merge.NTUP_TOP.e835_s1310_s1300_r3043_r2993_p937
mc11_7TeV.109311.AlpgenJimmyZtautaubbNp1_nofilter.merge.NTUP_TOP.e835_s1310_s1300_r3043_r2993_p937
mc11_7TeV.109312.AlpgenJimmyZtautaubbNp2_nofilter.merge.NTUP_TOP.e835_s1310_s1300_r3043_r2993_p937
mc11_7TeV.109313.AlpgenJimmyZtautaubbNp3_nofilter.merge.NTUP_TOP.e835_s1310_s1300_r3043_r2993_p937
mc11_7TeV.116250.AlpgenJimmyZeeNp0_Mll10to40_pt20.merge.NTUP_TOP.e959_s1310_s1300_r3043_r2993_p937
mc11_7TeV.116251.AlpgenJimmyZeeNp1_Mll10to40_pt20.merge.NTUP_TOP.e959_s1310_s1300_r3043_r2993_p937
mc11_7TeV.116252.AlpgenJimmyZeeNp2_Mll10to40_pt20.merge.NTUP_TOP.e944_s1310_s1300_r3043_r2993_p937
mc11_7TeV.116253.AlpgenJimmyZeeNp3_Mll10to40_pt20.merge.NTUP_TOP.e944_s1310_s1300_r3043_r2993_p937
mc11_7TeV.116254.AlpgenJimmyZeeNp4_Mll10to40_pt20.merge.NTUP_TOP.e944_s1310_s1300_r3043_r2993_p937
mc11_7TeV.116255.AlpgenJimmyZeeNp5_Mll10to40_pt20.merge.NTUP_TOP.e944_s1310_s1300_r3043_r2993_p937
mc11_7TeV.116260.AlpgenJimmyZmumuNp0_Mll10to40_pt20.merge.NTUP_TOP.e959_s1310_s1300_r3043_r2993_p937
mc11_7TeV.116261.AlpgenJimmyZmumuNp1_Mll10to40_pt20.merge.NTUP_TOP.e959_s1310_s1300_r3043_r2993_p937
mc11_7TeV.116262.AlpgenJimmyZmumuNp2_Mll10to40_pt20.merge.NTUP_TOP.e944_s1310_s1300_r3043_r2993_p937
mc11_7TeV.116263.AlpgenJimmyZmumuNp3_Mll10to40_pt20.merge.NTUP_TOP.e944_s1310_s1300_r3043_r2993_p937
mc11_7TeV.116264.AlpgenJimmyZmumuNp4_Mll10to40_pt20.merge.NTUP_TOP.e944_s1310_s1300_r3043_r2993_p937
mc11_7TeV.116265.AlpgenJimmyZmumuNp5_Mll10to40_pt20.merge.NTUP_TOP.e944_s1310_s1300_r3043_r2993_p937
```

W+jets

The W boson production in association with jets is simulated using ALPGEN generator interfaced with HERWIG/JIMMY.

```
mc11_7TeV.107280.AlpgenJimmyWbbFullNp0_pt20.merge.NTUP_TOP.e887_s1310_s1300_r3043_r2993_p937/
mc11_7TeV.107281.AlpgenJimmyWbbFullNp1_pt20.merge.NTUP_TOP.e887_s1310_s1300_r3043_r2993_p937/
mc11_7TeV.107282.AlpgenJimmyWbbFullNp2_pt20.merge.NTUP_TOP.e887_s1310_s1300_r3043_r2993_p937/
mc11_7TeV.107283.AlpgenJimmyWbbFullNp3_pt20.merge.NTUP_TOP.e887_s1310_s1300_r3043_r2993_p937/
mc11_7TeV.117284.AlpgenWccFullNp0_pt20.merge.NTUP_TOP.e887_s1310_s1300_r3043_r2993_p937/
mc11_7TeV.117285.AlpgenWccFullNp1_pt20.merge.NTUP_TOP.e887_s1310_s1300_r3043_r2993_p937/
mc11_7TeV.117286.AlpgenWccFullNp2_pt20.merge.NTUP_TOP.e887_s1310_s1300_r3043_r2993_p937/
mc11_7TeV.117287.AlpgenWccFullNp3_pt20.merge.NTUP_TOP.e887_s1310_s1300_r3043_r2993_p937/
mc11_7TeV.117293.AlpgenWcNp0_pt20.merge.NTUP_TOP.e887_s1310_s1300_r3043_r2993_p937/
mc11_7TeV.117294.AlpgenWcNp1_pt20.merge.NTUP_TOP.e887_s1310_s1300_r3043_r2993_p937/
mc11_7TeV.117295.AlpgenWcNp2_pt20.merge.NTUP_TOP.e887_s1310_s1300_r3043_r2993_p937/
mc11_7TeV.117296.AlpgenWcNp3_pt20.merge.NTUP_TOP.e887_s1310_s1300_r3043_r2993_p937/
mc11_7TeV.117297.AlpgenWcNp4_pt20.merge.NTUP_TOP.e887_s1310_s1300_r3043_r2993_p937/
mc11_7TeV.107680.AlpgenJimmyWenuNp0_pt20.merge.NTUP_TOP.e825_s1299_s1300_r3043_r2993_p937/
mc11_7TeV.107681.AlpgenJimmyWenuNp1_pt20.merge.NTUP_TOP.e825_s1299_s1300_r3043_r2993_p937/
mc11_7TeV.107682.AlpgenJimmyWenuNp2_pt20.merge.NTUP_TOP.e825_s1299_s1300_r3043_r2993_p937/
mc11_7TeV.107683.AlpgenJimmyWenuNp3_pt20.merge.NTUP_TOP.e825_s1299_s1300_r3043_r2993_p937/
mc11_7TeV.107684.AlpgenJimmyWenuNp4_pt20.merge.NTUP_TOP.e825_s1299_s1300_r3043_r2993_p937/
mc11_7TeV.107685.AlpgenJimmyWenuNp5_pt20.merge.NTUP_TOP.e825_s1299_s1300_r3043_r2993_p937/
mc11_7TeV.107690.AlpgenJimmyWmunuNp0_pt20.merge.NTUP_TOP.e825_s1299_s1300_r3043_r2993_p937/
mc11_7TeV.107691.AlpgenJimmyWmunuNp1_pt20.merge.NTUP_TOP.e825_s1299_s1300_r3043_r2993_p937/
mc11_7TeV.107692.AlpgenJimmyWmunuNp2_pt20.merge.NTUP_TOP.e825_s1299_s1300_r3043_r2993_p937/
mc11_7TeV.107693.AlpgenJimmyWmunuNp3_pt20.merge.NTUP_TOP.e825_s1299_s1300_r3043_r2993_p937/
mc11_7TeV.107694.AlpgenJimmyWmunuNp4_pt20.merge.NTUP_TOP.e825_s1299_s1300_r3043_r2993_p937/
mc11_7TeV.107695.AlpgenJimmyWmunuNp5_pt20.merge.NTUP_TOP.e825_s1299_s1300_r3043_r2993_p937/
mc11_7TeV.107700.AlpgenJimmyWtaunuNp0_pt20.merge.NTUP_TOP.e835_s1299_s1300_r3043_r2993_p937/
mc11_7TeV.107701.AlpgenJimmyWtaunuNp1_pt20.merge.NTUP_TOP.e835_s1299_s1300_r3043_r2993_p937/
mc11_7TeV.107702.AlpgenJimmyWtaunuNp2_pt20.merge.NTUP_TOP.e835_s1299_s1300_r3043_r2993_p937/
mc11_7TeV.107703.AlpgenJimmyWtaunuNp3_pt20.merge.NTUP_TOP.e835_s1299_s1300_r3043_r2993_p937/
mc11_7TeV.107704.AlpgenJimmyWtaunuNp4_pt20.merge.NTUP_TOP.e835_s1299_s1300_r3043_r2993_p937/
mc11_7TeV.107705.AlpgenJimmyWtaunuNp5_pt20.merge.NTUP_TOP.e835_s1299_s1300_r3043_r2993_p937/
```

QCD multijets

The QCD multijet background has been estimated running the matrix method over real data. The files used are those summarized earlier in the section of **Data Samples**.

Systematic MC samples

Usually the systematic uncertainties are evaluated varying ± 1 standard deviation the parameters that affect the measurement. Many of them can be evaluated applying the variation directly over the baseline $t\bar{t}$ sample. Nevertheless, there are systematic variations that can not be introduced at ntuple level and specific MC samples have to be generated. These ones are explained here:

Signal MC generator

POWHEG and MC@NLO generator programs have been used to evaluate the systematic uncertainty. Both samples have been generated with AFII mc11b at m_{top}=172.5 GeV. In order to evaluate the generator contribution alone both samples have performed the hadronization using HERWIG.

```
mc11_7TeV.105860.TTbar_PowHeg_Jimmy.merge.NTUP_TOP.e1198_a131_s1353_a139_r2900_p937/
mc11_7TeV.105200.T1_McAtNlo_Jimmy.merge.NTUP_TOP.e835_a131_s1353_a139_r2900_p937/
```

Hadronization

This systematic is evaluated using samples with the same generator (PowHeg) and different hadronisation models. It compares AFII mc11b Pythia with P2011C tune and Herwig.

```
mc11_7TeV.117050.TTbar_PowHeg_Pythia_P2011C.merge.NTUP_TOP.e1377_a131_s1353_a139_r2900_p937/
mc11_7TeV.105860.TTbar_PowHeg_Jimmy.merge.NTUP_TOP.e1198_a131_s1353_a139_r2900_p937/
```

Underlying Event

Comparison of the AFII mc11c samples generated with PowHeg+Pythia with different settings for the parameters affecting the multiple parton interaction (MPI).

```
ntuple_mc11_7TeV.117428.TTbar_PowHeg_Pythia_P2011.merge.NTUP_TOP.e1683_a131_s1353_a145_r2993_p937/
ntuple_mc11_7TeV.117429.TTbar_PowHeg_Pythia_P2011mpiHi.merge.NTUP_TOP.e1683_a131_s1353_a145_r2993_p937/
```

Color Reconnection

Comparison of AFII mc11c samples generated with PowHeg+Pythia P2011C with different tunes affecting color reconnection.

```
ntuple_mc11_7TeV.117428.TTbar_PowHeg_Pythia_P2011.merge.NTUP_TOP.e1683_a131_s1353_a145_r2993_p937/
ntuple_mc11_7TeV.117430.TTbar_PowHeg_Pythia_P2011noCR.merge.NTUP_TOP.e1683_a131_s1353_a145_r2993_p937
```

Initial and Final QCD state radiation

Both samples were generated with AcerMC but differ in the amount of initial and final state radiation (more or less radiation).

```
ntuple_mc11_7TeV.117862.AcerMCttbar_Perugia2011C_MorePS.merge.NTUP_TOP.e1449_a131_s1353_a145_r2993_p937/
ntuple_mc11_7TeV.117863.AcerMCttbar_Perugia2011C_LessPS.merge.NTUP_TOP.e1449_a131_s1353_a145_r2993_p937/
```

Proton PDF

The default $t\bar{t}$ signal has been generated with CT10 PDF. In addition, the NNPDF23 and the MSTW2008 have been considered to evaluate the systematic uncertainty. A problem in the ntuple generation produced empty PDF variables. In order to fix it, the PDF variables were stored separately in the the following ntuple:

```
user.dta.powhegp4.105860.ttbar_7TeV.TXT.mc11_v1.PDF.v8/
```

APPENDIX

G Top reconstruction packages

The collision data and MC samples used to perform the top-quark mass analysis, have been reconstructed following the recommendation provided by the Top Reconstruction Group. The prescriptions for the analysis performed with the ATLAS 2011 collision data are described in: `https://twiki.cern.ch/twiki/bin/viewauth/AtlasProtected/TopReconstructionGroup#Recommendations_for_2011_rel_17`

The software packages used for reconstructing the different objects involved in the analysis are the followings:

Muons
atlasoff/PhysicsAnalysis/TopPhys/TopPhysUtils/TopMuonSFUtils/tags/TopMuonSFUtils-00-00-15
atlasoff/PhysicsAnalysis/MuonID/MuonIDAnalysis/MuonEfficiencyCorrections/tags/MuonEfficiencyCorrections-01-01-00
atlasoff/PhysicsAnalysis/MuonID/MuonIDAnalysis/MuonMomentumCorrections/tags/MuonMomentumCorrections-00-05-03

Electrons
atlasoff/PhysicsAnalysis/TopPhys/TopPhysUtils/TopElectronSFUtils/tags/TopElectronSFUtils-00-00-18
atlasoff/Reconstruction/egamma/egammaAnalysis/egammaAnalysisUtils/tags/egammaAnalysisUtils-00-02-81
atlasoff/Reconstruction/egamma/egammaEvent/tags/egammaEvent-03-06-19

Jets
atlasperf/CombPerf/FlavorTag/JetTagAlgorithms/MV1Tagger/tags/MV1Tagger-00-00-01
atlasoff/Reconstruction/Jet/ApplyJetCalibration/tags/ApplyJetCalibration-00-01-03
atlasperf/CombPerf/JetETMiss/JetCalibrationTools/ApplyJetResolutionSmearing/tags/ApplyJetResolutionSmearing-00-00-03
atlasoff/PhysicsAnalysis/TopPhys/TopPhysUtils/TopJetUtils/tags/TopJetUtils-00-00-07
atlasoff/Reconstruction/Jet/JetUncertainties/tags/JetUncertainties-00-05-07
/Reconstruction/Jet/JetResolution/tags/JetResolution-01-00-00
atlasoff/PhysicsAnalysis/JetTagging/JetTagPerformanceCalibration/CalibrationDataInterface/tags/CalibrationDataInterface-00-01-02
atlasoff/PhysicsAnalysis/TopPhys/TopPhysUtils/JetEffiProvider/tags/JetEffiProvider-00-00-04
atlasoff/PhysicsAnalysis/TopPhys/MultiJesInputFiles/tags/MultiJesInputFiles-00-00-01

Missing E_T
atlasoff/Reconstruction/MissingETUtility/tags/MissingETUtility-01-00-09

Event Weighting
atlasoff/PhysicsAnalysis/TopPhys/FakesMacros/tags/FakesMacros-00-00-32
atlasoff/PhysicsAnalysis/AnalysisCommon/PileupReweighting/tags/PileupReweighting-00-00-17
atlasoff/PhysicsAnalysis/TopPhys/TopPhysUtils/WjetsCorrections/tags/WjetsCorrections-00-00-08

Event Quality
atlasoff/DataQuality/GoodRunsLists/tags/GoodRunsLists-00-00-98

The correct implementation of these packages has been validated against the ”event challenge” pages in which the analysers confront their results and compare them with the reference ones. The numbers obtained by the analysers should agree with the reference ones within certain tolerances. These tolerances vary depending on the sample, from less than 1% for $t\bar{t}$ signal until 20% for QCD background.

The systematic uncertainties have been evaluated following the Top Group Systematic prescriptions reported in:
`https://twiki.cern.ch/twiki/bin/viewauth/AtlasProtected/TopSystematicUncertainties2011`

Appendix

H Selection of the hadronic W boson

In order to select the jet pair associated to the hadronically decaying W boson, some requirements were imposed (Section 5.5.1). The values for these cuts were selected taking into account the efficiency and the purity of the sample at each stage. These quantities were defined as follow:

$$\text{efficiency} = \frac{\text{\# events passing the cut}}{\text{\# events satisfying the } t\bar{t} \to \ell + \text{jets preselection}}$$

$$\text{purity} = \frac{\text{\# jet pairs with correct matching of the truth hadronic } W \to qq \text{ decay}}{\text{\# events passing the cut}}$$

As commented in Section 5.5.1, exactly two *b*-tagged jets were required in the analysis, providing an initial efficiency of ~43% and a purity of ~31%. After that, each of the applied cuts was studied within a range of possible values. The selection of a specific value was motivated by obtaining a larger rejection of the combinatorial background while retaining enough statistics to not compromise the analysis. Nevertheless, in some cuts, as the transverse momentum of the jets, also other effects related with the JES uncertainty were considered for choosing the value. The cuts were applied consecutively.

Figures H.1, H.2, H.3 and H.4 display the distributions of the observables related with the cuts after applying the previous ones and before evaluating them. These figures show the contributions of the good combinations (black) and combinatorial background (red).

Tables H.1, H.2, H.3, H.4 and H.5 summarize the efficiency and the purity for each cut. Notice that the efficiency is calculated always with respect to the events that satisfy the standard top pre-selection. The selected values are marked in gray.

The figures found at the end of this analysis were 14% and 54% for efficiency and purity respectively. Most of the statistics was rejected with the requirement of exactly two *b*-tagged jets and the mass window of the jet pair candidate.

Table H.1: Cut in the p_T of the leading light jet.

Channel	**e+jets**		**μ+jets**	
p_T (GeV)	Efficiency (%)	Purity (%)	Efficiency (%)	Purity (%)
25	43.2	31.2	43.1	31.3
30	42.8	31.3	42.7	31.4
35	41.8	31.6	41.6	31.7
40	40.1	31.8	40.0	31.9

Table H.2: Cut in the p_T of the second light jet.

Channel	**e+jets**		**μ+jets**	
p_T (GeV)	Efficiency (%)	Purity (%)	Efficiency (%)	Purity (%)
25	40.1	31.8	40.0	31.9
30	35.2	31.0	35.2	31.3
35	30.2	29.6	30.2	29.9
40	25.3	28.0	25.3	28.2

Table H.3: Cut in the ΔR of the jet pair candidate.

Channel	**e+jets**		**μ+jets**	
ΔR	Efficiency (%)	Purity (%)	Efficiency (%)	Purity (%)
3.1	33.6	32.5	33.6	32.7
3.0	32.8	33.1	32.8	33.4
2.9	31.5	34.1	31.5	34.4
2.8	30.0	35.0	30.0	35.4

Table H.4: Cut in the invariant mass of the jet pair candidate.

Channel	**e+jets**		**μ+jets**	
m_{jj} (GeV)	Efficiency (%)	Purity (%)	Efficiency (%)	Purity (%)
25	21.0	48.7	21.2	48.8
20	19.2	51.1	19.3	51.4
15	16.6	53.6	16.7	53.8
10	12.8	55.8	12.9	55.7

Table H.5: Cut in the χ^2.

Channel	**e+jets**		**μ+jets**	
χ^2	Efficiency (%)	Purity (%)	Efficiency (%)	Purity (%)
40	16.0	54.0	16.1	54.1
30	15.3	54.1	15.4	54.3
20	14.1	54.3	14.1	54.5
10	11.2	54.6	11.3	54.7

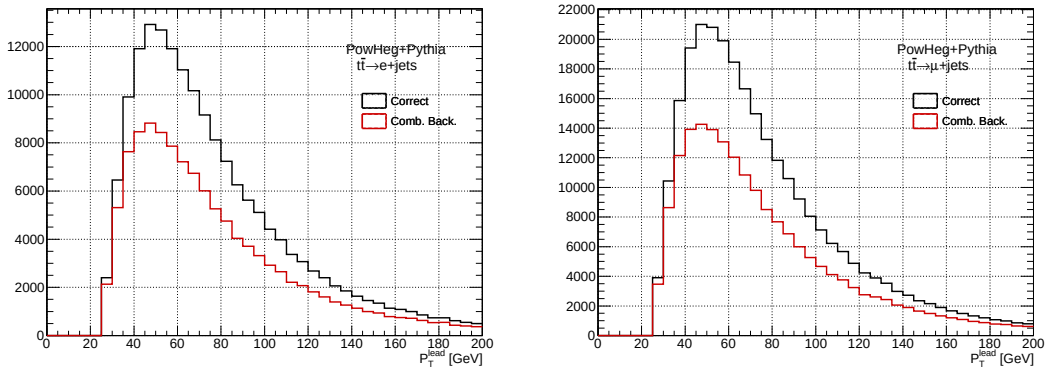

Figure H.1: p_T of the leading jet of the pair for the e + *jets* (left) and the μ + *jets* (right) channel.

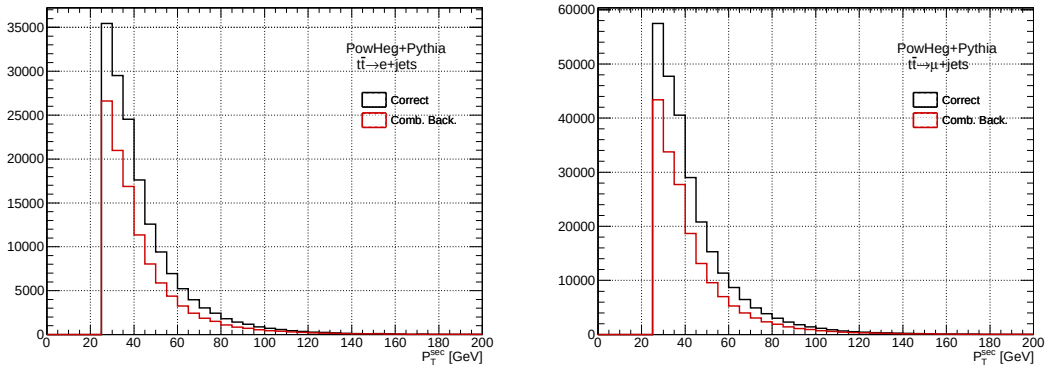

Figure H.2: p_T of the second jet fro the e + *jets* (left) and μ + *jets* (right) channel.

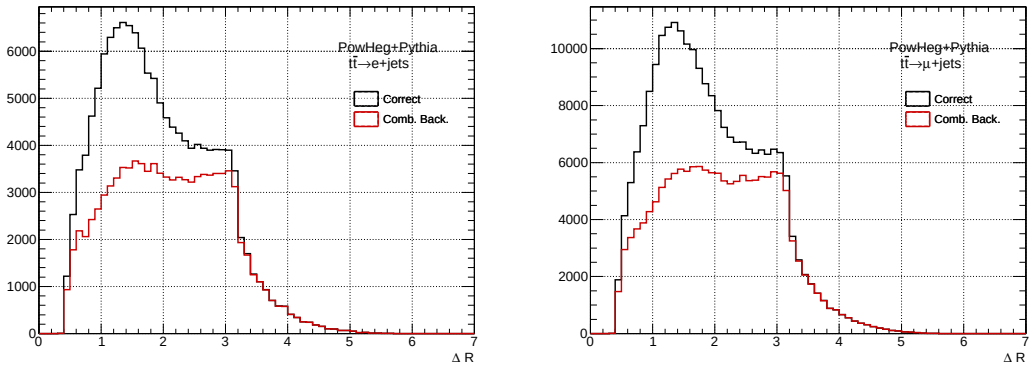

Figure H.3: ΔR between the light jets for the $e + jets$ (left) and $\mu + jets$ (right) channel.

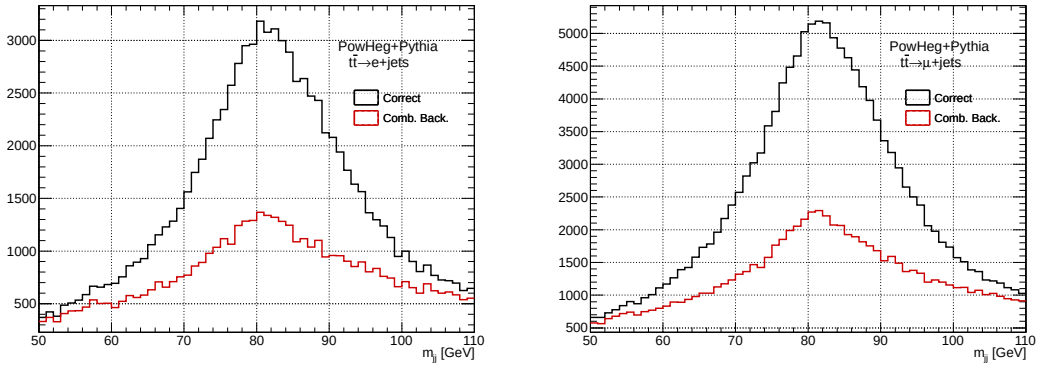

Figure H.4: Invariant mass of the jet pair candidate for the $e + jets$ (left) and $\mu + jets$ (right) channel.

APPENDIX

I In-situ calibration with the hadronic W

The in-situ calibration corrections (α_1, α_2) have been calculated for all events passing the cuts in Section 5.5.1 and their final distributions are shown in Figure 5.8. Here, these distributions are plotted again in Figure I.1 but presented separately for correct combinations (green) and combinatorial background (red).

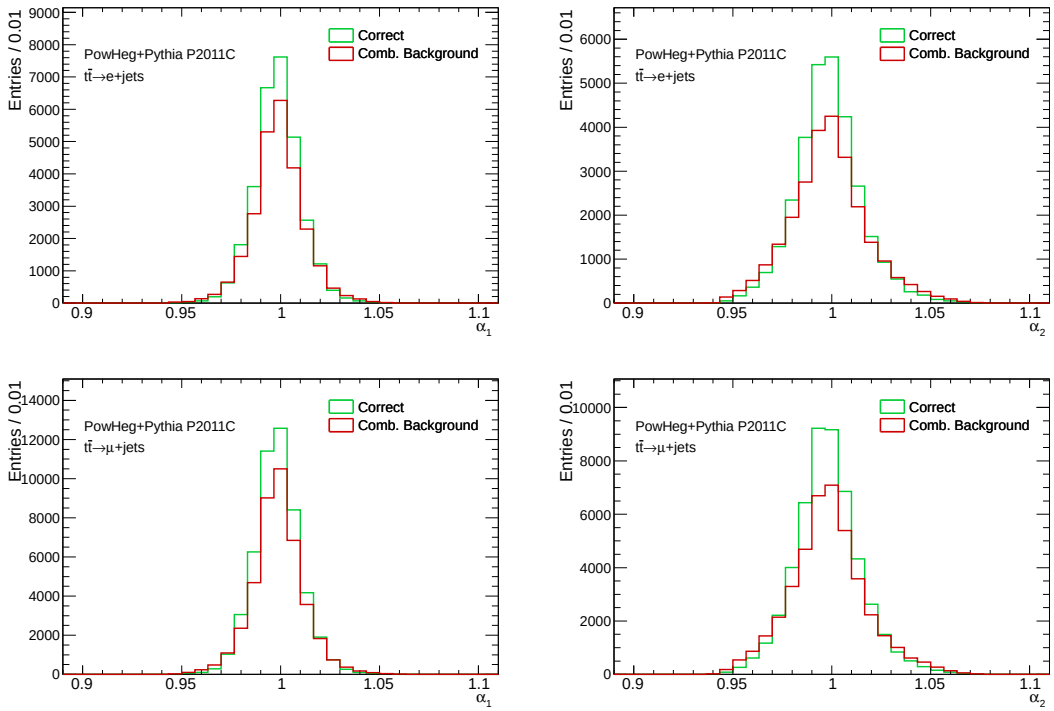

Figure I.1: $t\bar{t} \to \ell + jets$ MC correction factors α_1 (left) and α_2 (right) obtained from the in-situ calibration fit of the hadronically decaying W for the e+jets channel (upper row) and μ+jets channel (bottom row).

The fitted mass of the hadronic W candidate is also displayed separately for the correct and combinatorial background events in Figure I.2. The m_{jj} distributions are shown under two conditions: with (right) and without (left) in-situ calibration factors applied. The impact of the calibration is clearly seen

as the corresponding m_{jj} distributions becomes narrower. The combinatorial background exhibits broader distributions than the correct combinations.

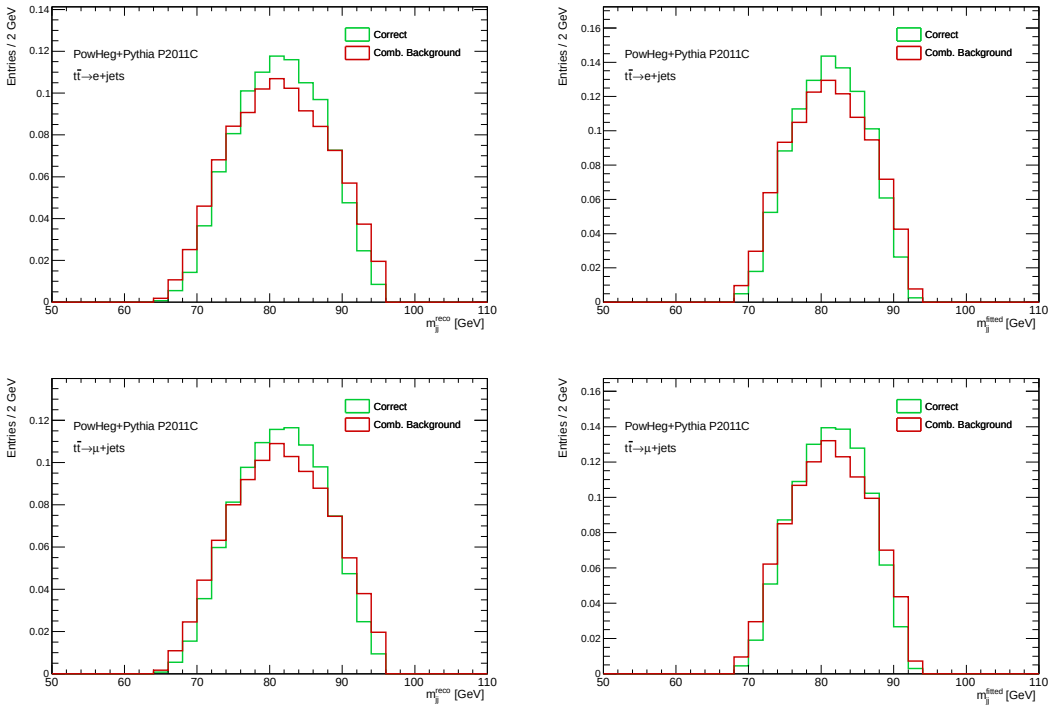

Figure I.2: MC study of the invariant mass of the jets associated to the hadronically decaying W in the $t\bar{t} \to e$ + jets channel (upper row) and $t\bar{t} \to \mu$ + jets channel (bottom row). Left: with the reconstructed jets before the in-situ calibration. Right: with the jets after the in-situ calibration.

APPENDIX

J

Hadronic W boson mass for determining the jet energy scale factor

Figure 5.10 presents the computed m_{jj} in data and $t\bar{t} \rightarrow \ell + jets$ MC. It shows a bias in the MC compared with data. The observed mismatch is attributed to a different jet energy calibration between both. This unbalance must be corrected for the proper use of the template method. Otherwise a bias in the m_{top} could be introduced. The m_{jj} is a good reference as it should be independent of the m_{top} and can be used to extract a robust jet energy scale factor.

Hence, a linearity test of the m_{jj} was performed using different MC samples with varying the m_{top} generated value. For each sample, the m_{jj} mean value (μ) was extracted by fitting the distribution with the following model:

- a Gaussian shape for the correct jet-pairs.
- a Novosibirsk distribution to shape the combinatorial background contribution.
- the fraction of signal and background is taken from the MC.

The independence and robustness of the m_{jj} was studied under two conditions:

- from those distributions constructed with the reconstructed jets (Figure J.1).
- from those distributions constructed with the jets once their energy have been corrected (Figure 5.11 in Section 5.5.1).

The results are presented in Figure J.1. They prove that this observable is robust and independent of the top-quark mass. Therefore, one can average all the mass points to extract a m_W mass in MC with all the available statistics. When that m_W mass is confronted with M_W^{PDG} a small deviation is found. The ratio $\alpha_{\text{JES}}^{\text{MC}} = m_W^{fitted}/M_W^{PDG}$ is presented in Table 5.3 in section 5.5.1.

This methodology needs to extract the $\alpha_{\text{JES}}^{\text{data}}$ from the fitted mass value (m_W^{fitted}) in real data (Figure 5.10). It must be said that the fitting of the real data distributions (which also contains correct and combinatorial background combinations plus the physics background) is improved by relating some parameters following the same ratios as in the MC fit (that is the means and the sigmas of the correct and combinatorial background as they are independent of m_{top}). Figure J.2 shows the relation between these parameters. The fraction of signal and combinatorial background was taken to be the average of the $1 - \epsilon$ [1] versus different mass points fit. These values correspond to ~55% for e+jets and μ+jets channels.

[1] ϵ is the fraction of correct combinations.

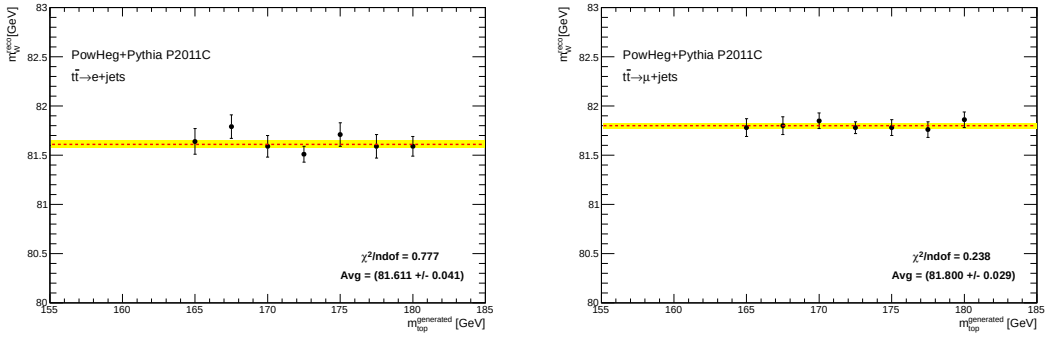

Figure J.1: Invariant mass of the reconstructed hadronically decaying W jet pair candidate versus $m_{\text{top}}^{\text{generated}}$ for $e + jets$ (left) and $\mu + jets$ (right) channels.

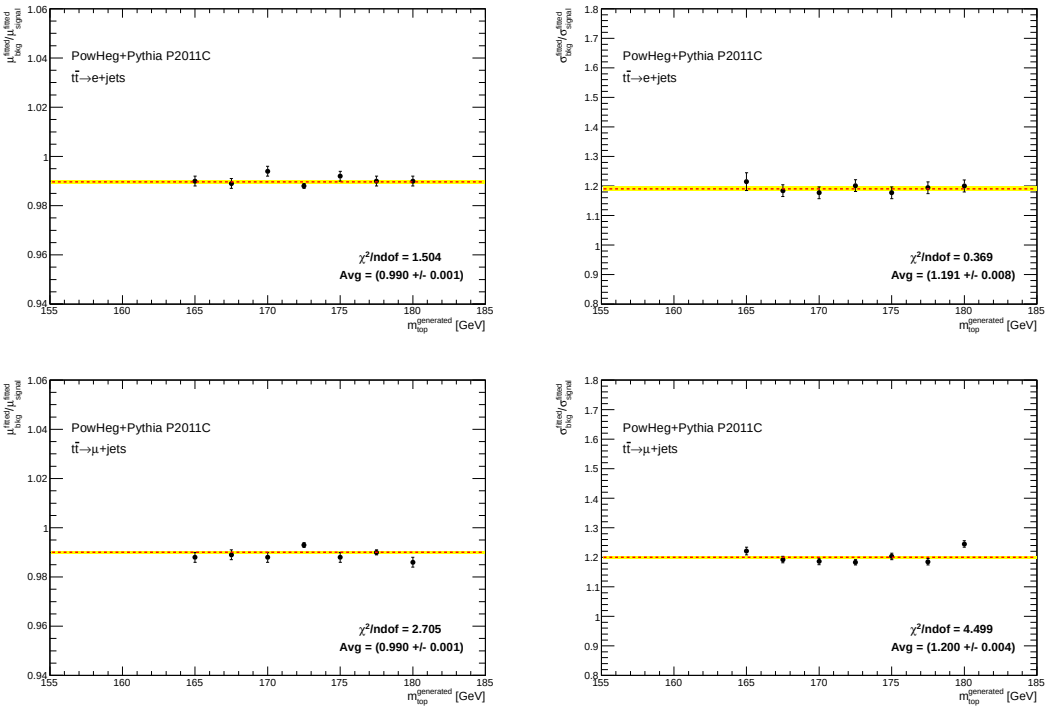

Figure J.2: Left: ratio between the mean of the combinatorial background and the mean of the correct combinations ($\mu_{bkg}^{fitted}/\mu_{signal}^{fitted}$). Right: ratio between the sigma of the combinatorial background and the sigma of the correct combinations ($\sigma_{bkg}^{fitted}/\sigma_{signal}^{fitted}$). The results are shown for the e+jets (upper row) and μ+jets (bottom row) channels.

Appendix

K Determination of neutrino's p_Z

The reconstruction of the leptonicaly decaying W is difficult because the ν escapes undetected. The $W \to \ell\nu$ decay leads to $E_{\mathrm{T}}^{\mathrm{miss}}$ in the event which here is attributed in full to the neutrino p_T. On the other hand, the longitudinal component of the ν momentum (p_z) has to be inferred from the energy-momentum conservation. The method used here is the same as in [138]:

$$W \to \ell\nu \quad \longrightarrow \quad p^W = p^\ell + p^\nu$$
$$\left(p^W\right)^2 = \left(p^\ell + p^\nu\right)^2 \quad \longrightarrow \quad M_W^2 = m_\ell^2 + 2(E^\ell, \boldsymbol{p}^\ell)\cdot(E^\nu, \boldsymbol{p}^\nu) + m_\nu^2 \tag{K.1}$$

In what follows, the tiny neutrino mass is neglected ($m_\nu \approx 0$). Also, the assumption is made that $p_T^\nu = E_{\mathrm{T}}^{\mathrm{miss}}$, thus the neutrino flies along the $E_{\mathrm{T}}^{\mathrm{miss}}$ direction. Basic relations are then:

$$p_x^\nu = E_{\mathrm{T}}^{\mathrm{miss}} \cos\phi_{E_{\mathrm{T}}^{\mathrm{miss}}} \quad \text{and} \quad p_y^\nu = E_{\mathrm{T}}^{\mathrm{miss}} \sin\phi_{E_{\mathrm{T}}^{\mathrm{miss}}}$$
$$E_\nu = \sqrt{E_{\mathrm{T}}^{\mathrm{miss}} + (p_z^\nu)^2}$$

Therefore the Equation K.1 can be written as follows:

$$M_W^2 = m_\ell^2 + 2E_\ell\sqrt{E_{\mathrm{T}}^{\mathrm{miss}} + (p_z^\nu)^2} - 2\left(p_x^\ell p_x^\nu + p_y^\ell p_y^\ell + p_z^\ell p_z^\nu\right)$$

where all the terms are known except p_z^ν, which is going to be computed solving the equation. For convenience one can write it down as a quadratic equation, where $(m_T^\ell)^2 = E_\ell^2 - (p_z^\ell)^2$ is the lepton transverse mass:

$$A(p_z^\nu)^2 + Bp_z^\nu + C = 0 \longrightarrow \begin{cases} A = (m_T^\ell)^2 \\ B = p_z^\ell\left(m_\ell^2 - M_W^2 - 2(p_x^\ell p_x^\nu + p_y^\ell p_y^\nu)\right) \\ C = E_\ell^2(E_{\mathrm{T}}^{\mathrm{miss}})^2 - \frac{1}{4}\left(M_W^2 - m_\ell^2 + 2(p_x^\ell p_x^\nu + p_y^\ell p_y^\nu)\right)^2 \end{cases}$$

Thus p_z^ν has two possible solutions:

$$p_z^\nu = -\frac{p_z^\ell\left(m_\ell^2 - M_W^2 - 2(p_x^\ell p_x^\nu + p_y^\ell p_y^\nu)\right)}{2(m_T^\ell)^2} \pm \frac{E_\ell\sqrt{\left[\left(M_W^2 - m_\ell^2 + 2(p_x^\ell p_x^\nu + p_y^\ell p_y^\nu)\right)^2 - 4(E_{\mathrm{T}}^{\mathrm{miss}})^2(m_T^\ell)^2\right]}}{2(m_T^\ell)^2} \tag{K.2}$$

Of the two p_z^ν solutions, only one did materialized in the event. The event analysis tries to distinguish which one is physical and which only mathematical.

Figure K.1 shows the graphical representation of the two p_z^ν solutions for different events. The red function describes the quadratic difference of the computed M_W with Equation K.1 and M_W^{PDG} as a function of the p_z^ν. The two minima, marked with black lines, correspond to the p_z^ν solutions (remember that

the p_z^νused was chosen according to the criteria given in Section 5.5.4). The blue line indicates the truth value and the green line corresponds to the computed one after the Globalχ^2 fit. Therefore, the figure on the left displays an event with a correct p_z^ν determination while figure on the right shows a wrong p_z^ν association.

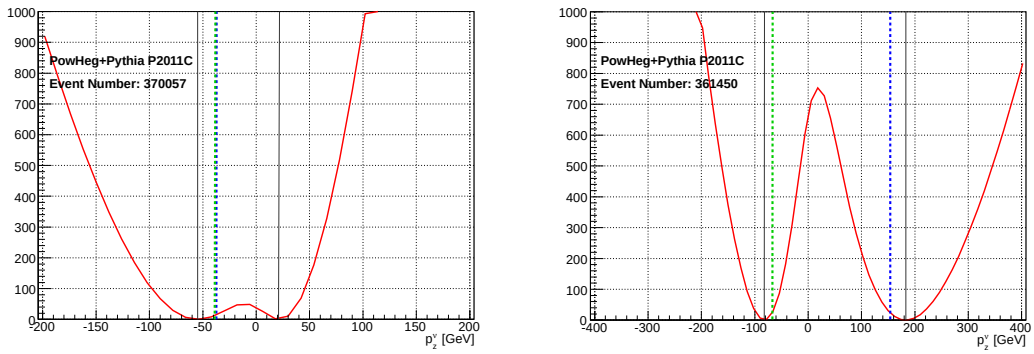

Figure K.1: Quadratic difference between the computed M_W and M_W^{PDG} ($(M_W(p_z^\nu) - M_W^{PDG})^2$) as a function of the p_z^ν. Left: Event with good p_z^ν selection since the final solution (green line) agrees with the truth value (blue line). Right: Event with wrong p_z^ν selection.

These solutions rely on the assumption that the neutrino is the only contributor to $E_{\mathrm{T}}^{\mathrm{miss}}$, which is not always the case. Moreover, under certain circumstances (detector resolution, particle misidentification, etc) the radicand of Equation K.2 is found to be negative and in principle no solution is available. In order to find a possible solution one must rescale the $E_{\mathrm{T}}^{\mathrm{miss}}$ in such a way that the radicand becomes null and at least one p_z^ν is found. Therefore, one has to recompute $E_{\mathrm{T}}^{\mathrm{miss}}$ value with the prescription of keeping the same direction $\phi_{E_{\mathrm{T}}^{\mathrm{miss}\prime}} = \phi_{E_{\mathrm{T}}^{\mathrm{miss}}}$. Of course, $E_{\mathrm{T}}^{\mathrm{miss}\prime}$ is the solution of the following quadratic equation:

$$\left[\left(M_W^2 - m_\ell^2 + 2(p_x^\ell E_{\mathrm{T}}^{\mathrm{miss}\prime}\cos\phi_{E_{\mathrm{T}}^{\mathrm{miss}}} + p_y^\ell E_{\mathrm{T}}^{\mathrm{miss}\prime}\sin\phi_{E_{\mathrm{T}}^{\mathrm{miss}}})\right)^2 - 4(E_{\mathrm{T}}^{\mathrm{miss}\prime})^2(m_T^\ell)^2\right] = 0$$

which again has two solutions:

$$E_{\mathrm{T}}^{\mathrm{miss}\prime} = \frac{\left(m_\ell^2 - m_W^2\right)\left[-\left(p_x^\ell\cos\phi_{E_{\mathrm{T}}^{\mathrm{miss}}} + p_y^\ell\sin\phi_{E_{\mathrm{T}}^{\mathrm{miss}}}\right) \pm (m_T^\ell)^2\right]}{2\left[(m_T^\ell)^2 - \left(p_x^\ell\cos\phi_{E_{\mathrm{T}}^{\mathrm{miss}}} + p_y^\ell\sin\phi_{E_{\mathrm{T}}^{\mathrm{miss}}}\right)\right]} \tag{K.3}$$

but only the positive solution is retained.

K.1 $E_{\mathrm{T}}^{\mathrm{miss}}$ when no p_z^ν solution is found.

As mentioned above, about 35% of the events have a negative value for the radicand of Equation K.2. That would mean that the p_z^ν would become complex.

On one hand, the charged lepton is usually very well reconstructed. On the other hand, the neutrino four-momentum is inferred from the reconstructed[1] $E_{\mathrm{T}}^{\mathrm{miss}}$. In this way, problems in the p_z^ν calculation point to a defective $E_{\mathrm{T}}^{\mathrm{miss}}$ determination.

[1]Of course, there is no such a thing like the reconstructed $E_{\mathrm{T}}^{\mathrm{miss}}$. This is an abuse of language to simplify the notation. The computation of the $E_{\mathrm{T}}^{\mathrm{miss}}$ is explained in Section 3.3.

Apart form the mathematical argument given above, in order to check that the $E_{\mathrm{T}}^{\mathrm{miss}}$ needs effectively a rescaling is by comparing the reconstructed $E_{\mathrm{T}}^{\mathrm{miss}}$ with the true neutrino properties (which are accessible in the MC.) Figure K.2 presents that comparison. As one can see, there are good reasons to rescale the $E_{\mathrm{T}}^{\mathrm{miss}}$ because the reconstructed one overestimates the p_{T}^{ν}. On the other hand, the $E_{\mathrm{T}}^{\mathrm{miss}}$ rescaling seems to work quite accurately as shown in Figure 5.13.

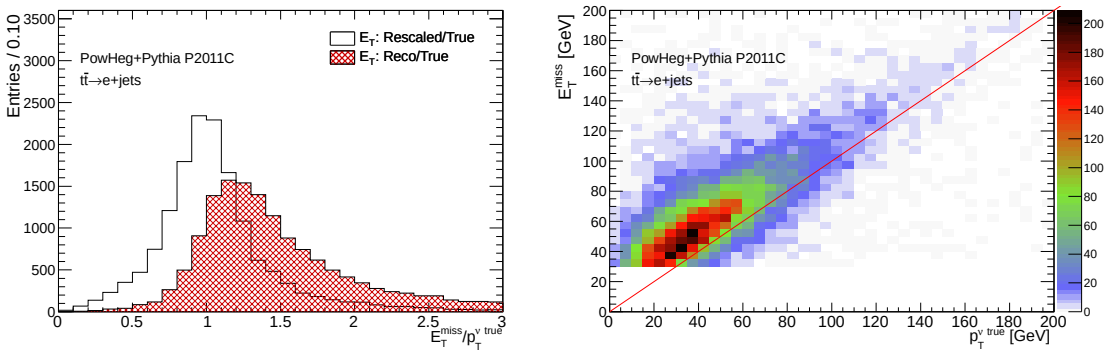

Figure K.2: Evaluation of the raw $E_{\mathrm{T}}^{\mathrm{miss}}$ for those events with initially complex solution for p_z^{ν}. Left: comparison of the raw reconstructed $E_{\mathrm{T}}^{\mathrm{miss}}/p_{\mathrm{T}}^{\nu\ \mathrm{true}}$ (red histogram) with the rescaled one (white histogram). Right: scatter plot of the raw reconstructed $E_{\mathrm{T}}^{\mathrm{miss}}$ vs. $p_{\mathrm{T}}^{\nu\ \mathrm{true}}$. Both plots show how the raw reconstructed $E_{\mathrm{T}}^{\mathrm{miss}}$ is over estimated ($E_{\mathrm{T}}^{\mathrm{miss}}/p_{\mathrm{T}}^{\nu\ \mathrm{true}}$ above 1 in the left plot, and above the diagonal in the right plot).

The performance of the $E_{\mathrm{T}}^{\mathrm{miss}}$ in ATLAS is reported in [131] where the biggest contributors to the distortion of the W transverse mass in $W \to \ell\nu$ decays are reported.

APPENDIX

L

Globalχ^2 formalism for the top-quark mass measurement

In the Globalχ^2 formalism the residuals vector $\boldsymbol{r}$ depend on the local and global variables of the fit: $\boldsymbol{r} = \boldsymbol{r}(\boldsymbol{t}, \boldsymbol{w})$, where $\boldsymbol{t}$ is the set of global parameters of the fit (which will be related with the top quark properties) and $\boldsymbol{w}$ is the set of local parameters of the fit (in its turn is related with the leptonically decaying W). Therefore one can build the χ^2 which has to be minimized with respect to the $\boldsymbol{t}$ parameters:

$$\chi^2 = \boldsymbol{r}^T(\boldsymbol{t}, \boldsymbol{w}) V^{-1} \boldsymbol{r}(\boldsymbol{t}, \boldsymbol{w}) \quad \longrightarrow \quad \frac{d\chi^2}{d\boldsymbol{t}} = 0 \tag{L.1}$$

where V is the covariance matrix of the residuals. The minimization condition gives:

$$\frac{d\chi^2}{d\boldsymbol{t}} = \left[\left(\frac{d\boldsymbol{r}}{d\boldsymbol{t}}\right)^T V^{-1} \boldsymbol{r}\right]^T + \left[\boldsymbol{r}^T V^{-1} \left(\frac{d\boldsymbol{r}}{d\boldsymbol{t}}\right)\right] = 2\left[\left(\frac{d\boldsymbol{r}}{d\boldsymbol{t}}\right)^T V^{-1} \boldsymbol{r}\right]^T = 0 \quad \longrightarrow \quad \left(\frac{d\boldsymbol{r}}{d\boldsymbol{t}}\right)^T V^{-1} \boldsymbol{r} = 0 \tag{L.2}$$

The minimization condition allows to compute the corrections ($\delta\boldsymbol{t}$) to the initial top fit parameters ($\boldsymbol{t}_0$). The minimum of the χ^2 occurs for the following set of global and local parameters: $\boldsymbol{t} = \boldsymbol{t}_0 + \delta\boldsymbol{t}$ and $\boldsymbol{w} = \boldsymbol{w}_0 + \delta\boldsymbol{w}$. The residuals at the minimum will change according to:

$$\begin{array}{l} \boldsymbol{t} = \boldsymbol{t}_0 + \delta\boldsymbol{t} \\ \boldsymbol{w} = \boldsymbol{w}_0 + \delta\boldsymbol{w} \end{array} \quad \longrightarrow \quad \boldsymbol{r} = \boldsymbol{r}_0 + \left(\frac{\partial \boldsymbol{r}}{\partial \boldsymbol{w}}\right)\delta\boldsymbol{w} + \left(\frac{\partial \boldsymbol{r}}{\partial \boldsymbol{t}}\right)\delta\boldsymbol{t}$$

Inserting the above expresion into Eq. L.2 and keeping up to the first order derivatives, one obtains:

$$\left(\frac{d\boldsymbol{r}}{d\boldsymbol{t}}\right)^T V^{-1} \left[\boldsymbol{r}_0 + \left(\frac{\partial \boldsymbol{r}}{\partial \boldsymbol{w}}\right)\delta\boldsymbol{w} + \left(\frac{\partial \boldsymbol{r}}{\partial \boldsymbol{t}}\right)\delta\boldsymbol{t}\right] = 0$$

$$\left(\frac{d\boldsymbol{r}}{d\boldsymbol{t}}\right)^T V^{-1} \boldsymbol{r}_0 + \left[\left(\frac{d\boldsymbol{r}}{d\boldsymbol{t}}\right)^T V^{-1} \left(\frac{\partial \boldsymbol{r}}{\partial \boldsymbol{w}}\right)\right]\delta\boldsymbol{w} + \left[\left(\frac{d\boldsymbol{r}}{d\boldsymbol{t}}\right)^T V^{-1} \left(\frac{\partial \boldsymbol{r}}{\partial \boldsymbol{t}}\right)\right]\delta\boldsymbol{t} = 0 \tag{L.3}$$

Local parameters fit.

The $\delta\boldsymbol{w}$ correction is first determined in the fit of the local parameters (or inner fit). One has to express again the minimization condition of the χ^2. Only this time it is computed just with respect to the $\boldsymbol{w}$ parameters set.

$$\frac{\partial\chi^2}{\partial\boldsymbol{w}} = 0 \quad \longrightarrow \quad \left(\frac{\partial \boldsymbol{r}}{\partial \boldsymbol{w}}\right)^T V^{-1} \boldsymbol{r} = 0 \quad \longrightarrow \quad \left(\frac{\partial \boldsymbol{r}}{\partial \boldsymbol{w}}\right)^T V^{-1} \boldsymbol{r}_0 + \left[\left(\frac{\partial \boldsymbol{r}}{\partial \boldsymbol{w}}\right)^T V^{-1} \left(\frac{\partial \boldsymbol{r}}{\partial \boldsymbol{w}}\right)\right]\delta\boldsymbol{w} = 0$$

$$\delta \boldsymbol{w} = -\left[\left(\frac{\partial \boldsymbol{r}}{\partial \boldsymbol{w}}\right)^T V^{-1}\left(\frac{\partial \boldsymbol{r}}{\partial \boldsymbol{w}}\right)\right]^{-1}\left(\frac{\partial \boldsymbol{r}}{\partial \boldsymbol{w}}\right)^T V^{-1}\boldsymbol{r}_0 \tag{L.4}$$

which already provides a solution for the local parameter set ($\boldsymbol{w}$).

Global parameters fit.

Reached this point is worth to mention that solving the inner fit ($\delta\boldsymbol{w}$) involves the calculation of the $\left[\left(\frac{\partial \boldsymbol{r}}{\partial \boldsymbol{w}}\right)^T V^{-1}\left(\frac{\partial \boldsymbol{r}}{\partial \boldsymbol{w}}\right)\right]$ matrix. This way, the possible correlation among the residuals that depend on $\boldsymbol{w}$ is computed and fed into the global fit.

The solving of the system requires to compute the derivative terms of $\boldsymbol{r} = \boldsymbol{r}(\boldsymbol{t}, \boldsymbol{w})$ with respect to $\boldsymbol{t}$ and $\boldsymbol{w}$ and also $d\boldsymbol{w}/d\boldsymbol{t}$. One of the keys of the Globalχ^2 technique is that the later derivative is not null: the parameters of the inner fit ($\boldsymbol{w}$) depend on the parameters of the outer fit ($\boldsymbol{t}$). Otherwise, if $\boldsymbol{w}$ were independent of $\boldsymbol{t}$, then one would have to face a normal χ^2 fit with two independent parameters.

$$d\boldsymbol{r} = \frac{\partial \boldsymbol{r}}{\partial \boldsymbol{t}}d\boldsymbol{t} + \frac{\partial \boldsymbol{r}}{\partial \boldsymbol{w}}d\boldsymbol{w} \quad \longrightarrow \quad \frac{d\boldsymbol{r}}{d\boldsymbol{t}} = \frac{\partial \boldsymbol{r}}{\partial \boldsymbol{t}} + \frac{\partial \boldsymbol{r}}{\partial \boldsymbol{w}}\frac{d\boldsymbol{w}}{d\boldsymbol{t}} \tag{L.5}$$

The $d\boldsymbol{w}/d\boldsymbol{t}$ term can be computed from Eq. L.4 and gives:

$$\frac{d\boldsymbol{w}}{d\boldsymbol{t}} = -\left[\left(\frac{\partial \boldsymbol{r}}{\partial \boldsymbol{w}}\right)^T V^{-1}\left(\frac{\partial \boldsymbol{r}}{\partial \boldsymbol{w}}\right)\right]^{-1}\left(\frac{\partial \boldsymbol{r}}{\partial \boldsymbol{t}}\right)^T V^{-1}\left(\frac{\partial \boldsymbol{r}}{\partial \boldsymbol{t}}\right) \tag{L.6}$$

Inserting Eq. L.4 into Eq. L.3 and performing the matrix algebra, one reaches:

$$\left(\frac{d\boldsymbol{r}}{d\boldsymbol{t}}\right)^T V^{-1}\boldsymbol{r}_0 + \left[\left(\frac{d\boldsymbol{r}}{d\boldsymbol{t}}\right)^T V^{-1}\left(\frac{\partial \boldsymbol{r}}{\partial \boldsymbol{t}}\right)\right]\delta\boldsymbol{t} = 0$$

$$\delta \boldsymbol{t} = -\left[\left(\frac{d\boldsymbol{r}}{d\boldsymbol{t}}\right)^T V^{-1}\left(\frac{\partial \boldsymbol{r}}{\partial \boldsymbol{t}}\right)\right]^{-1}\left(\frac{d\boldsymbol{r}}{d\boldsymbol{t}}\right)^T V^{-1}\boldsymbol{r}_0 \tag{L.7}$$

which allows to compute the corrections, $\delta\boldsymbol{t}$, to the set of global parameters (related with the top quark properties).

APPENDIX

M Probability density functions

In this appendix summarizes the probability density functions (p.d.f.) which are used for the fit of the mass distribution.

M.1 Lower tail exponential distribution

The exponential distribution is well known (for example [139]) and commonly used for lifetime determination as well as for radioactive decays studies. The usual shape is to have a maximum at 0 followed by an exponential decay towards positive values. In our implementation, the distribution has a maximum, however, not at 0 but at a cut-off value and the exponential tail occurs towards smaller values. The cut-off has been implemented using $\theta(m_0 - x)$ as the Heaviside step function. The p.d.f. properties, as expected value and variance, can be expressed as:

Variable and parameters:

symbol	type	property
x	positive real number	variable
m_0	positive real number	cut-off value
λ	positive real number	steepness of the tail

Probability density function:

$$f(x; m_0, \lambda) = \left[\frac{1}{\lambda \left(1 - e^{-m_0/\lambda}\right)} \, e^{(x - m_0)/\lambda} \right] \theta(m_0 - x) \tag{M.1}$$

Expected value:

$$E(x) = \frac{m_0 - \lambda}{1 - e^{-m_0/\lambda}} \tag{M.2}$$

Variance:

$$V(x) = \frac{e^{-m_0/\lambda}}{\left(1 - e^{-m_0/\lambda}\right)^2} \left[\lambda^2 \left(e^{m_0/\lambda} - 2 \right) + 2 m_0 \lambda - m_0^2 \right] \tag{M.3}$$

Cumulative distribution:

$$F(x; m_0, \lambda) = \int_0^x f(x'; m_0, \lambda) \, dx' = 1 - \frac{1 - e^{(x - m_0)/\lambda}}{1 - e^{-m_0/\lambda}} \, \theta(m_0 - x) \tag{M.4}$$

An example of lower tail exponential distribution is shown in Figure M.1 (green line).

M.2 Lower tail exponential with resolution model

The experimental resolution may affect the shape of the observables distributions. Let's consider a Gaussian resolution model. Let be $G(x; m, \sigma)$ the probability to observe a mass value of x, when the true mass value is m and the experimental resolution is σ. The convolution of the lower tail exponential p.d.f. (Apendix M.1) with a Gaussian resolution function leads to the following p.d.f:

$$f(x; m_0, \lambda, \sigma) = f \otimes G = \int_0^\infty f(m; m_0, \lambda) \cdot G(x; m, \sigma)\, dm \tag{M.5}$$

Variable and parameters:

symbol	type	property
x	positive real number	variable
m_0	positive real number	cut-off mass
λ	positive real number	steepness of the exponential tail
σ	positive real number	mass resolution

Probability density function:

$$f(x; m_0, \lambda, \sigma) = \frac{e^{(x-m_0)/\lambda}}{1-e^{-m_0/\lambda}} \frac{e^{\sigma^2/2\lambda^2}}{2\lambda} \left[\mathrm{Erf}\left(\frac{-(x-m_0)\lambda - \sigma^2}{\sqrt{2}\lambda\sigma} \right) + \mathrm{Erf}\left(\frac{x\lambda + \sigma^2}{\sqrt{2}\lambda\sigma} \right) \right] \tag{M.6}$$

Expected value:

$$E(x) = m_0 - \lambda + \frac{m_0 e^{-m_0/\lambda}}{1-e^{-m_0/\lambda}} \tag{M.7}$$

Variance:

$$V(x) = \frac{\left(\lambda^2+\sigma^2\right)\left(1+e^{-2m_0/\lambda}\right) - e^{-m_0/\lambda}\left(m_0^2 + 2(\lambda^2+\sigma^2)\right)}{\left(1-e^{-m_0/\lambda}\right)^2} \tag{M.8}$$

Cumulative distribution:

$$F(x; m_0, \lambda, \sigma) = \int_0^x f(x'; m_0, \lambda, \sigma)\, dx' =$$

$$\frac{e^{(x-m_0)/\lambda} e^{\sigma^2/2\lambda^2} \left[\mathrm{Erf}\left(\frac{x\lambda+\sigma^2}{\sqrt{2}\lambda\sigma} \right) - \mathrm{Erf}\left(\frac{(x-m_0)\lambda+\sigma^2}{\sqrt{2}\lambda\sigma} \right) \right] - e^{-m_0/\lambda} \mathrm{Erf}\left(\frac{x}{\sqrt{2}\sigma} \right) + \mathrm{Erf}\left(\frac{x-m_0}{\sqrt{2}\sigma} \right)}{2\left(1-e^{-m_0/\lambda}\right)} \tag{M.9}$$

One of the features of this distribution is that (contrary to a Gaussian distribution) m_0 is not the most probable value. Figure M.1 compares a Gaussian distribution with $f(x; m_0, \lambda, \sigma)$ given by Equation M.6.

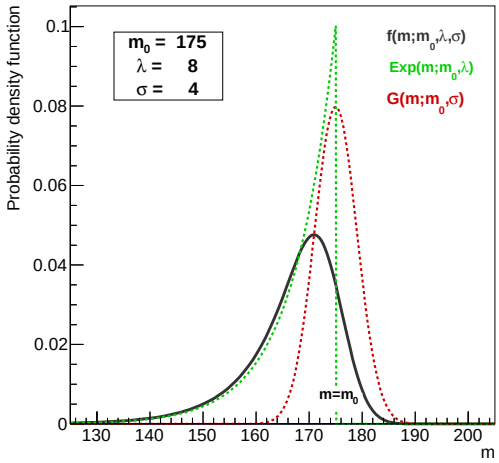

Figure M.1: Comparison of the p.d.f.'s for a Gaussian (red dashed line), a lower tail exponential (green dashed line) and a lower tail exponential with resolution model (black line). All p.d.f.'s make use of the same m_0, σ and λ values (175, 8 and 4 respectively). The Gaussian peaks at m_0 but the lower tail exponential with resolution model peaks at a lower value clearly shifted from m_0.

In that figure, both distributions have the same m_0 and σ values. While the most probable value for the Gaussian is the m_0, the lower tail exponential with resolution model peaks at $m < m_0$. The $f(x; m_0, \lambda, \sigma)$ has also a non symmetric shape. While its upper tail is quite close to a Gaussian tail, its lower tail departs more from the Gaussian.

M.3 Novosibirsk probability distribution

The Novosibirsk p.d.f. may be regarded as a sort of distorted Gaussian distribution. It is parametrized as follows:

Variable and parameters:

symbol	type	property
x	real number	variable
x_0	real number	most probable value (or peak position)
σ	positive real number	width of the peak
Λ	positive real number	parameter describing the tail

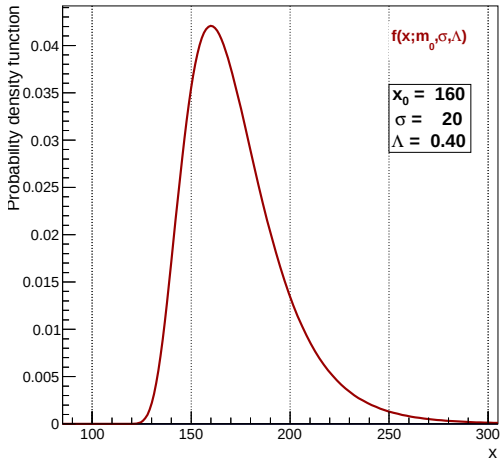

Figure M.2: An example of the Novosibirsk p.d.f.

Probability density function:

$$f(x; x_0, \sigma, \lambda) = e^{-\frac{1}{2}\left[\left(\frac{\ln q_y}{\Lambda}\right)^2 + \Lambda^2\right]}$$

$$\ln q_y = 1 + \Lambda\left(\frac{x - x_0}{\sigma}\right)\left(\frac{\sinh(\Lambda\sqrt{\ln 4})}{\Lambda\sqrt{\ln 4}}\right) \tag{M.10}$$

An example of the Novosibirsk p.d.f. is shown in figure M.2.

APPENDIX

N Study of the physics background

The irreducible physics background has been defined as all the SM processes (excluding $t\bar{t}$) that produce a final topology similar to the $t\bar{t} \rightarrow \ell$ + jets and satisfy the selection criteria applied through the analysis sections. After the Globalχ^2 fit, the physics background has been reduced to $\approx$ 5% (Table 5.5). The main contribution comes from the production of single top events (amounting around the 50% of the total). The shape of the $m_{\rm top}$ distribution due to the irreducible physics background is computed from the sum of all processes. This distribution includes, of course, the single top events which could introduce a mass dependent in its shape.

In order to asses the effect of the single top events in the $m_{\rm top}$ background distribution, the single top MC samples generated at different $m_{\rm top}$ masses were used. The obtained $m_{\rm top}$ physics background distribution (including single top) has been studied at each generated mass point, from 165 GeV to 180 GeV. The shape of this distribution was modelled by a Novosibirsk function (Appendix M).

The values of the Novosibirsk parameters (μ_{phys_bkg}, σ_{phy_bkg} and Λ_{phy_bkg}) have been extracted. Figures N.1, N.2 and N.3 display the dependence of each parameter with respect to the input single top mass point. All distributions are compatible with a flat distribution. Therefore, one can assume that the parameters describing the physics background do not depend on the input top-quark mass. So the influence of single top events in the worst of the cases will be very mild.

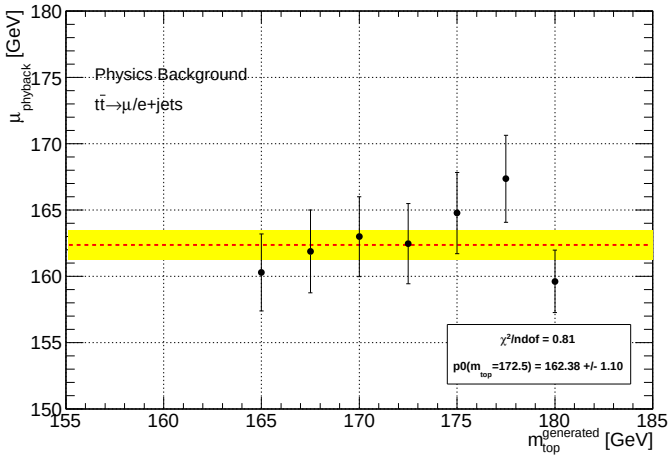

Figure N.1: Fitted μ_{phy_bkg} as a function of the true single top-quark mass.

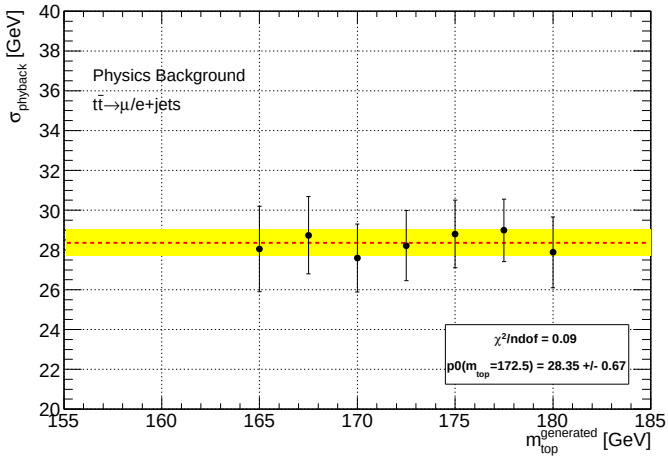

Figure N.2: Fitted σ_{phy_bkg} parameters as a function of the true single top-quark mass.

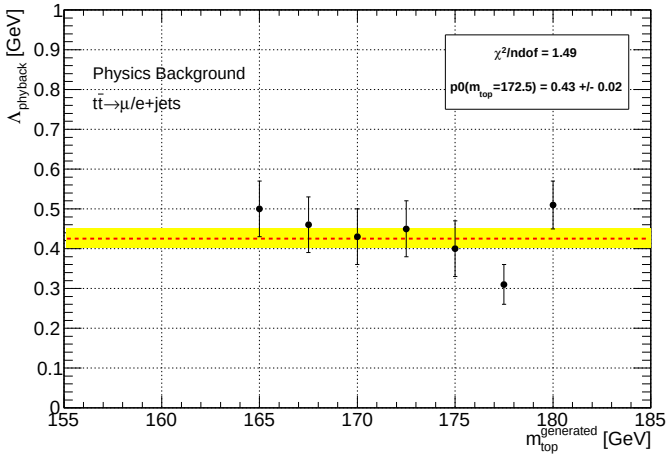

Figure N.3: Fitted Λ_{phy_bkg} parameters as a function of the true single top-quark mass.

APPENDIX

O Mini-template linearity test

The linearity of the mini-template method with respect to the generated top-quark mass has been evaluated in the same way that for the template method. At each mass point 500 pseudoexperiments have been performed, each randomly filled using the content of the top-quark mass histogram for the nominal MC sample with the same number of entries. The physic background has neither been included in this test since it exhibited a flat dependence with the generated mass (Appendix N).

Figure O.1 (left) shows the difference between the fitted top-quark mass versus the generated top-quark mass (true value). As one can see, there is a quite large dispersion. Although it must be noted that the each sample has a different statistics. Actually, the point at m_{top}=172.5 GeV had 10 M of events while the other had 5 M of events. Moreover this sample also exhibits a better prediction than the rest, thus evidences that the mini-template method is quite statistics dependent. This was somewhat expected, as the accurate determination of the parameters of the distribution will improve with the statistics of the sample.

The pull distributions are produced and fitted with a Gaussian. The width of the pull distribution as a function of the top-quark mass generated is shown in Figure O.1 (right). The average value is close to unity (1.042±0.015) which indicates a quite good estimation of the statistical uncertainty.

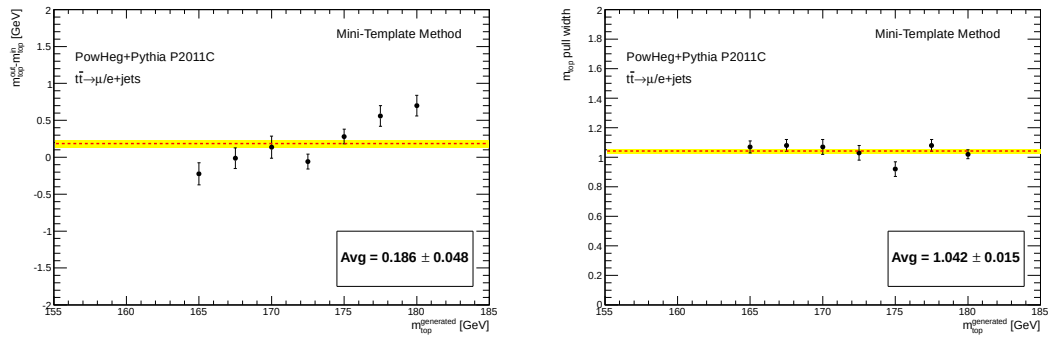

Figure O.1: Left: difference between the fitted top mass with the mini-template and the generated mass as a function of the generated top-quark mass. Right: Width of the pull distributions as a function of the generated top-quark mass.

APPENDIX

P Validation of the *b*-jet energy scale using tracks

The *b*-quark originated jets play an important role in many ATLAS physics analyses. Therefore, the knowledge of the *b*-jet energy scale (*b*-JES) is of great importance for the final results. Among others, the top-quark mass measurement performed in the $t\bar{t} \rightarrow \ell + jets$ channel, which contains two *b*-tagged jets in the final state, is strongly affected by the *b*-JES uncertainty, leading one of the dominant systematic uncertainties. In this way, a huge effort has been done by the collaboration in order to understand, reduce and validate the *b*-JES uncertainty.

The *b*-JES quantifies how well the energy of the reconstructed jet reflects the energy of the *b*-parton coming from the hard interaction. MC and data studies have been performed to evaluate the relative difference in the single hadron response of inclusive jets and *b*-jets. The *b*-JES uncertainty has been computed adding quadratically the both following contributions: the uncertainty in the calorimeter response for *b*-jets with respect to the response of the inclusive jets [140] and the uncertainty on the MC modelling that includes, among others, the production and fragmentation of *b*-quarks [69]. This uncertainty has been tested using a track based method which compares the p_{T} of the jet measured by the calorimeter and by the Inner detector.

Data and Monte-Carlo samples

This analysis was performed with $p-p$ collisions recorded by the ATLAS detector during 2010 at $\sqrt{s}$ = 7 TeV. Only data periods with stable beam and perfect detector operation were considered, amounting to an integrated luminosity of $\mathcal{L}$ = 34 pb^{-1}. The `MinBias`, `L1Calo` and `JetEtMiss` data streams were used together in order to increase the statistics and cover a wide p_{T} spectrum.

The MC sample used to perform the analysis was the QCD di-jet sample produced with PYTHIA generator program with MC10 tune. The QCD di-jet samples cover an extensive p_{T} range, from ~10 GeV to ~2000 GeV.

Notice that, in order to validate the *b*-JES uncertainty to measure the m_{top}, the first attempt was to use the $t\bar{t}$ sample. Nevertheless, the low statistics of the sample made this option unfeasible.

Object reconstruction and selection

An event selection was applied in order to keep well reconstructed events. The requirements applied were the following:

- **Event selection:** at least one good vertex was required. Moreover, those events with more than 500 tracks or 50 jets were rejected to avoid events poorly reconstructed.

- **Track selection:** tracks were reconstructed as explained in Chapter 3. Each track associated to a jet had to have a p_{T} >1 GeV. A hit requirement was also imposed: $N_{PIX} > 1$ and $N_{SCT} \geqslant 6$. In addition, cuts in the transverse and longitudinal impact parameters respect to the primary vertex (PV) were applied: $d_0^{PV} \leqslant 1.5$ mm and $z_0^{PV} \cdot \sin\theta \leqslant 1.5$ mm. These cuts ensured a good tracking quality and minimized the contributions from photon conversions and from tracks not arising from the PV.

- **Jet selection:** jets were reconstructed with the Anti-Kt algorithm with a cone size of R = 0.4. These jets were calibrated at EM+JES scale (Section 3.3). A jet quality criteria was applied to identify and reject jets reconstructed from energy deposits in the calorimeters originating from hardware problems. Moreover, jets with a p_{T} larger than 20 GeV and $|\eta|$<2.5 were required. These jets had to be isolated and contain, at least, one track passing the track selection.

- ***b*-jet selection:** the *b*-jets were selected with the SV0 tagger [142]. This tagger iteratively reconstructs a secondary vertex in jets and calculates the decay length with respect to the PV. The decay length significance calculated by the algorithm is assigned to each jet as tagging weight. Only those jets with a weight>5.85 were identify as *b*-jets. The *b*-tagging SF were applied to MC in order to match the real data *b*-tagging efficiency and mis-tag rates.

Calorimeter *b*-JES validation using tracks

In order to validate the *b*-JES and its uncertainty, an extension of the method used to validate the JES uncertainty was proposed [141]. The method compares the p_{T} of the jet measured by the calorimeter and by the ID tracker. This comparison is done trough the r_{trk} variable which is defined as follows:

$$r_{trk} = \frac{|\sum p_{\mathrm{T}}^{track}|}{p_{\mathrm{T}}^{jet}} \tag{P.1}$$

where the p_{T}^{jet} is the transverse momentum of the reconstructed jet measured by the calorimeter and the $\sum p_{\mathrm{T}}^{track}$ is the total transverse momentum of the tracks pointing to the jet. The track-to-jet association is done using a geometrical selection: all tracks with a p_{T} >1 GeV located within a cone of radius R = 0.4 around the jet axis are linked to the jet (ΔR(jet, track)<0.4) . The mean transverse momentum of these tracks provides an independent test of the calorimeter energy scale over the entire measured p_{T} range within the tracking acceptance. The r_{trk} distribution decreases at low p_{T} bins due to the p_{T} cut of the associated tracks. In order to correct for this p_{T} dependence, instead of r_{trk} the double ratio of charged-to-total momentum observed in data and MC is used:

$$R_{r_{trk}} = \frac{[\langle r_{trk}\rangle]_{data}}{[\langle r_{trk}\rangle]_{MC}} \tag{P.2}$$

$\langle r_{trk} \rangle$ corresponds to the mean value of the r_{trk} distribution extracted from data and MC. This R variable can be built for inclusive jets ($R_{r_{trk},inclusive}$) and b-tagged jets ($R_{r_{trk},b-jet}$). Finally, the relative response of b-jets to inclusive jets, R', is used to validate the b-JES uncertainty. The R' variable is defined as:

$$R' = \frac{R_{r_{trk},b-jet}}{R_{r_{trk},inclusive}} \tag{P.3}$$

Systematic uncertainties

The most important systematic sources affecting the r_{trk}, R and R' variables are the following:

- **MC Generator:** this takes into account the choice of an specific generator program. The analysis was performed with PYTHIA (as default) and HERWIG++ (as systematic variation). The variation of data to MC ratios was taken as the systematic uncertainty.
- b**-tagging efficiency and mis-tag rate:** in order to evaluate the b-tagging systematic uncertainty, the SF values were changed by $\pm 1\sigma$. The analysis was repeated and the ratio re-evaluated. The resulting shift was associated to the systematic uncertainty.
- **Material description:** the knowledge on the tracking efficiency modelling in MC was evaluated in detail in [143]. The systematic uncertainty on the tracking efficiency of isolated tracks increased from 2% ($|\eta_{track}| < 1.3$) to 4% ($1.9 < |\eta_{track}| < 2.1$) for tracks with $p_{\mathrm{T}} > 500$ MeV.
- **Tracking in jet core:** high track densities in the jet core influences the tracking efficiency due to shared hits between tracks, fake tracks and lost tracks. In order to evaluate this effect a systematic uncertainty of 50% on the loss of efficiency was assigned. The change of the ratio distribution due to this systematic was evaluated using MC truth charged particles and the relative shift was taken as the systematic uncertainty.
- **Jet energy resolution:** this systematic quantifies the impact of the jet energy resolution uncertainty on the measurement. A randomised energy amount, that corresponds to a resolution smearing of 10%, was added to each jet. The difference in the ratio was calculated and taken as the systematic uncertainty.

Results

The analysis was performed using different bins in p_{T} and rapidity. The accessible kinematic p_{T} range was from 20 GeV to 600 GeV and the binning was chosen in order to keep enough statistics. The rapidity rage was split up in three bins: $|y| < 1.2$, $1.2 \leqslant |y| < 2.1$ and $2.1 \leqslant |y| < 2.5$.

Figure P.1(a), P.1(c) and P.1(e) show the $R_{r_{trk},b-jets}$ ratio of data to MC. An agreement within 2% in the bin $|y| < 1.2$, within 4% in the bin $1.2 \leqslant |y| < 2.1$ and within 6% in the bin $2.1 \leqslant |y| < 2.5$ was obtained. The systematic uncertainties, displayed in Figures P.1(b), P.1(d) and P.1(f), were found of the order of 3%, 4% and 8% for the same rapidity ranges respectively. The larger contributions came from the material description and MC generator.

The R' distributions can be seen in Figures P.2(a), P.2(c) and P.2(e). The results show an agreement within 2% in the bin $|y| < 1.2$, within 2.5% in the bin $1.2 \leqslant |y| < 2.1$ and 6% for the bin $2.1 \leqslant |y| < 2.5$.

In order to compute the systematic uncertainty of R' several assumptions were done. For example, at first order the uncertainties associated with the tracking efficiency and material description were taken as fully correlated and cancelled. In addition, the jet p_{T} resolution for inclusive and *b*-jets was considered to be of the same order for hight p_{T} and of the order of 2 per mille for low p_{T}, therefore this systematic was also neglected. Thus, the significant systematic uncertainties on R' arose from the MC generator choice and *b*-tagging calibration. These ones were evaluated and added in quadrature to compute the final systematic uncertainty being of the order of 3% for the first two rapidity bins and 6% for the most external rapidity bin (Figures P.2(b), P.2(d) and P.2(f)).

Summing up, a new R' variable was defined to estimate the relative *b*-jet energy scale uncertainty for anti-Kt jets with a ΔR = 0.4 and calibrated with the EM+JES scheme. This method validated the calorimeter *b*-JES uncertainty using tracks and improved the knowledge of the jet energy scale of the *b*-jets. These results were reported in an ATLAS publication [69]. Posteriorly, the validation of the *b*-JES uncertainty with $t\bar{t}$ events were also performed providing a more accurate *b*-JES validation for the m_{top} analyses [144].

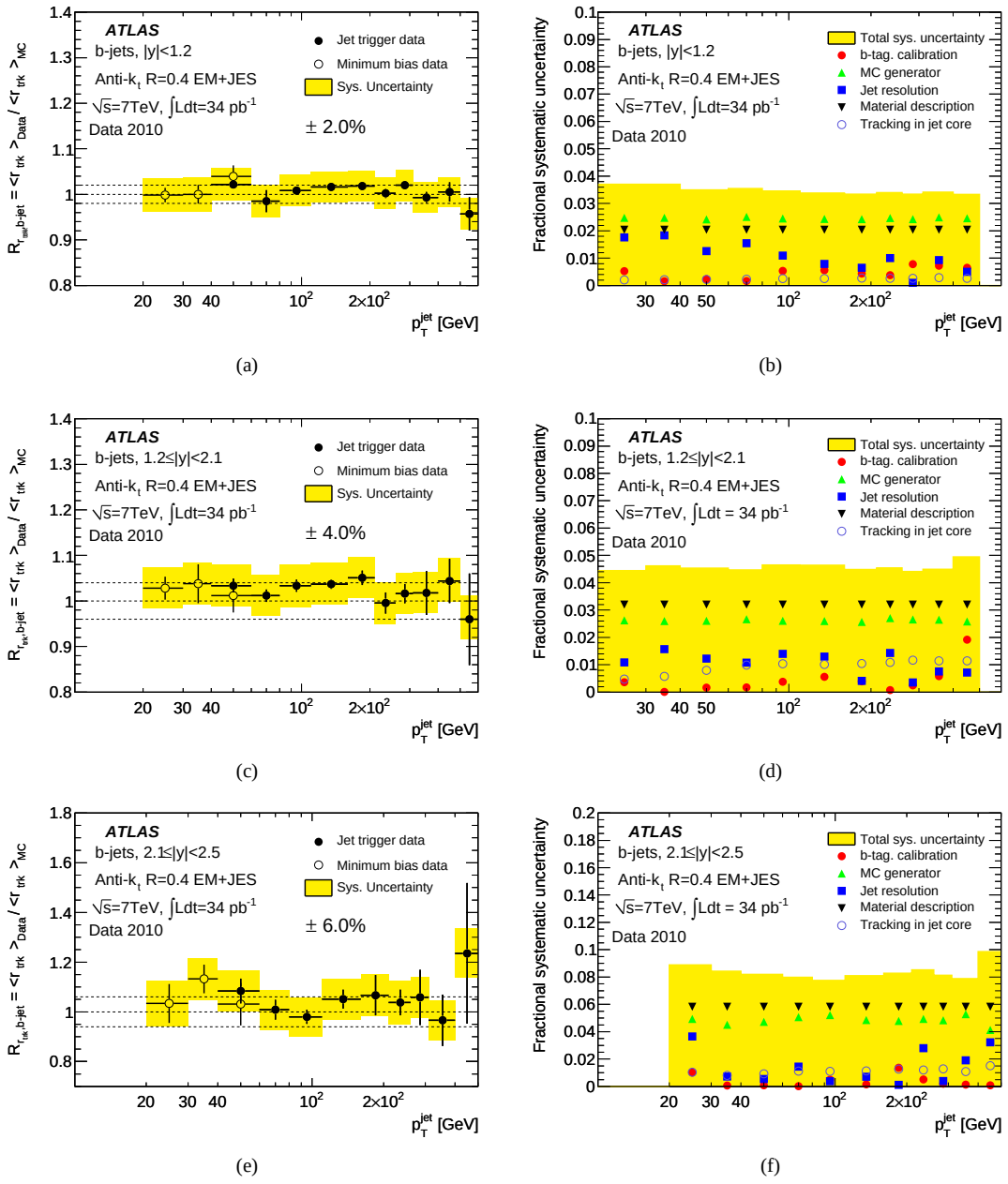

Figure P.1: $R_{r_{trk},b-jet}$ variable (left) and its fractional systematic uncertainty (right) as a function of p_{T}^{jet} for $|y|<1.2$ (upper), $1.2 \leqslant |y| <2.1$ (middle) and $2.1 \leqslant |y| < 2.5$ (bottom). The dashed lines indicate the estimated uncertainty from the data and MC agreement. Only statistical uncertainties are shown on the data points.

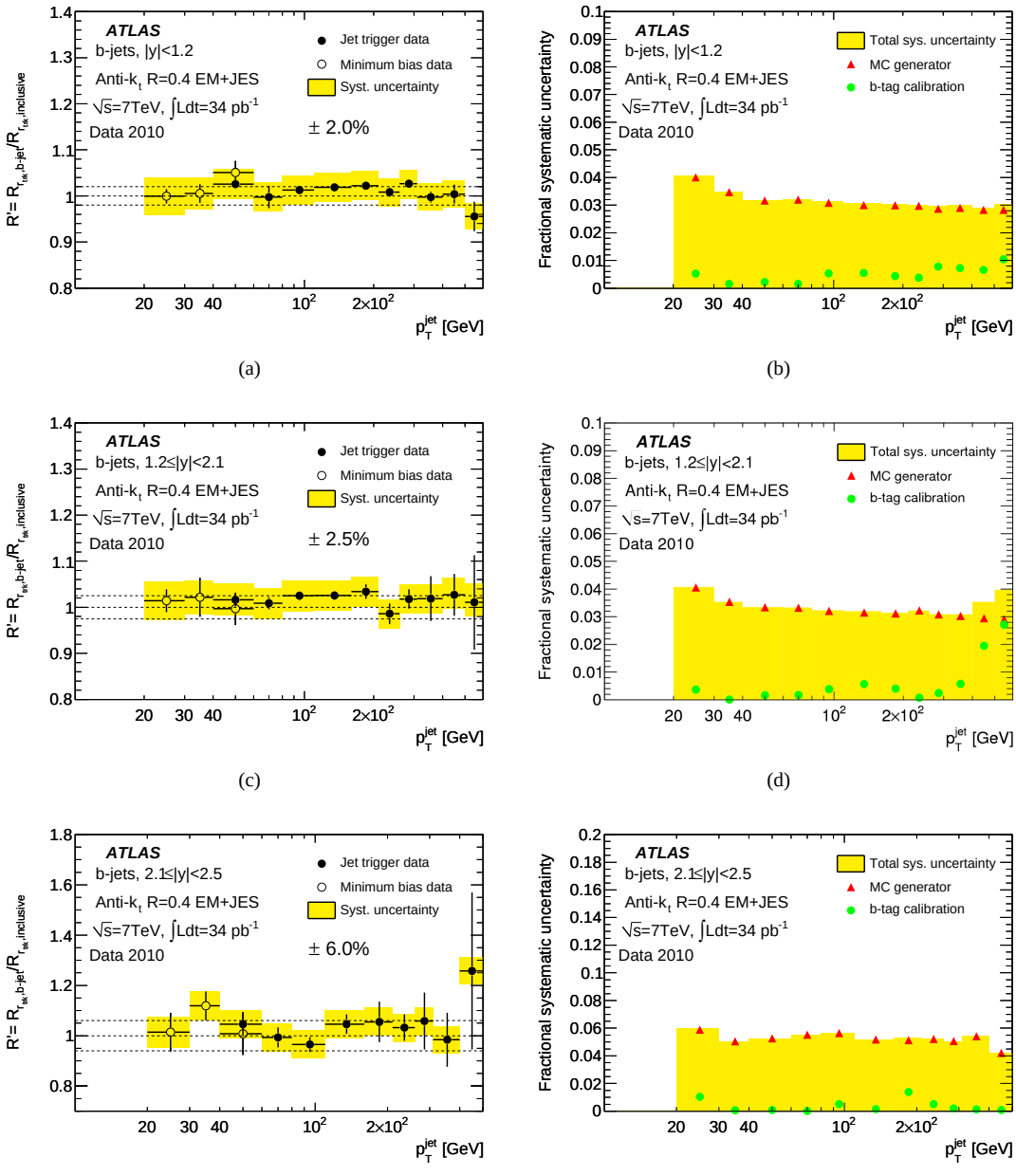

Figure P.2: The ratio R' (left) and the fractional systematic uncertainty (right) as a function of p_{T}^{jet} for $|\ y\ |$<1.2 (upper), 1.2 $\leqslant|\ y\ |$<2.1 (middle) and 2.1 $\leqslant|\ y\ |<$ 2.5 (bottom). The dashed lines indicate the estimated uncertainty from the data and MC agreement. Only statistical uncertainties are shown on the data points.

Bibliography

[1] R. Taylor Rev.Mod.Phys **63** (1991) 573.

[2] H. Kendall Rev.Mod.Phys **63** (1991) 597.

[3] J. Fiedman Rev.Mod.Phys **63** (1991) 615.

[4] Particle Data Group Collaboration, K. Nakamura et al., *Review of particle physics*, J.Phys.G **G37** (2010) 075021.

[5] S. Novaes, *Standard model: An Introduction*, arXiv:hep-ph/0001283 [hep-ph].

[6] LHC Collaboration, *Observation of a new particle in the search for the Standard Model Higgs boson with the ATLAS detector at the LHC*, Physics Letters B **716** (2012) no. 1, 1 – 29. http://www.sciencedirect.com/science/article/pii/S037026931200857X.

[7] *ATLAS Physics Summary Plots*, https://twiki.cern.ch/twiki/bin/view/AtlasPublic/CombinedSummaryPlots. Accessed: 2013-08-01.

[8] B. Martin and G. Shaw, *Particle Physics*. Manchester Physics Series. Wiley, 1997. http://books.google.es/books?id=T4fDQgAACAAJ.

[9] *First Planck results: the Universe is still weird and interesting*, http://arstechnica.com/science/2013/03/first-planck-results-the-universe-is-still-weird-and-interesting/. Accessed: 2013-07-30.

[10] CDF Collaboration Collaboration, F. Abe et al., *Observation of top quark production in $\overline{p}p$ collisions*, Phys.Rev.Lett. **74** (1995) 2626–2631, arXiv:hep-ex/9503002 [hep-ex].

[11] D0 Collaboration Collaboration, S. Abachi et al., *Observation of the top quark*, Phys.Rev.Lett. **74** (1995) 2632–2637, arXiv:hep-ex/9503003 [hep-ex].

[12] A. Quadt, *Top quark physics at hadron colliders*, The European Physical Journal C - Particles and Fields **48** (2006) no. 3, 835–1000. http://dx.doi.org/10.1140/epjc/s2006-02631-6.

[13] Tevatron Electroweak Working Group, for the CDF and D0 Collaborations Collaboration, *Combination of CDF and D0 results on the mass of the top quark using up to 5.8 fb-1 of data*, arXiv:1107.5255 [hep-ex].

[14] ATLAS and CMS Collaboration, *Combination of ATLAS and CMS results on the mass of the top quark using up to 4.9 fb^{-1} of data*, ATLAS-CONF-2012-095, CMS PAS TOP-12-001, 2013. https://cds.cern.ch/record/1418847.

[15] *Statistical combination of top quark pair production cross-section measurements using dilepton, single-lepton, and all-hadronic final states at s = 7 TeV with the ATLAS detector*, Tech. Rep. ATLAS-CONF-2012-024, CERN, Geneva, Mar, 2012.

[16] *Measurement of the top quark pair production cross section in the single-lepton channel with ATLAS in proton-proton collisions at 8 TeV using kinematic fits with b-tagging*, Tech. Rep. ATLAS-CONF-2012-149, CERN, Geneva, Nov, 2012.

[17] *Search for s-Channel Single Top-Quark Production in pp Collisions at* $\sqrt{s}$ *= 7 TeV*, Tech. Rep. ATLAS-CONF-2011-118, CERN, Geneva, Aug, 2011.

[18] ATLAS Collaboration, *Measurement of the t-channel single top-quark production cross section in pp collisions at with the ATLAS detector*, Physics Letters B **717** (2012) no. 45, 330 – 350. http://www.sciencedirect.com/science/article/pii/S0370269312009781.

[19] ATLAS Collaboration, *Evidence for the associated production of a W boson and a top quark in ATLAS at*, Physics Letters B **716** (2012) no. 1, 142 – 159. http://www.sciencedirect.com/science/article/pii/S0370269312008489.

[20] ATLAS Collaboration Collaboration, G. Aad et al., *Measurement of the top quark charge in pp collisions at* $\sqrt{s}$ *= 7 TeV with the ATLAS detector*, arXiv:1307.4568 [hep-ex].

[21] CDF Collaboration Collaboration, T. Aaltonen et al., *Forward-Backward Asymmetry in Top Quark Production in* $p\bar{p}$ *Collisions at sqrts* = 1.96 *TeV*, Phys.Rev.Lett. **101** (2008) 202001, arXiv:0806.2472 [hep-ex].

[22] D0 Collaboration Collaboration, V. M. Abazov et al., *Forward-backward asymmetry in top quark-antiquark production*, Phys.Rev. **D84** (2011) 112005, arXiv:1107.4995 [hep-ex].

[23] ATLAS Collaboration, *Measurement of the charge asymmetry in top quark pair production in pp collisions at* $\sqrt{s}$ *=7* TeV *using the ATLAS detector*, The European Physical Journal C **72** (2012) no. 6, . http://dx.doi.org/10.1140/epjc/s10052-012-2039-5.

[24] ATLAS Collaboration, G. Aad et al., *Observation of Spin Correlation in* $t\bar{t}$ *Events from pp Collisions at* $\sqrt{s}$*=7* TeV *using the ATLAS Detector*, Phys. Rev. Lett. **108** (2012) . http://link.aps.org/doi/10.1103/PhysRevLett.108.212001.

[25] *Search for CP violation in single top quark events in pp collisions at* $\sqrt{s}$ *= 7 TeV with the ATLAS detector*, Tech. Rep. ATLAS-CONF-2013-032, CERN, Geneva, Mar, 2013.

[26] ATLAS Collaboration, *Measurement of the W boson polarization in top quark decays with the ATLAS detector*, Journal of High Energy Physics **2012** (2012) no. 6, 1–46. http://dx.doi.org/10.1007/JHEP06%282012%29088.

[27] ATLAS Collaboration, *Search for FCNC single top-quark production at with the ATLAS detector*, Physics Letters B **712** (2012) no. 45, 351 – 369. http://www.sciencedirect.com/science/article/pii/S0370269312005394.

[28] *Search for FCNC top quark processes at 7 TeV with the ATLAS detector*, Tech. Rep. ATLAS-CONF-2011-061, CERN, Geneva, Apr, 2011.

[29] *A search for* $t\bar{t}$ *resonances in the lepton plus jets final state with ATLAS using 14* fb^1 *of pp collisions at* $\sqrt{s}$ = 8 *TeV*, Tech. Rep. ATLAS-CONF-2013-052, CERN, Geneva, May, 2013.

[30] M. C. Smith and S. S. Willenbrock, *Top quark pole mass*, Phys.Rev.Lett. **79** (1997) 3825–3828, arXiv:hep-ph/9612329 [hep-ph].

[31] U. Langenfeld, S. Moch, and P. Uwer, *Measuring the running top-quark mass*, Phys.Rev. **D80** (2009) 054009, arXiv:0906.5273 [hep-ph].

[32] A. Buckley, J. Butterworth, S. Gieseke, D. Grellscheid, S. Hoche, et al., *General-purpose event generators for LHC physics*, Phys.Rept. **504** (2011) 145–233, arXiv:1101.2599 [hep-ph].

[33] F. Jegerlehner, M. Y. Kalmykov, and B. A. Kniehl, *On the difference between the pole and the MSbar masses of the top quark at the electroweak scale*, Phys.Lett. **B722** (2013) 123–129, arXiv:1212.4319 [hep-ph].

[34] *The LEP Electroweak Working Group*, http://lepewwg.web.cern.ch/LEPEWWG/. Accessed: 2013-11-30.

[35] A. Pich, *The Standard model of electroweak interactions*, arXiv:0705.4264 [hep-ph].

[36] M. Baak, M. Goebel, J. Haller, A. Hoecker, D. Kennedy, et al., *The Electroweak Fit of the Standard Model after the Discovery of a New Boson at the LHC*, Eur.Phys.J. **C72** (2012) 2205, arXiv:1209.2716 [hep-ph].

[37] S. Alekhin, A. Djouadi, and S. Moch, *The top quark and Higgs boson masses and the stability of the electroweak vacuum*, Phys.Lett. **B716** (2012) 214–219, arXiv:1207.0980 [hep-ph].

[38] G. Degrassi, S. Di Vita, J. Elias-Miro, J. R. Espinosa, G. F. Giudice, et al., *Higgs mass and vacuum stability in the Standard Model at NNLO*, JHEP **1208** (2012) 098, arXiv:1205.6497 [hep-ph].

[39] D0 Collaboration Collaboration, V. M. Abazov et al., *Measurement of the $t\bar{t}$ production cross section using dilepton events in $p\bar{p}$ collisions*, Phys.Lett. **B704** (2011) 403–410, arXiv:1105.5384 [hep-ex].

[40] L. Evans and P. Bryant, *LHC Machine*, J. Instrum. **3** (2009) S08001.

[41] *CERN webpage*, https://home.web.cern.ch. Accessed: 2013-06-1.

[42] *The accelerator complex*, http://home.web.cern.ch/about/accelerators. Accessed: 2013-08-1.

[43] O. S. Brning, P. Collier, P. Lebrun, S. Myers, R. Ostojic, J. Poole, and P. Proudlock, *LHC Design Report*. CERN, Geneva, 2004.

[44] ATLAS Collaboration, *The ATLAS experiment at the CERN Large Hadron Collider*, J. Instrum. **3** S08003.

[45] G. L. e. a. Bayatian, *CMS Physics: Technical Design Report Volume 1: Detector Performance and Software*. Technical Design Report CMS. CERN, Geneva, 2006.

[46] A. A. e. a. Alves, *The LHCb Detector at the LHC*, J. Instrum. **3** (2008) no. LHCb-DP-2008-001. CERN-LHCb-DP-2008-001, S08005.

[47] ALICE Collaboration, *ALICE: Physics Performance Report, volume I*, Tech. Rep. CERN-LHCC-2003-049, CERN, Geneva, Nov, 2003.

[48] *TOTEM*, http://home.web.cern.ch/about/experiments/moedal. Accessed: 2013-10-1.

[49] *LHCf*, http://home.web.cern.ch/about/experiments/moedal. Accessed: 2013-10-1.

[50] *MOEDAL*, http://home.web.cern.ch/about/experiments/moedal. Accessed: 2013-10-1.

[51] *ATLAS magnet system: Technical Design Report, 1*. Technical Design Report ATLAS. CERN, Geneva, 1997.

[52] *Data Quality Information for 2010 and 2011 Data*, https://twiki.cern.ch/twiki/bin/view/AtlasPublic/RunStatsPublicResults2010. Accessed: 2013-06-1.

[53] *ATLAS Luminosity Public Results*, https://twiki.cern.ch/twiki/bin/view/AtlasPublic/LuminosityPublicResults. Accessed: 2013-06-1.

[54] ATLAS Collaboration, *Expected performance of the ATLAS experiment: detector,trigger and physics*. CERN, Geneva, 2009.

[55] N. Wermes and G. Hallewel, *ATLAS pixel detector: Technical Design Report*. Technical Design Report ATLAS. CERN, Geneva, 1998.

[56] S. Haywood, L. Rossi, R. Nickerson, and A. Romaniouk, *ATLAS inner detector: Technical Design Report*. Technical Design Report ATLAS. CERN, Geneva, 1997.

[57] ATLAS Collaboration, *ATLAS first level trigger: Technical design report*, 1998.

[58] P. Jenni, M. Nessi, M. Nordberg, and K. Smith, *ATLAS high-level trigger, data-acquisition and controls: Technical Design Report*. Technical Design Report ATLAS. CERN, Geneva, 2003.

[59] ATLAS Collaboration Collaboration, G. e. a. Aad, *Performance of the ATLAS Trigger System in 2010*, Eur. Phys. J. C **72** (Oct, 2011) 1849. 63 p. Comments: 50 pages, 64 figures.

[60] *Inner Detector Geometry Frames*, https://twiki.cern.ch/twiki/bin/viewauth/Atlas/InDetGeometryFrames. Accessed: 2013-06-1.

[61] P. F. kesson, T. Atkinson, M. J. Costa, M. Elsing, S. Fleischmann, A. N. Gaponenko, W. Liebig, E. Moyse, A. Salzburger, and M. Siebel, *ATLAS Tracking Event Data Model*, Tech. Rep. ATL-SOFT-PUB-2006-004. ATL-COM-SOFT-2006-005. CERN-ATL-COM-SOFT-2006-005, CERN, Geneva, Jul, 2006.

[62] F. Akesson, M. J. Costa, D. Dobos, M. Elsing, S. Fleischmann, A. Gaponenko, K. Gnanvo, P. T. Keener, W. Liebig, E. Moyse, A. Salzburger, M. Siebel, and A. Wildauer, *ATLAS Inner Detector Event Data Model*, Tech. Rep. ATL-SOFT-PUB-2007-006. ATL-COM-SOFT-2007-015, CERN, Geneva, Dec, 2007.

[63] *Performance of primary vertex reconstruction in proton-proton collisions at* $\sqrt{s}$ *=7 TeV in the ATLAS experiment*, Tech. Rep. ATLAS-CONF-2010-069, CERN, Geneva, Jul, 2010.

[64] B. Acharya et al., *Object selection and calibration, background estimations and MC samples for the Winter 2012 Top Quark analyses with 2011 data*, ATL-COM-PHYS-2012-224, 2012. https://cds.cern.ch/record/1427721.

[65] N. Benekos et al., *Lepton trigger and identification for the Winter 2011 top quark analyses*, Tech. Rep. ATL-COM-PHYS-2011-123, CERN, Geneva, Feb, 2011. Supporting document for Winter 2011 top physics measurements.

[66] *MuidMuonCollection*, `https://twiki.cern.ch/twiki/bin/viewauth/AtlasProtected/MuidMuonCollection`. Accessed: 2013-07-30.

[67] *Performance of the Reconstruction and Identification of Hadronic Tau Decays with ATLAS*, Tech. Rep. ATLAS-CONF-2011-152, CERN, Geneva, Nov, 2011.

[68] M. Cacciari, G. P. Salam, and G. Soyez, *The Anti-k(t) jet clustering algorithm*, JHEP **0804** (2008) 063, `arXiv:0802.1189 [hep-ph]`.

[69] ATLAS Collaboration, G. Aad et al., *Jet energy measurement with the ATLAS detector in proton-proton collisions at* $\sqrt{s} = 7$ *TeV*, `arXiv:1112.6426 [hep-ex]`.

[70] ATLAS Collaboration, *Pile-up subtraction and suppression for jets in ATLAS*, ATLAS-CONF-2013-083, 2013. `https://cds.cern.ch/record/1570994/`.

[71] *Commissioning of the ATLAS high-performance b-tagging algorithms in the 7 TeV collision data*, Tech. Rep. ATLAS-CONF-2011-102, CERN, Geneva, Jul, 2011.

[72] *Performance of Missing Transverse Momentum Reconstruction in ATLAS with 2011 Proton-Proton Collisions at sqrts = 7 TeV*, Tech. Rep. ATLAS-CONF-2012-101, CERN, Geneva, Jul, 2012.

[73] *ATLAS Stand-Alone Event Displays*, `https://twiki.cern.ch/twiki/bin/view/AtlasPublic/EventDisplayStandAlone#Top_events`. Accessed: 2013-06-1.

[74] S. Haywood, *Offline Alignment and Calibration of the Inner Detector*, Tech. Rep. ATL-INDET-2000-005, CERN, Geneva, Mar, 1999.

[75] *Mapping the material in the ATLAS Inner Detector using secondary hadronic interactions in 7 TeV collisions*, Tech. Rep. ATLAS-CONF-2010-058, CERN, Geneva, Jul, 2010.

[76] O. J. A. R. T. S. J. Blusk, S Buchmuller and S. Viret, *Proceedings Of The First LHC Detector Alignment Workshop*, .

[77] F. Heinemann, *Track Based Alignment of the ATLAS Silicon Detectors with the Robust Alignment Algorithm*, Tech. Rep. arXiv:0710.1166. ATL-INDET-PUB-2007-011, CERN, Geneva, Aug, 2007.

[78] T. Gttfert and S. Bethke, *Iterative local Chi2 alignment algorithm for the ATLAS Pixel detector*. PhD thesis, Wurzburg U., May, 2006. Presented 26 May 2006.

[79] P. Bruckman, A. Hicheur and S. Haywood, *Global* χ^2 *approach to the alignment of the ATLAS silicon tracking detectors*, ATLAS Note ATL-INDET-PUB-2005-002.

[80] ATLAS Collaboration, *Athena: The ATLAS common framework developer guide*, 2004.

[81] *Error Scaling Facility for Measurements on a Track*, `https://twiki.cern.ch/twiki/bin/viewauth/AtlasComputing/ScalingMeasErrorOnTrack`. Accessed: 2013-10-01.

[82] C. Escobar, C. Garca, and S. Marti i Garca, *Alignment of the ATLAS Silicon Tracker and measurement of the top quark mass*. PhD thesis, Valencia, Universitat de Valncia, Valencia, 2010. Presented on 09 Jul 2010.

[83] A. Andreazza, V. Kostyukhin, and R. J. Madaras, *Survey of the ATLAS pixel detector components*, .

[84] S. M. Gibson and A. R. Weidberg, *The ATLAS SCT alignment system and a comparative study of misalignment at CDF and ATLAS*. PhD thesis, U. Oxford, Oxford, 2004. Presented on 04 Jun 2004.

[85] A. Keith Morley, *Electron Bremsstrahlung Studies and Track Based Alignment of the ATLAS Detector*. PhD thesis, Melbourne U., 2010.

[86] *Alineator*, `http://twiki.ific.uv.es/twiki/bin/view/Atlas/Alineator`. Accessed: 2013-10-01.

[87] *IFIC: Instituto de Fisica Corpuscular*, `https:http://ific.uv.es`. Accessed: 2013-10-01.

[88] *ScaLAPACK Home Page*, `http://www.netlib.org/scalapack/scalapack_home.html`. Accessed: 2013-11-01.

[89] *ScaLAPACKScalable Linear Algebra PACKage*, `http://www.netlib.org/scalapack/`. Accessed: 2013-11-01.

[90] J. Alison, B. Cooper, and T. Goettfert, *Production of Residual Systematically Misaligned Geometries for the ATLAS Inner Detector*, Tech. Rep. ATL-INDET-INT-2009-003. ATL-COM-INDET-2009-003, CERN, Geneva, Oct, 2009. Approval requested a second time to resolve issues in CDS.

[91] *CosmicSimulation*, `https://twiki.cern.ch/twiki/bin/viewauth/AtlasComputing/CosmicSimulation#Filtering_the_primary_muons`. Accessed: 2013-11-01.

[92] *Cosmic Simulation in rel 13: Samples*, `https://twiki.cern.ch/twiki/bin/view/Main/CosmicSimulationSamples#Overview`. Accessed: 2013-11-01.

[93] B. Pinto and the Atlas Collaboration, *Alignment data stream for the ATLAS inner detector*, Journal of Physics: Conference Series **219** (2010) no. 2, 022018. `http://stacks.iop.org/1742-6596/219/i=2/a=022018`.

[94] *Top level tags in the ATLAS Geometry Database*, `https://twiki.cern.ch/twiki/bin/viewauth/AtlasComputing/AtlasGeomDBTags`. Accessed: 2013-10-01.

[95] A. Ahmad, D. Froidevaux, S. Gonzlez-Sevilla, G. Gorfine, and H. Sandaker, *Inner Detector as-built detector description validation for CSC*, Tech. Rep. ATL-INDET-INT-2007-002. ATL-COM-INDET-2007-012. CERN-ATL-COM-INDET-2007-012, CERN, Geneva, Jun, 2007.

[96] S. Haywood, *Determination of SCT Wheel Positions*, Tech. Rep. ATL-INDET-2001-007, CERN, Geneva, Jul, 2001.

[97] P. e. a. Ryan, *The ATLAS Inner Detector commissioning and calibration*, Eur.Phys.J. **C70** (2010) 787–821, `arXiv:1004.5293 [hep-ph]`.

[98] *Alignment Performance of the ATLAS Inner Detector Tracking System in 7 TeV proton-proton collisions at the LHC*, Tech. Rep. ATLAS-CONF-2010-067, CERN, Geneva, Jul, 2010.

[99] O. Brandt and P. Bruckman de Rentstrom, *Hit Quality Selection for Track-Based Alignment with the InDetAlignHitQualSelTool in M8+*, Tech. Rep. ATL-COM-INDET-2009-015, CERN, Geneva, May, 2009.

[100] ATLAS Collaboration, *Alignment of the ATLAS Inner Detector Tracking System with 2010 LHC proton-proton collisions at $\sqrt{s}$ = 7 TeV*, ATLAS-CONF-2011-012, 2011. `https://cds.cern.ch/record/1334582?ln=en`.

[101] ATLAS Collaboration Collaboration, *Study of alignment-related systematic effects on the ATLAS Inner Detector tracking*, Tech. Rep. ATLAS-CONF-2012-141, CERN, Geneva, Oct, 2012.

[102] A. Andreazza, V. Kostyukhin, and R. J. Madaras, *Survey of the ATLAS Pixel Detector Components*, Tech. Rep. ATL-INDET-PUB-2008-012. ATL-COM-INDET-2008-006, CERN, Geneva, Mar, 2008.

[103] ATLAS Collaboration Collaboration, *Performance of the ATLAS Detector using First Collision Data*, J. High Energy Phys. **09** (May, 2010) 056. 65 p.

[104] ATLAS Collaboration Collaboration, *Charged-particle multiplicities in pp interactions at $\sqrt{s}$ = 900 GeV measured with the ATLAS detector at the LHC*, Phys.Lett. **B688** (2010) 21–42, `arXiv:1003.3124 [hep-ex]`.

[105] ATLAS Collaboration Collaboration, *J/ Performance of the ATLAS Inner Detector*, Tech. Rep. ATLAS-CONF-2010-078, CERN, Geneva, Jul, 2010.

[106] ATLAS Collaboration Collaboration, *Estimating Track Momentum Resolution in Minimum Bias Events using Simulation and $K_s$in $\sqrt{s}$ = 900* GeV *collision data*, Tech. Rep. ATLAS-CONF-2010-009, CERN, Geneva, Jun, 2010.

[107] ATLAS Collaboration Collaboration, *Kinematic Distributions of K0s and Lambda decays in collision data at sqrt(s) = 7 TeV*, Tech. Rep. ATLAS-CONF-2010-033, CERN, Geneva, Jul, 2010.

[108] CMS Collaboration Collaboration, *LHC Combination: Top mass*, Tech. Rep. CMS-PAS-TOP-12-001, CERN, Geneva, 2012.

[109] ATLAS Collaboration Collaboration, *Determination of the Top-Quark Mass from the ttbar Cross Section Measurement in pp Collisions at $\sqrt{s}$ = 7 TeV with the ATLAS detector*, . ATLAS-CONF-2011-054.

[110] CMS Collaboration, *Determination of the top quark mass from the $t\bar{t}$ cross section measured by CMS at $\sqrt{s}$ = 7 TeV*, `arXiv:1201.5336 [hep-ex]`.

[111] CMS Collaboration, C. Collaboration, *Determination of the top-quark pole mass and strong coupling constant from the t/bartt production cross section in pp collisions at $\sqrt{s}$ = 7 TeV*, Tech. Rep. arXiv:1307.1907. CMS-TOP-12-022. CERN-PH-EP-2013-121, CERN, Geneva, Jul, 2013. Comments: Submitted to Phys. Lett. B.

[112] S. Alioli, P. Fernandez, J. Fuster, A. Irles, S.-O. Moch, et al., *A new observable to measure the top-quark mass at hadron colliders*, `arXiv:1303.6415 [hep-ph]`.

[113] ATLAS Collaboration Collaboration, *Measurement of the Top-Quark Mass using the Template Method in pp Collisions at root(s)=7 TeV with the ATLAS detector*, Tech. Rep. ATLAS-CONF-2011-033, CERN, Geneva, Mar, 2011.

[114] ATLAS Collaboration Collaboration, G. Aad et al., *Measurement of the top quark mass with the template method in the $t\bar{t}$ -gt; lepton + jets channel using ATLAS data*, Eur.Phys.J. **C72** (2012) 2046, arXiv:1203.5755 [hep-ex].

[115] *Measurement of the Top Quark Mass from $\sqrt{s}$ = 7 TeV ATLAS Data using a 3-dimensional Template Fit*, Tech. Rep. ATLAS-CONF-2013-046, CERN, Geneva, May, 2013.

[116] ATLAS Collaboration Collaboration, *Top quark mass measurement in the e channel using the mT2 variable at ATLAS*, Tech. Rep. ATLAS-CONF-2012-082, CERN, Geneva, Jul, 2012.

[117] CMS Collaboration Collaboration, *Measurement of the top quark mass using the B-hadron lifetime technique*, Tech. Rep. CMS-PAS-TOP-12-030, CERN, Geneva, 2013.

[118] S. Frixione, P. Nason, and C. Oleari, *QCD computation with Parton Shower simulations: The POWHEG method*, J. High Energy Phys. **11** (2007) 070.

[119] T. Sjöstrand, S. Mrenna, and P. Z. Skands, *PYTHIA 6.4 Physics and Manual*, JHEP **05** (2006) 026, arXiv:hep-ph/0603175.

[120] P. Skands, *Tuning Monte Carlo generators: The Perugia tunes*, Phys. Rev. D **82** (2010) 074018.

[121] M. Aliev, H. Lacker, U. Langenfeld, S. Moch, P. Uwer, and M. Wiedermann, *HATHOR, HAdronic Top and Heavy quarks cross section calculatoR*, Comput. Phys. Commun. **182** (2011) 1034–1046.

[122] B. Kersevan and E. Richter-Was, *The Monte Carlo event generator AcerMC version 1.0 with interfaces to PYTHIA 6.2 and HERWIG 6.3*, Comput. Phys. Commun. **149** (2003) 142.

[123] M. Bahr, S. Gieseke, M. A. Gigg, D. Grellscheid, K. Hamilton, O. Latunde-Dada, S. Platzer, P. Richardson, M. H. Seymour, A. Sherstnev, J. Tully, and B. R. Webber, *Herwig++ Physics and Manual*, arXiv:0803.0883. Program and additional information available from http://projects.hepforge.org/herwig.

[124] ATLAS Collaboration Collaboration, G. Aad et al., *The ATLAS Simulation Infrastructure*, Eur.Phys.J. **C70** (2010) 823–874, arXiv:1005.4568 [physics.ins-det].

[125] J. Allison et al., *Geant4 developments and applications*, IEEE Trans. Nucl. Sci. **53** (2006) 270–278.

[126] W. Lukas, *Fast Simulation for ATLAS: Atlfast-II and ISF*, ATL-SOFT-PROC-2012-065, ATL-COM-SOFT-2012-137, 2012.

[127] K. Becker, A. Cortes Gonzalez, V. Dao, F. Derue, K. Gellerstedtf, D. Hirschbuehl, J. Howarth, H. Khandanyan, F. Kohn, T. M. Liss, M. A. Owen, M. Pinamonti, E. Shabalina, P. Sturm, A. Succurro, T. Theveneaux-Pelzerd, W. Wagner, W. H. Bell, and J. Sjolin, *Mis-identified lepton backgrounds in top quark pair production studies for EPS 2011 analyses*, Tech. Rep. ATL-COM-PHYS-2011-768, CERN, Geneva, Jun, 2011.

[128] ATLAS Collaboration Collaboration, G. Aad et al., *Measurement of the charge asymmetry in top quark pair production in pp collisions at $\sqrt{s}$ = 7 TeV using the ATLAS detector*, Eur.Phys.J. **C72** (2012) 2039, arXiv:1203.4211 [hep-ex].

[129] ATLAS Collaboration Collaboration, G. Aad et al., *Improved luminosity determination in pp collisions at sqrt(s) = 7 TeV using the ATLAS detector at the LHC*, arXiv:1302.4393 [hep-ex].

[130] K. Nakamura et al., *Review of particle physics*, J.Phys.G **G37** (2010) 075021.

[131] ATLAS Collaboration, *Performance of Missing Transverse Momentum Reconstruction in ATLAS with 2011 Proton-Proton Collisions at $\sqrt{s}$ = 7 TeV*, ATLAS-CONF-2012-101, 2012. https://cds.cern.ch/record/1463915.

[132] S. Frixione, P. Nason, and B. Webber, *Matching NLO QCD computations and parton shower simualtions*, J. High Energy Phys. **08** (2003) 007.

[133] *Measurement of the jet multiplicity in top anti-top final states produced in 7 TeV proton-proton collisions with the ATLAS detector*, Tech. Rep. ATLAS-CONF-2012-155, CERN, Geneva, Nov, 2012.

[134] X. Artru and G. Mennesier Nucl. Phys. B **70** (1974) 93.

[135] *ROOT*, http://root.cern.ch/drupal/. Accessed: 2013-11-30.

[136] T. Muta, *Foundations of Quantum Chromodinamics: An Introduction to Perturbative Methods in Gauge Theories*, vol. 78 of *World Scientific Lectures Notes in Physics*. World Scientific Publicshing, Singapore, 2010.

[137] S. Z. Zhi-zhong Xing, He Zhang, *Updated Values of Running Quark and Lepton Masses*, Phys.Rev. **D77** (2008) 113016.

[138] C. Escobar, *Alignment of the ATLAS silicon tracker and measurement of the top quark mass*. PhD thesis, Universitat de València, Estudi General, July, 2010. CERN-THESIS-2010-092.

[139] F. James, *Statistical methods in experimental physics*. World Scientific, 2006.

[140] ATLAS Collaboration Collaboration, G. e. a. Aad, *Single hadron response measurement and calorimeter jet energy scale uncertainty with the ATLAS detector at the LHC*, Eur. Phys. J. C **73** (Mar, 2012) 2305. 36 p. Comments: 24 pages plus author list (36 pages total), 23 figures, 1 table, submitted to European Physical Journal C.

[141] ATLAS Collaboration Collaboration, *ATLAS jet energy scale uncertainties using tracks in proton proton collisions at $\sqrt{s}$ = 7 TeV*, Tech. Rep. ATLAS-CONF-2011-067, CERN, Geneva, May, 2011.

[142] ATLAS Collaboration Collaboration, *Performance of the ATLAS Secondary Vertex b-tagging Algorithm in 7 TeV Collision Data*, Tech. Rep. ATLAS-CONF-2010-042, CERN, Geneva, Jul, 2010.

[143] ATLAS Collaboration Collaboration, G. Aad et al., *Charged-particle multiplicities in pp interactions measured with the ATLAS detector at the LHC*, New J.Phys. **13** (2011) 053033, arXiv:1012.5104 [hep-ex].

[144] ATLAS Collaboration Collaboration, *Jet energy measurement and systematic uncertainties using tracks for jets and for b-quark jets produced in proton-proton collisions at $\sqrt{s}$ = 7 TeV in the ATLAS detector*, Tech. Rep. ATLAS-CONF-2013-002, CERN, Geneva, Jan, 2013.